Summer 2014

Investigation and Optimization of a New Compact Superconducting Cavity for Deflecting and Crabbing Applications

Subashini Uddika De Silva
Old Dominion University

INVESTIGATION AND OPTIMIZATION OF A NEW COMPACT SUPERCONDUCTING CAVITY FOR DEFLECTING AND CRABBING APPLICATIONS

by

Subashini Uddika De Silva
B.S. September 2004, University of Colombo
M.S. May 2008, Old Dominion University

A Dissertation Submitted to the Faculty of
Old Dominion University in Partial Fulfillment of the
Requirements for the Degree of

DOCTOR OF PHILOSOPHY

PHYSICS

OLD DOMINION UNIVERSITY
August 2014

Approved by:

Jean R. Delaven (Director)

Geoffrey A. Krafft (Member)

Gail E. Dodge (Member)

Alexander L. Godunov (Member)

Hani E. Elsayed-Ali (Member)

ABSTRACT

INVESTIGATION AND OPTIMIZATION OF A NEW COMPACT SUPERCONDUCTING CAVITY FOR DEFLECTING AND CRABBING APPLICATIONS

Subashini Uddika De Silva
Old Dominion University, 2014
Director: Dr. Jean R. Delayen

Deflecting and crabbing structures have many applications in current accelerator systems. The primary use of a deflecting cavity is to separate a single beam into multiple beams. A crabbing cavity enables the head-on collision at the interaction point in particle colliders in order to increase the luminosity. The early uses of the deflecting structures have been in the early 1960s; these structures were disk loaded structures operating at room temperature. The crabbing structure which was installed at the KEK electron-positron collider was the first and only operational superconducting cavity of that kind. The most common design of superconducting deflecting and crabbing cavities is a squashed-elliptical geometry operating in a TM_{110}-like mode; at low frequencies these structures become challenging due to the large geometrical shapes. Recently, compact deflecting and crabbing structures have been studied for numerous accelerator applications not limited to deflecting or crabbing of beams, but also for beam diagnostics, emittance exchange etc. The rf-dipole design, which is presented here, has evolved from the parallel-bar design and is a new compact deflecting and crabbing design with attractive properties at low frequencies and is operating in a TE_{11}-like mode. The parallel-bar design has been optimized into the rf-dipole design primarily to maximize the net deflection with low and balanced peak surface fields and also to maximize the shunt impedance. The geometries have also been modified to increase the separation between the higher order modes, suppress multipacting conditions and reduce multipole components. The design geometries have been improved for mechanical stability in order to withstand thermal and pressure fluctuations under operating conditions. Two superconducting rf-dipole deflecting and crabbing cavities have been designed and optimized at 499 MHz for the Jefferson Lab 12 GeV Upgrade and at 400 MHz for a crabbing cavity for the LHC Luminosity Upgrade. The design optimization, fabrication, and test results of the first prototypes of both designs are presented in detail.

TO MY MOTHER

For all you are,
and all the sacrifices you have made
throughout the years...
"Thank you, Amma."
I'm so grateful,
and I will always love you...

ACKNOWLEDGEMENTS

I would like to first thank my research adviser Dr. Jean Delayen, for giving me this unique opportunity to work on this new deflecting and crabbing design and having faith in me to work on this project. Thank you for having patience and always guiding me to perform to my very best whether doing research work, writing a research article, or giving a presentation. I was given every possibility to expand my knowledge on the subject and all the opportunities to present my work in the presence of the accelerator science community. It has been a very rewarding journey to work under his guidance where I have learned and accomplished enormously.

Huge thanks to Dr. Gail Dodge, who was the Chair of Department of Physics at the time I joined ODU, for suggesting me to join Dr. Delayen to work on my thesis research. Thank you for advising and supporting me in my work and mentoring me to pass through the hard times.

I am particularly grateful to Dr. Geoffrey Krafft, the Director for Center for Advanced Studies of Accelerators (CASA) at Jefferson Lab, for being a good critique on my research and for the valuable insights and regular feedback that have helped me to improve my work.

I would also like to thank Dr. Godunov and Dr. Hani Elsayed-Ali for being in my PhD thesis committee. Thank you for the ideas and suggestions to improve my work during the thesis evaluation meetings.

I am especially grateful to Dr. Hari Areti at Jefferson Lab for encouraging me every step of the way during my research activities and for the financial support through JSA. I am especially grateful to Dr. Peter Kneisel, for his help and support and always being around the corner whenever we required advice or suggestion in our experiments. I am honored to have learned and worked with one of pioneers in superconducting rf field.

I would like to thank Dr. Lepsha Vuskovic, the Graduate Program Director at ODU for the continuous advices given, not only on the academics, but also on a personal level since the day I started my graduate studies. Many thanks go to all the professors at ODU for teaching and making the learning experience an enjoyable one. I am also thankful to all the former and current staff at ODU for helping me on multiple occasions, both during my teaching and research work.

A very special thank goes HyeKyoung Park, from the Engineering Division at Jefferson Lab, for sharing her knowledge and ideas in completing the cavity fabrication work successfully and helping me throughout in all the cavity tests. I have learned so much working with her. I am sincerely thankful for all the late nights, extended hours of experiments and data taking, and most importantly the friendship.

I am thankful to Erk Jensen at CERN and Alessandro Ratti at LBNL for the support and encouragement given for my research. I would like to thank Terry Grimm, Dmitry Gorelov, Chase Boulware and Nick Miller at Niowave Inc. for the work carried out on fabricating the 400 MHz crabbing cavity. Huge thank goes to Zenghai Li for always helping with the issues related to the subject matter and the collaborative work done on the rf-dipole design, and both Zenghai Li and Lixin Ge for assisting me with the SLAC ACE3P Suite. I would also like to thank Rama Calaga at CERN for always finding time to answer the questions I had related to the LHC high luminosity upgrade.

Working at Jefferson Lab I had the opportunity to learn from the best in the SRF field. I would like to thank Haipeng Wang, Frank Marhauser, John Mammoser, Curt Hovater and John Musson for support and willingness to share their expertise with me since the very early days at Jefferson Lab. I am undoubtedly grateful to Charlie Reece for the support given for my experimental work at Jefferson Lab, Joe Preble and Tony Reilly for facilitating all the activities from cavity fabrication, treatment to rf testing. Especially, I am thankful to Tom Powers for helping me in the cavity tests, Kirk Davis for all the support in preparation for the rf tests, and Rongli Geng for the guidance in surface treatment techniques. Many thank to Alicia Hoffler who have helped me since my very first day at Jefferson Lab, on numerous occasions.

I am extremely thankful to Danny Forehand for frequent assistance during cavity processing and preparation, Pete Kushnick for support with cryogenics, Larry Turlington for the assistance given on the cavity drawings, and Bill Clemens for doing wonders in welding the 499 MHz cavity. I greatly appreciate the support received by Era Perry in working at the chemical lab. Great thanks go to Roland Overton for allowing us to utilize his work space and equipment during the measurements frequently. I would also like to thank Casy Apeldoorn, Dave McCay and all the staff at the machine shop at Jefferson Lab for all the machining work.

I am sincerely thankful to Chris Hopper and Alex Castilla the partners in crime for the endless support and being there during my research work in helping out with

the experimental work, in numerous discussions, late night endeavors at the lab in preparing the cavities for rf tests, and for always doing it with a smile. I would also like to thank Kevin Mitchell for numerous support given for carrying out my experimental work.

I owe all my success to Amma (my mother) who has always dreamed big for us and letting me come far away from home and going through all the hard times to see that I will fulfill my dreams. You have always given me strength, encouraged me, and pushed me to perform the very best in everything I do. Thank you for the overwhelming love and infinite tolerance. I would also like to thank my father and my brother for always supporting my decisions and helping me to make them a reality. Also my Mama and Punchi for the unconditional love and inspiration.

Special thanks to Janardan Upadhyay for being extremely supportive, all the time I needed help. Most importantly, I would like to thank Senthilraja Singaravelu for the constant support. A special thanks to Rasika Jayatillake for being a dear friend and a sister to me all these years since our high school days and supporting immensely to go through all the good and bad times during the days at ODU. Big thank to all my Sri Lankan friends who have made my stay in Norfolk enjoyable and memorable.

Last but not the least I would like to express gratitude to Dr. Ariyarathne, Dr. Jayanetti, Dr. Rosa, Dr. Wijerathne and Dr. Lelwala and the entire faculty at the Department of Physics at UoC for encouraging me to pursue graduate studies.

The list is endless, but I would like to thank all who have helped me in every way during this journey.

TABLE OF CONTENTS

LIST OF TABLES

LIST OF FIGURES

CHAPTER 1

INTRODUCTION

Superconducting radio-frequency (rf) technology, which marked 50 years in 2011, has evolved over the years in pushing higher limits of operation. The main advantages of superconducting resonant cavities are high gradients in cw operation, high shunt impedance, and reduced operating costs due to low power dissipation. These cavities have about five orders of magnitude lower losses compared to normal conducting copper cavities, and have achieved specifications that are not possible with normal conducting rf cavities. The resonant cavities operating at room temperature are primarily limited by the ohmic losses in the cavity.

Currently there are large machines that have operated and are operating using the superconducting technology with pure niobium cavities or copper cavities sputtered with niobium. The facilities Transposable Ring Intersecting Storage Accelerator in Nippon (TRISTAN) at KEK - High Energy Accelerator Research Organization in Japan, the Large Electron-Positron (LEP) at Conseil Européen pour la Recherche Nucléaire (CERN) and the Hadron Electron Ring Facility (HERA) at Deutsches Elektronen-Synchrotron (DESY), Germany have been discontinued. Some of the accelerators that are in operation at present with superconducting rf cavities are the Superconducting Darmstadt Electron Linear Accelerator (S-DALINAC) at Technical University of Darmstadt, Germany, the Cornell Electron Storage Ring (CESR) at Cornell University, USA, the Continuous Electron Beam Accelerator Facility (CEBAF) and the Free Electron Laser Facility (FEL) at Thomas Jefferson National Accelerator Facility (TJNAF), USA, the B-Factory at KEK in Japan, the light sources in Taiwan and Canada, DIAMOND light source in UK, SOLEIL, the French National Synchrotron Facility, the Superconducting Electron-Positron Linear Collider at Tesla Facility in Hamburg, Germany, the Spallation Neutron Source (SNS) at Oak Ridge National Laboratory (ORNL), USA, the Large Hadron Collider (LHC) at CERN. Future particle accelerators that will be using the superconducting rf technology are the European x-ray laser project - XFEL at DESY in Germany, the Energy Recovery Linac (ERL) at Cornell Univeristy, the Facility for Rare Isotope Beams (FRIB) at

Michigan State University, USA, European Spallation Source (ESS) at Lund, Sweden, and upgrade of the Linac Coherent Light Source (LCLS-II) at SLAC National Laboratory, USA.

1.1 DEFLECTING AND CRABBING CAVITIES

The primary use of superconducting rf cavities is to impart energy to charged particles such as electrons, positrons, protons, antiprotons, and heavy ions. The most common rf cavity design is the elliptical geometry that operates in a TM_{010} mode [1], where the longitudinal momentum is generated by the on axis longitudinal electric field. The elliptical rf cavities are widely used in acceleration for high beta particles, whereas the spoke cavities are preferred for low-beta and medium-beta [2, 3] acceleration and are applicable for high-beta applications as well [4]. RF quadrupole, quarter-wave and half-wave resonators [3, 5] are mostly used for low-beta low-frequency applications.

Some rf structures can also be used to generate electromagnetic fields that gives a transverse momentum to the charged particles, called deflecting and crabbing cavities. The rf structures are the same for both deflecting and crabbing of bunches, the only difference being the rf phase at which the transverse momentum is applied. In deflecting cavities a net transverse momentum is applied at the center of the bunch for bunch separation. In crabbing cavities the transverse momentum is applied at the head and tail of the bunch in opposite direction in order to rotate the bunch, enabling head-on collision of bunches at the interaction point in colliders. These cavities serve a variety of purposes in different accelerator applications that are not limited to rf separation and crabbing of bunches. Deflecting and crabbing cavities are also used for beam diagnostics, transverse and longitudinal emittance exchange in beams, and x-ray pulse compression.

Deflecting and crabbing cavities have been designed and operated since the early 1960's. A number of rf geometries have been designed that function as deflecting and crabbing cavities; the squashed elliptical geometry operating in TM_{110} mode being the most common design. In this geometry the transverse momentum is due to the interaction with the transverse magnetic field. In deflecting and crabbing cavities operating in TE-like or TEM-like modes, the transverse momentum is by both transverse electric and magnetic fields with major contribution from the transverse electric field.

1.2 MOTIVATION

Recently superconducting deflecting and crabbing cavities for particle accelerators and colliders have been an area of intense research. The future particle accelerators and colliders pushing the energy and luminosity frontiers and with multi-experimental stations have set forth tighter specifications, requiring higher operating transverse gradients with strict dimensional constraints. Superconducting deflecting and crabbing cavities have become the preferred option because they achieve higher operating transverse gradients. This reduces the number of rf cavities required in achieving the design specifications and also reduces operational costs compared to the room temperature options.

Early designs of deflecting and crabbing cavities were squashed elliptical geometries operating in TM_{110}-type mode. These cavities tend to have large transverse dimensions. Therefore these designs are not favorable in low frequency applications where the cavities become very large. Lately, the research has focused on designing and developing compact deflecting and crabbing structures that operate in TE-like or TEM-like modes. The goal of the research described here is to design a new compact superconducting deflecting and crabbing cavity. We started with the superconducting parallel-bar design, which is one of the new compact deflecting and crabbing cavity design operating in TEM-like mode. The parallel-bar design with two parallel TEM lines in a rectangular-shaped outer conductor generates a transverse electric field which produces the main contribution to the transverse momentum. This design has been further optimized into a cylindrical-shaped design with trapezoidal-shaped loading elements in order to achieve high gradients with low and balanced peak surface fields. This design has improved higher order mode properties, mechanical stability, and relaxed multipacting levels. The optimized design, named the "rf-dipole" has a similar on axis field configuration to that of the parallel-bar and does not change the fundamental operating mode.

The compact rf-dipole cavity is being considered for several deflecting and crabbing applications. Current applications are the 499 MHz deflecting cavity proposed for the Jefferson Lab 12 GeV upgrade and the 400 MHz crabbing cavity for the proposed LHC high luminosity upgrade. Two proof-of-principle cavities have been designed, developed and tested, as discussed in this thesis.

1.3 ORGANIZATION OF THE DISSERTATION

Chapter 2 gives a brief outline of the electrodynamics of rf cavities and cavity fundamentals. RF properties related to resonant cavities are derived, furthermore related to deflecting and crabbing cavities. This chapter also describes the theories on superconductivity and rf properties of superconducting structures. Chapter 2 continues with a discussion of rf limitations on cavity performance.

Chapter 3 explains the detailed concepts of deflecting and crabbing cavities and expands upon the two applications of the rf-dipole design with design specifications and dimensional requirements.

Chapter 4 introduces the important parameters relevant to our detailed design optimization for the parallel-bar design to the rf-dipole design, which was carried out by gradually modifying the geometries and improving the rf properties such as cavity gradient, peak surface fields, and shunt impedance.

Next, chapter 5 gives the detailed calculation on the higher order modes (HOM) for all the parallel-bar and rf-dipole designs and improvements in the HOM spectra with the design evaluation. The wakefield analysis shows the mode excitation for varying bunch parameters for the rf-dipole deflecting and crabbing cavities.

When considering real time operation of these rf cavities with beam, an important issue is the field non-uniformity in the transverse voltage across the beam aperture. Chapter 6 describes the geometry dependence of the field non-uniformity with a detailed calculation of multipole components. This chapter also shows the effective ways the rf-dipole geometry can be modified to suppress the multipole components.

Chapter 7 presents the in depth analysis of multipacting levels in parallel-bar and rf-dipole cavities, with critical resonant energy regions on the cavity and order of multipacting levels.

The mechanical analysis provided in Chapter 8 presents the behavior of the rf-dipole cavity under external pressure, radiation pressure and other mechanical vibrations. The details of the improved rigidity in the rf-dipole cavity with the design evolution are also explained. The study shows the stresses and frequency fluctuations experienced by the cavities due to the mechanical effects.

Chapter 9 covers the details of the fabrication process of manufacturing the rf-dipole cavities including forming and machining the parts. Also described is the trimming of the parts to obtain the design frequency and the process of electron beam welding.

For superconducting rf cavities a clean and smooth inner cavity surface, close to a pure Nb surface, is vital in achieving higher rf performance. The procedure of surface treatment and processing, and assembly of the cavities prior to rf testing are presented in Chapter 10.

Chapter 11 presents the results of the rf measurements obtained at cryogenic temperatures of 4.2 K and 2.0 K. Further measurements are given on the mechanical properties of the rf-dipole cavities.

The summarized results and conclusions are given in Chapter 12.

CHAPTER 2

CAVITY FUNDAMENTALS

RF cavities are important components in any particle accelerator. The most common use of rf cavities is to impart energy to the traversing particles. For different applications of particle accelerators, rf cavities have been optimized for different purposes, not limited to accelerating particles. Accelerating rf structures with a longitudinal electric field imparts energy to the beam. On the other hand, deflecting and crabbing rf cavities are optimized to maximize the transverse momentum provided to a particle.

An rf cavity is a structure with a electromagnetic field in it, sinusoidal in time. When properly phased with the particle bunches it imparts momentum to the particles. Depending on the electromagnetic mode, the rf structures can generate a longitudinal or transverse momentum. The geometry is optimized at the required mode and operating frequency, in order to maximize the performance of the particular mode.

2.1 ELECTROMAGNETICS OF RF STRUCTURES

An ideal cavity is a vacuum volume enclosed by perfectly conducting surfaces. The fields in cavity are solutions of Maxwell equations

$$\begin{aligned} \vec{\nabla} \cdot \vec{E} &= 0\,, \\ \vec{\nabla} \times \vec{B} &= \frac{1}{c^2}\frac{\partial \vec{E}}{\partial t}\,, \\ \vec{\nabla} \times \vec{E} &= -\frac{\partial \vec{B}}{\partial t}\,, \\ \vec{\nabla} \cdot \vec{B} &= 0\,, \end{aligned} \tag{1}$$

and the wave equation

$$\left(\nabla^2 - \frac{1}{c^2}\frac{\partial^2}{\partial t^2}\right)\left\{ \begin{array}{c} \vec{E} \\ \vec{B} \end{array} \right\} = 0\,, \tag{2}$$

with boundary conditions $\hat{n} \times \vec{E} = 0$ and $\hat{n} \cdot \vec{B} = 0$, where $\hat{n}$ is the unit vector normal to the cavity surface. $\vec{E}$ and $\vec{H}$ are electric and magnetic fields in the cavity with

$\vec{B} = \mu_0 \vec{H}$ where μ_0 is the free-space permeability. The boundary conditions reflect the absence of any parallel electric field or normal magnetic field components at the surface.

The solution of the electromagnetic fields for a cylindrical geometry will be of the form

$$\begin{aligned} \vec{E}(x,y,z,t) &= \vec{E}(x,y)e^{j(kz-\omega t)}, \\ \vec{H}(x,y,z,t) &= \vec{H}(x,y)e^{j(kz-\omega t)}, \end{aligned} \tag{3}$$

where k is the wave number and $\omega = 2\pi f$, the angular frequency of the cavity.

Two sets of solutions exist for the wave equation in a cylindrically symmetric cavity, based on the boundary conditions which are referred to as transverse magnetic (TM) and transverse electric (TE) modes. For a cylindrical cavity with radius R and length L the solutions are given by

$$\text{TM Modes:} \begin{cases} E_z = E_0 \cos\left(\frac{p\pi z}{L}\right) J_m\left(\frac{x_{mn} r}{R}\right) \cos(m\phi), \\ E_r = -E_0 \frac{p\pi R}{L x_{mn}} \sin\left(\frac{p\pi z}{L}\right) J'_m\left(\frac{x_{mn} r}{R}\right) \cos(m\phi), \\ E_\phi = E_0 \frac{mp\pi R^2}{r L x_{mn}^2} \sin\left(\frac{p\pi z}{L}\right) J_m\left(\frac{x_{mn} r}{R}\right) \sin(m\phi), \\ H_z = 0, \\ H_r = jE_0 \frac{m\omega R^2}{c\eta r x_{mn}^2} \cos\left(\frac{p\pi z}{L}\right) J_m\left(\frac{x_{mn} r}{R}\right) \sin(m\phi), \\ H_\phi = jE_0 \frac{\omega R}{c\eta x_{mn}} \cos\left(\frac{p\pi z}{L}\right) J'_m\left(\frac{x_{mn} r}{R}\right) \cos(m\phi), \end{cases} \tag{4}$$

and

$$\text{TE Modes:} \begin{cases} H_z = H_0 \sin\left(\frac{p\pi z}{L}\right) J_m\left(\frac{x'_{mn} r}{R}\right) \cos(m\phi), \\ H_r = H_0 \frac{p\pi R}{L x'_{mn}} \cos\left(\frac{p\pi z}{L}\right) J'_m\left(\frac{x'_{mn} r}{R}\right) \cos(m\phi), \\ H_\phi = -H_0 \frac{mp\pi R^2}{r L (x'_{mn})^2} \cos\left(\frac{p\pi z}{L}\right) J_m\left(\frac{x'_{mn} r}{R}\right) \sin(m\phi), \\ E_z = 0, \\ E_r = jH_0 \frac{m\eta\omega R^2}{cr(x'_{mn})^2} \sin\left(\frac{p\pi z}{L}\right) J_m\left(\frac{x'_{mn} r}{R}\right) \sin(m\phi), \\ E_\phi = jH_0 \frac{\eta\omega R}{c x'_{mn}} \sin\left(\frac{p\pi z}{L}\right) J'_m\left(\frac{x'_{mn} r}{R}\right) \cos(m\phi), \end{cases} \tag{5}$$

where c is the speed of light, η is the free space impedance, ω is the frequency of each mode, J_m is the m^{th} order Bessel function of first kind and J'_m is its derivative. The x_{mn} and x'_{mn} are the n^{th} zero of the Bessel functions J_m and J'_m of order m

respectively. The modes are categorized as TM_{mnp} or TE_{mnp} where m, n, and p are integers that corresponds to the number of sign changes of E_z or H_z in ϕ, r, and z directions considering a cylindrical coordinate system. The frequency of TM and TE modes are given by

$$\omega_{TM_{mnp}} = c\sqrt{\left(\frac{x_{mn}c}{R}\right)^2 + \left(\frac{p\pi}{L}\right)^2}, \tag{6}$$

$$\omega_{TE_{mnp}} = c\sqrt{\left(\frac{x'_{mn}c}{R}\right)^2 + \left(\frac{p\pi}{L}\right)^2}. \tag{7}$$

The lowest modes of the two sets are TM_{010} mode and TE_{111} mode. TM_{0np} are the modes with a non-zero longitudinal electric field component on axis, and the TM_{010} mode, for which the field profile is shown in Fig. 1, is the fundamental mode used for acceleration.

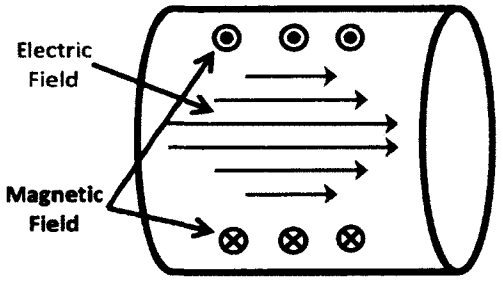

FIG. 1. Electric and magnetic fields of the TM_{010} mode in a cylindrical cavity.

In 1970 very encouraging results were achieved with the pillbox geometry operating in TM_{010} mode that demonstrated peak electric and magnetic fields of 70 MV/m and 108 mT with an 8.5 GHz cavity fabricated with reactor grade niobium [6]. However, the cylindrical-shaped geometry is not the ideal shape due to multipacting levels, a detrimental condition in rf cavities; that was experienced in the magnetic field region in the pillbox cavity [7]. Therefore the geometry was modified to elliptical-shaped geometries with elliptical arcs at the equator and iris as shown in Fig. 2 [8]. The very first numerical calculations showed no multipacting trajectories, which was confirmed by experimental results [9]. The detailed optimization carried out on the elliptical geometries has resulted further in improvements with reduced peak field ratios that is favorable in achieving high cavity performance [1].

The TM_{110} mode is a common mode for deflecting and crabbing of particles.

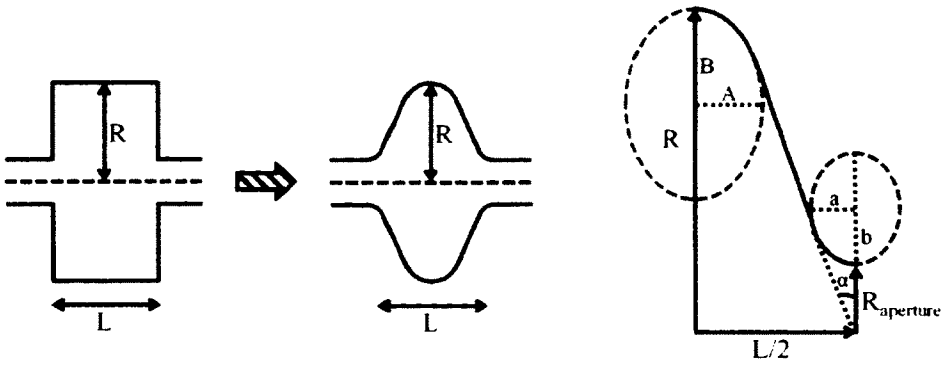

FIG. 2. Transition from pillbox cavity to elliptical cavity.

In the TM_{110} mode the on axis longitudinal electric field is zero and there is a transverse magnetic field component. For a symmetrical geometry this mode has two polarizations with the same frequency that generate a transverse momentum in two directions perpendicular to one another. Therefore the geometry is adapted into a squashed elliptical shape to remove the degeneracy of the two polarizations. The field distribution for a TM_{110} mode in a squashed elliptical geometry is shown in Fig. 3.

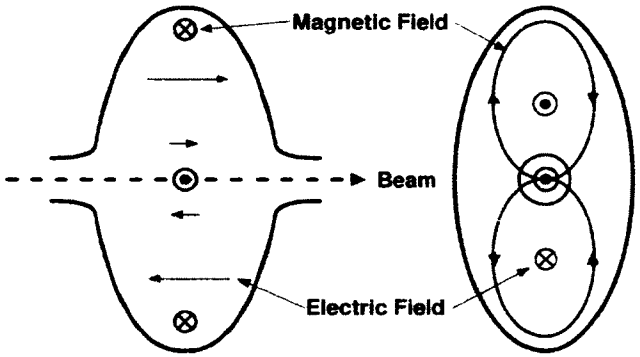

FIG. 3. Electric and magnetic fields for the TM_{110} mode in a squashed elliptical cavity.

The TE_{111} mode also has an on-axis transverse electric field as shown in Fig. 4. However, this mode cannot be used as a deflecting mode due to the fact that the net effect from the electric field is canceled by the magnetic field component when integrated along the beam line.

For a cylindrical pill box cavity with radius R and length L the electric and

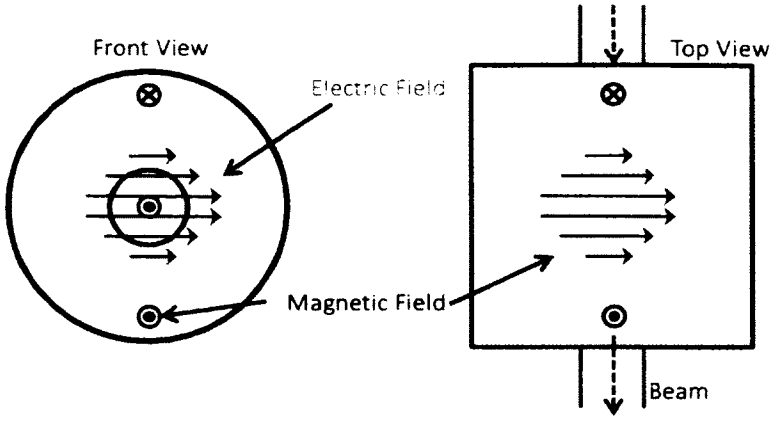

FIG. 4. Electric and magnetic fields for the TE_{111} mode in a cylindrical cavity.

magnetic field components can be derived from equations 4 and 5, and are given by

$$\text{TM}_{010}\text{ Mode: } \begin{cases} E_z = E_0 J_0\left(\frac{x_{01} r}{R}\right) e^{-j\omega t}, \\ H_\phi = -j\frac{E_0}{\eta} J_1\left(\frac{x_{01} r}{R}\right) e^{-j\omega t}. \end{cases} \tag{8}$$

$$\text{TM}_{110}\text{ Mode: } \begin{cases} E_z = E_0 J_1\left(\frac{x_{11} r}{R}\right)\cos(\phi) e^{-j\omega t}, \\ H_r = jE_0\frac{1}{k\eta r} J_1\left(\frac{x_{11} r}{R}\right)\sin(\phi) e^{-j\omega t}, \\ H_\phi = jE_0\frac{1}{\eta} J_1'\left(\frac{x_{11} r}{R}\right)\cos(\phi) e^{-j\omega t}, \end{cases} \tag{9}$$

$$\text{TE}_{111}\text{ Mode: } \begin{cases} H_z = H_0\frac{\eta^2}{c}\sin\left(\frac{\pi z}{L}\right) J_1\left(\frac{x'_{11} r}{R}\right)\cos(\phi) e^{-j\omega t}, \\ H_r = H_0\frac{\pi R}{L x'_{11}}\cos\left(\frac{\pi z}{L}\right) J_1'\left(\frac{x'_{11} r}{R}\right)\cos(\phi) e^{-j\omega t}, \\ H_\phi = -H_0\frac{\pi R^2}{r L (x'_{11})^2}\cos\left(\frac{\pi z}{L}\right) J_1\left(\frac{x'_{11} r}{R}\right)\sin(\phi) e^{-j\omega t}, \\ E_r = jH_0\frac{\eta}{kr}\sin\left(\frac{\pi z}{L}\right) J_1\left(\frac{x'_{11} r}{R}\right)\sin(\phi) e^{-j\omega t}, \\ E_\phi = jH_0\eta\sin\left(\frac{\pi z}{L}\right) J_1'\left(\frac{x'_{11} r}{R}\right)\cos(\phi) e^{-j\omega t}, \end{cases} \tag{10}$$

where $x_{01} = 2.405$, x_{11}=3.832, and x'_{11}=1.841 are the first zeroes of J_0, J_1, and J_1'.

For TM-type cavities operating in the TM_{010} or TM_{110} mode the frequency of the mode does not depend on the longitudinal dimensions of the cavity. However, to maximize the acceleration or deflection of a particle during the transit through the cavity, the time varying field must point in the same direction. Therefore, for

maximum acceleration the length of the cavity is equal to the distance traveled during one-half the rf period which is a half-wavelength. Additionally, for TM_{110} cavities one of the transverse dimensions exceeds the other in order to separate the two polarizations of the TM_{110} mode. The dependence of the frequency on the cavity dimensions leads to large shapes at low frequencies. However, feasible cavity geometries are possible at higher operating frequencies.

Another type of solution for the wave equation in multi-connected geometries is the TEM-type mode where both longitudinal electric and magnetic fields are zero. In TEM-type cavities, for velocity-of-light particles, both length and transverse dimensions are of the order of one half-wavelength [10]. Therefore, these types of cavities may be used for low frequency applications where TM-type elliptical cavities would be excessively large. TEM-type cavities that are used for acceleration are quarter wave resonators, half-wave resonators and single or multi-spoke cavities [3, 5, 11]. The transverse electromagnetic fields on axis in TEM-type cavities make these designs ideal candidates for deflecting and crabbing cavities. Figure 5 shows the field distribution for a TEM-type deflecting and crabbing cavity design, named the parallel-bar design [10].

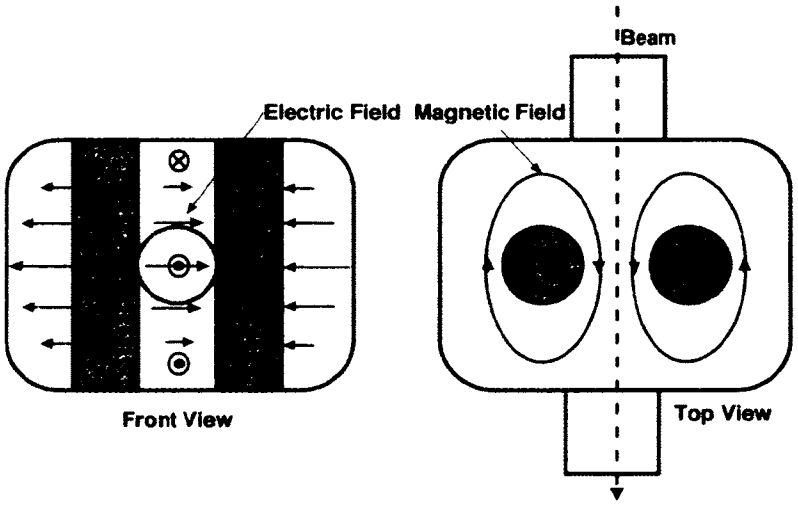

FIG. 5. Electric and magnetic fields of TEM-type parallel-bar cavity.

In actual applications, the rf cavities have more complex geometries than the cylindrical cavities because they are optimized to achieve best performance and to avoid any limitations during operation. These rf geometries cannot be optimized using analytical methods and therefore require numerical codes such as Superfish

[12], which is a 2-D code, or 3-D codes such as MAFIA, CST Microwave Studio [13], or HFSS [14].

2.2 CAVITY PROPERTIES

2.2.1 TRANSVERSE VOLTAGE

In deflecting and crabbing cavities the transverse momentum ($\vec{p}_t$) experienced by a particle passing along the beam axis is a direct result of the interaction of the particle and the transverse electric and magnetic field components present in the cavity.

$$\vec{p}_t = \int_{-\infty}^{\infty} \vec{F}_t \, \mathrm{d}t = \frac{q}{v} \int_{-\infty}^{+\infty} \left[\vec{E}_t + (\vec{v} \times \vec{B}_t) \right] \mathrm{d}z, \tag{11}$$

where $\vec{F}_t$ is the transverse Lorentz Force, q is the charge of the particle, $\vec{v}$ is the velocity of the particle of magnitude v, and $\vec{E}_t$ and $\vec{B}_t$ are the corresponding transverse electric and magnetic field components. Equation (11) is strictly valid only when the longitudinal velocity is much larger that the transverse velocity, and when the velocity does not change in the cavity.

The Panofsky-Wenzel Theorem [15, 16] relates the transverse momentum acquired by the particle to the gradient of the longitudinal electric field along the beam axis under the assumption that the particle travels at a constant velocity on a straight line:

$$\begin{aligned} \vec{p}_t &= -i\frac{q}{\omega} \int_{-\infty}^{+\infty} \vec{\nabla}_t E_z \, \mathrm{d}z \,, \\ &= -i\frac{q}{\omega} \lim_{r_0 \to 0} \frac{1}{r_0} \int_{-\infty}^{+\infty} [E_z(r_0, z) - E_z(0, z)] \, \mathrm{d}z, \end{aligned} \tag{12}$$

where ω is the frequency of the deflecting mode, r_0 is the transverse offset in the direction of the deflection from the beam axis, and E_z is the longitudinal electric field component at the offset r_0. This theorem is valid for any type of deflecting mode of any geometry. The entire length along the beam line must be considered in determining the transverse voltage since a small amount of the transverse field extends into the beam apertures at the ends of the cavity.

For a pure TEM-type parallel-bar design [10] or TE-type rf-dipole design [17], the transverse field components on axis that contribute to the net deflection are of

the form

$$\vec{E}_t = \vec{E}_x(z)\cos(\omega t), \tag{13}$$

$$\vec{H}_t = \vec{H}_y(z)\sin(\omega t). \tag{14}$$

Hence, for a particle with velocity $\beta = 1$, the transverse voltage is given by

$$V_t = \int_{-\infty}^{+\infty} \left[E_x(z)\cos\left(\frac{\omega z}{c}\right) + cB_y(z)\sin\left(\frac{\omega z}{c}\right)\right] \mathrm{d}z. \tag{15}$$

The optimal effective length of the structure along the beam line for a particle traveling at the velocity of light will be of the order of $n\lambda/2$ where λ is the free-space wavelength of the deflecting mode and n is the number of pairs of bars. We define the transverse deflecting field by

$$E_t = \frac{V_t}{n\lambda/2}, \tag{16}$$

where V_t is the transverse voltage acquired by the particle. In all the geometries presented here $n = 1$, and therefore

$$E_t = \frac{V_t}{\lambda/2}. \tag{17}$$

The half-wavelength was chosen as the reference length in the definition of the transverse deflecting field instead of the cavity length since $\lambda/2$ is constant whereas the cavity length is a free optimization parameter that may be different between various designs.

2.2.2 SHUNT IMPEDANCE

An important figure of merit for any rf cavity that relates to the performance is the unloaded quality factor (Q_0), which is the ratio between the stored energy (U) and power dissipated (P_{diss}) through the surface per radian

$$Q_0 = \frac{\omega U}{P_{diss}}. \tag{18}$$

The stored energy in an rf cavity is given by

$$U = \frac{1}{2}\varepsilon_0 \int_V \mid \vec{E} \mid^2 \mathrm{d}v = \frac{1}{2}\mu_0 \int_V \mid \vec{H} \mid^2 \mathrm{d}v. \tag{19}$$

and power dissipation is given by

$$P_{diss} = \frac{1}{2} R_s \int_S \mid \vec{H} \mid^2 \mathrm{d}s. \tag{20}$$

where $\vec{E}$ and $\vec{H}$ are the electric and magnetic fields in the cavity.

The shunt impedance (R_{sh}) for an rf cavity, defined as

$$R_{sh} = \frac{V^2}{P_{diss}}. \tag{21}$$

is related to the cavity voltage (V) and dissipated power through the cavity surface (P_{diss}). The corresponding transverse shunt impedance that relates to a transverse cavity voltage (V_t) is referred to as R_t.

The other parameter of interest is the product of transverse shunt impedance (R_t) and surface resistance (R_s) that is related to the geometrical factor (G) and transverse $[R/Q]$ for the cavity

$$R_t R_s = \frac{V_t^2}{P_{diss}} \frac{G}{Q_0} = \frac{V_t^2}{\omega U} \frac{\omega U}{P_{diss}} \frac{G}{Q_0} = \left[\frac{R}{Q}\right]_t G. \tag{22}$$

The geometrical factor defined as

$$G = Q_0 R_s, \tag{23}$$

is a parameter that is only dependent on the cavity shape, and is independent of the size and material. The transverse $[R/Q]$ is defined as

$$\left[\frac{R}{Q}\right]_t = \frac{V_t^2}{\omega U}. \tag{24}$$

2.3 RF POWER COUPLING

The electromagnetic fields in any rf cavity are produced by the rf power generated and transmitted by an external power source such as power amplifiers or high power klystrons. The rf power is transferred to the cavity by rf power couplers, which are a very important auxiliary components in achieving the maximum cavity performance. The fundamental power couplers have been extensively studied for producing good coupling in rf cavities operating at a wide range of frequencies and power requirements [18, 19]. The two main choices of rf couplers are coaxial couplers and waveguides. The preference of a coupler type in any cavity system is governed by the cavity frequency, cavity type, use of standing wave or travelling wave, maximum rf power required to be transmitted, and pulsed or continuous wave (cw) operation. The coaxial type couplers are more compact compared to waveguides where the size of the waveguide coupler are determined by the cutoff frequency.

The strength of coupling is determined by how strongly the power coupler couples to the fundamental operating mode and is characterized by the external quality factor Q_{ext} defined as

$$Q_{ext} = \frac{\omega U}{P_e} . \tag{25}$$

where ω is the cavity resonant frequency, U is the stored energy of the cavity and P_e is the power exiting the cavity through the power coupler. Strong coupling gives low Q_{ext} values and vice versa for weak coupling as shown by Eq. 25. The rf power transmitted into the cavity is measured by another coupler named the pickup field probe represented by the quality factor Q_t. The total power leaving the cavity includes the power dissipated in the cavity (P_{diss}), the transmitted power (P_t) and the reflected power (P_e) is given by

$$P_{tot} = P_{diss} + P_r + P_t , \tag{26}$$

which relates to the corresponding quality factors as

$$\frac{1}{Q_L} = \frac{1}{Q_0} + \frac{1}{Q_{ext}} + \frac{1}{Q_t} . \tag{27}$$

including each loss mechanism present in the cavity. The quality factor of the pickup field probe is in the range of $10^{10} - 10^{12}$, therefore negligible in evaluating the total

power required. and simplifies the loaded quality factor as following

$$\frac{1}{Q_L} = \frac{1}{Q_0} + \frac{1}{Q_{ext}}. \tag{28}$$

The coupler interaction with the cavity is characterized by the coupling parameter (β) defined as

$$\beta = \frac{P_e}{P_{diss}} = \frac{Q_0}{Q_e}. \tag{29}$$

$$Q_L = \frac{Q_0}{1+\beta}. \tag{30}$$

A larger coupling parameter implies that more power leaks out through the coupler compared to power dissipated through the cavity walls where optimum coupling is achieved at $\beta = 1$.

2.4 HIGHER ORDER MODES

The parasitic modes in any resonant rf structure are the modes present in the cavity, in addition to the fundamental operating mode that are excited by the beam. Those modes with frequencies below the operating frequency are named lower order modes (LOM). The modes with similar frequencies and different field configuration are named as similar order modes (SOM). The modes with frequencies above the operating frequency are the higher order modes (HOM). In single-cell elliptical rf structures the TM_{010}, which is the accelerating mode, is the lowest mode in the geometry. This makes the TM_{110}-type deflecting and crabbing cavity present with lower order modes that require special couplers such as notch filters to damp them. The TEM-type parallel-bar cavity and the TE-type rf-dipole cavity are deflecting and crabbing rf geometries with no lower modes.

As the beam passes through the cavity, these modes may be excited and may lead to energy losses in the beam. The beam-induced power depends on the intensity and the natural decay time of each mode when any other coupler is not present. The intensity of each mode is determined by the longitudinal and transverse $[R/Q]$, and the natural decay time given by $\tau_n = Q_{0,n}/\omega_n$ where ω_n is the frequency of each mode and $Q_{0,n}$ is its unloaded quality factor.

For an rf cavity the higher order modes consist of accelerating modes or transverse modes with net deflection in the horizontal or vertical direction. The contribution

of the accelerating modes are only from the on-axis longitudinal electric field (E_z). where the accelerating voltage is given by

$$V_{z,n} = \int_{-\infty}^{+\infty} E_{z,n} e^{-j\omega_n t} \mathrm{d}z \,. \tag{31}$$

where longitudinal $[R/Q]$ for those modes are given by

$$\left[\frac{R}{Q}\right]_{z,n} = \frac{V_{z,n}^2}{\omega_n U} = \frac{\left|\int_{-\infty}^{+\infty} E_{z,n} e^{-j\omega_n t} \mathrm{d}z\right|^2}{\omega_n U} \,. \tag{32}$$

For any transverse mode the corresponding voltage is given by

$$V_{t,n} = \int_{-\infty}^{+\infty} \left[E_{t,n} \pm jcB_{t,n}\right] e^{-j\omega_n t} \mathrm{d}z \,, \tag{33}$$

determined from the on-axis transverse electric fields (E_t) and magnetic fields (B_t) of each mode. The transverse $[R/Q]$ can then be calculated using Eq. 24

$$\left[\frac{R}{Q}\right]_{t,n} = \frac{V_{t,n}^2}{\omega_n U} = \frac{\left|\int_{-\infty}^{+\infty} \left[E_{t,n} \pm jcB_{t,n}\right] e^{-j\omega_n t} \mathrm{d}z\right|^2}{\omega_n U} \,. \tag{34}$$

RF cavities are the primary source of losses due to wakefields and resulting beam instabilities. In an rf cavity the longitudinal and transverse impedance thresholds for given beam parameters define the accepted levels of higher order mode excitation below which the instabilities can be minimized. The longitudinal effects may lead to energy spread in the beam. In addition, a beam at an offset to the beam axis may generate transverse effects that can lead to emittance growth and instabilities due to transverse instabilities. Rigorous damping is required to extract the generated higher order mode power out of the cavity, with sufficient coupling to those modes, in order to keep the mode excitation below the required impedance thresholds.

The modes excited by the charged particles may affect other particles in the same bunch or particles in bunches trailing behind, depending on the decay time of the wakefields. The resultant shorter wakefields mostly act on the same bunch leading to single bunch effects, which depend more on the $[R/Q]$ as the decay times are relatively small. The multiple bunch effects have larger decay times and act on trailing bunches as well. In a linear accelerator the effects of higher order modes are single pass effects.

However in a recirculating linac or storage rings with multi pass beams the effects may be cumulative depending on the decay time of each excited mode that may lead to multiple bunch instabilities. Since the $[R/Q]$ and $Q_{0,n}$ of each mode are properties of the cavity, damping of unwanted modes is achieved by additional couplers added to the design, and the new decay time is given by $\tau = Q_{L,n}/\omega_n$ where $Q_{L,n}$ is the loaded quality factor of each mode. The resultant longitudinal and transverse impedances are reduced and given by

$$Z_{z,n} = \left[\frac{R}{Q}\right]_n Q_{L,n}\,, \tag{35}$$

$$Z_{t,n} = \frac{\omega_n}{c}\left[\frac{R}{Q}\right]_n Q_{L,n}\,. \tag{36}$$

With strong damping achieved from the higher order mode dampers, the longitudinal and transverse impedances can then be suppressed to accepted levels.

2.5 MULTIPOLE COMPONENTS

Azimuthal asymmetry in rf structures generates a non-uniform fields across the beam aperture [20]. The non-uniformity of the transverse rf fields produces a varying transverse momentum experienced by the particles in the bunch that may lead to perturbations in the beam. These non-uniform transverse fields can generate higher orders of transverse momentum components apart from the first order transverse momentum that corresponds to the deflecting or crabbing voltage. A quantitative representation of the multipole components is derived similarly to the multiple components present in a magnet with equivalent terms of magnetic multipole strengths.

The fields in magnets are often expressed in terms of multipole components

$$B(r,\phi) = \sum_{n=1}^{\infty} C_n(r,\phi) r^{n-1} e^{j(n-1)\phi}\,, \tag{37}$$

where the coefficients C_n characterize the magnitude and orientation of each multipole component and n indicates the order of multipoles. The order $n = 1$ is the dipole component, $n = 2$ is the quadrupole component, $n = 3$ is the sextupole component, $n = 4$ is the octupole component, and so on. The strength of the multipole fields is dependent on the distance from the center of the axis and varies as r^{n-1} for each order n. The coefficients C_n can be written as $C_n = |C_n|e^{jn\phi_n}$ where ϕ_n represents the phase of C_n and multipoles with $\phi_n = 0$ gives the normal components

while $\phi_n = \pi/2$ gives the skew components. The standard representation of multipole fields for a magnet [21] can be expressed as

$$B(r,\phi) = B_{ref} \sum_{n=1}^{\infty} (a_n + jb_n) \left(\frac{r}{r_{ref}}\right)^{n-1} e^{j(n-1)\phi} . \tag{38}$$

where B_{ref} is the reference magnetic field at a given radius of r_{ref}, a_n are the normal multipole components and b_n are the skew components of order n.

Similarly, close to the beam axis, the electro-magnetic fields in an rf cavity within the beam aperture can be represented by Eq. (38) [22]. Magnetic multipoles are static components and have no dependence on the longitudinal position of the particles within a bunch. On the contrary, multipole components in an rf cavity have a time dependence and therefore depend on the rf phase of the particle. The general representation of time dependent multipole fields for an rf cavity that produces a resultant longitudinal or transverse momentum can be given as

$$E_{acc}(r,\phi,z,t) = E_z(r,\phi,z)e^{j\omega t} = \sum_{n=0}^{\infty} E_z^{(n)}(z) r^n e^{jn\phi} e^{j\omega t} . \tag{39}$$

The multipole fields of order n, $E_z^{(n)}(z)$ along the beam line can be obtained by using the Fourier series expansion of $E_z(r,\phi,z)$

$$E_z^{(n)}(z) = \frac{1}{2\pi}\frac{1}{r^n}\int_0^{2\pi} E_z(r,\phi,z)e^{jn\phi}\mathrm{d}\phi , \tag{40}$$

$$= \frac{1}{2\pi}\frac{1}{r^n}\int_0^{2\pi} E_z(r,\phi,z)\left[\cos(n\phi) + j\sin(n\phi)\right]\mathrm{d}\phi . \tag{41}$$

The first term in Eq. 41 gives the normal multipole components and the terms associated with $\sin(n\phi)$ give the skew multipole components for an rf cavity. Then the time dependent multipole components are given by

$$E_{acc}^{(n)}(z,t) = E_z^{(n)}(z)e^{j\omega t} = \frac{1}{2\pi}\frac{1}{r^n}\int_0^{2\pi} E_z(r,\phi,z)\left[\cos(n\phi) + j\sin(n\phi)\right]e^{j\omega t}\mathrm{d}\phi . \tag{42}$$

The zeroth component $\left(E_z^{(0)}(z)\right)$ reproduces the accelerating voltage in the cavity and is zero for the deflecting and crabbing cavities and $\left(E_z^{(1)}(z)\right)$ is the dipole component which contributes to the deflecting voltage. The transverse momentum

imparted by the higher order multipole fields ($n > 0$) is given by

$$\Delta p_t^{(n)}(z) = \frac{1}{c} r^{n-1} \int_{-\infty}^{+\infty} F_t^{(n)}(z) \mathrm{d}z, \tag{43}$$

and can be determined using the Panofsky-Wenzel Theorem [15]

$$\begin{aligned} \Delta p_t^{(n)}(z) &= -j\frac{q}{\omega} \int_{-\infty}^{+\infty} \nabla_t E_z^{(n)}(z) e^{j\omega t} \mathrm{d}z\,, & (44) \\ &= -j\frac{q}{\omega} n r^{n-1} \int_{-\infty}^{+\infty} E_{acc}^{(n)}(z,t) \mathrm{d}z\,, & (45) \end{aligned}$$

or by using Lorentz Force

$$\Delta p_t^{(n)}(z) = \frac{q}{c} r^{n-1} \int_{-\infty}^{+\infty} \left[E_t^{(n)}(z) e^{j\omega t} + jcB_t^{(n)}(z) e^{j\omega t} \right] \mathrm{d}z\,, \tag{46}$$

where $t = z/c$.

For relativistic particles traversing through an rf cavity, the multipole components are defined following the standard definition for magnets [23] as

$$A_z^{(n)} + jB_z^{(n)} = \frac{1}{qc} F_t^{(n)}(z) \quad \left[\mathrm{T/m^{n-1}}\right]\,, \tag{47}$$

The above equation can be expressed for both following the Panofsky-Wenzel Theorem or Lorentz force method as

$$\begin{aligned} A_z^{(n)} + jB_z^{(n)} &= -j\frac{n}{\omega} E_{acc}^{(n)}(z,t) = -j\frac{n}{\omega} E_z^{(n)}(z) e^{j\omega t}\,, \quad \text{or} & (48) \\ &= \frac{1}{c} \left[E_t^{(n)}(z) + jcB_t^{(n)}(z) \right] e^{j\omega t}\,, & (49) \end{aligned}$$

$$a_n + jb_n = \int_{-\infty}^{+\infty} \left[A_z^{(n)} + jB_z^{(n)} \right] \mathrm{d}z \quad \left[\mathrm{T/m^{n-2}}\right]\,. \tag{50}$$

Following the above definition the normal and skew multipole components are given by b_n and a_n respectively. The dipole component with order $n = 1$ determines the transverse voltage for deflecting and crabbing cavities. The term associated with $\sin(\omega t)$ of $E_{acc}^{(n)}$ gives the transverse voltage seen by a particle on crest of the deflecting voltage and the term associated with $\cos(\omega t)$ gives the corresponding crabbing voltage. Similar to magnets the higher order multipole components present in an rf cavity contribute to various beam perturbations [23], hence must be reduced to

acceptable levels. These higher order multipole components can be minimized by modifying the rf-dipole geometry especially near the beam aperture region as presented in Chapter 6.

2.6 SUPERCONDUCTIVITY

Superconductivity, discovered in 1911 by Kammerlingh-Onnes [24], is a phenomenon where below a certain temperature, called the critical temperature (T_c), some materials show a sudden drop of the dc electrical resistance to zero. This is in contrast to normal conductors, such as copper, that show a non-zero electrical resistance even at low temperatures. Many superconducting materials have been found to-date with critical temperatures that vary over a wide range. These materials consist of metals, alloys, and ceramics which are high temperature (high-T_c) superconductors. Some of those materials that have been used in the past and are currently being used with materials that are under study are listed in Table 1.

TABLE 1. Critical temperatures of some superconducting materials.

Superconducting Material	Critical Temperature (T_c) [K]
Al	1.2
In	3.4
Sn	3.7
Hg	4.2
Ta	4.5
Pb	7.2
Nb	9.3
NbTi	10.0
NbN	16.0
Nb_3Sn	18.3
MgB_2	39.0
$YBa_2Cu_3O_{7-\delta}$	92.0
$HgBa_2Ca_2Cu_3O_8$	133.0 - 135.0

2.6.1 CRITICAL MAGNETIC FIELD

One other unique feature of superconductors is the ability to completely expel an externally applied magnetic field when cooled down below the critical temperature. This effect, in which the superconductor behaves as a perfect diamagnet, is called the Meissner effect, discovered by Meissner and Ochsenfeld in 1933 [25]. As shown

in Fig. 6 the magnetic field is completely expelled as the superconductor is cooled down below the critical temperature. whereas in a perfect conductor the field passes through the conductor. The superconductor behaves similarly and remains a perfect diamagnet when the external magnetic field is applied after the it is cooled down below the critical temperature. The surface currents created at the surface generate a magnetic field that cancels the external magnetic field inside the superconductor. These surface currents do not decay with time due to the zero resistance in the superconductor.

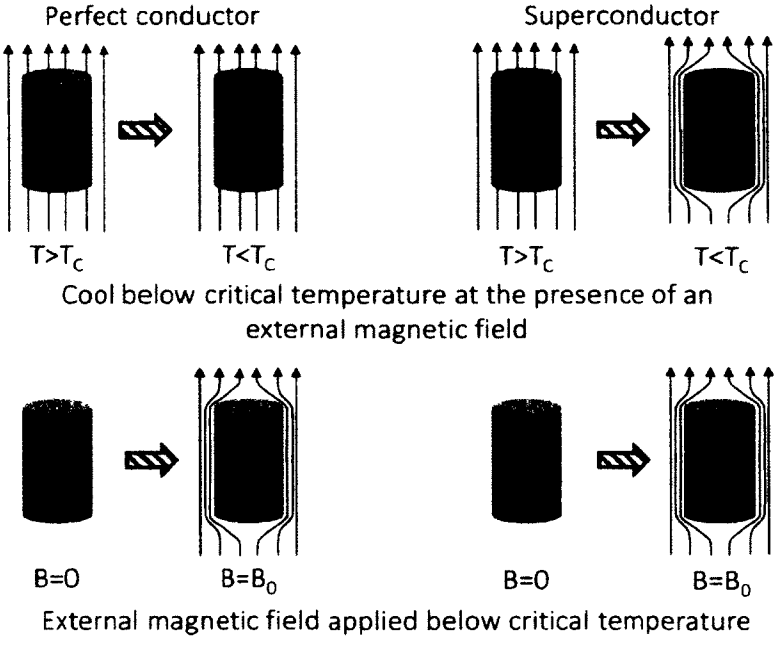

FIG. 6. Expulsion of an external magnetic field in a superconductor below T_c under the Meissner effect.

This condition is in effect as long as the applied external magnetic field is below a certain value called the critical magnetic field (B_c). This implies that the surface currents must be below a certain maximum in order to maintain the superconductivity in the material. The critical magnetic field (B_c) is dependent on the temperature and is approximately given by

$$B_c(T) = B_c(0)\left[1 - \left(\frac{T}{T_c}\right)^2\right] . \tag{51}$$

2.6.2 TYPES OF SUPERCONDUCTORS

There are two types of superconductors named Type I and Type II, depending on the change in superconducting state as function of the external magnetic field. In Type I superconductors, the superconductivity is lost instantly when the applied external magnetic field reaches the critical magnetic field as shown in Fig. 7. and then becomes a normal conductor. However, with Type II superconductors such as niobium, there is a mixed state between the superconducting state and the normal state as shown in Fig. 7. The magnetization ($M = \bar{B} - \mu_0 H$) of Type I and Type II superconductors is shown in Fig. 8.

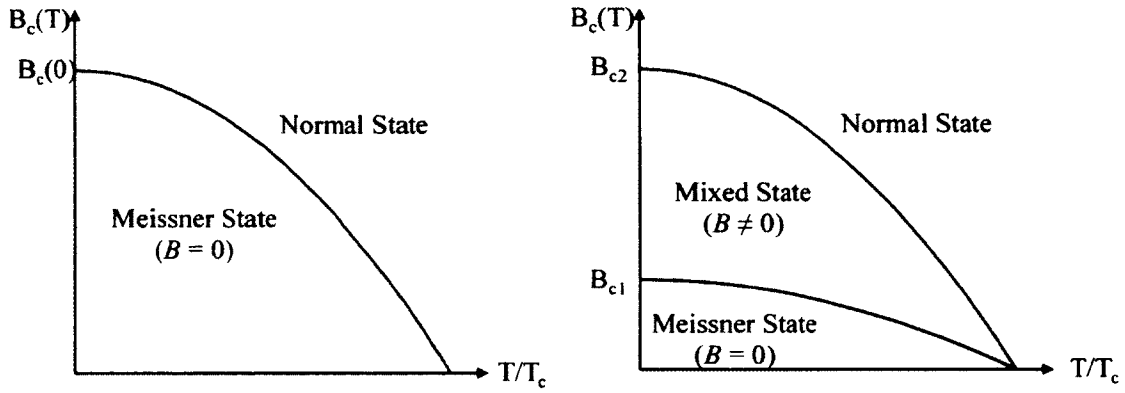

FIG. 7. Critical magnetic field and temperature phase diagrams for Type I (left) and Type II (right) superconductors.

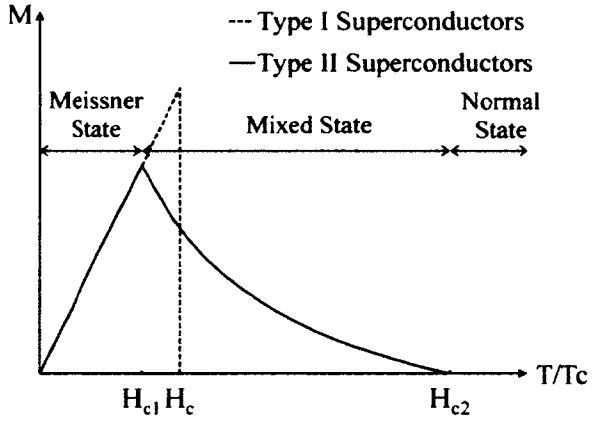

FIG. 8. Magnetization of Type I (left) and Type II (right) superconductors.

For Type II superconductors below the lower critical field (H_{c1}) the external magnetic field is completely expelled, and it is partially expelled up to the upper

critical field (H_{c2}). In the mixed state between H_{c1} and H_{c2}, the field penetrates in the form of quantized vortices also called fluxoids. with a magnetic flux quantum of $\phi_0 = \pi\hbar/e$. The density of the fluxoids increases with the applied external magnetic field and the material becomes a normal conductor above H_{c2}.

2.6.3 THEORIES OF SUPERCONDUCTORS

The two-fluid model proposed by Gorter and Casimir in 1934 [26] gave a phenomenological macroscopic theory of superconductivity, based on thermodynamic properties of superconductors. The model consists of normal and superfluid components where a finite fraction of electrons are condensed into a superfluid, that extends over the entire volume.

Based on the two-fluid model in 1935, F. London and H. London developed two equations that describe the perfect diamagnetism of superconductors [27]. The theory is governed by the microscopic electric and magnetic fields of superconductors. The two-fluid model separates the electrons into a superfluid component with density n_s and velocity v_s and a normal component with density n_n and velocity v_n with a total electron density of $n = n_s + n_n$. The super electrons are accelerated by a constant electric field $\vec{E}$

$$m\frac{\partial \vec{v}_s}{\partial t} = e\vec{E}\,, \tag{52}$$

and the supercurrent density is given by

$$\vec{J}_s = -en_s\vec{v}\,, \tag{53}$$

which gives the first London equation

$$\frac{\partial \vec{J}_s}{\partial t} = \frac{n_s e^2}{m}\vec{E}\,, \tag{54}$$

where n_s is the density of the superelectrons, m is the electron mass and e is the charge of an electron.

The superelectrons are not affected by the normal electrons that follow the usual scattering mechanism that produces conductivity (σ_n) in a normal fluid. Therefore, for normal electrons the current density is given by

$$\vec{J}_n = \sigma_n\vec{E}\,. \tag{55}$$

Combining the first London equation with one of the Maxwell equations

$$\vec{\nabla} \times \vec{E} = -\frac{\partial \vec{B}}{\partial t} . \tag{56}$$

gives the second London equation

$$\frac{m}{n_s e^2} \vec{\nabla} \times \vec{J}_s = -\vec{B} . \tag{57}$$

Combining the second London equation with another Maxwell equation

$$\vec{\nabla} \times \vec{B} = \mu_0 \vec{J}_s , \tag{58}$$

gives

$$\nabla^2 \vec{B} - \frac{\mu_0 n_s e^2}{m} \vec{B} = 0 , \tag{59}$$

which represents the penetration of an externally applied magnetic field into the superconductor. This field decay is valid not only for the time derivative of $\vec{B}$ but also for $\vec{B}$ itself, as stated by the Meissner effect, where the magnetic field inside a superconductor is zero. This gives the dependence of field penetration on length

$$B(x) = B(0) exp \left[-\frac{x}{\lambda_L} \right] , \tag{60}$$

where

$$\lambda_L = \left[\frac{m}{\mu_0 n_s e^2} \right]^{1/2} , \tag{61}$$

and $B(0)$ is the external magnetic field at the surface of the superconductor. The magnetic field drops exponentially inside the superconductor as shown in Fig. 9. The depth at which the magnetic field decays by a factor of $1/e$ is called the London penetration depth (λ_L), one of the important physical quantities of a superconductor.

The temperature dependence of the penetration depth is derived from the two-fluid model and is given by

$$\lambda_L(T) = \frac{\lambda_L(0)}{\sqrt{1 - \left(\frac{T}{T_c}\right)^4}} . \tag{62}$$

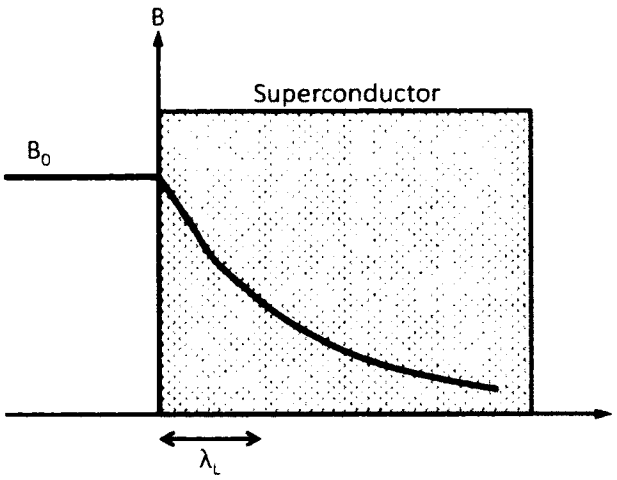

FIG. 9. Exponential decay of the external magnetic field near the surface of a superconductor.

The London equations are local equations that relate the current density at a point with the vector potential at the same point. However, due to the discrepancy in the measurements of the penetration depth with the theoretical values obtained from the London equations, in 1950 Pippard proposed a non local generalization with a characteristic dimension called the Pippard coherence length (ξ_0) [28]. This coherence length describes the distance over which the superconducting state decays, similar to the mean free path (l) in normal metals. Using the uncertainty principle the coherence length for a pure metal is defined as

$$\xi_0 \approx \frac{\hbar v_F}{\pi \triangle(0)} \approx 0.18 \frac{\hbar v_F}{k_B T_c}, \tag{63}$$

where v_F is the Fermi velocity, $\triangle(0)$ is the energy gap that forms at the Fermi surface in the superconducting state at absolute zero, and k_B is the Boltzmann constant.

The Ginzburg Landau theory [29] of superconductors proposed in 1950 introduces the order parameter $\psi(\vec{r})$ that describes the local concentration of superconducting electrons. The order parameter $\psi(\vec{r}) = |\psi| exp(i\varphi(\vec{r}))$ is a complex wave function with amplitude $|\psi|$, which gives the probability of the presence of superconducting electrons, and phase $\varphi(\vec{r})$, which gives the moment of superconducting currents. The order parameter is zero above the transition temperature and non-zero below. Based on the Ginzburg-Landau parameter $\kappa = \frac{\lambda_L}{\xi}$ the superconductors are categorized as

- Type I Superconductors - $\kappa = \frac{\lambda_L}{\xi} < \frac{1}{\sqrt{2}}$
- Type II Superconductors - $\kappa = \frac{\lambda_L}{\xi} > \frac{1}{\sqrt{2}}$

where κ is roughly constant ratio over temperature.

In 1957, a complete theory of superconductivity was presented by Bardeen, Cooper and Schreiffer called the BCS theory [30, 31] that gives a microscopic description instead of the previous phenomenological macroscopical representations. The condensation of the Cooper pairs is the foundation of the BCS theory of superconductivity, where Cooper pair interaction dominates over the repulsive Coulomb force.

The theory is based on the existence of Cooper pairs that are pairs of electrons at low temperature, which have lower energy than the two individual electrons [32]. The pairing of electrons is a quantum effect due to electron-phonon interactions. In the crystal lattice, the rapid movement of electrons causes a momentary perturbation of the ions in the lattice. A displaced ion due to a passing electron with momentum $\mathbf{k}_1$, returns to the original position in an oscillating manner that results in creation of phonons of momentum $\mathbf{q}$. The phonon interaction with a second electron of momentum $\mathbf{k}_2$, as shown in Fig. 10, lowers its energy and emits another phonon that interacts with the first electron. The back and forth movement of the phonons pairs the electrons, minimizing their energy. The distance between two paired electrons is the BCS coherence length (ξ_0).

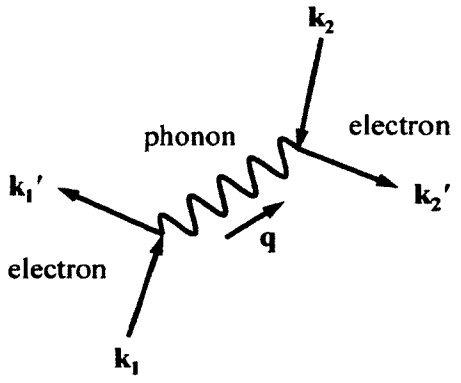

FIG. 10. Phonon interaction with an electron pair that forms a Cooper pair.

The attraction of electrons occurs when the corresponding momenta of the the paired electrons are within a range of certain momentum of $\Delta k = m\omega_n/k_F$ where ω_n

is the average phonon frequency and k_F is the Fermi momentum. Thus, according to BCS theory the electrons within a thin spherical layer of the Fermi surface are attracted in the process of forming Cooper pairs. Therefore, the number of Cooper pairs formed are limited by the availability of empty states. The energy is minimized for a paired electron with momenta $\mathbf{k_1}$ and $\mathbf{k_2}$ as $\mathbf{q} \rightarrow 0$ in $\mathbf{k_1} + \mathbf{k_2} = \mathbf{q}$, pairing electrons with equal and opposite momenta ($\mathbf{k_1} = -\mathbf{k_2}$). The momentum is conserved during the transition from one energy state to the other.

The single electrons, which are fermions, obey the Pauli exclusion principle, whereas the Cooper pairs act as bosons with same energy level, and opposite moments and spins. For two electrons in a Cooper pair with a background Fermi level at $T = 0$, the zero momentum wave function is of the form

$$\Psi\left(\mathbf{r_1}, \mathbf{r_2}\right) = \sum_{\mathbf{k}} g_{\mathbf{k}} e^{i\mathbf{k}\cdot(\mathbf{r_1}-\mathbf{r_2})} \left(|\uparrow_1\downarrow_2\rangle - |\downarrow_1\uparrow_2\rangle\right) , \tag{64}$$

where g_k are weighting coefficients and $\uparrow$ and $\downarrow$ are up and down spin states of the electrons. Substituting the wave function in the Schrödinger equation gives

$$\left(E - 2\epsilon_{\mathbf{k}}\right) g_{\mathbf{k}} = \sum_{\mathbf{k'}>\mathbf{k_F}} V_{\mathbf{kk'}} g_{\mathbf{k'}} . \tag{65}$$

where

$$V_{\mathbf{kk'}} = \frac{1}{\mathrm{v}} \int_{\mathrm{v}} V(\mathbf{r}) e^{i(\mathbf{k}-\mathbf{k'})\cdot\mathbf{r}} \mathrm{d}^3 r . \tag{66}$$

Following the mean field approximation for the interaction, $V_{\mathbf{kk'}}$ is

$$V_{\mathbf{kk'}} = \begin{cases} -V & \text{for} \quad \epsilon_F < \epsilon_{\mathbf{k}} < \epsilon_F + \hbar\omega_c , \\ 0 & \text{otherwise} , \end{cases} \tag{67}$$

for a transition from state with momentum $\mathbf{k}$ to $\mathbf{k'}$ up to the cutoff energy of $\hbar\omega_c$.

The Hamiltonian of the system can be written as

$$H_p = \sum_{\mathbf{k},\sigma} \epsilon_{\mathbf{k}} c^{\dagger}_{\mathbf{k},\sigma} c_{\mathbf{k},\sigma} + \sum_{\mathbf{k},\mathbf{k'}} V_{\mathbf{kk'}} c^{\dagger}_{\mathbf{k}\uparrow} c^{\dagger}_{-\mathbf{k}\downarrow} c_{-\mathbf{k'}\downarrow} c_{\mathbf{k'}\uparrow} , \tag{68}$$

where $c_{\mathbf{k}\sigma}$ and $c^{\dagger}_{\mathbf{k}\sigma}$ are the annihilation and creation operators of an electron of momentum $\mathbf{k}$, and σ is the spin of $\uparrow$ and $\downarrow$. The first term is the kinetic energy and

second term represents the phono mediated electron-electron interaction. In a normal state the operator $c_{\mathbf{k}\uparrow}c_{-\mathbf{k}\downarrow}$ average out to zero when no formed Cooper pairs. The simplified Hamiltonian then can be written as

$$H_p = \sum_{\mathbf{k},\sigma} \epsilon_{\mathbf{k}} c^{\dagger}_{\mathbf{k},\sigma} c_{\mathbf{k},\sigma} + \sum_{\mathbf{k},\mathbf{k}'} V_{\mathbf{k}\mathbf{k}'} \Big[c^{\dagger}_{\mathbf{k}\uparrow} c^{\dagger}_{-\mathbf{k}\downarrow} \langle c_{-\mathbf{k}'\downarrow} c_{\mathbf{k}'\uparrow} \rangle + \langle c_{-\mathbf{k}\downarrow} c_{\mathbf{k}\uparrow} \rangle^{\dagger} c_{-\mathbf{k}'\downarrow} c_{\mathbf{k}'\uparrow} - \langle c_{-\mathbf{k}\downarrow} c_{\mathbf{k}\uparrow} \rangle^{\dagger} \langle c_{-\mathbf{k}'\downarrow} c_{\mathbf{k}'\uparrow} \rangle \Big] , \quad (69)$$

and the energy gap is defined as

$$\Delta_{\mathbf{k}} = \sum_{\mathbf{k}'} V_{\mathbf{k}\mathbf{k}'} \langle c_{-\mathbf{k}'\uparrow} c_{-\mathbf{k}'\downarrow} \rangle . \quad (70)$$

The resultant Hamiltonian including energy gap can be written as

$$H_p = \sum_{\mathbf{k},\sigma} \epsilon_{\mathbf{k}} c^{\dagger}_{\mathbf{k},\sigma} c_{\mathbf{k},\sigma} + \sum_{\mathbf{k}} \left[\Delta^{\dagger}_{\mathbf{k}} c_{-\mathbf{k}\downarrow} c_{\mathbf{k}\uparrow} + \Delta_{\mathbf{k}} c^{\dagger}_{\mathbf{k}\uparrow} c^{\dagger}_{-\mathbf{k}\downarrow} \right] . \quad (71)$$

The Hamiltonian can be diagonalized following the Bogoliubov linear transformations. The new Fermi operators of $\gamma_{\mathbf{k}\uparrow}$ and $\gamma_{\mathbf{k}\downarrow}$ are defined as

$$\gamma_{\mathbf{k}\uparrow} = u_{\mathbf{k}} c_{\mathbf{k}\uparrow} - v_{\mathbf{k}} c^{\dagger}_{\mathbf{k}\downarrow} , \quad (72)$$

$$\gamma_{\mathbf{k}\downarrow} = u_{\mathbf{k}} c_{\mathbf{k}\downarrow} + v_{\mathbf{k}} c^{\dagger}_{\mathbf{k}\uparrow} , \quad (73)$$

such that $|u_{\mathbf{k}}|^2 + |v_{\mathbf{k}}|^2 = 1$. The terms $u_{\mathbf{k}}$ and $v_{\mathbf{k}}$ are determined by extracting the coefficients of $\gamma_{-\mathbf{k}\uparrow}\gamma_{\mathbf{k}\downarrow}$ and $\gamma^{\dagger}_{\mathbf{k}\downarrow}\gamma^{\dagger}_{-\mathbf{k}\uparrow}$. The diagonalized Hamiltonian is then written as

$$H = \sum_{\mathbf{k},\sigma} E_{\mathbf{k}} \gamma^{\dagger}_{\mathbf{k},\sigma} \gamma_{\mathbf{k},\sigma} , \quad (74)$$

where $E_{\mathbf{k}}$ is the energy of fermionic elementary excitations of Bogoliubov quasi-particles. The BCS ground state gives the vacuum state for the quasi-particles with the wave function expressed as

$$|\Psi_g\rangle = \prod_{\mathbf{k}} \left(u_{\mathbf{k}} + v_{\mathbf{k}} c^{\dagger}_{\mathbf{k}\uparrow} c^{\dagger}_{\mathbf{k}\downarrow} \right) |0\rangle , \quad (75)$$

where $|0\rangle$ is the vacuum state with no particles present. The summation in Eq. 74 gives the increase in energy above the ground state for the quasi-particle fermions

where operator $\gamma_{\mathbf{k}}$ describe the excitations of the elementary quasi-particles. The resultant energy of the excitations is given by

$$E_{\mathbf{k}} = \sqrt{\epsilon_{\mathbf{k}}^2 + |\Delta_{\mathbf{k}}|^2}\,. \tag{76}$$

where $\Delta_{\mathbf{k}}$ gives the minimum excitation energy and $E_{\mathbf{k}}$ is the energy of an elementary excitation of momentum $\hbar\mathbf{k}$. The energy gap ($\Delta_{\mathbf{k}}$) separates the energy levels of the elementary excitations called the level of condensation of the Cooper pairs, from the ground state in the superconductor.

The energy gap $\Delta_{\mathbf{k}}$ defined in Eq. 70 can be reexpressed with the operators $\gamma_{\mathbf{k}\sigma}$ as

$$\Delta_{\mathbf{k}} = -\sum_{\mathbf{k}'} V_{\mathbf{k}\mathbf{k}'} u_{\mathbf{k}}^{\dagger} v_{\mathbf{k}'} \left\langle 1 - \gamma_{\mathbf{k}'\uparrow}^{\dagger}\gamma_{\mathbf{k}'\uparrow} - \gamma_{\mathbf{k}'\downarrow}^{\dagger}\gamma_{\mathbf{k}'\downarrow} \right\rangle\,, \tag{77}$$

where simplifying further, a self-consistent equation for $\Delta_{\mathbf{k}}$ is obtained as

$$\Delta_{\mathbf{k}} = -\frac{1}{2}\sum_{\mathbf{k}'} V_{\mathbf{k}\mathbf{k}'} \frac{\Delta_{\mathbf{k}'}}{\sqrt{|\epsilon_{\mathbf{k}'}|^2 + |\Delta_{\mathbf{k}'}|^2}}\,. \tag{78}$$

Following the mean field approximation given in Eq. 67 where $V_{\mathbf{k}\mathbf{k}'} = -V$, $\Delta_{\mathbf{k}}$ can be written as

$$\Delta_{\mathbf{k}} = \begin{cases} \Delta & \text{for} \quad |\epsilon_{\mathbf{k}}| \text{ and } |\epsilon_{\mathbf{k}'}| \leq \hbar\omega_c\,, \\ 0 & \text{otherwise}\,, \end{cases} \tag{79}$$

with

$$\frac{1}{V} = \frac{1}{2}\sum_{\mathbf{k}} \frac{1}{E_{\mathbf{k}}}\,. \tag{80}$$

that is independent of $\mathbf{k}$. The corresponding integral form can be written as

$$\frac{1}{N(0)V} = \int_0^{\hbar\omega_c} \frac{\mathrm{d}\epsilon}{\sqrt{\Delta^2 + \epsilon^2}} = \frac{1}{\sinh\left(\frac{\hbar\omega_c}{\Delta}\right)}\,, \tag{81}$$

$$\Delta = \frac{\hbar\omega_c}{\sinh\left(\frac{1}{N(0)V}\right)} \approx 2\hbar\omega_c e^{-1/N(0)V}\,. \tag{82}$$

evaluated up to the Cooper energy, $\epsilon_c = \hbar\omega_c$.

Elementary excitations of quasi-particles follow the Fermi-Dirac statistics. The probability of an excited state of $\mathbf{k}$ at a finite temperature is then given by the Fermi

function

$$f(E_{\mathbf{k}}) = \frac{1}{1 + e^{\frac{E_{\mathbf{k}}}{kT}}}, \tag{83}$$

where k is the Boltzmann's constant and T is the absolute temperature. This state with the probability of $2f$ does not participate in formation of Cooper pairs. Therefore, the probability that a state may participate in the formation of a superconducting state is $1 - 2f$. Thus

$$\Delta_{\mathbf{k}} = -\sum_{\mathbf{k}'} V_{\mathbf{k}\mathbf{k}'} u_{\mathbf{k}}^{\dagger} v_{\mathbf{k}'} \left[1 - 2f(E_{\mathbf{k}})\right] . \tag{84}$$

$$= -\frac{1}{2}\sum_{\mathbf{k}'} V_{\mathbf{k}\mathbf{k}'} \frac{\Delta_{\mathbf{k}'}}{\sqrt{|\epsilon_{\mathbf{k}'}|^2 + |\Delta_{\mathbf{k}'}|^2}} \left[1 - 2f(E_{\mathbf{k}})\right] . \tag{85}$$

Similarly, following the mean field approximation the self consisting form is given by

$$\frac{1}{V} = \frac{1}{2}\sum_{\mathbf{k}} \frac{1}{E_{\mathbf{k}}} \tanh\left(\frac{E_{\mathbf{k}}}{2kT}\right) , \tag{86}$$

and in the integral form

$$\frac{1}{N(0)V} = \int_0^{\frac{\hbar\omega_c}{2kT_c}} \frac{\tanh(x)}{x} \mathrm{d}x , \tag{87}$$

is obtained at the critical temperature (T_c) where $x = \epsilon/2kT_c$. At critical temperature the energy gap vanishes ($\Delta(T) = 0$) that gives the relation $E_{\mathbf{k}} = \epsilon_{\mathbf{k}}$.

The solution of Eq. 87 is

$$kT_c \approx 1.13\,\hbar\omega_c\, e^{-1/N(0)V} . \tag{88}$$

Comparing Eqs. 82 and 88 gives

$$\frac{\Delta(0)}{kT_c} \approx 1.764 , \tag{89}$$

differs from the theory for different material due to differences in the election-phonon interaction length, which is the BCS coherence length (ξ_0).

The temperature dependence of the energy gap near T_c is predicted to be

$$\frac{\Delta(T)}{\Delta(0)} \approx 1.764 \left(1 - \frac{T}{T_c}\right)^{1/2} . \tag{90}$$

The energy gap is nearly constant at low temperature and vanishes at the critical temperature as significant number of quasi-particles are thermally excited where the material becomes normal.

2.6.4 SURFACE RESISTANCE

The surface impedance is a useful way of representing the behavior of a metal in the presence of an electromagnetic field especially at high frequencies. For any metal the surface impedance is described as

$$Z = R + jX\,. \tag{91}$$

where R is the surface resistance and X is the surface reactance where are both real quantities. The surface impedance can be defined as the ratio of tangential fields at the metal surface

$$Z = \frac{4\pi}{c}\left|\frac{E_x}{H_y}\right|_{z=0} = \frac{E_x}{\int_0^\infty J_x \mathrm{d}z} = j\frac{4\pi k}{c}\left[\frac{E_x}{\frac{\partial E_x}{\partial z}}\right]_{z=0}, \tag{92}$$

where $k = \omega/c$ is the wave number and ω is the frequency of the applied field. In normal conductors, the field variation in x and y is slow compared to that in z. Therefore in determining the field, the incidence of a plane wave on an infinite conducting surface is considered along with the intrinsic material properties of the metal in determining the surface impedance. Following Maxwell's equations and Ohm's law in the local limit the current density (J) is given by

$$J = \sigma E\,, \tag{93}$$

where σ is the conductivity and E is the applied electric field that exponentially decays into the metal with the characteristic length called skin depth (δ) given by

$$\delta = \sqrt{\frac{2}{\mu_0 \omega \sigma}}\,. \tag{94}$$

The surface impedance is then given by,

$$Z = (1+j)\sqrt{\frac{\mu_0 \omega}{2\sigma}}\,. \tag{95}$$

At very low temperatures experiments have shown that the skin depth (δ) over which the fields decay becomes shorter than the electron mean free path (l), which is the distance traveled by electrons before scattering. As a result the surface impedance becomes independent of the conductivity and the local limit of the applied field is no longer valid since the electrons do not experience a constant electric field over the mean free path. The new effect is called the anomalous skin effect [33] where the current density has a complex form compared to that given in Eq. 93 as proposed by Chambers [34]. The current density is now related to the electric field over the volume of the size of the mean free path and the non-local relationship is given by

$$\vec{J}(\vec{r},t) = \frac{3\sigma}{4\pi l}\int_V \frac{\vec{R}\left[\vec{R}\cdot\vec{E}\left(\vec{r}',t-\vec{R}/v_F\right)\right]}{R^4} e^{-R/l}\mathrm{d}\vec{r}' \,, \tag{96}$$

with $\vec{R} = \vec{r}' - \vec{r}$. The corresponding surface resistance in the extreme anomalous limit is expressed as

$$R(l\to\infty) = 3.79\times 10^5 \omega^{2/3}\left(\frac{l}{\sigma}\right)^{1/3} \,, \tag{97}$$

where l/σ is a material constant.

A superconductor has no dc resistivity at constant dc current. This behavior can be explained by the two-fluid model. The dc current present in the superconductor does not produce any field that prevents any current generated by the normal or super electrons (Cooper pairs). Also, the collisions of Cooper pairs with the lattice defects, impurities or phonons are insufficient to separate the electron pairs. Therefore Cooper pairs flow in a lossless equilibrium state [35]. However, the time-dependent magnetic field that penetrates into the superconducting surface due to the Meissner effect generates an electric field. This electric field produces small currents due to the oscillations of the normal electrons that leads to a finite power dissipation. In a superconductor the small time-dependent current is carried by both super electrons and normal electrons. The complex conductivity

$$\sigma = \sigma_n + j\sigma_s \,, \tag{98}$$

has a real part contributed by the normal electrons given by

$$\sigma_n = \frac{n_n e^2 \tau_n}{m} . \tag{99}$$

and an imaginary part corresponding to that of Cooper pairs with conductivity

$$\sigma_s = \frac{2n_s e^2}{m\omega} . \tag{100}$$

where n_n and n_s are the densities of the normal and super electrons, τ_n is the relaxation time of normal electrons, and e and m are charge and mass of an electron.

The surface resistance of superconductors according to the two-fluid model can be written as

$$R \simeq \frac{1}{\lambda_L} \frac{\sigma_n}{\sigma_s^2} , \tag{101}$$

with

$$\sigma_n = \frac{n_n e^2 l}{m v_F} \propto l \exp\left(-\frac{\triangle(T)}{k_B T}\right) \quad \text{and} \quad \sigma_s = \frac{2n_s e^2}{m\omega} = \frac{1}{\mu_0 \lambda_L^2 \omega} , \tag{102}$$

where λ_L is the London penetration depth, v_F is the Fermi velocity. The simplified surface resistance (R_s) is given by

$$R_s \propto \lambda_L^3 \omega^2 l \exp\left(-\frac{\triangle(T)}{k_B T}\right) . \tag{103}$$

where $\triangle$ is the energy gap and k_B is the Boltzmann constant. For niobium the modified expression includes the coherence length (ξ) given by

$$R_s \propto \lambda_L^3 \left(1 + \frac{\xi}{l}\right)^{3/2} \omega^2 l \exp\left(-\frac{\triangle(T)}{k_B T}\right) . \tag{104}$$

The surface resistance (R_s) of superconductors is a function of temperature (T) and frequency (ω) of the applied field, and depends on material properties such as the critical temperature (T_c), energy gap (Δ), coherence length (ξ), penetration depth (λ_L), and mean free path (l). A good approximation of surface resistance for $T < T_c/2$ and $\hbar\omega \ll \triangle$ can be expressed as

$$R_s \sim \frac{A}{T}\omega^2 \exp\left(-\frac{\triangle(T)}{k_B T}\right) + R_{res} = R_{BCS} + R_{res} , \tag{105}$$

where R_{res} is the residual resistance. Besides, R_{BCS} the residual surface resistance

(R_{res}) is a temperature-independent parameter that is affected by impurities, trapped flux, absorbed gasses or microscopic particles. The calculation of R_{BCS} is done using numerical methods [36] where Fig. 11 shows the temperature dependence on the BCS surface resistance below T_c for several frequencies. At very low temperatures $R_{BCS} \rightarrow 0\ \Omega$ and the power dissipation is dominated by the residual losses.

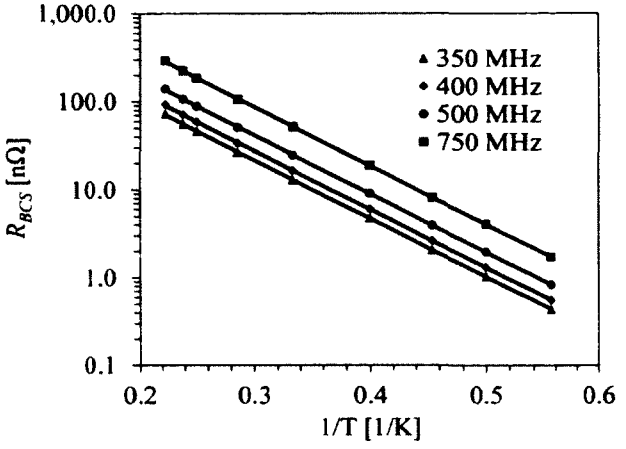

FIG. 11. Temperature dependence of the BCS surface resistance (R_{BCS}) of niobium below T_c at frequencies of 350 MHz, 400 MHz, 500 MHz and 750 MHz.

2.7 CAVITY LOSSES

The ideal performance of superconducting cavities is achieved when the surface resistance contributing to surface losses is equal to the theoretical BCS resistance [36], and the unloaded quality factor (Q_0) is constant with the increasing rf fields. Ultimately, the cavity would reach a threshold point called a quench when the peak magnetic field reaches the critical magnetic field (B_c). Multiple effects contribute to cavity losses in superconducting rf cavities that limit the performance in achieving high Q_0 or high field gradients.

2.7.1 RESIDUAL LOSSES

The residual losses impact the unloaded quality factor directly reducing it at any rf field due to the increase in the surface resistance. One of the loss mechanisms is from trapped dc magnetic flux in the cavity during the cool down through the critical temperature (T_c) [37]. Any impurities present in the cavity will prevent flux escaping

from the superconductor unlike in a pure superconductor where the magnetic field is completely expelled from the interior at temperatures below T_c.

Absorbed gasses during the cavity cool down also contributes to the temperature independent residual losses. Therefore a very slow cool down process is preferred. in bringing the cavity to room temperature after baking, which minimizes the absorption of gasses such as hydrogen. carbon dioxide, carbon monoxide or water [38].

An additional source of hydrogen absorption on the surface is from the process of chemical etching. The hydrogen produced during the chemical reactions gets absorbed during longer processing times, specifically with increasing temperatures of the acid mixture. Furthermore, the absorbed hydrogen is released during cool down of the cavity and forms a layer of hydride precipitation that degrades the cavity intrinsic quality factor drastically. known as the 'Q-disease' [39, 40]. Extensive investigations have shown that in the transition temperatures of 170 K to 77 K with a cooling rate of 1.0 K/min the residual losses may increase by $10 - 40$ nΩ, and can be overcome by cooling the cavity faster during this temperature range.

2.7.2 FIELD EMISSION

Electron field emission is one of the loss mechanisms that occurs at high electric field levels limiting the gradient achieved by the superconducting rf cavities [41, 42]. Protrusions or impurities on the cavity inner surface at high electric field regions can be field emitters. With the increasing rf field the field emitters generate an electron current leading to excessive heating and x-rays produced by bremsstrahlung. The increase in power dissipation due to bombarding electrons leads to an exponential drop in the cavity unloaded quality factor. hence limiting the achievable gradient. Occasionally. the active field emitters are processed and the gradient will be recovered. Otherwise, a higher gradient cannot be achieved unless the input rf power is increased.

The process of field emission is explained by the theory developed by Fowler and Nordheim [44]. As shown in Fig. 12 the electrostatic potential (Φ) barrier confines the electrons at Fermi energy (ϵ_F), escaping from the metallic wall, in to the vacuum. At high electric fields the potential is lowered where the energetic electrons tunnel through the finite barrier into the the vacuum. According to the Fowler and Nordheim theory the electron current density (J) as a function of electric field (E)

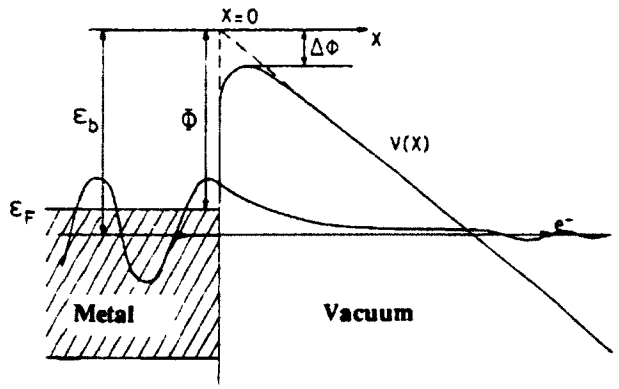

FIG. 12. Electrostatic potential of the metal-vacuum interface with a high electric field applied [43].

for dc field emission from an ideal surface is given by [43],

$$J = \frac{1.54 \times 10^{-6} E^2}{\Phi} \exp\left(-\frac{6.83 \times 10^9 \Phi^{3/2}}{E}\right) . \tag{106}$$

The modified electron current density for superconductors, including the enhancement factor (β) is given by [43],

$$J = k\frac{1.54 \times 10^{-6} (\beta E)^{5/2}}{\Phi} \exp\left(-\frac{6.83 \times 10^9 \Phi^{3/2}}{\beta E}\right) , \tag{107}$$

where k is the effective emitting surface and the enhancement factor ranges from 10 s to 100 s.

Frequently, field emission is observed in superconducting rf cavities at high rf fields limiting the peak electric fields achieved below 40 MV/m. Improved techniques followed in maintaining clean conditions during cavity surface processing and assembly have facilitated in achieving higher peak electric fields far above 40 MV/m.

2.7.3 THERMAL BREAKDOWN

Thermal breakdown is the sudden transition of the superconducting state to the normal state with a sharp drop in the cavity unloaded quality factor. Defects such as pits on the cavity surface at high magnetic field regions will increase the current

flow with increased power dissipation. With the excessive localized heating the surrounding area becomes normal conducting as the temperature rises above T_c. This will lead to a further increase in the power dissipation and the cavity will quench, since the heat generated at the spot exceeds that that can be evacuated by the liquid helium bath. The breakdown field [45] can be estimated for a defect with radius r_d as

$$H_{tb} = \sqrt{\frac{4\kappa_T(T_c - T_b)}{r_d R_d}}, \tag{108}$$

where κ_T is the thermal conductivity of niobium, R_d is the surface resistance of the defect and T_b is the temperature of the liquid helium bath.

2.7.4 MULTIPACTING

Multipacting is a phenomenon of continuous generation of secondary electrons upon the impact of primary electrons on the cavity wall. The secondary electrons emitted from the cavity surface are then accelerated by the rf field and may eventually impact the cavity wall again, producing more secondary electrons. This increase in electron current may lead to an electron avalanche.

The number of generated secondary electrons depends on surface conditions and material type and on the impact energy of the primary electron. The electron current increases exponentially if the number of emitted electrons exceeds the number of impacting ones and if the trajectories satisfy certain resonance conditions. Multipacting therefore occurs at certain field levels and causes a sharp reduction in the cavity Q_0 due to the energy gained by the electrons and by heating of the surface due to the impacting electrons.

For the cavity designs presented in this work we have studied multipacting levels up to the field levels above the operating transverse voltage. The resonant particles, with the impact energy and corresponding mulitpacting orders for the parallel-bar and rf-dipole cavities are explained in (Chapter 7).

CHAPTER 3

APPLICATIONS

Applications of deflecting and crabbing rf cavities as name suggests, primarily fall into one of the two categories, in which a bunch receives either a transverse displacement or a rotation. Deflecting and crabbing cavities are not limited to generating a transverse momentum for applications to rf separation or crabbing beams. These rf structures are also used in applications in beam diagnostics, emittance exchange in beams and x ray generation using compressed beams [46, 47, 48].

Compact rf-dipole cavities presented here are a very attractive design for low frequency deflecting and crabbing applications. Our design can be considered for a number of deflecting and crabbing applications. Two of the applications are the Jefferson Lab 12 GeV upgrade that requires a deflecting cavity system operating at 499 MHz, and the LHC high luminosity upgrade that requires a 400 MHz crabbing system. Two rf-dipole structures have been designed, prototyped, and tested for the above two mentioned applications. In this chapter the motivation for designing this new cavity is discussed. Other possible applications are also reviewed.

3.1 CONCEPT OF DEFLECTING STRUCTURES

The early application of deflecting/crabbing cavities was in rf deflecting systems designed to separate high energy particle beams [49]. The Panofsky-Wenzel Theorem [15] describes the concept of generating a transverse momentum using electromagnetic fields in an rf structure. A deflecting cavity system can separate a single beam into multiple beams by applying a transverse momentum to the center of the bunches to displace the bunch off axis at an angle as shown in Fig. 13. The transverse momentum acquired by each bunch depends on the phase of the rf field when the bunch traverses the cavity.

The transverse momentum needed to be generated by the deflecting cavity, as shown in Fig. 14, is dependent on the angle of displacement (θ) and the energy of

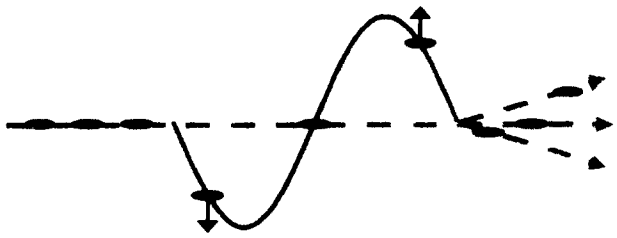

FIG. 13. Bunch separation in a deflecting cavity system.

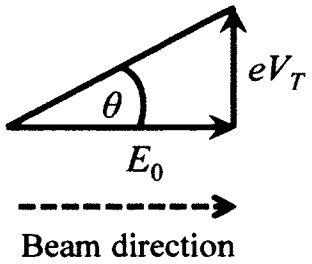

FIG. 14. Dependence of angle of displacement on beam energy and transverse voltage.

the particle (E_0) as given by

$$\theta = \arctan\left[\frac{eV_t}{E_0}\right] \sim \frac{eV_t}{E_0}. \tag{109}$$

$$V_t = E_0\,[eV]\,\theta\,[rad]. \tag{110}$$

3.2 CONCEPT OF CRABBING STRUCTURES

The crab crossing concept was proposed in 1988 by R.B. Palmer [50]. He suggested using a crabbing cavity system to increase the luminosity in a linear collider by allowing the head on collision of bunches at the interaction point. This concept was also applied to collider rings [51]. The peak luminosity is the measurement of number of collisions per unit reaction cross section per second. For two bunches with head on collision the peak luminosity is given by [52]

$$\mathcal{L} = \frac{N_1 N_2 f_c}{2\pi\left(\sigma_{x1}^2 + \sigma_{x2}^2\right)\left(\sigma_{y1}^2 + \sigma_{y2}^2\right)}, \tag{111}$$

where N_1 and N_2 are the number of particles in the colliding bunches, f_c is the revolution frequency and σ_{x1}^2, σ_{x2}^2, σ_{y1}^2, and σ_{y2}^2 are the rms transverse beam sizes of each bunch. For a collider ring with identical bunches the reduced expression can also be written in terms of emittances and betatron amplitude functions

$$\mathcal{L} = \frac{N^2 f_c \gamma}{4\pi\sqrt{\varepsilon_x \beta_x^* \varepsilon_y \beta_y^*}}. \tag{112}$$

where ε_x, ε_y are the normalized emittances and β_x^*, β_y^* are betatron amplitude functions of the two beams realted to the transverse rms beam size as $\sigma_{x,y} = \sqrt{\frac{\varepsilon_{x,y}\beta_{x,y}}{\gamma}}$. The luminosity is dependent on the number of interactions between the particles in the colliding bunches.

In a linear or circular collider the colliding bunches have fewer interactions when the bunches do not overlap at the interaction points as shown in Fig. 15.

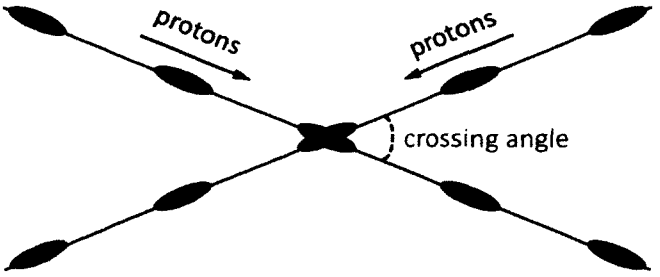

FIG. 15. Bunch collision at the interaction point in a particle collider.

A transverse momentum applied at the head and tail of the bunch in the opposite direction as shown in Fig. 16 rotates the bunch and enables head on collision at the interaction point as shown in Fig. 17. The overlapped bunches increase the number of interactions and therefore increases the luminosity.

The crabbing cavities are placed on the beam line at zero crossing and operate with a $\pm 90^o$ synchronous rf phase. A set of crabbing cavities are used after the interaction point to compensate the induced kicks which otherwise may lead to beam instabilities.

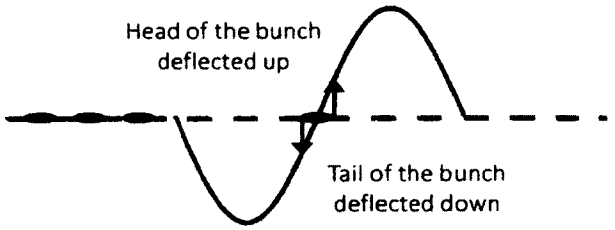

FIG. 16. Bunch rotation in a crabbing system.

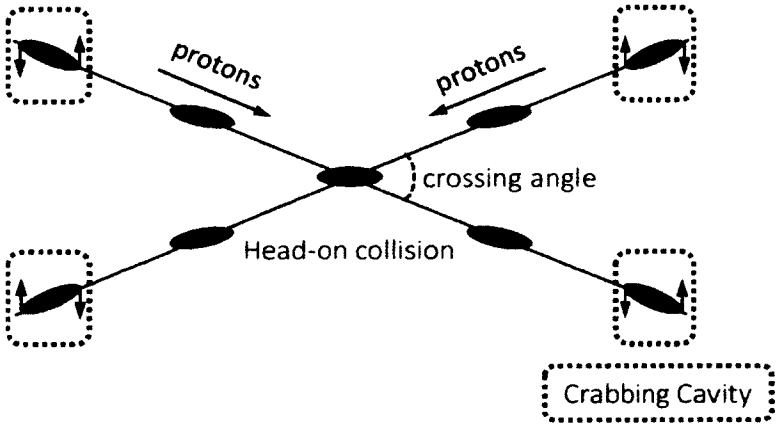

FIG. 17. Head-on bunch collision at the interaction point in a particle collider.

3.3 HISTORY OF DEFLECTING AND CRABBING STRUCTURES

Superconducting deflecting and crabbing cavity designs have been in operation successfully in the past. The first experimental attempt in designing deflecting cavities was the 2.856 GHz rectangular deflecting cavity that successfully deflected a 150 MeV electron beam at the Mark III linear electron accelerator at Stanford University in 1960 [49]. Following that success, in the early 1960's concurrent work was pursued at CERN [53], SLAC [54] and BNL [55], leading to more advanced designs such as the multi-cell TM_{11}-type disk loaded waveguide structure [56]. The first superconducting rf deflecting structure of 2.865 GHz operating frequency was designed at KfK Karlsruhe in collaboration with CERN [57]. The 104-cell standing wave rf particle separator cavity installed at CERN in 1977 was capable of delivering a deflection in the vertical plane and was operating in bi-periodic TM_{110} mode as shown in Fig. 18. The deflecting cavity was in operation until 1981 and is at IHEP since 1998.

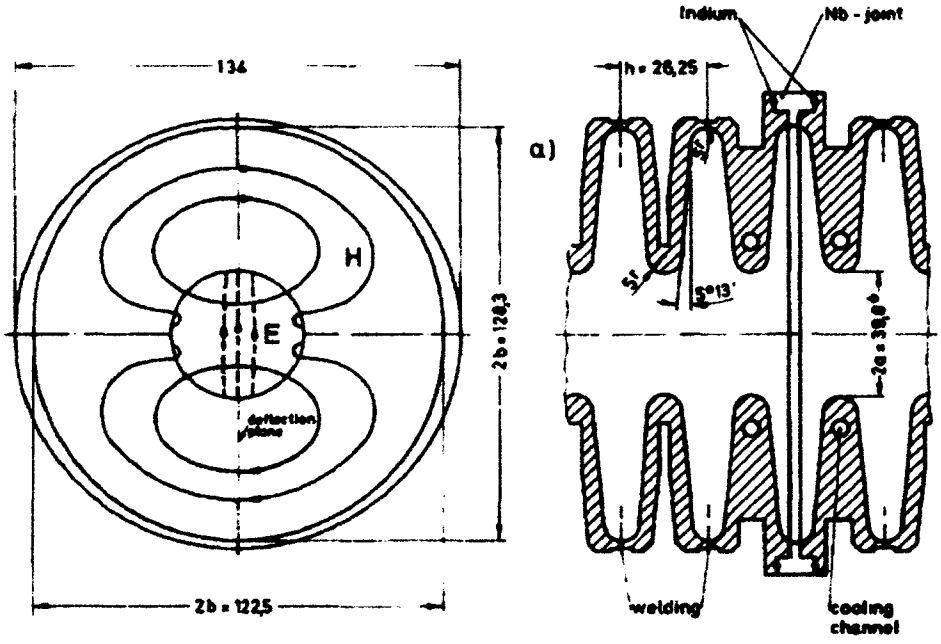

FIG. 18. CERN superconducting rf separator.

The first superconducting crabbing cavity system was developed and installed in 2007 at KEK [58] for the KEKB electron-positron collider. The crabbing cavity operating at 508.9 MHz shown in Fig. 19 was the first and only crabbing system in operation in a particle collider. The squashed elliptical geometry operates in a

TM_{110}-like mode in which the transverse momentum is produced by the interaction with the transverse magnetic field. Two systems were installed successfully at the low energy (LER) and high energy (HER) rings and achieved the design value of 1.44 MV transverse voltage. The crabbing system was in operation from 2006 to 2010.

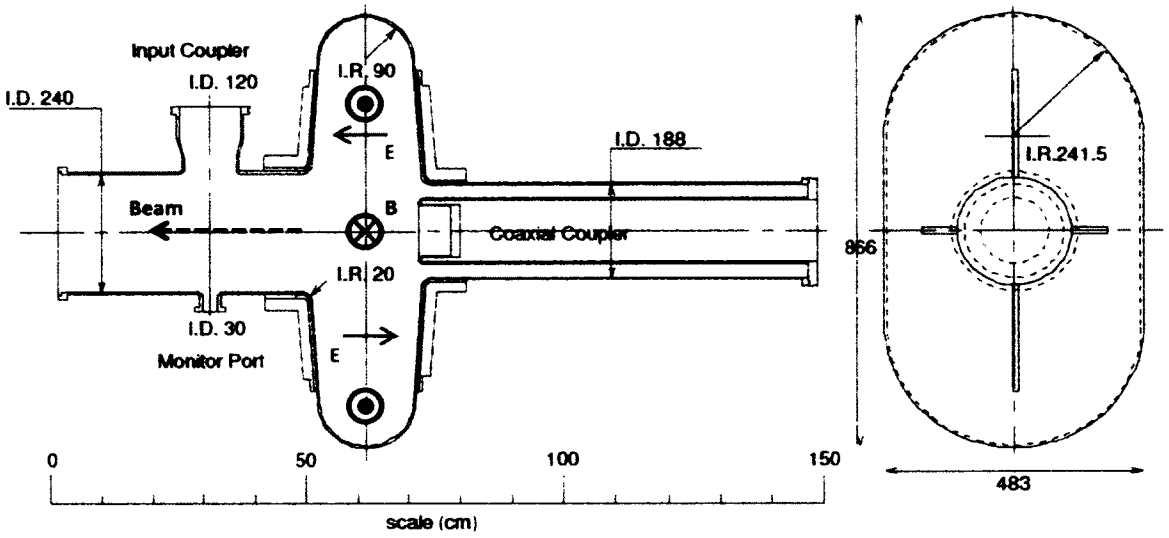

FIG. 19. KEK crabbing cavity.

3.4 JEFFERSON LAB 12 GEV UPGRADE

The Jefferson Lab operates the Continuous Electron Beam Accelerator Facility (CEBAF) that accelerate multiple energy beam up to a maximum energy of 6 GeV for nuclear and particle physics experiments [59].

3.4.1 6 GEV MACHINE

The recirculating electron beam is accelerated by two parallel superconducting linacs with superconducting rf cavities operating at 1497 MHz. The two linacs (north and south linac) are connected by set of arcs that recirculate the beam of different energies. The lowest arc carries the highest energy beam, and highest arc carries the beam with the lowest energy. The beam gains energy while passing through each linac up to 5 times. The CEBAF accelerator is capable of transporting the electron beam into three experimental halls A,B and C for fixed target experiments as shown in Fig. 20. The halls A and C receive a beam current of 150 μA and hall B a beam

of 0.1 μA. The principal machine parameters are given in Table 2.

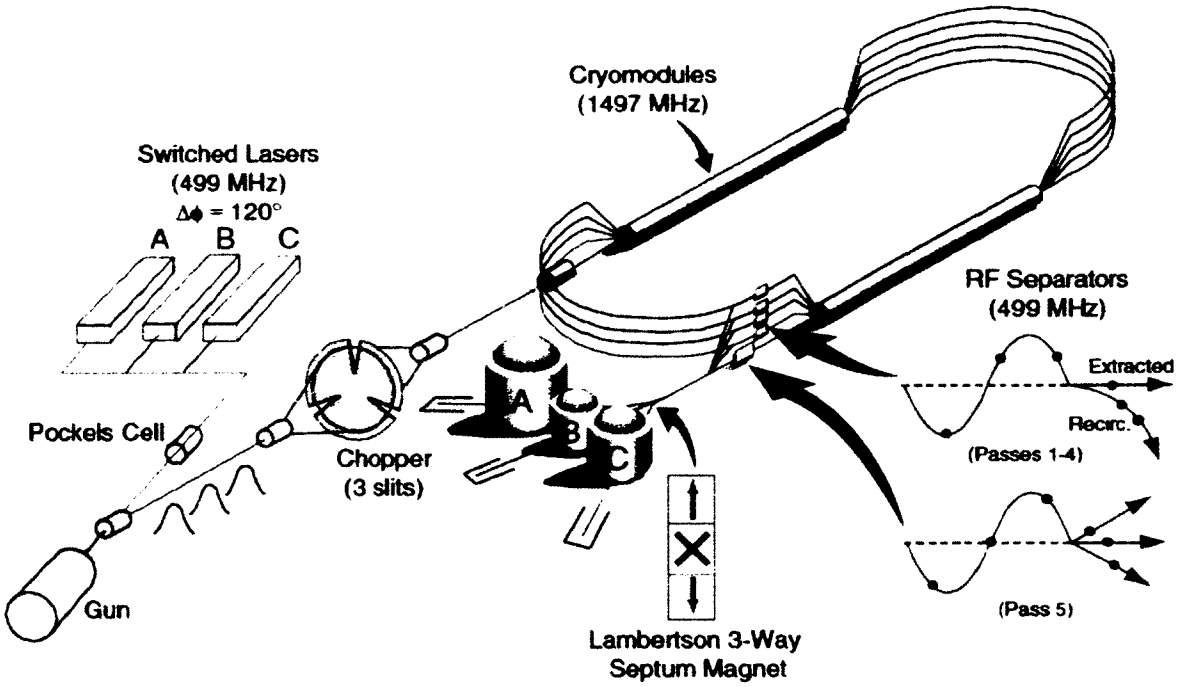

FIG. 20. Schematic of CEBAF accelerator.

The beam extraction system consists of a horizontal and vertical rf separator system as shown in Fig. 21. The horizontal rf separator system extracts the beam at the end of the south linac before being recirculated to the arc and transported to the experimental halls. The vertical rf separator system separates the beam transported to the 3 experimental halls.

3.4.2 12 GEV MACHINE

The Jefferson Lab is currently in the process of upgrading the CEBAF accelerator to an energy of 12 GeV [60, 61]. The upgrade adds another experimental hall (Hall D) to the CEBAF accelerator as shown in Fig. 22, and will run experiments with an electron beam of 12.2 GeV. The 3 experimental halls A,B, and C will receive an electron beam of maximum energy 11.023 GeV. The addition of the new arc will transport the beam through the final pass to hall D.

TABLE 2. CEBAF machine parameters

Parameter	Value	Units
Energy	6.0	GeV
Number of passes	5	
Average Current (Halls A and C)	1150	μA
Average Current (Hall B)	1100	nA
Bunch Charge	<0.3	pC
Repetition Rate (per hall)	499	MHz
Transverse Beam Size (rms)	~ 80	μm
Bunch Length (rms)	300/90	fs/μm
Beam Power	<1.0	MW
Number of Accelerating Cavities	338	
Fundamental Mode Frequency	1497	MHz
Cells/Cavity	5	
Average Cavity Accelerating Gradient	7.5	MV/m
Cavity Operating Temperature	2.08	K

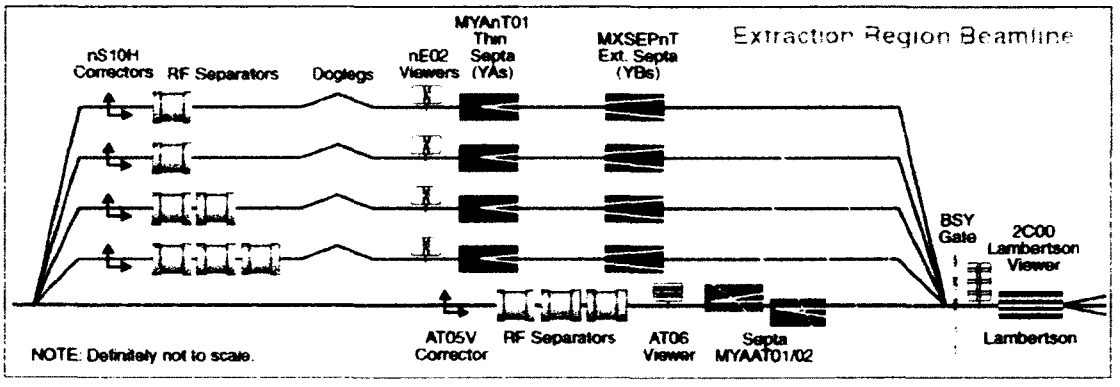

FIG. 21. Beam extraction system.

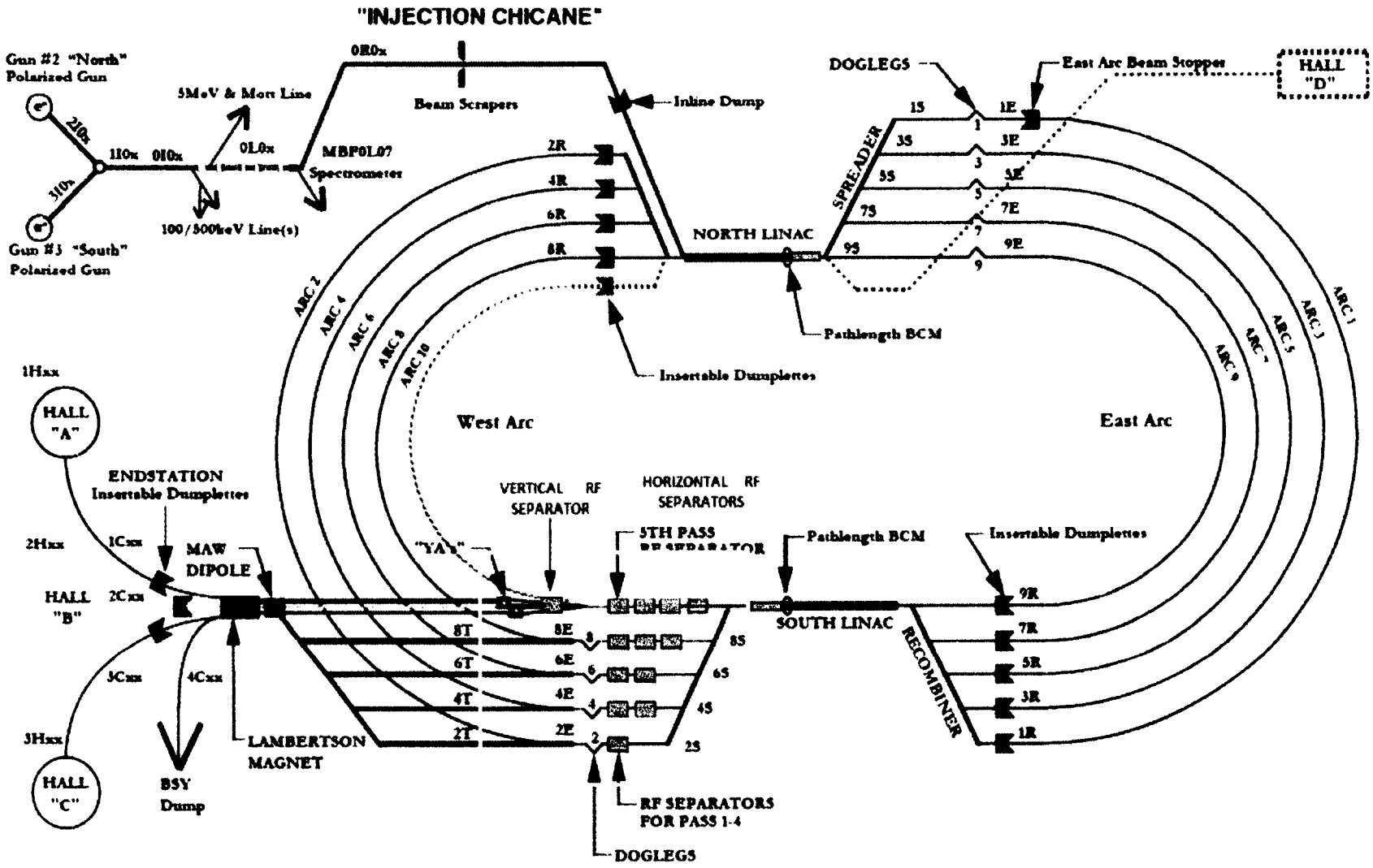

FIG. 22. Schematic of CEBAF 12 GeV accelerator.

Additional 5 cryomodules for each linac are added to achieve the maximum energy of 12 GeV. The cryomodules contain eight 7-cell accelerating cavities. The beam currents are reduced compared to the 6 GeV beam due to the limitation in the beam power of 1 MW from the beam dumps that have not been upgraded.

TABLE 3. 12 GeV CEBAF machine parameters

Parameter	Value	Units
Energy	12.0/11.0	GeV
Number of passes (A,B,C/D)	5/5.5	
Maximum Current (Halls A and C)	85.0	μA
Maximum Current (Halls B and D)	5.0	μA

3.4.3 RF SEPARATOR SYSTEMS

The beam extraction in the 6 GeV machine consists of a normal conducting rf separator system, as shown in Fig. 23, operating at 499 MHz at 1/3 of the fundamental rf frequency of 1497 MHz. The rf separator cavity operating in TEM-type mode consisted of a two 4-rod structures as shown in Fig. 24 [62, 63]. The 12 GeV upgrade also requires an upgrade in the rf separator systems. With the 12 GeV upgrade, the addition of the new arc that transports the beam to hall D requires a set of rf separators at the highest energy beam line, to separate the beam from the arc to experimental halls, which was not needed in the 6 GeV operation. This will be achieved with an additional 4 normal conducting rf separator cavities as shown in Fig. 22. The increased beam energy in the 2^{nd} pass will increase the number of separator cavities to two, while number of separator cavities in the 1^{st}, 3^{rd}, and 4^{th} beam passes will be sufficient to manage the increase in the beam energies as shown in Fig. 22.

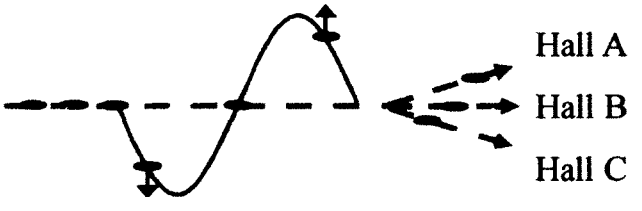

FIG. 23. Beam separation in the CEBAF accelerator.

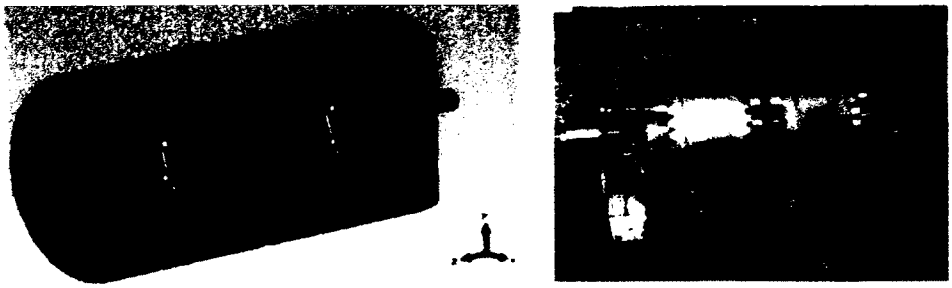

FIG. 24. Beam separation in the CEBAF accelerator.

The 12 GeV upgrade also requires a new vertical separator system due to the doubled beam energy. Two design options are considered in the vertical rf separator system using an upgraded normal conducting system or a possibility of using a superconducting separator system. The normal conducting cavity requires 6 4-rod cavities to achieve the required deflection, while a single rf-dipole cavity operated as a superconducting rf separator can accomplish the same deflection.

The addition of the 5^{th} arc limits the longitudinal space available for the vertical rf separator system. The additional dimensional constraints shown in Fig. 25 has space constraints in both vertically with 45 cm between 4^{th} pass and 5^{th} pass beam lines and horizontally with 30 cm due to a low conducting water line.

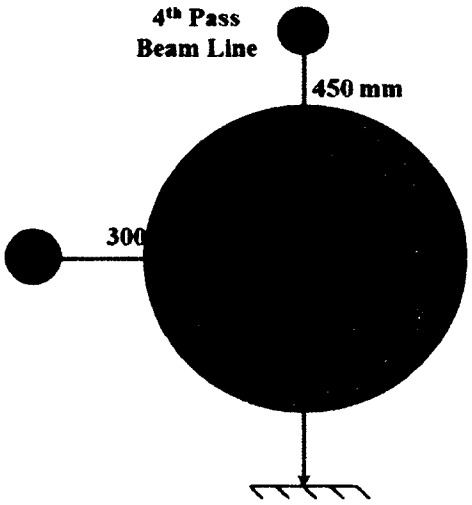

FIG. 25. Dimensional constraints in the vertical rf separator system.

The maximum energy beam to halls A and C requires a vertical separation of 17 mm at the entrance of the Lambertson magnet. and an undeflected beam to hall B [64]. A set of 7 quadrupole magnets amplifies the separation given by the rf separators. This only requires a total vertical separation of 297 μrad from the rf separator system. The peak transverse voltage calculated as in Eq. 110 is 3.3 MV for a maximum beam energy of 11.023 GeV.

3.5 LHC HIGH LUMINOSITY UPGRADE

The Large Hadron Collider (LHC) at CERN is currently the world's largest and highest energy particle accelerator [65]. The 26.7 km long synchrotron machine was designed to collide two proton beams of 14 TeV energy. LHC is expected to study some of the fundamental questions in physics, including basic laws of interactions and forces in elementary particles.

Figure 26 shows the schematic of LHC that consists of eight straight sections and eight arcs [66]. It primarily consists of rf structures that boosts the energy, superconducting magnets that guide the proton beam around the accelerator ring. Magnets include 1232 dipole magnets, that bends the beam, about 450 quadrupole magnets for focusing, and magnets that squeeze the beam prior to the collision in order to increase the luminosity.

Prior to the main accelerator the particles traverse a series of systems as given in Table 4 that successively increases the energy. The particles from the SPS are injected to the LHC over a period of 20 minutes, that are accelerated during that period to the peak energy of 7 TeV. The circulated beams are made to collide at 4 interaction points named ATLAS, CMS, ALICE, and LHC-B as shown in Fig. 27. Out of the four interaction regions ATLAS and CMS experiments at interaction points 1 and 5 (IP1 and IP5) are the two with high luminosity aiming a peak luminosity of 10^{34} cm^2s^{-1}. The two low luminosity experiments of LHC-B for B-physics at IP8, aiming a peak luminosity of 10^{32} cm^2s^{-1} and ALICE at IP2, aiming a peak luminosity of 10^{27} cm^2s^{-1}, for lead-lead ion collisions.

3.5.1 HIGH LUMINOSITY UPGRADE

The successful operation of the LHC, with the high luminosity experiments carried out at ATLAS and CMS experiments has led to the recent discovery of Higgs boson [67, 68]. The high luminosity upgrade, planned to take place in 2020-2021,

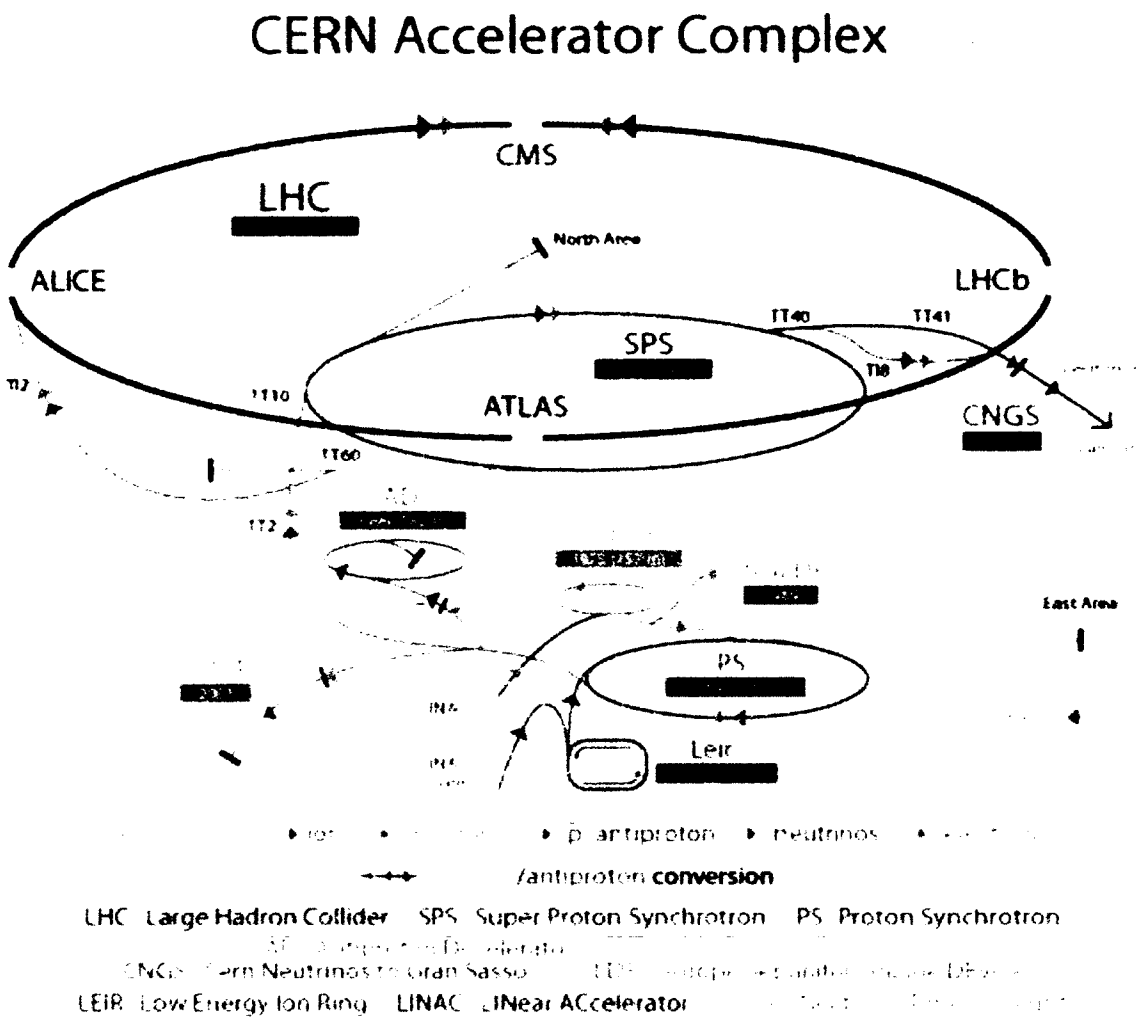

FIG. 26. Schematic of Large Hadron Collider (LHC).

TABLE 4. Accelerator systems in CERN-LHC.

System	Beam Energy
LINAC2	50 MeV
PSB - Proton Synchrotron Booster	1.4 GeV
PS - Proton Synchrotron	26 GeV
SPS - Super Proton Synchrotron	450 GeV
LHC - Large Hadron Collider	7 TeV

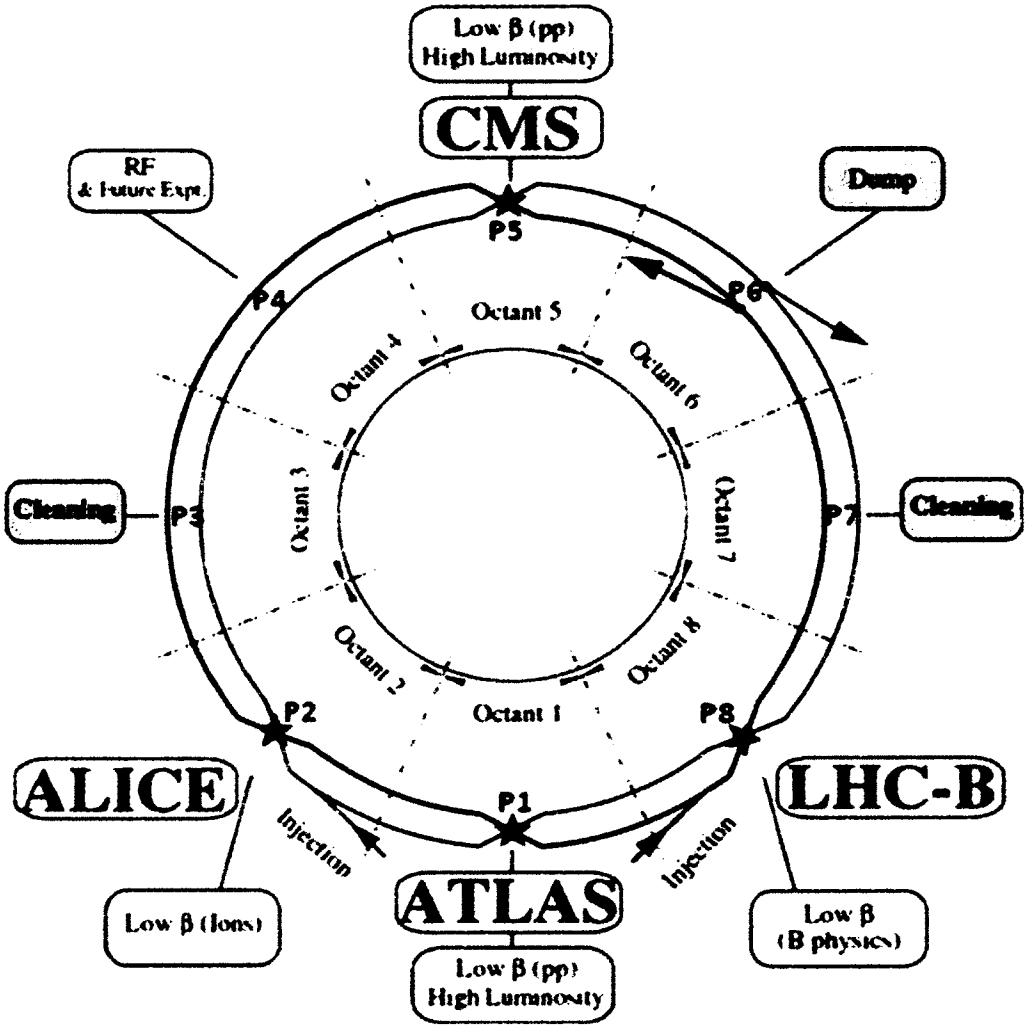

FIG. 27. Schematic of LHC with interaction regions.

is necessary to explore full capacity of LHC, due to a saturation of the luminosity at 1×10^{34} cm^{2}s^{-1}. The upgrade will facilitate performance on more accurate measurements, and the observation of rare processes and broader exploration of the high energy frontier. The main objective of the luminosity upgrade is to facilitate a peak luminosity of 5×10^{34} cm^{2}s^{-1} with an integrated luminosity of 250 fb^{-1} per year, which will be achieved by reducing the beam spot size at interaction point and adding crabbing cavities to improve the beam over lap. Crabbing cavities are also expected to allow luminosity leveling by varying the crabbing voltage; otherwise the achievable luminosity would be limited due to pile-up of events per crossing. Interaction point beam spot size can be further reduced by reducing betatron amplitudes (β^*) at collision point from 0.55 m to 0.15m. This requires a configuration in hardware, with high field superconducting magnets to squeeze the beam.

The beam parameters for the upgrade and nominal operation are shown in Table 5 [69, 70, 71]. LHC can be operated with bunch spacings of 25 ns or 50 ns without any substantial changes to the injectors, accelerating systems, or detector configurations. The peak luminosity can be increased by a factor of 7-10 with crabbing cavities where as with no crabbing cavities the increase will be about 3.5 times the nominal value.

TABLE 5. LHC nominal and upgrade parameters.

Parameter	Nominal	Upgrade	Unit
Energy (E_0)	7.0		TeV
Protons/Bunch (N_b)	1.15	1.7 - 2.0	10^{11}
Average Current (I_{beam})	0.58	1.12 - 0.89	A
No. of Bunches (n_b)	2808	2808 - 1404	
Bunch Spacing	25 - 50		ns
σ_z (rms)	7.55		cm
ε_n (x, y)	2.5	2.5 - 3.75	μm
$\beta^*_{x,y}$ (IP$_{1,5}$)	0.55	0.15 - 0.25	m
Crabbing Frequency	-	400	MHz
Crabbing Angle (θ_c)	285	470 - 580	μrad
Peak Luminosity ($\mathcal{L}$)	1.0	7 - 10	$\times 10^{34}$ cm^{2}s^{-1}
Pile-up events per crossing	19	44 - 280	

3.5.2 CRABBING SYSTEM FOR LHC UPGRADE

Crabbing cavities are an important in case of increasing the luminosity in particle colliders with head-on bunch collision. In addition, crabbing cavities further support in maintaining a larger crossing angle between the two incoming particle beams. For particle colliders with high beam currents, such as the LHC operating at 7 TeV, this is a necessity to reduce the pile-up of protons near the collision point and besides the increasing luminosity.

Two local crabbing systems will be placed at the two high luminosity interaction points of IP_1 and IP_5 [72]. Beam crossing at IP_1 is in the vertical plane and in the horizontal plane at IP_5, to minimize beam beam effects [73]. This would require one of the crabbing systems with vertical crabbing of bunches while another system with horizontal crabbing. Each crabbing system will consist of set of cavities on either side of each interaction point. The required transverse voltage per beam per side for the first crabbing system is determined by [74],

$$V_{t,1} = \frac{cE_0 \tan(\theta_c/2)}{\omega\sqrt{\beta_{crab}\beta^*}\sin\left(\psi^x_{cc\to ip}\right)} \tag{113}$$

where E_0 is the beam energy, ω is the rf frequency of the crabbing cavity, β_{crab} and β^* are the beta functions at the cavity and interaction point respectively, and $\psi^x_{cc\to ip}$ is the phase advance from the cavity to the interaction point. The transverse voltage for the crabbing system after the interaction point is given by $V_{t,2} = -R_{22}V_{t,1}$ where R_{22} is the (2,2) element of the optical transport matrix for the beam-line components between the two crabbing systems. Crabbing cavity parameters are listed in Table 6.

TABLE 6. Specifications for crabbing cavities.

Parameter	Value	Unit
Frequency	400	MHz
Crabbing voltage per beam per side	10	MV
β_{crab}	~5	km
β^*	15	cm
θ_c	470 - 580	μm
Beam Pipe Radius	42	mm
Cavity Radius	<145	mm

The crabbing cavities have strict dimensional constraints due to space limitations with the two parallel beam lines as shown in Fig. 28 [69]. The beam line separation of 194 mm with a beam aperture radius of 42 mm restricts the cavity radius to be less than 150 mm. Therefore the cryomodule will incorporate both beam lines in the design.

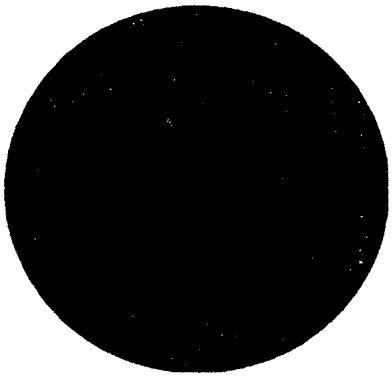

FIG. 28. Dimensional constraints of crabbing cavities.

3.6 OTHER APPLICATIONS

Deflecting and crabbing cavities can be used in multiple applications in addition to those described above. Some of the those applications are described below.

3.6.1 BEAM DIAGNOSTICS

Deflecting rf structures are also used for beam diagnostics, where the cavities are operated in an alternate phase to that of $\phi = 0^o$ or $\phi = 90^o$ as in deflecting or crabbing applications for bunch length measurements [46]. The alternate phase delivers a transverse momentum that introduces a correlation between the longitudinal and transverse momenta. The deflected bunch is projected onto a screen where the voltage gradient across the bunch and the transverse bunch size on the screen gives bunch length.

3.6.2 X-RAY PULSE COMPRESSION

Another application of crabbing rf structures is to generate high intensity x-ray beams with very short pulses in storage rings [47]. Typically, in storage rings the circulating electron bunches produce synchrotron radiation pulses in the order of 10

ps. Crabbing cavities are used to generate x-ray pulses in the time scale of ~ 0.1 ps. A transverse force is applied to rotate the bunch in order to generate a vertical displacement of electrons correlated to their longitudinal position. The subpicosecond slices of the bunch then produce very short x-ray pulses.

3.6.3 EMITTANCE EXCHANGE

Emittance exchange of bunches uses deflecting rf structures to interchange the longitudinal emittance with transverse emittance [48]. The emittance exchange is achieved by placing a transverse deflecting mode radio-frequency cavity in a magnetic chicane that is used to reduce the longitudinal emittance in free electron lasers (FELs). In addition to reducing the transverse emittance, the bunch length is also simultaneously compressed.

CHAPTER 4

DESIGN OPTIMIZATION

The deflecting and crabbing cavities of frequencies 499 MHz and 400 MHz for the Jefferson Lab 12 GeV upgrade and LHC high luminosity upgrade have specific design requirements. These requirements set forth the need of compact rf geometries with high operating gradients and high shunt impedance. In designing a cavity for the two applications mentioned above we started with the design evolution of the TEM-type parallel-bar cavity and ultimately arrived at a TE-type rf-dipole cavity. In this chapter, the process of optimizing the cavity design is discussed in detail. Our final cavity design shows improved rf properties that achieve the design requirements.

The optimization process can be expressed in general as follows

$$\mathcal{O}\left(f_0, E_t, E_p, B_p, R_t\left(G, \left[\frac{R}{Q}\right]_t\right)\right) = \mathcal{F}\left(r_0, R, L, d_n, r_n\right) \tag{114}$$

where f_0 is the cavity frequency, E_t is the transverse electric field, E_p and B_p are the peak electric and magnetic fields, R_t is the transverse shunt impedance. The design parameters include fixed and varying parameters. The beam aperture radius (r_0) is fixed by the beam specifications. The varying parameters delivers the optimum output with constant design frequency f_0, maximum E_t and R_t, and minimum E_p and B_p. The key design parameters are the cavity radius (R), cavity length (L), and design parameters of the loading elements (d_n) primarily consisting of bar height, bar length. The curving radii (r_n) of different edges in the design are of equal importance in reducing E_p and B_p. Some of the resultant parameters are inter-related, such as the R_t that depends on the geometrical factor (G), and transverse $\left[\frac{R}{Q}\right]$ that depends on E_t. The methodical optimization carried out on outer conductor and inner loading element design parameters have resulted in rf designs with low surface fields at high operating gradients, high shunt impedance and wider higher order mode spectra.

The transverse momentum acquired by a particle in deflecting and crabbing structures is proportional to the transverse voltage, and therefore to the peak surface fields. However, in superconducting structures, the peak surface electric and magnetic fields cannot exceed certain values. The peak surface electric field (E_p) is limited by field

emission [45, 75] at high field gradients. The contaminant particles or any protrusions present on the surface give rise to field enhancement at localized high electric field regions, emitting electrons from the surface, as explained in Chapter 2. The emitting electrons traveling with the rf field may collide with the cavity surface, depositing heat on the cavity surface. The extreme electron currents may lead to a thermal breakdown due to excess heating, also reducing the quality factor (Q_0) exponentially, hence limiting the achievable peak surface electric field. Due to the advanced cleaning and chemical processing techniques in treating the cavity surfaces, at present the superconducting cavities can reliably reach maximum tolerable peak electric field levels in excess of 50 MV/m.

The peak surface magnetic field (B_p) for Type II superconductors is confined by the theoretical limit of lower critical magnetic field (B_{c1}), which for Nb is 170 mT [45]. Superconducting rf cavities in the early days often showed the achievable peak surface magnetic field levels considerably lower than the theoretical one. Any defects present on the cavity surface in high magnetic field regions is as a limiting factor that leads to a local increase of the temperature resulting in excess power dissipation and eventually thermal breakdown [45, 75], reducing the achievable field level, as explained in Chapter 2. The improved surface treatment techniques have now improved the performance of superconducting rf cavities that are capable of achieving peak surface magnetic fields closer to the theoretical limit.

Due to the limitations in the peak surface fields, the superconducting deflecting and crabbing cavity designs presented here were optimized to minimize the corresponding ratios of E_p/E_t and B_p/E_t in order to maximize the net deflection while keeping the surface fields at a minimum. The peak surface field ratio given by B_p/E_p is equally important in designing superconducting cavities with well-balanced peak surface fields. A higher peak field ratio could result a high peak surface magnetic field or a very low peak surface electric field and vice versa for a low peak field ratio. In either case the operating voltage of the cavity may be limited by just one of the peak surface field limits mentioned above. Therefore it is desirable to balance the peak field ratio such that the operating limits are met simultaneously. Furthermore, whether the cavities will be used in deflecting or crabbing applications, they will necessarily be in small number. On the other hand they must achieve their design performance in order to be operational. Thus the peak surface electric and magnetic

field must be limited to values that can be reached with a high probability, sufficiently below the highest that have been demonstrated at low frequency [76]. Given the state of the art we have chosen $E_p \simeq 35$ MV/m and $B_p \simeq 70$ mT (and therefore $B_p/E_p \simeq 2$ mT/(MV/m)) as design values. This ratio would be slightly less than 2 mT/(MV/m) for cavities operating at 4.2 K and slightly more for cavities operating at ~2.0 K.

4.1 COMPUTATIONAL METHODS IN 3D EIGENMODE SIMULATOR

The electromagnetic fields for each resonant mode present in an rf geometry are obtained by solving the Maxwell's equations given in Eq. 1 with the boundary conditions and assuming the resonant structure is lossless. The resonant frequencies and the rf properties described in Sec. 2.2 are then determined by the corresponding solutions. Electromagnetic problems related to complex geometries cannot be solved purely by the means of analytical methods. In such instances, numerical methods are followed to obtain the solutions to the eigenmode problem. Numerical methods follow a discrete formulation of the Maxwell's equations in their integral form [77]. Several techniques exist, such as Finite Difference Method (FDM), Boundary Element Method (BEM), Finite Element Method (FEM), Finite Volume Method (FVM), and Finite Integration Technique (FIT). CST Studio Suite [13] follows the Finite Integration Technique proposed by Weiland [77, 78]. The FIT solution is obtained by decomposing the volume into a grid with multiple cells, named mesh and solving the Maxwell's equations in the form of grid equations.

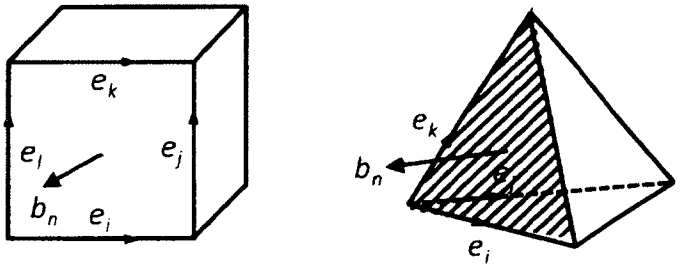

FIG. 29. A single meshing element in hexahedral (left) and tetrahedral (right) type mesh.

The CST Microwave Studio supports two types of meshing in discretizing the volume as shown in Fig. 29. The hexahedral mesh uses a staircase type meshing

with non-equidistant step sizes to model the curved boundaries. With the tetrahedral meshing a more refined mesh can be utilized by reducing the approximation of the curved surfaces. that generate mesh cells close to the ideal shape of the rf structure. The accuracy of the eignmode solution depends directly on the number of mesh elements used in the numerical computation. An accurate frequency for each is obtained at an accuracy of 10^{-6} in CST Microwave Studio. The number of mesh elements required to achieve accurate results are determined with repetitive calculation on mesh convergence.

4.2 PARALLEL-BAR DESIGN

The TEM-type parallel-bar deflecting/crabbing cavity in its simplest form consists of two $\lambda/2$ TEM parallel lines connecting the top and bottom plates as shown in Fig. 30 [10]. The number of fundamental modes is determined by the number of TEM parallel lines in the cavity, thus the TEM-type parallel-bar cavity has two fundamental degenerate modes. In the 0-mode the parallel lines oscillate in phase, cancelling the transverse field between the lines. In the other degenerate mode (the π-mode) in which the parallel lines oscillate out of phase, the transverse electric field between the lines, produces the deflection.

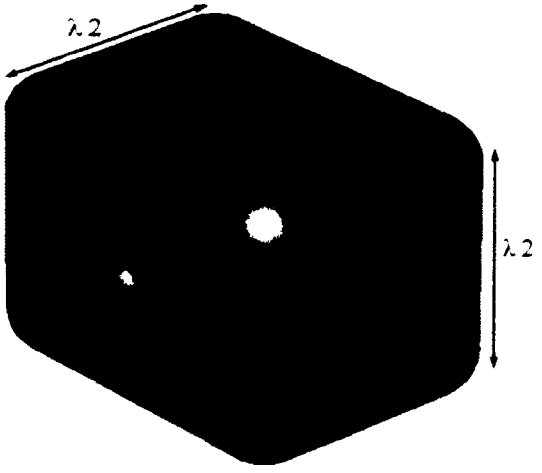

FIG. 30. Parallel-bar geometry with a rectangular-shaped outer conductor and cylindrical loading elements.

The electric field distribution of the deflecting mode (π-mode) is shown in Fig. 31. The transverse electric field is concentrated between the parallel bars, where the

magnetic field is maximum on the top and bottom plane as shown in Fig. 31 and the electric field is maximum on the mid plane between the parallel bars.

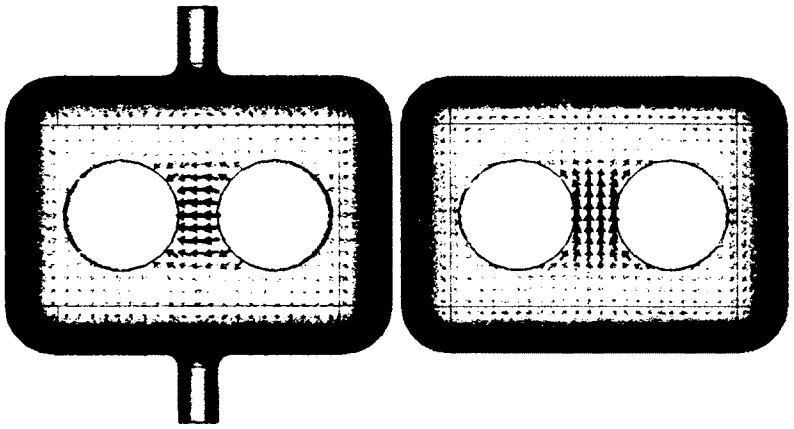

FIG. 31. Electric field (left) on the mid plane and magnetic field (right) on the top plane for the fundamental deflecting mode.

In the 0-mode the transverse electric field is cancelled between the bars (Fig. 32), however there is a longitudinal component remaining near the ends of the cavity so this mode would operate as an accelerating mode. The transverse field is stronger between the bars and the side walls of the cavity. Likewise the magnetic field circles enclosing both the parallel bars as shown in Fig. 32.

The degeneracy of the two fundamental modes (π-mode and 0-mode) is slightly removed by $\sim$1 MHz with the inclusion of the beam pipe. The modes are further separated by rounding the edges on the top and bottom plane. The contribution to the separation of the two modes by the rounded edges around each axis shown in Fig. 33 are not identical, where the rounded edges along y direction has no contribution while the curvature along x direction gives the maximum separation (Fig. 34).

The rounded edges give rise to a magnetic field in the vertical direction between the parallel bars and the front and end plates of the rectangular-shaped cavity, which is otherwise zero. Therefore the parallel-bar deflecting and crabbing cavity has both electric and magnetic field components along the beam axis. The corresponding field components at a normalized stored energy of 1.0 J are shown in Fig. 35. The net deflection seen by a particle with velocity $\beta = v/c = 1$ is determined as in Eq. (15). where transverse electric field is of cosine form (even) and magnetic field is of sinusoidal form (odd). The main contribution to the net deflection is by the horizontal

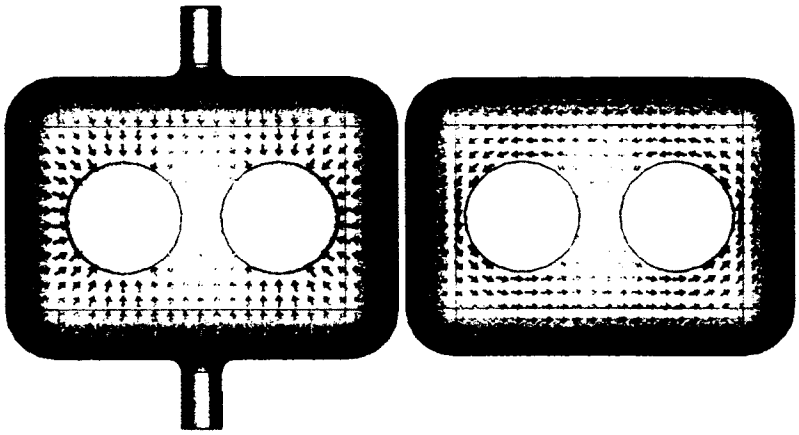

FIG. 32. Electric field (left) on the mid plane and magnetic field (right) on the top plane for the fundamental accelerating mode.

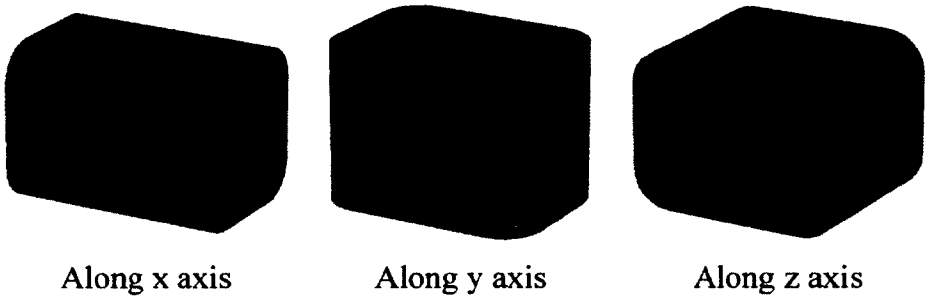

FIG. 33. Rounding of edges along different axes.

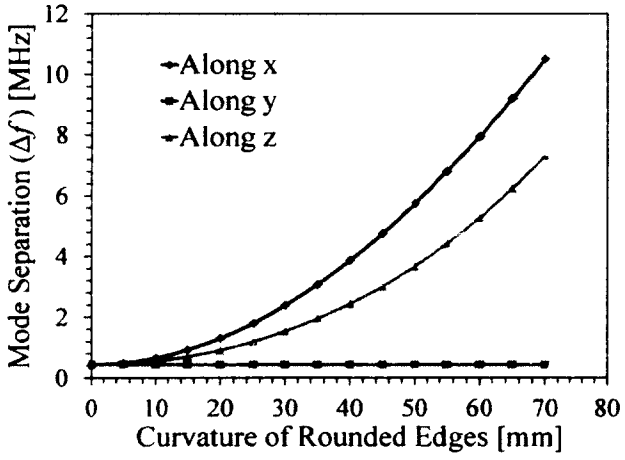

FIG. 34. Mode separation between the fundamental modes with the rounded edges.

electric field component (E_x) while the vertical magnetic field (H_y) component opposes the net deflection lowering the net transverse voltage as shown in Fig. 36. However the effect from the magnetic field component is comparatively small.

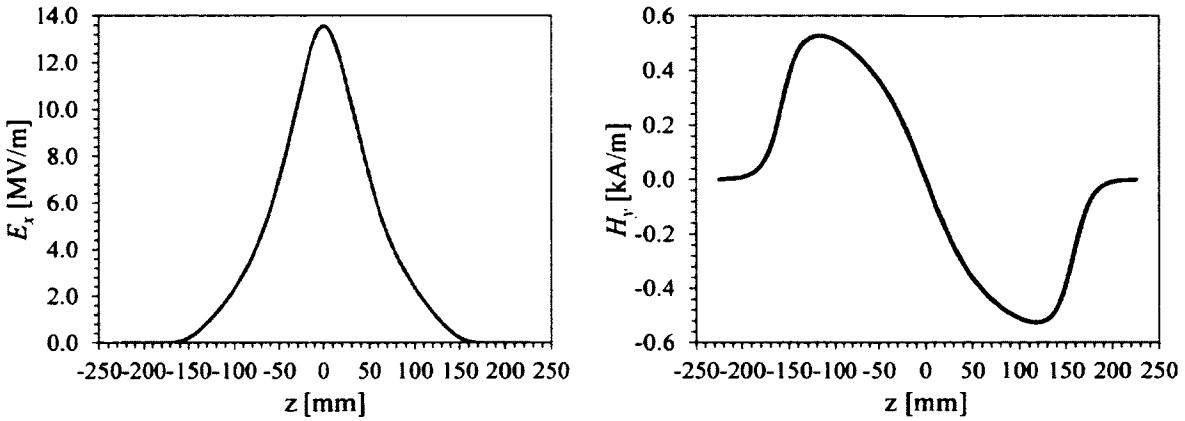

FIG. 35. Transverse electric and magnetic field components along the beam axis, at an energy content of 1.0 J in a 499 MHz parallel-bar cavity shown in Fig. 30.

The TEM-type parallel-bar cavity has no on-axis longitudinal electric field component. The longitudinal electric field increases transversely in horizontal direction as shown in Fig. 37. The off axis longitudinal electric field can also be used to determine the net deflection using Eq. 12. The net deflection calculated in the direct integral method and using Panofsky-Wenzel Theorem (Eq. 12) are in agreement within 0.07%.

4.3 DESIGN EVOLUTION

A series of parallel-bar cavity geometries with different outer conductors and parallel loading elements (Fig. 38) were analyzed at both 499 MHz and 400 MHz, and compared in identifying a design with optimal properties [79, 80]. The design properties for each design were analyzed using the 3D eigenmode solver in CST Microwave Studio [13].

4.3.1 499 MHZ DEFLECTING CAVITY

The 499 MHz deflecting cavity design for the rf separator system, with a fixed beam aperture diameter of 40 mm, was optimized and is expected to achieve a total transverse voltage of 5.6 MV. The parallel-bar geometry was adapted by changing

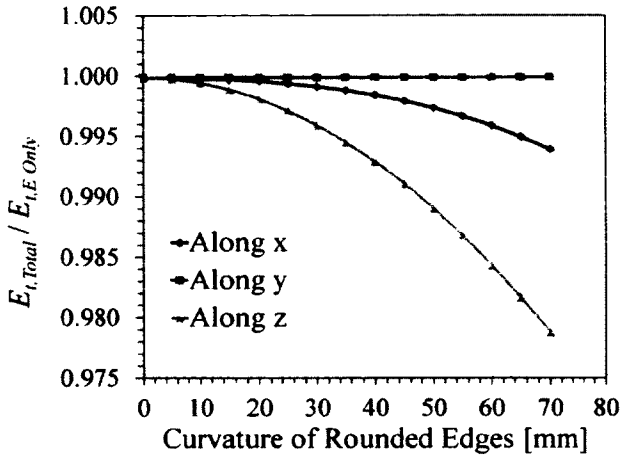

FIG. 36. Electric field and magnetic field contribution to the transverse deflection with varying curvature on the rounded edges.

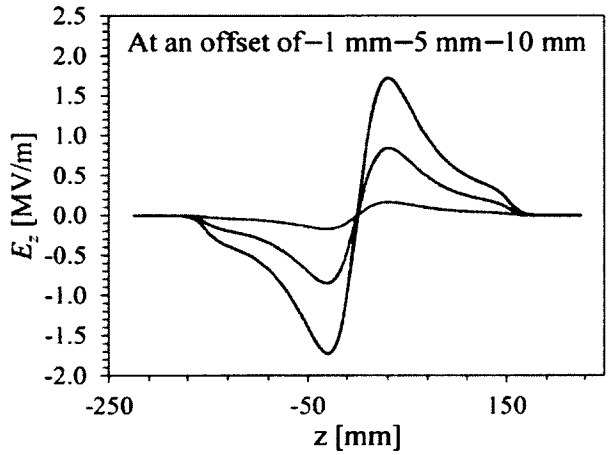

FIG. 37. Longitudinal electric field component along the beam axis at an offset of 1 mm, 5 mm, and 10 mm at an energy content of 1.0 J in a 499 MHz parallel-bar cavity shown in Fig. 30.

the rectangular-shaped outer conductor into a cylindrical-shaped design, specifically to increase the mode separation in the higher order mode (HOM) spectrum [81, 82]. Furthermore the parallel loading elements were adapted in such a way to maximize the net deflection with low and well-balanced peak surface fields.

Design (A)

The parallel-bar cavity design proposed by the analytical model [10] shown by Design (A) in Fig. 39 has cylindrical loading elements in a rectangular-shaped outer conductor. The length of the cavity is $\lambda/2$, however the cavity height is slightly greater than $\lambda/2$ with the adjustments made to achieve the design frequency of 499 MHz, due to the rounded edges of the cavity. In this design the radius of the cylindrical loading elements is optimized with a fixed outer conductor in order to maximize the net deflection and minimize peak surface fields, by minimizing the ratios of E_p/E_t and B_p/E_t as shown in Fig. 40. Increasing radius of the cylindrical loading elements changes the frequency of the fundamental mode, and is adjusted with by slightly increasing in the cavity height, as shown in Fig. 41.

The R_tR_s is determined as given in Eq. (22) and has quadratic dependence with the radius of the cylindrical parallel bars as shown in Fig. 42. It can be noticed that the radius that maximizes the shunt impedance is close to the one that minimizes the peak surface fields.

The radius of the rounded edges of the cavity is directly related to the frequency separation of the two fundamental modes, as the beam line ports contribute little to the frequency separation. The increase in curvature increases the mode separation, but also increases the peak surface field ratios of E_p/E_t and B_p/E_t about 4% and 1.5% and reduces shunt impedance about 4%, for a rounding radius of 100 mm. The considerably small change has less impact on the rf properties, but higher curvatures limit the radius of the cylindrical loading elements. Therefore the curvature of the rounded edges was selected to be 50 mm; this gives a mode separation of ~11 MHz. The low mode separation could make the damping of the higher-order modes more challenging. It should be noted however that the deflecting mode is always the lowest frequency mode.

The cavity width has negligible effect on the peak surface field ratios of E_p/E_t and B_p/E_t, as changes as low as $\sim$ 5% and $\sim$ 2% respectively for an increase of 140 mm. However, it has a considerable effect on R_tR_s where the shunt impedance

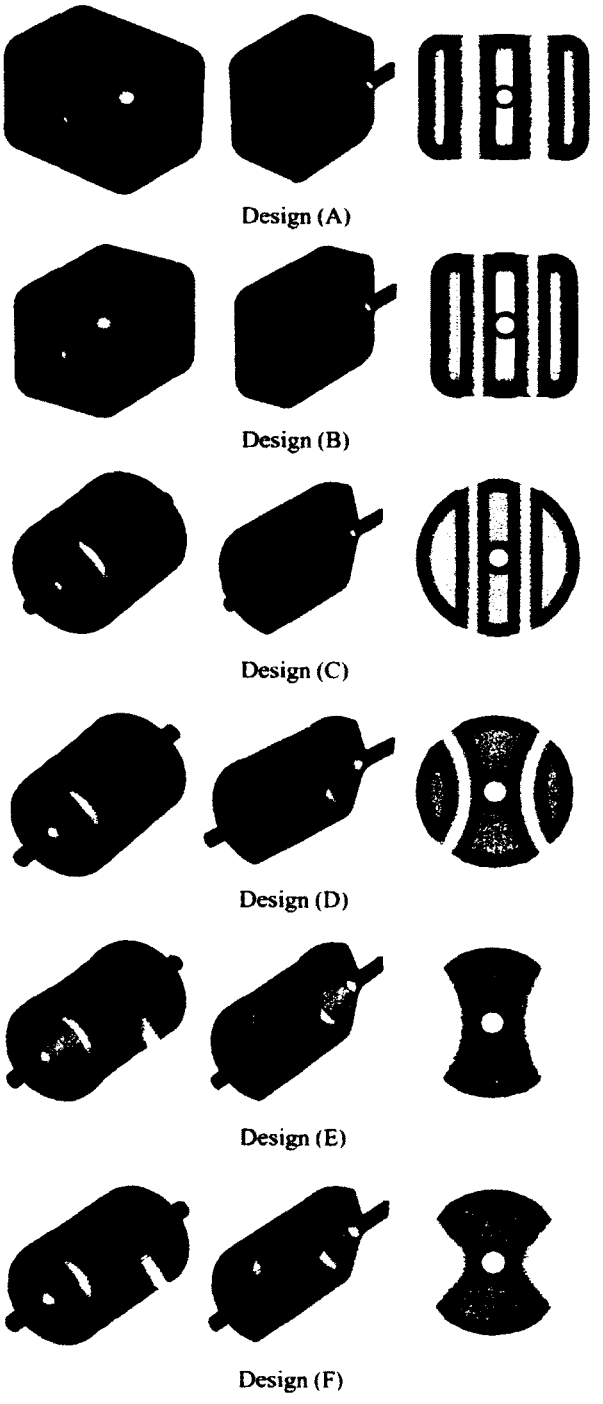

FIG. 38. Evolution of the parallel-bar cavity geometry into the rf-dipole geometry and cross sections of each design.

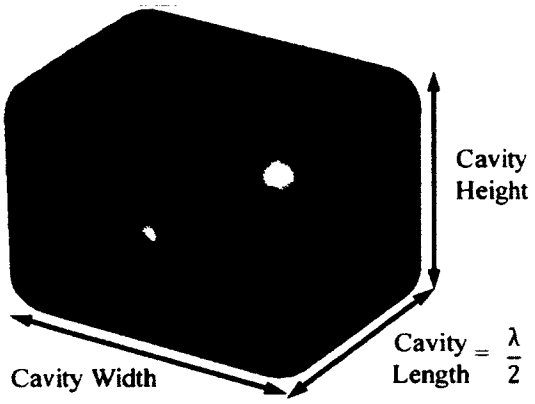

FIG. 39. Design parameters of optimization for the parallel-bar design with rectangular outer conductor and cylindrical loading elements.

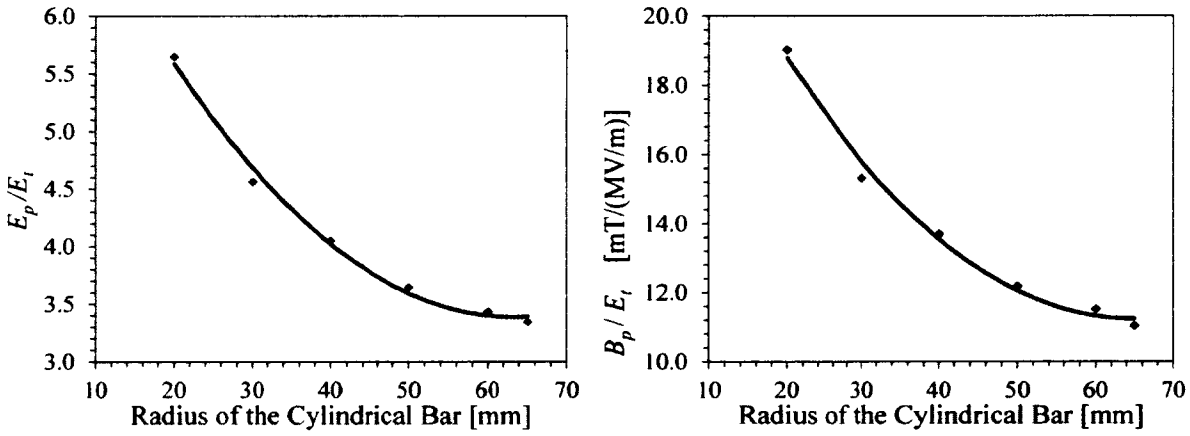

FIG. 40. Ratios of peak surface electric field (E_p) and magnetic field (B_p) to the transverse electric field (E_t) with varying radius of cylindrical parallel bars.

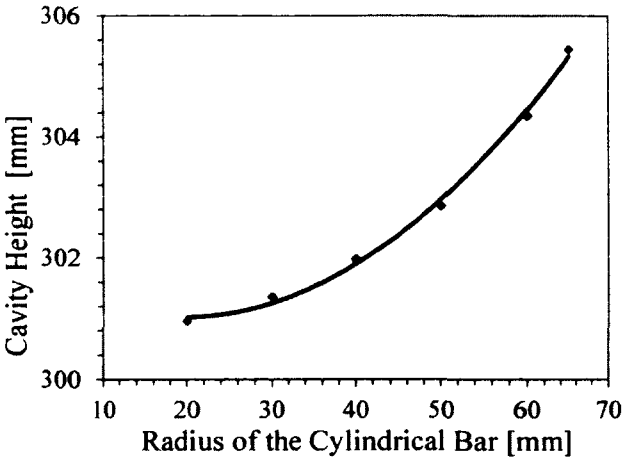

FIG. 41. Cavity height change with varying radius of cylindrical parallel bars at constant frequency of 499 MHz.

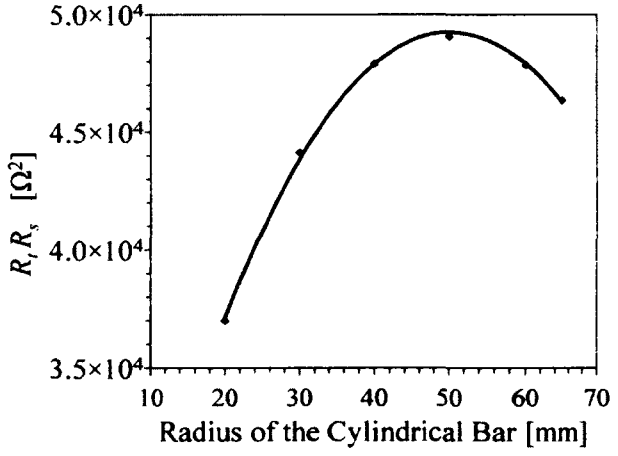

FIG. 42. Product of transverse shunt impedance (R_t) and surface resistance (R_s) with varying radius of cylindrical parallel bars.

increases with increasing cavity width as shown in Fig. 43.

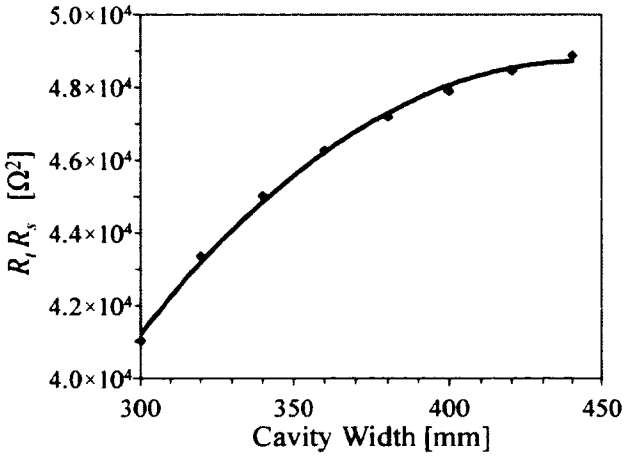

FIG. 43. Product of transverse shunt impedance (R_t) and surface resistance (R_s) with varying cavity width of parallel-bar design with rectangular-shaped outer conductor and cylindrical loading elements.

The electric and magnetic fields of the Design A are shown in Fig. 44. The peak surface fields for this design are shown in Fig. 45, where the peak electric field is concentrated in the middle of the bars and the peak magnetic field is highest on the top and bottom surfaces of the bars and cavity. At a smaller radius both electric and magnetic peak fields between the parallel bars are high, resulting higher ratios of E_p/E_t and B_p/E_t. As the radius is increased the design properties improve due to the increase in the transverse electric field component along the beam line and the decreasing surface fields.

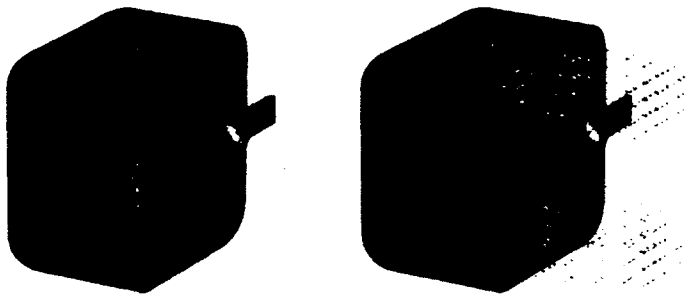

FIG. 44. Electric (left) and magnetic (right) fields in the parallel-bar design with cylindrical loading elements.

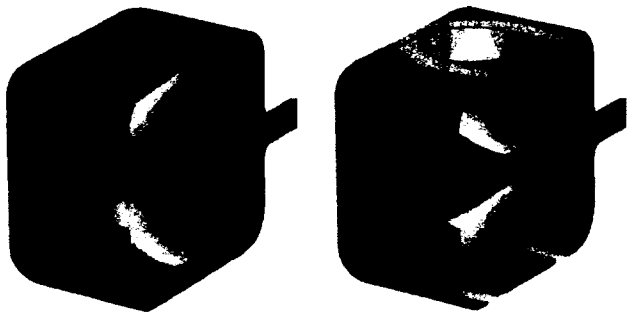

FIG. 45. Surface electric (left) and magnetic (right) fields in the parallel-bar design with cylindrical loading elements.

The design properties of the parallel-bar deflecting cavity are shown in Table 7. The resultant peak surface field ratios to the transverse electric field are $E_p/E_t = 3.45$ and $B_p/E_t = 11.47$ mT/(MV/m). Therefore a cavity required to deliver a transverse voltage of 3 MV needs to operate at a peak surface electric field of $E_p = 34.5$ MV/m and at a peak surface magnetic field of $B_p = 114.7$ mT. which is somewhat higher than the achievable practical limit. In pure TEM-modes $E_p/H_p = Z_0 \simeq 377\ \Omega$, the impedance of vacuum (irrespective of geometry) or $B_p/E_p = 3.33$ mT/(MV/m). In order to achieve a better balanced peak surface field ratio of 2.0 the peak surface magnetic field would then need to be reduced at the expense of an increased peak surface electric field.

TABLE 7. Properties of the geometries of 499 MHz designs shown in Fig. 38.

Parameter							Units
Frequency of π mode	499.0	499.0	499.0	499.0	499.0	499.0	MHz
Frequency of 0 mode	509.7	517.4	660.4	860.4	1022.0	1036.1	MHz
Frequency of nearest mode	509.7	517.4	626.1	763.5	754.3	777.0	MHz
$\lambda/2$ of π mode	300.4	300.4	300.4	300.4	300.4	300.4	mm
Cavity Length (Iris to iris)	300.4	406.5	424.0	400.0	450.0	440.0	mm
Cavity Height	304.3	304.6	-	-	-	-	mm
Cavity Width	400.0	300.0	-	-	-	-	mm
Cavity Diameter	-	-	318.0	272.8	250.5	241.2	mm
Aperture Diameter	40.0	40.0	40.0	40.0	40.0	40.0	mm
Bar Length	-	286.5	274.0	260.0	295.0	260.0	mm
Bar Diameter / Width	120.0	70.0	60.0	65.0	-	-	mm
Bar Height / Curved Height	304.3	304.6	157.7	262.4	204.0	-	mm
Bar Inner Height	-	-	-	-	-	50.0	mm
Angle	-	-	-	-	-	50.0	deg
Deflecting Voltage (V_t[1])	0.30	0.30	0.30	0.30	0.30	0.30	MV
Peak Electric Field (E_p[1])	3.45	1.83	2.08	2.55	2.85	2.86	MV/m
Peak Magnetic Field (B_p[1])	11.47	6.05	6.47	5.42	5.12	4.38	mT
B_p/E_p	3.33	3.30	3.12	2.12	1.80	1.53	mT/(MV/m)
Energy Content (U[1])	0.049	0.030	0.032	0.033	0.036	0.029	J
Geometrical Factor (G)	80.9	67.0	67.4	87.7	94.2	105.9	Ω
$[R/Q]_t$	591.7	935.9	887.3	866.8	807.7	982.5	Ω
$R_t R_s$	4.8×10^4	6.3×10^4	6.0×10^4	7.6×10^4	7.6×10^4	1.0×10^5	Ω^2

[1] At $E_t = 1$ MV/m

Optimization of Loading Elements

It is also clear that the effective deflecting length is equally important in increasing the resultant deflection in the parallel-bar deflecting and crabbing cavities, due to the localized transverse fields between the parallel loading elements. Therefore the peak surface fields for a given deflecting field can be reduced by increasing the effective deflecting length along the beam line. Three design structures shown in Fig. 46 were analyzed in order to optimize the effective length of deflection [83]. The designs have identical rectangular outer conductor as in Design (A), while modifying the parallel bar orientation to maximize the net deflection. In each design the cross section orientation is maximized to achieve the largest possible effective length, also curving adequately to minimize higher field concentration on edges, enabling more distributed surface fields. All the three designs with increased effective deflecting length have improved properties compared to the parallel-bar cavity with cylindrical loading elements and also have more uniform field between the parallel bars along the beam line.

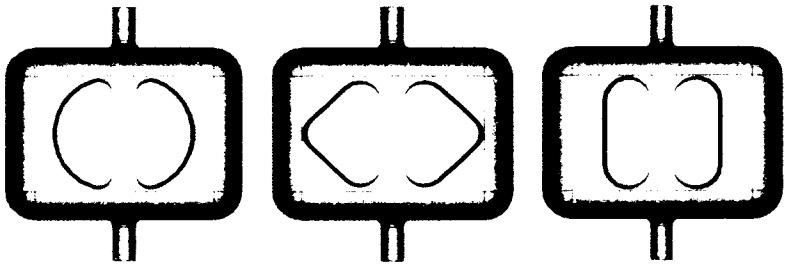

FIG. 46. Parallel-bar cavity designs with different cross sections.

The design properties are comparable as shown in Table 8 between the designs with half-circular-shaped and triangular-shaped loading elements. However the design with race-track-shaped loading elements is preferable in reducing peak surface fields with further optimizations described below.

Design (B)

The parallel-bar design with a race-track-shaped loading element in a rectangular-shaped outer conductor was further improved by varying bar width and the bar length, which are the key optimizing parameters for this design as shown in Fig. 47.

TABLE 8. Properties of parallel-bar cavities with different cross sections shown in Fig. 46.

Parameter				Units
E_p^2	2.29	2.3	2.21	MV/m
B_p^2	5.95	5.96	5.75	mT/(MV/m)
$[R/Q]_t$	1043.5	969.0	992.5	Ω
G	68.3	69.3	69.4	Ω
$R_t R_s$	7.1×10^4	6.7×10^4	6.9×10^4	Ω^2

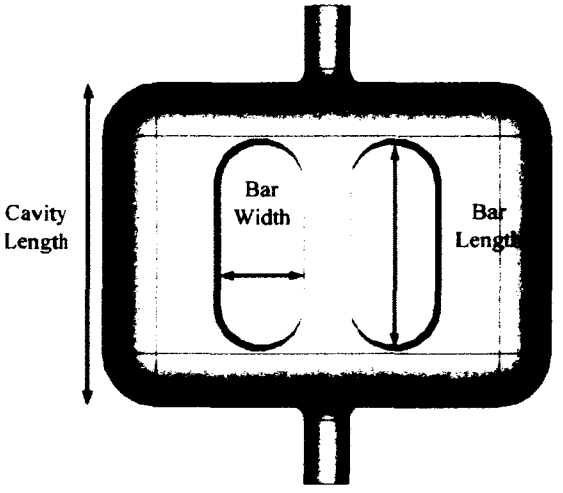

FIG. 47. Design parameters of optimization for the parallel-bar design with rectangular outer conductor and race-track-shaped loading elements.

As seen earlier the longer effective deflecting length gives a higher net deflection and the bar width optimizes the spread of the surface electric field on the bar as well as the surface magnetic field on the top and bottom surfaces in the cavity. The dependence of design properties on the bar width and length of the parallel-bar cavity is shown in Fig. 48. The ratio E_p/E_t decreases with the increasing bar length. The width of the race-track-shaped loading elements optimizes the spread of the surface fields as shown in Fig. 49. The strong peak fields at the edges of narrow parallel bars increases both E_p/E_t and B_p/E_t. In the opposite, wider parallel bars with rounding of the edges reduce the achieved net deflection. The R_tR_s drops rapidly with the increasing bar width.

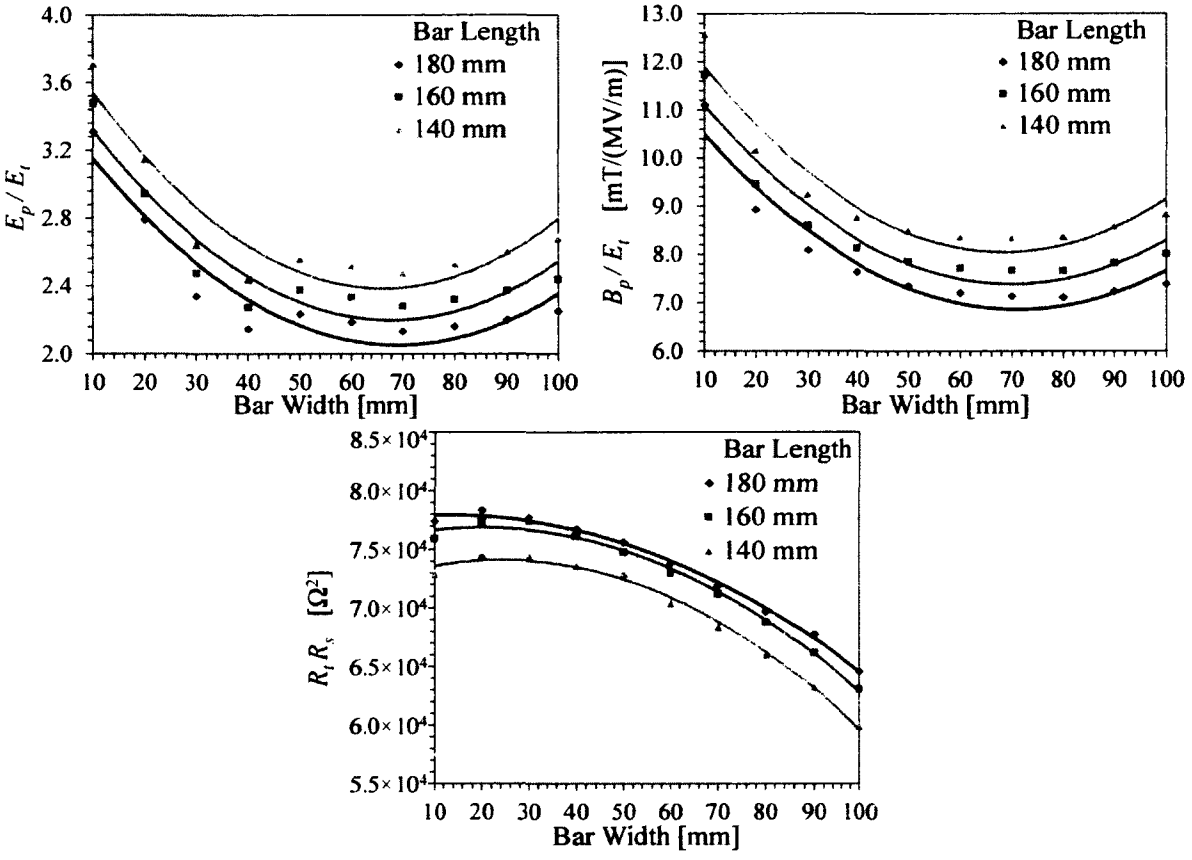

FIG. 48. Ratios of peak surface electric field (E_p) and magnetic field (B_p) to the transverse electric field (E_t) and R_tR_s with varying bar width and bar length for race-track-shaped parallel bars.

Similar to Design (A), the cavity height increases gradually with increasing bar length and bar height, at constant frequency (Fig. 50). Likewise, the cavity width has

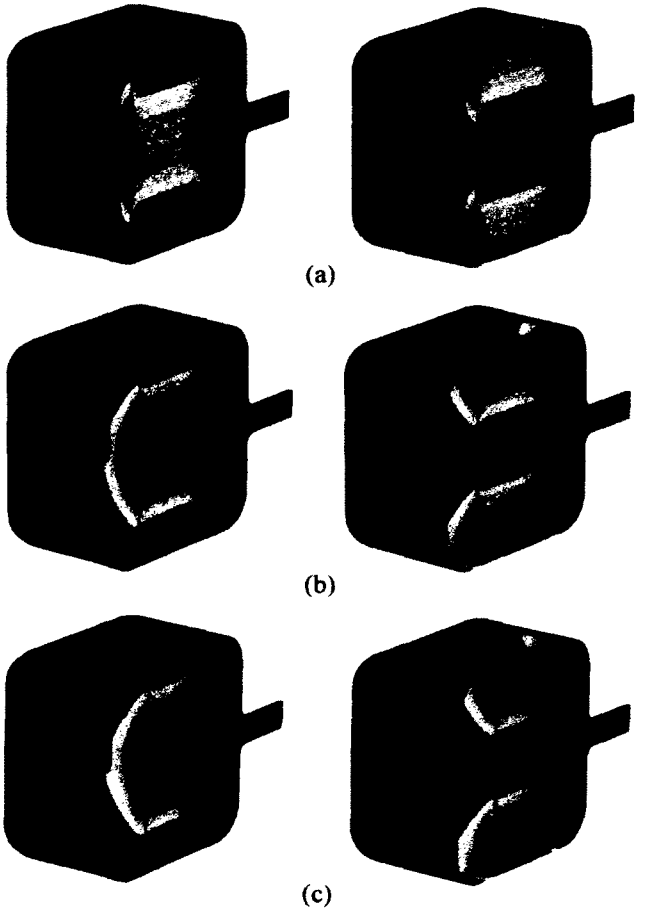

FIG. 49. Surface electric (left) and magnetic (right) field at bar widths of (a) 20mm, (b) 60 mm and (c) 100 mm.

negligible impact on peak surface field ratios, with a considerable impact on $R_t R_s$. However, the optimized Design (B) has the smallest width possible with optimized bar width.

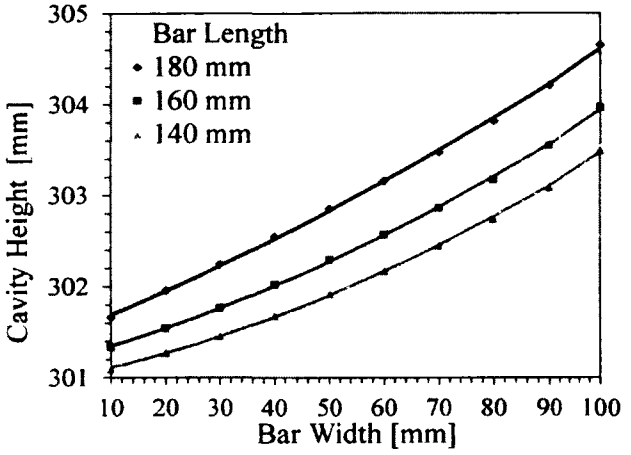

FIG. 50. Cavity height with varying bar width and bar length for race-track-shaped parallel bars.

In the parallel-bar cavity the transverse electric field is concentrated between the two parallel bars, therefore the bar length can be further optimized with the cavity length, by increasing both bar length and the cavity length. The optimum effective deflecting length is when the bar length in the order of $\lambda/2$ as shown in Fig. 51. $R_t R_s$ is maximized at a shorter cavity and bar length, where the drop in $R_t R_s$ is lesser compared to the reduction achieved in peak surface field ratios.

The field content and surface fields in Fig. 52, shows that the transformation in the geometry does not alter the fundamental on axis field configuration. The final design properties of the optimized parallel-bar cavity with a rectangular outer conductor and a race-track-shaped loading elements are given in Table 7. The design geometry shows significant improvement on both peak surface electric and magnetic fields of 50%. The peak surface fields are substantially reduced; however this geometry still has a peak field ratio of $B_p/E_p = 3.3$ mT/(MV/m), higher than desirable. The width is reduced substantially making the design more compact. However the mode separation between the fundamental modes is still only $\simeq$18 MHz. Also the large flat surfaces make the design prone to deformations due to radiation pressure and sensitivity to liquid helium pressure fluctuations. This can lead to a mixing of modes with a longitudinal electric field present in the fundamental deflecting mode [84].

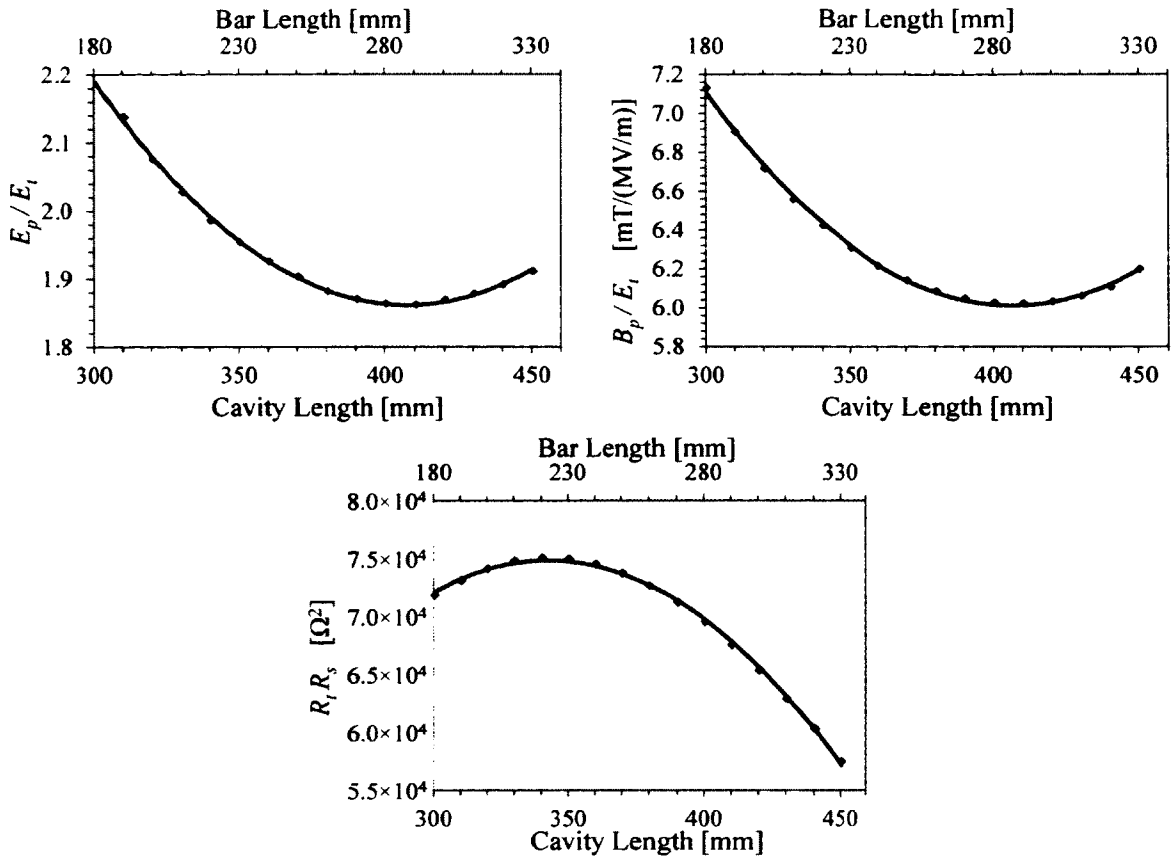

FIG. 51. Ratios of peak surface electric field (E_p) and magnetic field (B_p) to the transverse electric field (E_t) and R_tR_s with varying cavity length for race-track-shaped parallel bars.

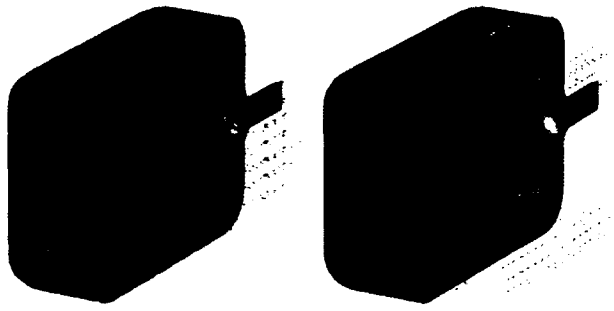

FIG. 52. Electric (left) and magnetic (right) field profile of the parallel-bar design with race-track-shaped loading elements.

Design (C)

The parallel-bar cavity design is further modified with a cylindrical outer conductor, keeping the race-track-shaped loading elements as shown in Fig. 53, in order to increase the mode separation. The important parameters of optimization are the bar width, bar length, and the cavity length. The bar height is primarily depends on the cavity diameter. The design also incorporates sloped end plates for efficient chemical processing of the cavity inner surface and increased stiffness. The dependence of the end plate slope on E_p/E_t, B_p/E_t and R_tR_s are shown in Fig. 54. The shunt impedance saturates with the increasing slope, where the peak surface field ratios continue to slightly increase, therefore an end plate slope of 40 mm is selected in this design, also considering the feasibility in fabrication.

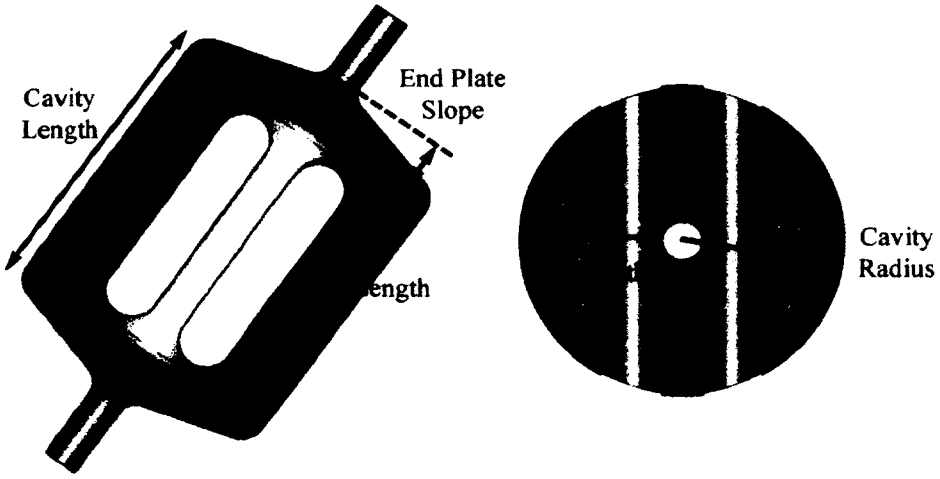

FIG. 53. Design parameters of optimization for the parallel-bar design with rectangular outer conductor and race-track-shaped loading elements.

The bar width, bar length and cavity length are optimized in a similar manner as in Design (B). The dependence of the peak field ratios of E_p/E_t, B_p/E_t and R_tR_s are shown in Fig. 55. The parallel-bar design with cylindrical-shaped outer conductor shows similar variation in the peak surface field ratios with increasing bar width for different bar lengths, resulting in an equivalent minimum in the bar width of 65 mm. The R_tR_s in Design (C) decreases as the bar width increases, but with a smaller drop compared to Design (B) due to the difference in the field content.

The cavity radius increases almost linearly with increasing bar width and bar height as the frequency is kept constant at 499 MHz (Fig. 56). This increase in radius

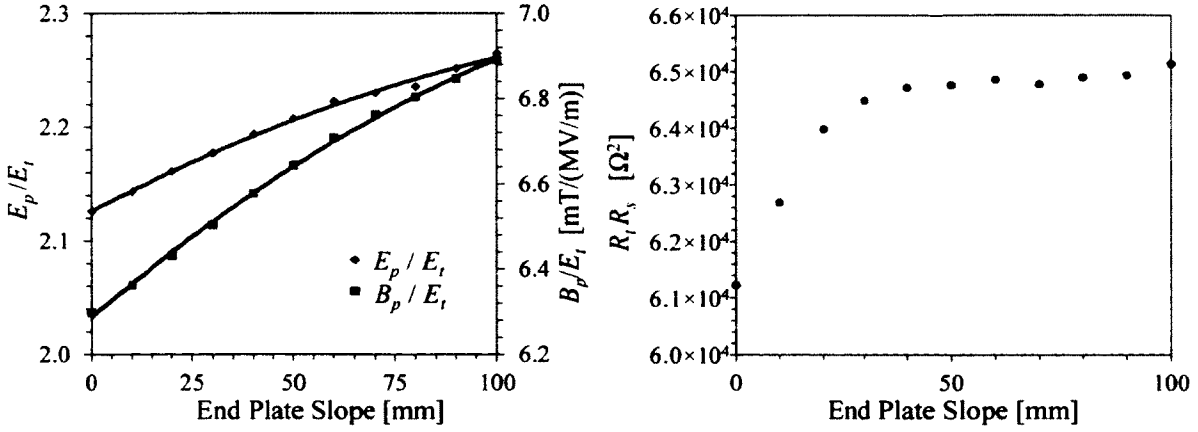

FIG. 54. Ratios of peak surface electric field (E_p) and magnetic field (B_p) to the transverse electric field (E_t) and $R_t R_s$ with varying end plate slope.

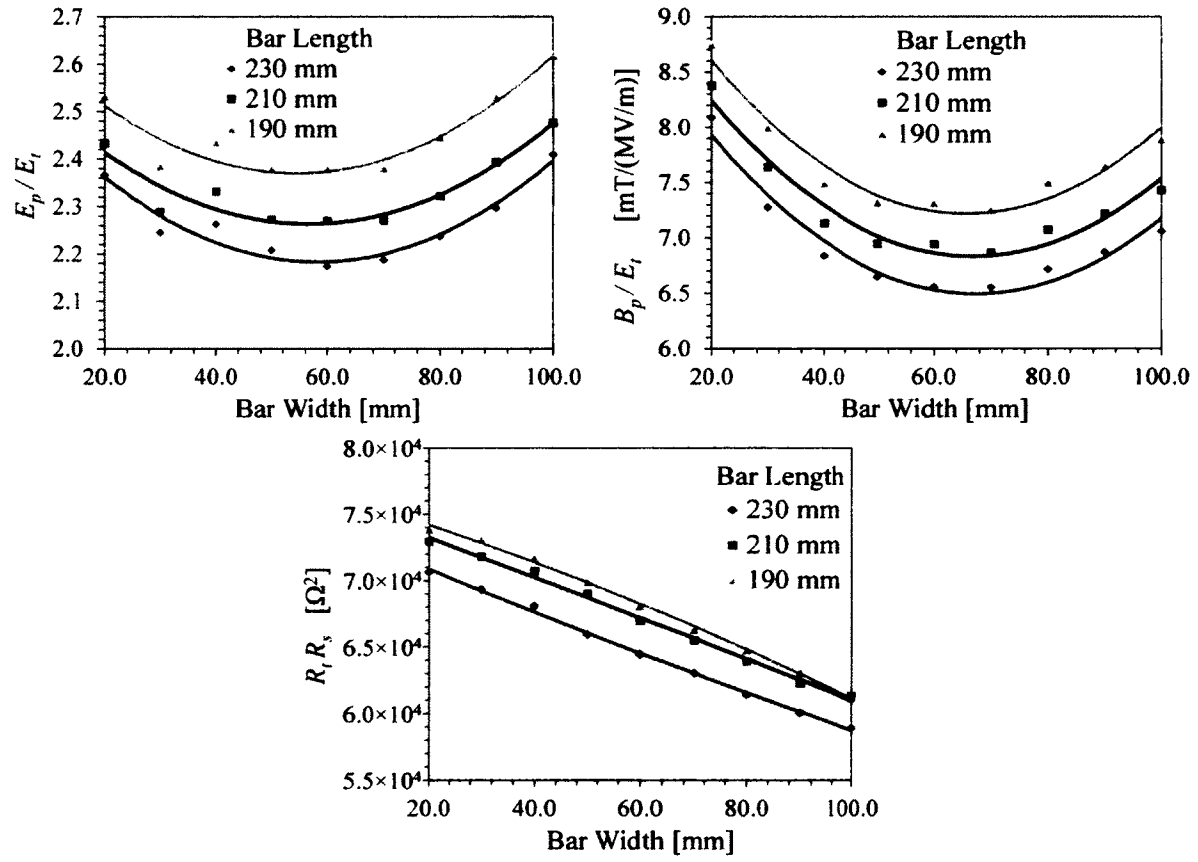

FIG. 55. Ratios of peak surface electric field (E_p) and magnetic field (B_p) to the transverse electric field (E_t) and $R_t R_s$ with varying bar width and bar length for race-track-shaped parallel bars with cylindrical outer conductor.

makes the transverse dimensions somewhat larger compared to the respective design with rectangular outer conductor. The design with the cylindrical outer conductor has a significantly-improved mode separation between the two fundamental modes of 127 MHz compared to the $\simeq$18 MHz in the previous design. This geometry also has an increasing mode separation in the higher order modes spectrum.

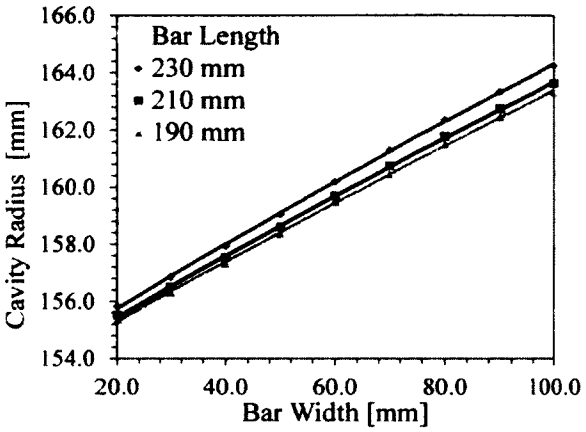

FIG. 56. Cavity radius with varying bar width and bar length for race-track-shaped parallel bars with cylindrical outer conductor.

The electric and magnetic field (Fig. 57) in this design contributes to the transverse voltage as defined for TEM-type design. One limitation in this design is that it still has a high peak surface magnetic field (Fig. 58) and a far-from-optimal B_p/E_p. The properties of this design are shown in Table 7. Since the parallel bars are constraining the volume for the magnetic field, it is desirable to curve the parallel loading elements to reduce the peak surface magnetic field by increasing the magnetic field volume.

Design (D)

This design is further optimized with curved loading elements as shown in Fig. 59. The main optimizing parameters are the bar width and the curvature of the bars, as shown in Fig. 59. The effect of the curving radius and the width of the parallel bars on E_p/E_t and B_p/E_t is shown in Fig. 60. As the curvature radius is reduced the peak surface magnetic field decreases and the peak surface electric field increases. At very high curvatures (i.e. >400 mm) the design properties are similar to those of the straight parallel bars. Also E_p/E_t and B_p/E_t are independent of the optimum

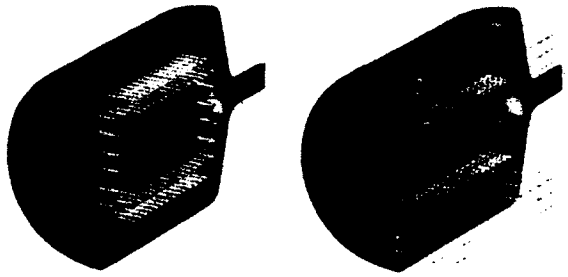

FIG. 57. Electric (left) and magnetic (right) field profile of the parallel-bar design with cylindrical outer conductor and race-track-shaped loading elements.

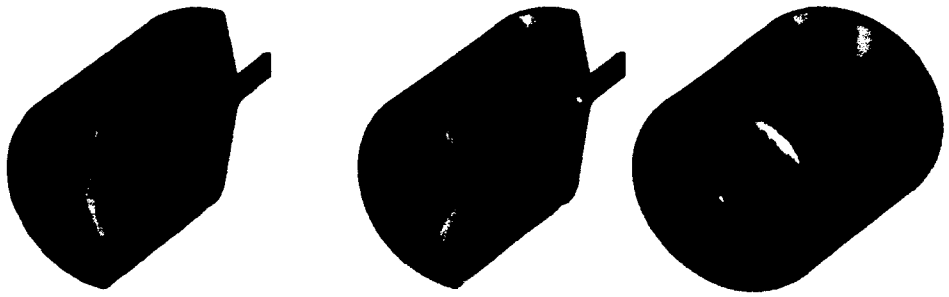

FIG. 58. Surface electric (left) and magnetic (right) field of the parallel-bar design with cylindrical outer conductor and race-track-shaped loading elements.

bar width for varying curvature radius. This clearly shows that the curvature can be used to balance the peak surface electric and magnetic fields. The $R_t R_s$ decreases slowly for both increasing bar curvature radius and bar width. Therefore a smaller bar curvature radius and a bar width is preferred to achieve higher shunt impedance. The cavity radius has a uniform and small increase with the bar width and bar curvature radius as shown in Fig. 61.

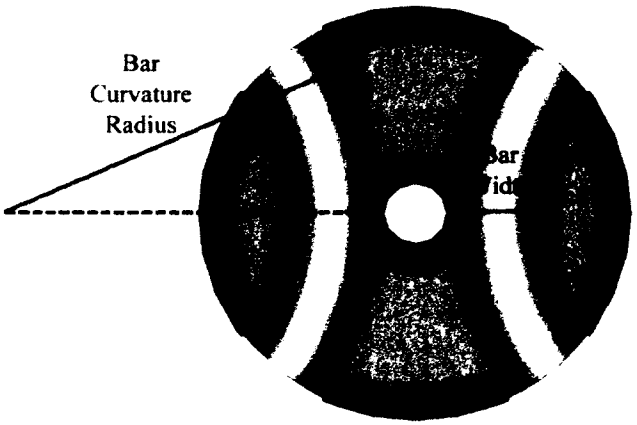

FIG. 59. Design parameters of optimization for the parallel-bar design with cylindrical outer conductor and curved race-track-shaped loading elements.

In Designs (A), (B), and (C) the parallel-bar configuration is strictly parallel, where change in the bar separation will cause compensating changes in the inductance and capacitance, leaving the frequency almost constant. When the bars are curved as in Design (D) by keeping the bar separation constant, the inductance can be varied by changing the curvature of the bar surface. As the bars are curved a change in separation causes different relative changes in capacitance and inductance, yielding a change in frequency.

The variation in peak surface electric and magnetic fields (E_p and B_p) for different bar widths and curvature radii, as shown in Fig. 62, gives the optimum bar width and the dependence on the peak field ratio (B_p/E_p). The peak surface electric field is reduced by increasing the bar curvature and the peak surface magnetic field is reduced by increasing the bar width. The two parameters of the bar width and curvature radii are optimized to reduce both surface electric and magnetic fields. As the bar width increases from 30 mm, for all curvature radii, both peak electric and magnetic fields decrease and reach a minimum for a bar width of ~60 mm beyond

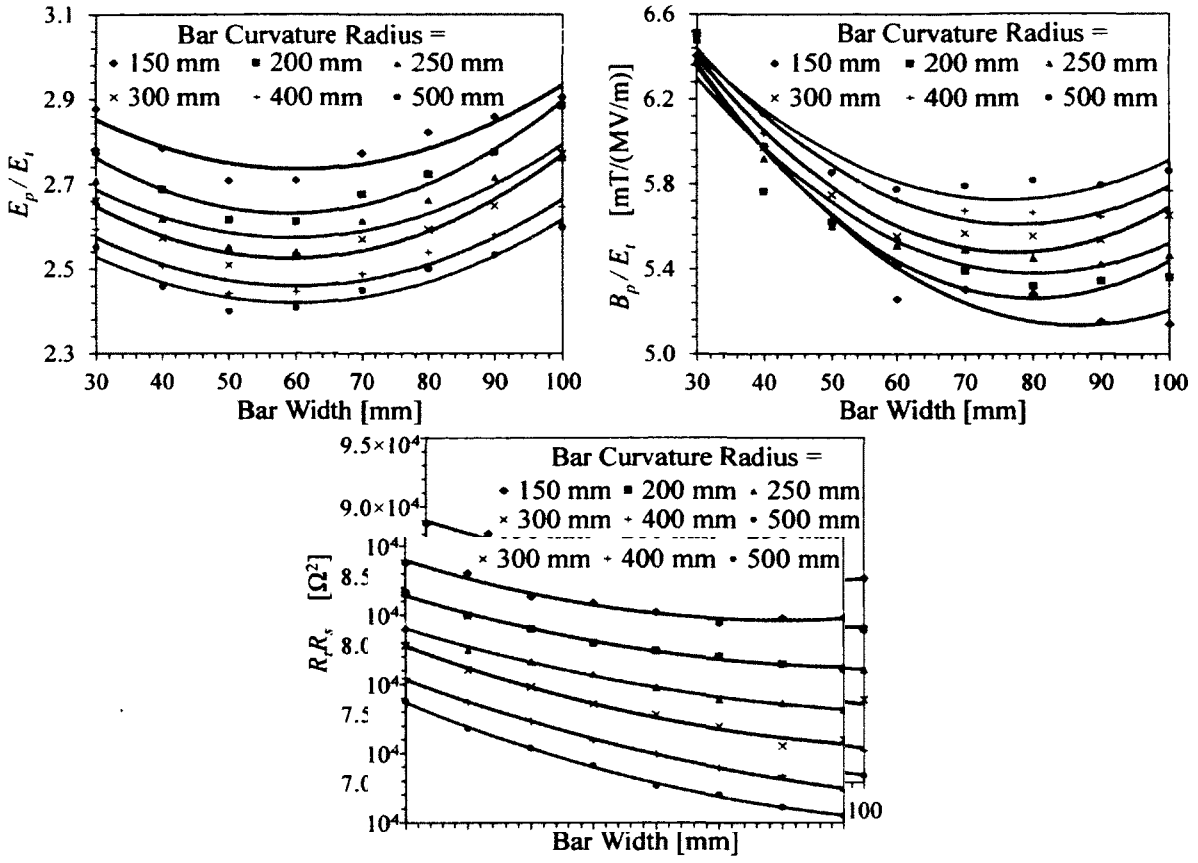

FIG. 60. Ratios of peak surface electric field (E_p) and magnetic field (B_p) to the transverse electric field (E_t) and $R_t R_s$ with varying bar width and radius of bar curvature for race-track-shaped parallel bars.

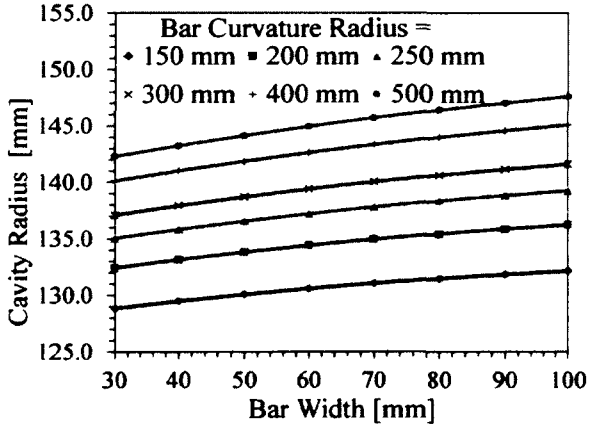

FIG. 61. Cavity radius with varying bar width and radius of bar curvature for race-track-shaped parallel bars.

which they increase again. This clearly shows that eventually it is difficult to lower both peak fields simultaneously, only their ratio can be varied. The peak field ratio shown in Table 7 can be easily reduced to ~2.0 mT/(MV/m). There is a significant increase in $R_t R_s$ due to the higher geometrical factor. Thus far, this design has the highest mode separation and the fundamental accelerating mode is no longer the lowest HOM mode.

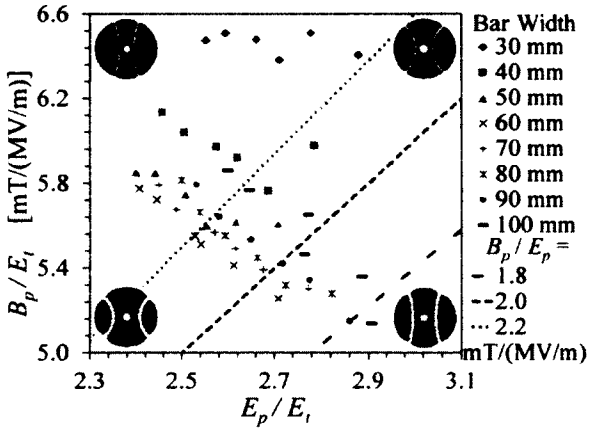

FIG. 62. Ratios of peak surface electric field (E_p) and magnetic field (B_p) to the transverse electric field (E_t) with varying bar width and radius of bar curvature for race-track-shaped curved parallel bars.

Further optimized bar length with cavity length, gives an optimum cavity length close to $\lambda/2$ as shown in Fig. 63.

The electromagnetic field profile and surface fields of Design (D) shows the consistency in the fundamental mode and also the reduced surface magnetic field.

Design (E)

In analyzing the HOM spectrum which is presented in detail in Chapter 5, it was noticed that there are modes with field content only between the cavity outer surface and outer surface of the parallel bar while, in the deflecting mode, the fields are very small in that region. Therefore the parallel-bar design can be modified by increasing the bar width and merging it with the outer surface of the cavity as shown in Fig. 38: Design (E). This reduces the number of HOMs in a given frequency range as the area between the outer conductor and the bars is reduced, the modes with field in that area disappear as their frequency goes to infinity. This also reduces

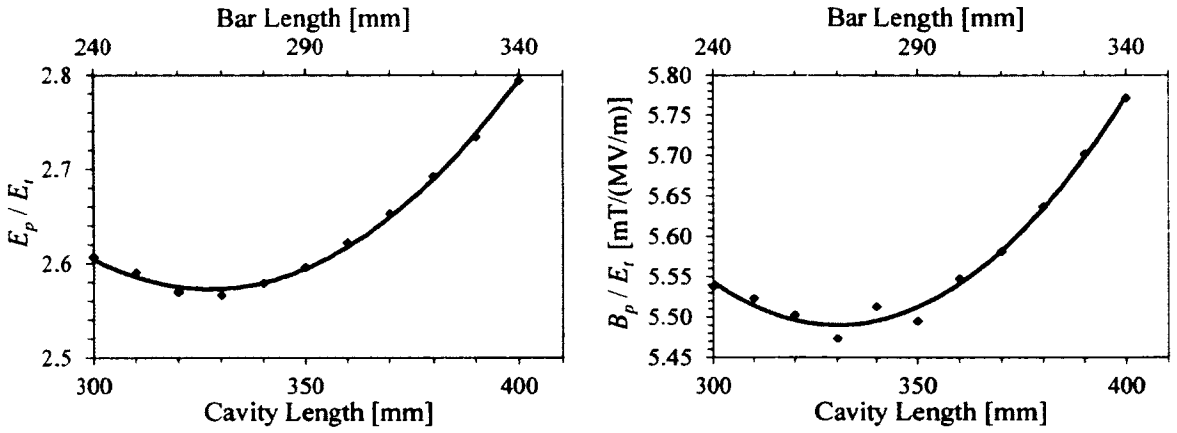

FIG. 63. Ratios of peak surface electric field (E_p) and magnetic field (B_p) to the transverse electric field (E_t) with varying bar length and cavity length for race-track-shaped curved parallel bars.

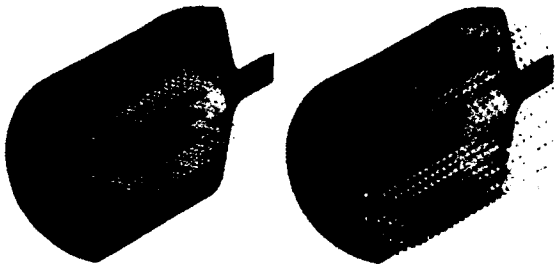

FIG. 64. Electric (left) and magnetic (right) field profile of the parallel-bar design with curved loading elements.

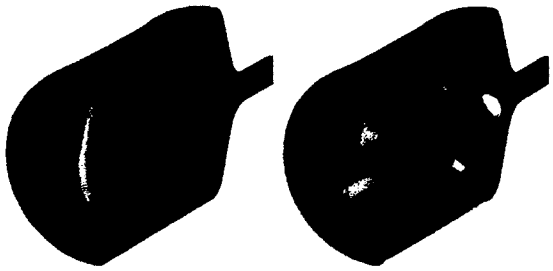

FIG. 65. Surface electric (left) and magnetic (right) field of the parallel-bar design with curved loading elements.

the opportunity for multipacting (Chapter 7) in the deflecting mode [85]. With the merging of the walls the Design (E) becomes a design operating in a TE-like mode. In the transition from the Design D to Design E the field components near the axis are absolutely identical and the modes of operation are the same.

The main parameter that optimizes the peak surface fields is the curvature of the bar (Fig. 66). The dependence of the curvature on the peak fields are shown in Fig. 67 and cavity radius is shown in Fig. 68. The change to the TE-like operating mode has a larger impact on the cavity radius, that increases drastically, but independently of the cavity length. By keeping the bar separation constant and varying the curvature the inductance varies, therefore this can be used to reduce the peak surface magnetic field. For smaller curvatures of bar radius the peak electric field is higher and drops faster as the curvature increases. In this case the peak surface magnetic field is relatively lower due to the wider spread of the surface fields. At larger radii of bar curvatures the peak surface magnetic field increases drastically as the bars are nearly vertical similarly to the Design (D) of the parallel-bar cavity. The bar length and the cavity length are optimized to determine the optimum effective deflecting length. The properties of the optimized design, shown in Table 7, are quite comparable with the properties of the previous design, but with a better HOM spectrum. The $R_t R_s$ is high at smaller bar curvature radii and drops faster as the curvature increase.

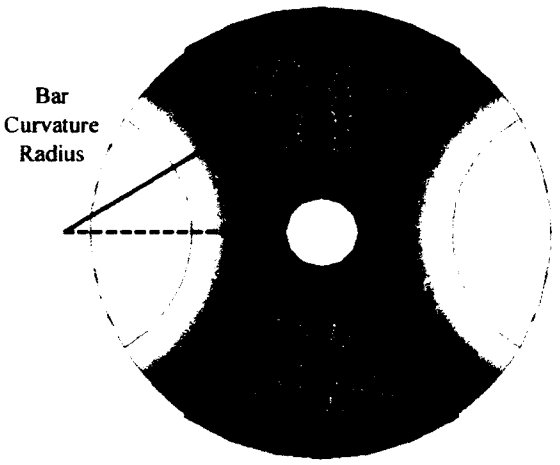

FIG. 66. Design parameter of optimization for the parallel-bar design with bars merged onto cavity surface.

The field profile and surface fields of the optimized Design (E) are shown in Fig. 69 and Fig. 70.

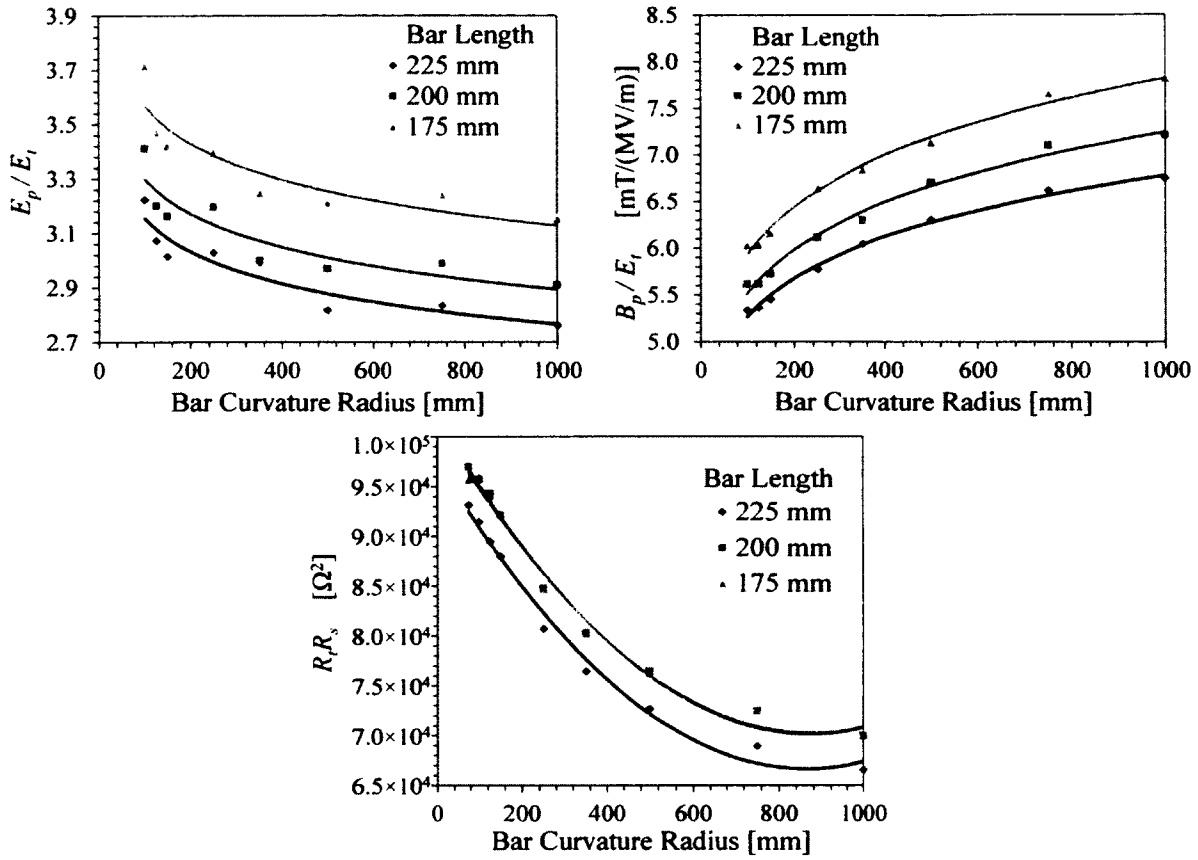

FIG. 67. Ratios of peak surface electric field (E_p) and magnetic field (B_p) to the transverse electric field (E_t) and $R_t R_s$ with varying radius of bar curvature for parallel bars merged onto the cavity surface.

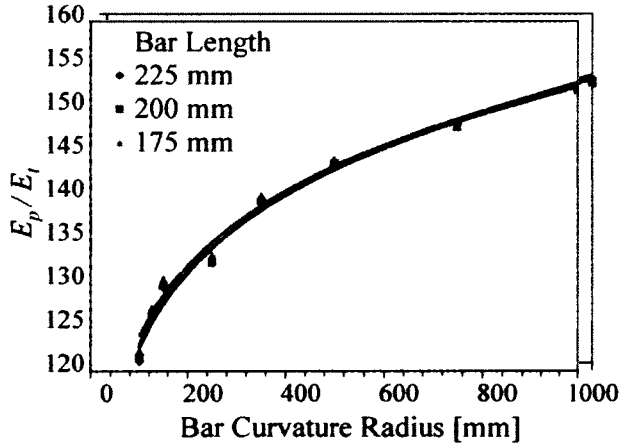

FIG. 68. Cavity radius with varying radius of bar curvature for parallel bars merged onto the cavity surface.

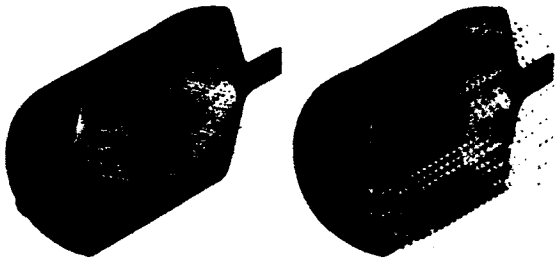

FIG. 69. Electric (left) and magnetic (right) field profile of the parallel-bar design with parallel bars merged onto the cavity surface.

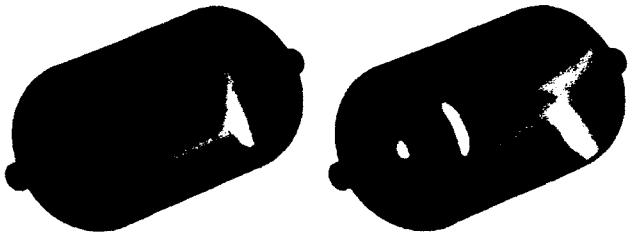

FIG. 70. Surface electric (left) and magnetic (right) field of the parallel-bar design with parallel bars merged onto the cavity surface.

Design (F)

In the parallel-bar design with bars merged onto the cavity surface [Design (E): Fig. 38] the curvature controls the peak surface fields. This design restricts the optimization since it affects both surface fields simultaneously. Therefore the design is adapted further by varying the bar shape into a trapezoidal shape. The design has two key parameters: the inner bar height and angle as shown in Fig. 71 that are varied to control both peak surface fields independently. The cavity length and bar length are again changed simultaneously for different bar shapes to determine the optimum cavity length and bar length that minimize the surface fields as shown in Fig. 72. The peak surface electric field decreases with increasing inner bar height due to the increase in the surface area of the higher surface field. However this increases the peak surface magnetic field as the magnetic field gets stronger at top and bottom of the cavity. The peak surface electric field is higher for smaller angles while the peak surface magnetic field is lower. The dependence of cavity length and the bar

length on the peak surface fields are similar for different bar shapes. However the change in peak surface electric field is higher than that of peak surface magnetic field. The $R_t R_s$ is higher at smaller angles and at smaller bar heights.

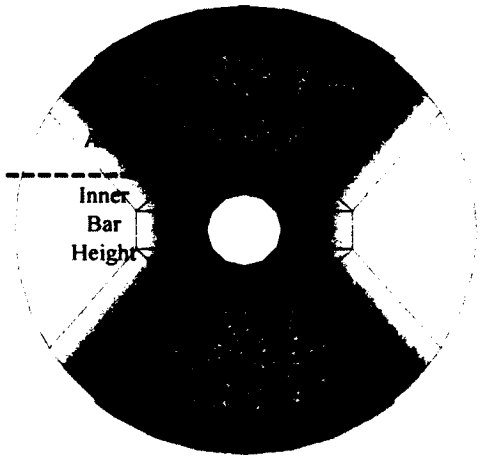

FIG. 71. Design parameters of optimization for the rf-dipole design with trapezoidal-shaped bars.

As the cavity length increase the $R_t R_s$ drops gradually. Cavity radius relates linearly to the increasing cavity length, bar length for different angles as shown in Fig. 73. With increasing parameters of cavity length, bar length, and angle, the cavity radius drops making the designs more compact. For the full range of possible angles varying from 20 deg to 60 deg the range of cavity radius is $\sim \lambda/4$, where the parallel-bar cavity with trapezoidal-shaped loading elements can be visualized as evolved into two opposite $\lambda/4$ resonators in transverse direction.

The bar shape was optimized for different inner bar heights and angles to further minimize the peak surface fields with a balanced peak field ratio (B_p/E_p). The B_p/E_p decreases for smaller inner bar heights and larger angles as shown in Fig. 74. Reducing the bar height reduces the peak surface magnetic field, but increases the peak surface electric field and can be reduced by increasing the angle. However the inner bar height is limited in this design by the chosen beam aperture diameter of 40 mm to maintain the field uniformity across the beam aperture. The trapezoidal shaped bars have been curved appropriately to reduce field enhancement.

The properties of this design are shown in Table 7. The peak surface electric field is invariant, however the peak surface magnetic field is reduced by 16%. For a final

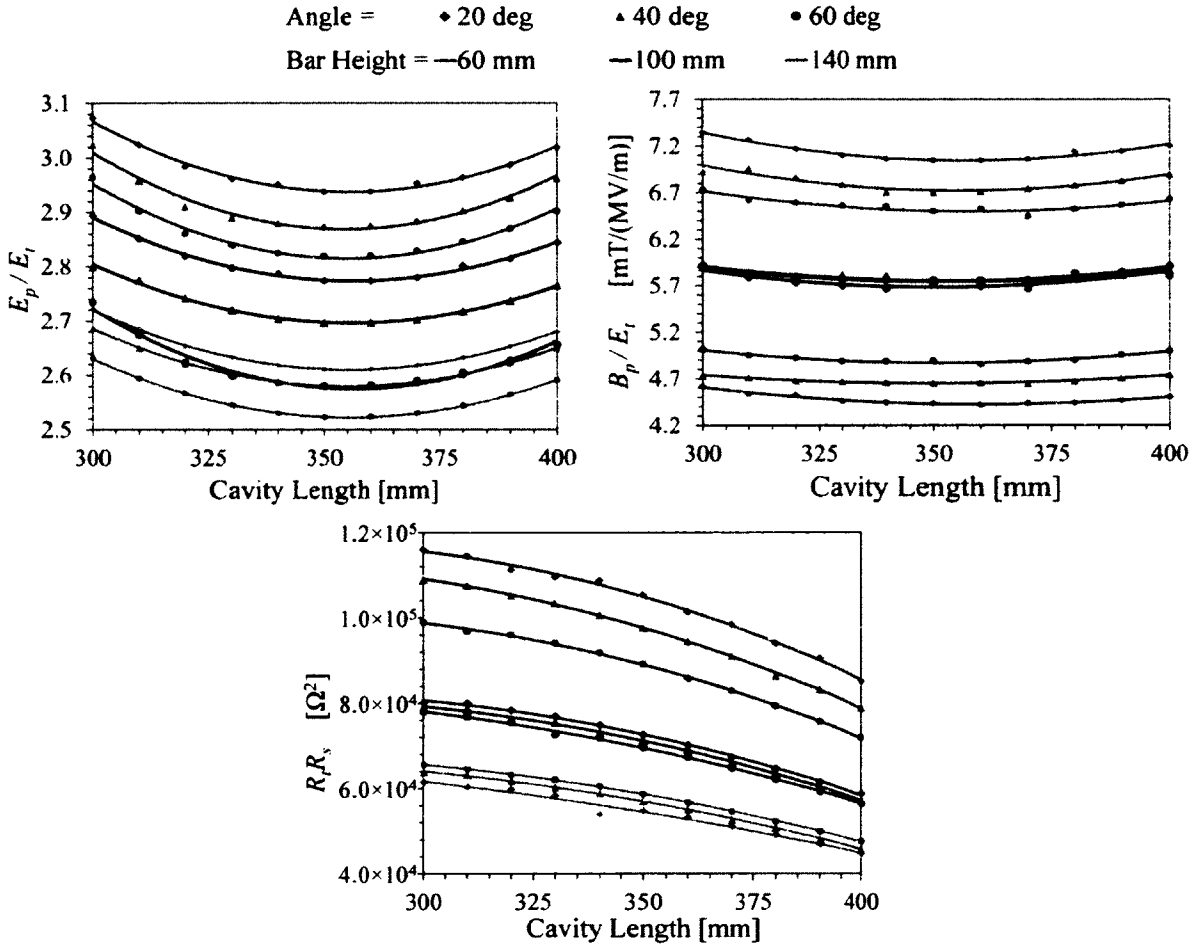

FIG. 72. Ratios of peak surface electric field (E_p) and magnetic field (B_p) to the transverse electric field (E_t) and $R_t R_s$ with varying cavity length and bar length for different angles and inner bar heights of the trapezoidal-shaped parallel bars.

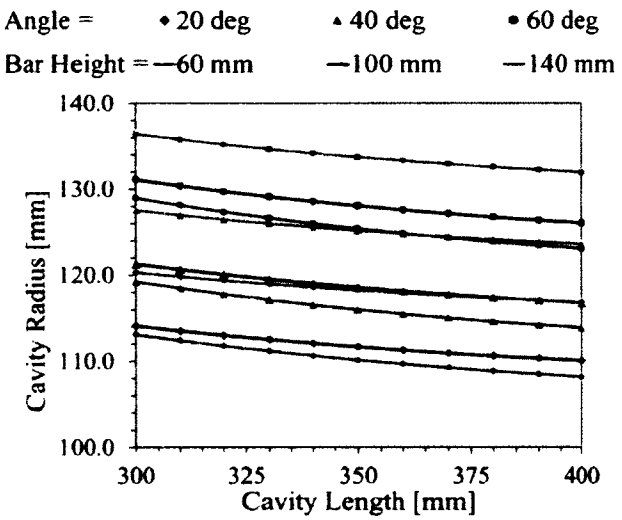

FIG. 73. Cavity radius with varying cavity length and bar length for different angles and inner bar heights of the trapezoidal-shaped parallel bars.

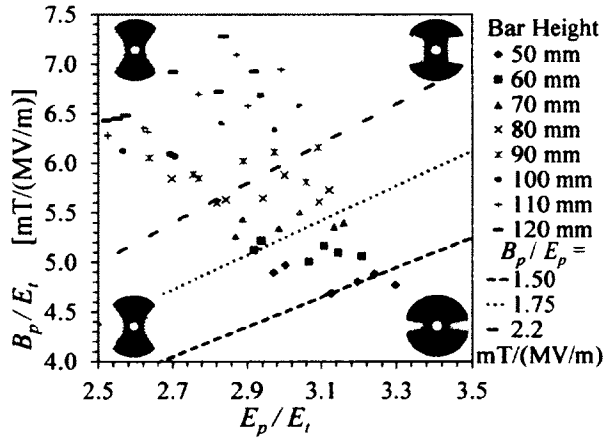

FIG. 74. Ratios of peak surface electric field (E_p) and magnetic field (B_p) to the transverse electric field (E_t) with varying angle and inner bar height of the trapezoidal-shaped parallel bars.

cavity design operating at 5 MV of transverse voltage the peak surface electric field will be of 48 MV/m and 73 mT for the peak surface magnetic field with a field ratio of 1.53 mT/(MV/m).

The advantage of cylindrical-shaped design with trapezoidal bars is the ability to reduce surface magnetic fields with wider bars connecting to the outer wall. This design has the widest HOM spectrum compared to previous designs with a 278 MHz separation between the 499 MHz fundamental deflecting mode and the nearest higher-order mode. Furthermore the straight sections of inner bar height create a more uniform transverse electric field across the beam aperture. The design with the trapezoidal bars has the highest geometrical factor and $R_t R_s$, reducing the power dissipation in the walls. Additionally this design has the smallest transverse dimensions compared to other designs. The field profile and the surface field of optimized final geometry with cylindrical outer conductor and trapezoidal-shaped parallel bars are shown in Fig. 75. This geometry is essentially an rf-dipole geometry.

FIG. 75. Field profile and peak surface fields of the rf-dipole cavity with cylindrical outer conductor and trapezoidal-shaped parallel bars.

4.3.2 400 MHZ CRABBING CAVITY

The crabbing system for the LHC high luminosity upgrade needs rf structures operating at 400 MHz and a net transverse voltage of 10 MV. The system has strict dimensional constraints with a large beam aperture diameter of 84 mm (Table. 6). One of the major constraints is the requirement on the cavity diameter to be less than 300 mm.

The initial specification of crabbing of the bunches in a single direction required

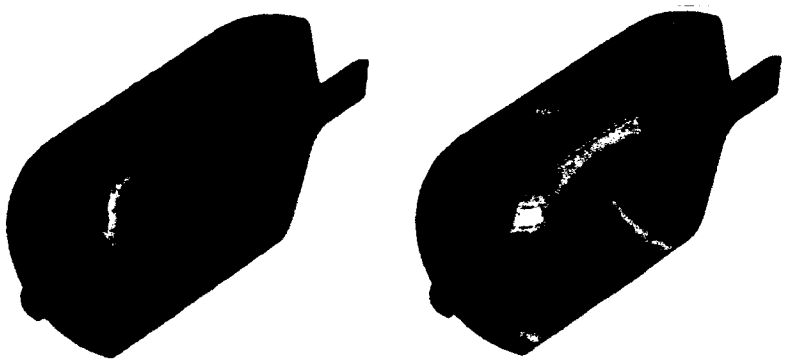

FIG. 76. Surface electric (left) and magnetic (right) field of the rf-dipole cavity with cylindrical outer conductor and trapezoidal-shaped parallel bars.

the transverse dimensional constraints to be applied horizontally. This led to the design of an elliptical-shaped parallel-bar design as shown in Fig. 77 evolving from rectangular-shaped outer conductors and straight loading elements [81, 79].

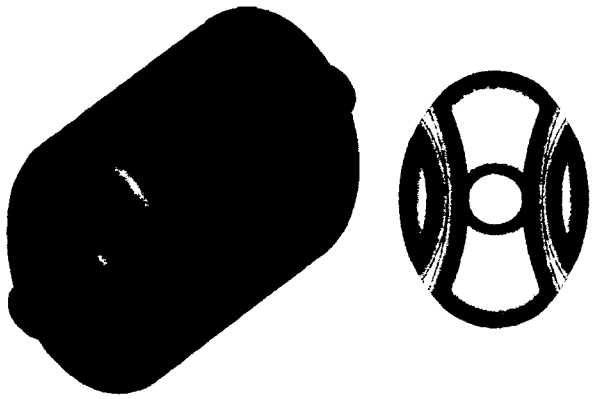

FIG. 77. 400 MHz elliptically-shaped parallel-bar design.

The key parameters of the elliptical cavity are the bar width and the curvature of the bars optimized within the limits of the elliptical-shaped outer conductor. The dependence of bar width and the curvature of the bars on E_p/E_t, B_p/E_t and $R_t R_s$ are shown in Fig. 78. The optimized design parameters are a bar width of 60 mm and a bar curvature of 400 mm, where E_p/E_t and B_p/E_t are at minimum, selected without compromising the transverse shunt impedance. The rf properties of the elliptical-shaped parallel-bar design in comparison to that of the rectangular-shaped

parallel-bar design are shown in Table. 9.

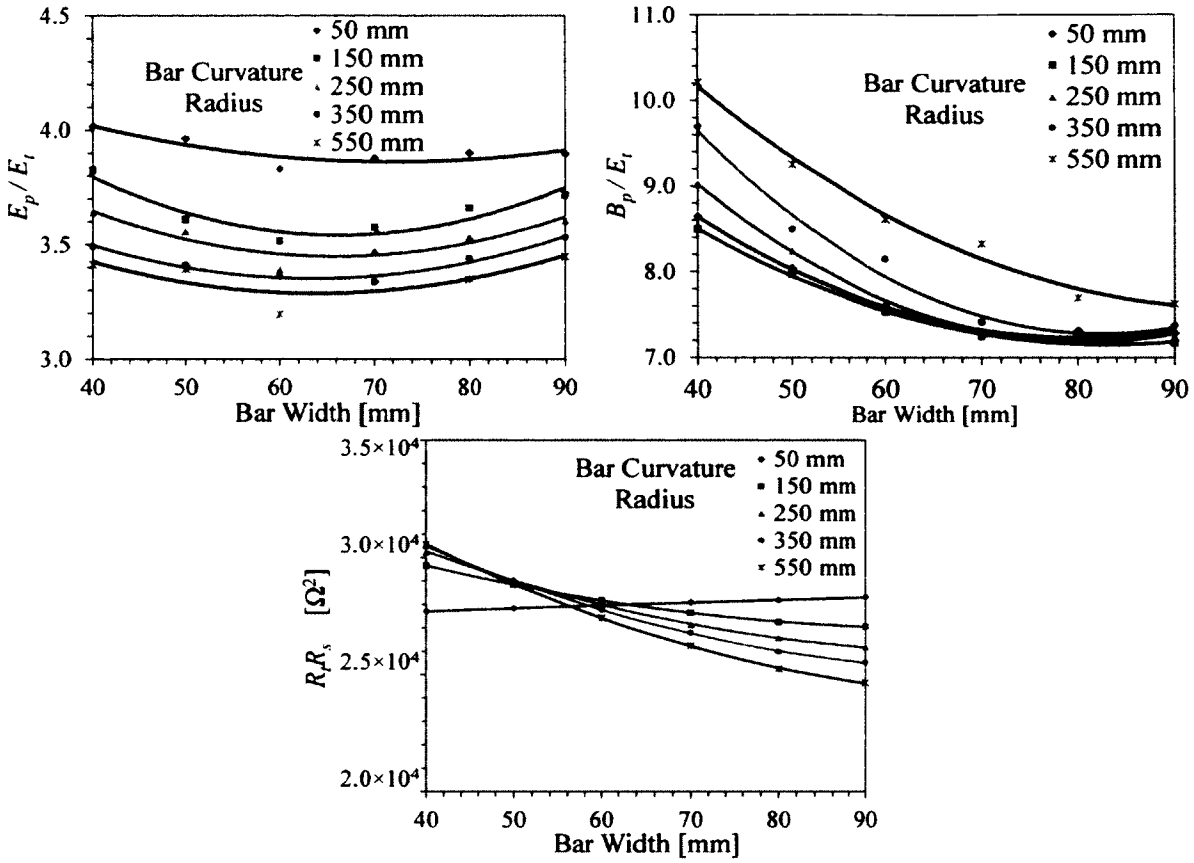

FIG. 78. Ratios of peak surface electric field (E_p) and magnetic field (B_p) to the transverse electric field (E_t), and transverse shunt impedance ($R_t R_s$) with varying bar width and bar curvature for the 400 MHz elliptical-shaped cavity.

A half scaled cavity with exact half dimensions of the elliptical-shaped design was fabricated by Niowave Inc [86]. The 800 MHz model was manufactured in Al as a prototype in validating the fundamental operating mode and identifying higher order modes where the details are presented in Appendix A.

The 400 MHz crabbing cavity requirements with crabbing of the beam in both horizontal and vertical direction necessitate a compact design with axial symmetry. A series of cylindrical-shaped parallel-bar designs at 400 MHz were studied as shown in Fig. 79. The rf designs show similar field profiles and dependence of rf properties on the design parameters as presented in the series of geometries at 499 MHz. The rf properties properties of the optimized designs are given in Table. 10, compared at a constant length with the cavity diameter adjusted to maintain the operating mode frequency at 400 MHz.

TABLE 9. Properties of the rectangular-shaped and elliptical-shaped parallel-bar designs.

Parameter			Units
Frequency of π mode	400.0	400.0	MHz
Frequency of 0 mode	413.1	611.6	MHz
$\lambda/2$ of π mode	374.7	374.7	mm
Cavity Length	456.7	485.0	mm
Cavity Height	384.4	408.6	mm
Cavity Width	400.0	290.0	mm
Aperture Diameter	84.0	84.0	mm
Bar Length	332.0	330.0	mm
Bar Width	85.0	60.0	mm
Deflecting Voltage ($V_t{}^1$)	0.375	0.375	MV
Peak Electric Field ($E_p{}^1$)	2.18	3.40	MV/m
Peak Magnetic Field ($B_p{}^1$)	7.50	7.71	mT
B_p/E_p	3.44	2.27	mT/(MV/m)
Energy Content (U^1)	0.176	0.141	J
Geometrical Factor (G)	83.9	109.4	Ω
$[R/Q]_t$	317.9	255.7	Ω
$R_t R_s$	2.7×10^4	2.8×10^4	Ω^2

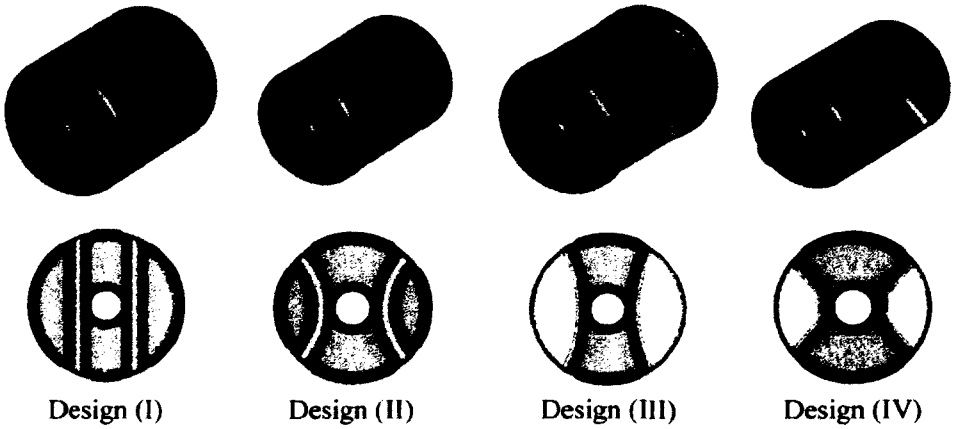

FIG. 79. 400 MHz cylindrical-shaped designs with different loading elements.

TABLE 10. Properties of the cylindrical-shaped designs with different loading elements shown in Fig. 79

Parameter					Units
Frequency of π mode	400.0	400.0	400.0	400.0	MHz
Frequency of 0 mode	492.6	651.0	673.3	729.5	MHz
Frequency of nearest mode	492.6	581.5	585.4	593.4	MHz
$\lambda/2$ of π mode	374.7	374.7	374.7	374.7	mm
Cavity Length	520.0	520.0	520.0	520.0	mm
Cavity Diameter	406.8	356.0	375.3	339.8	mm
Aperture Diameter	84.0	84.0	84.0	84.0	mm
Bar Length	345.0	345.0	345.0	345.0	mm
Bar Width (At waist)	65.0	65.0	-	-	mm
Bar Height / Curved Height	398.0	324.0	350.0	-	mm
Bar Inner Height	-	-	-	80.0	mm
Angle	-	-	-	50.0	deg
Deflecting Voltage ($V_t{}^1$)	0.375	0.375	0.375	0.375	MV
Peak Electric Field ($E_p{}^1$)	2.67	3.27	3.25	3.82	MV/m
Peak Magnetic Field ($B_p{}^1$)	7.89	7.83	7.99	7.09	mT
B_p/E_p	3.0	2.39	2.46	1.86	mT/(MV/m)
Energy Content (U^1)	0.14	0.17	0.2	0.19	J
Geometrical Factor (G)	92.7	112.0	112.1	119.7	Ω
$[R/Q]_t$	388.7	321.2	281.8	312.2	Ω
$R_t R_s$	3.6×10^4	3.6×10^4	3.2×10^4	3.7×10^4	Ω^2

The parallel-bar design with the straight bars has the largest diameter, and drops as the loading elements are curved where the design with the trapezoidal-shaped bars has the smallest diameter. All the designs have similar peak surface field ratios where Design (IV) has more balanced surface field distribution at a ratio of 1.86 mT/(MV/m). The important parameters in this design are the bar inner height and angle as shown in Fig. 80, that are also optimized to achieve the balanced peak surface field ratio. The Design (IV) with trapezoidal-shaped parallel-bars delivers the highest mode separation between the operating mode and the next higher order mode. As shown in Fig. 81 the optimized design has a smaller bar height and a larger angle that minimizes the ratios of peak surface field to the transverse electric field and transverse shunt impedance. The cavity radius is independent of the bar height as shown in Fig. 82 however, can be reduced with a smaller angle at the trapezoidal-shaped loading elements. Therefore, an optimum angle of 50 deg is selected with the smallest bar height.

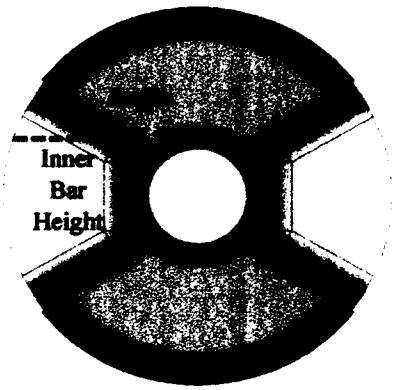

FIG. 80. Design prameters of optimization for the 400 MHz rf-dipole design.

The strong dependence of the rf frequency on the cavity diameter puts constraints on the cavity dimensions. As a solution, a square rf-dipole design was proposed as shown in Fig. 83 with identical field configuration and similar rf properties as shown in Table. 11 [87] but smaller size than the cylindrical cavity. With the transverse dimensions fixed, the frequency of the fundamental mode is adjusted by changing the curvature of the cavity edges. The square-shaped marks the next generation of rf-dipole design fully adapted and integrated in meeting the design specifications of LHC crabbing system [88, 89].

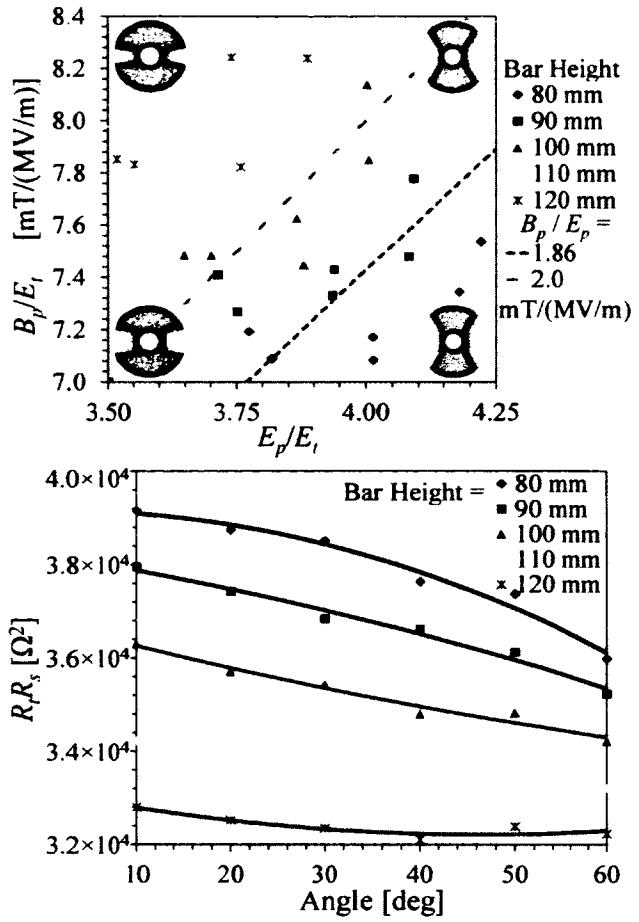

FIG. 81. Ratios of peak surface electric field (E_p) and magnetic field (B_p) to the transverse electric field (E_t) (top) and R_tR_s (bottom) with varying angle and inner bar height of the 400 MHz trapezoidal-shaped loading elements.

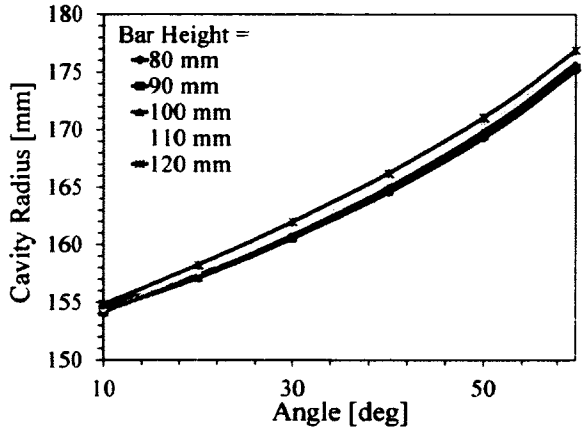

FIG. 82. Cavity radius with varying angle and inner bar height of the 400 MHz trapezoidal-shaped parallel bars.

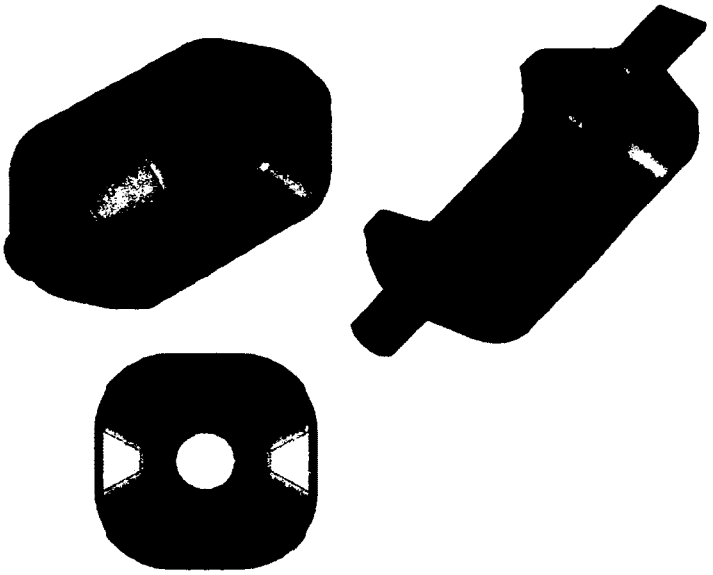

FIG. 83. 400 MHz square-shaped rf-dipole design.

TABLE 11. Properties of the cylindrical and square shaped 400 MHz rf-dipole geometries.

Parameter			Units
Frequency of π mode	400.0	400.0	MHz
Frequency of 0 mode	887.0	727.4	MHz
Frequency of nearest mode	589.5	593.2	MHz
$\lambda/2$ of π mode	375.0	375.0	mm
Cavity Length	527.2	597.2	mm
Cavity Diameter	339.9	295.0	mm
Aperture Diameter	84.0	84.0	mm
Bar Length	350.0	350.3	mm
Bar Inner Height	80.0	85.0	mm
Angle	50.0	30.0	deg
Deflecting Voltage ($V_t{}^1$)	0.375	0.375	MV
Peak Electric Field ($E_p{}^1$)	3.90	3.86	MV/m
Peak Magnetic Field ($B_p{}^1$)	7.13	6.90	mT
B_p/E_p	1.83	1.79	mT/(MV/m)
Energy Content (U^1)	0.019	0.018	J
Geometrical Factor (G)	138.7	115.0	Ω
$[R/Q]_t$	287.2	315.7	Ω
$R_t R_s$	4.0×10^4	3.6×10^4	Ω^2

4.4 BEAM APERTURE DEPENDENCE

The parallel-bar rf-dipole designs can be used for many deflecting/crabbing cavity applications due its compactness and attractive properties of low peak surface fields, high net deflection, and the absence of lower-order modes while the frequency of the nearest higher-order mode is of the order of 1.5 times that of the fundamental. The diameter of the beam aperture and the design frequency are the two important parameters in designing parallel-bar rf-dipole geometries. The design can be scaled to obtain the required design frequency as the frequency is inversely related to the cavity dimensions. The 499 MHz rf-dipole cavity with trapezoidal-shaped loading elements and cylindrical outer conductor was also analyzed for varying beam aperture radius and angle of the trapezoidal-shaped parallel bars by adjusting the inner bar height proportionally (Fig. 84).

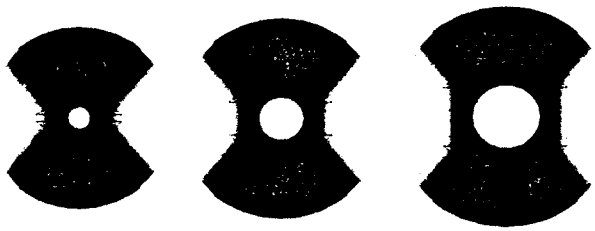

FIG. 84. RF-dipole cavity designs with trapezoidal-shaped parallel bars of varying beam aperture diameter and inner bar height for a given angle.

The dependence of E_p/E_t and B_p/E_t on the beam aperture is shown in Fig. 85. As expected the peak fields increase as the beam aperture is increased. The B_p/E_p shown in Fig. 86 gives the peak field ratio for different beam aperture diameter normalized to the half wavelength of the cavity, and different angles of the trapezoidal-shaped bars. The dotted lines shows the constant ratios of normalized beam aperture diameter. Therefore the angle can be used to set the peak field ratio as needed by the design parameters for a given design frequency and beam aperture diameter. As shown in Fig. 87 larger beam aperture radii make the design geometries to have large cavity radii.

The transverse electric field ($E_{t,Total}$) determined using both on-axis electric and magnetic field components as given in Eqs. (15) and (17) is compared to the contribution only from the on-axis transverse electric field ($E_{t,EOnly}$) with varying beam

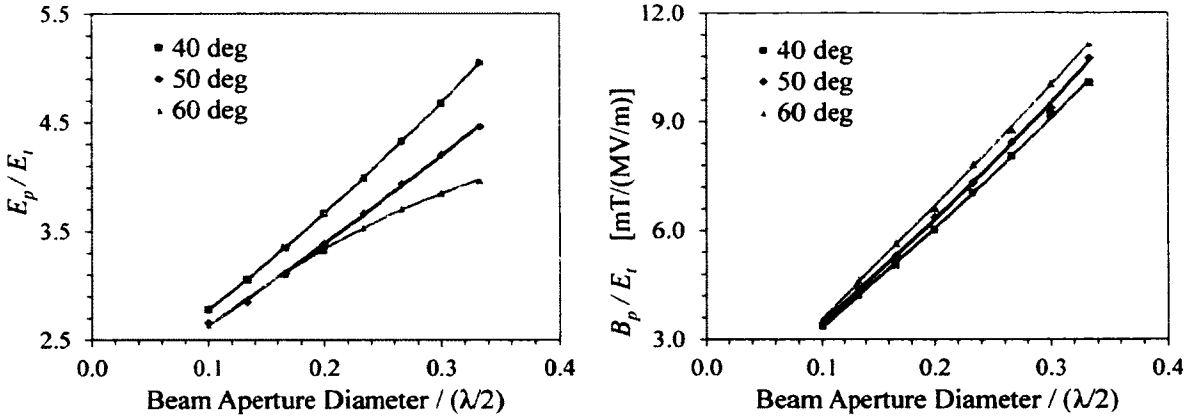

FIG. 85. Ratios of peak surface electric field (E_p) and magnetic field (B_p) to the transverse electric field (E_t) with varying beam aperture diameter and angle for rf-dipole design with trapezoidal-shaped bars.

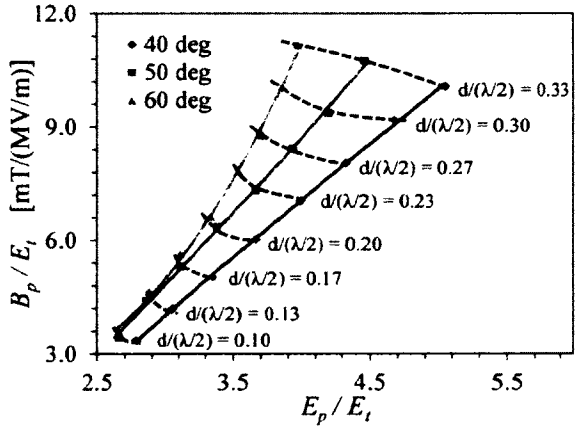

FIG. 86. Ratios of peak surface magnetic field (B_p) to the electric field (E_p) with varying beam aperture diameter and angle for rf-dipole design with trapezoidal-shaped bars.

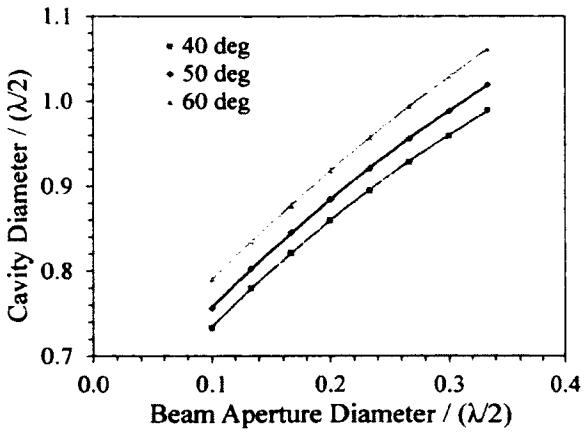

FIG. 87. Cavity diameter with varying beam aperture diameter and angle for rf-dipole design with trapezoidal-shaped bars.

aperture diameter. The $E_{t,Total}/E_{t,EOnly}$ dependence on the normalized beam aperture diameter to the half wavelength of the cavity is shown in Fig. 88. As the beam aperture is increased the deflecting voltage due to electric field on axis decreases faster than the deflecting voltage due to the on axis magnetic field. Therefore the negative contribution from the magnetic field is larger at large aperture reducing the net deflecting voltage. The ratio approaches zero as the beam aperture diameter approaches the cavity diameter; this would correspond to a cylindrical cavity operating in the TE_{111} mode which, according to the Panofsky-Wenzel Theorem [15, 16] produces no deflecting voltage. The magnetic field contribution is directly due to the on-axis magnetic field component with the fields confined between the end plates and bars. Since the slope of the end plates and the bar length have not been changed while scaling the designs for different aperture the contribution on $E_{t,Total}/E_{t,EOnly}$ with beam aperture variation has little dependency on the angle of the trapezoidal-shaped bars.

The $[R/Q]_t$ drops drastically as the beam aperture increases. Irrespective of the increase in geometrical factor (G) the resulting $R_t R_s$ also decreases in the order of d^2 with the beam aperture diameter (d) as shown in Fig. 89.

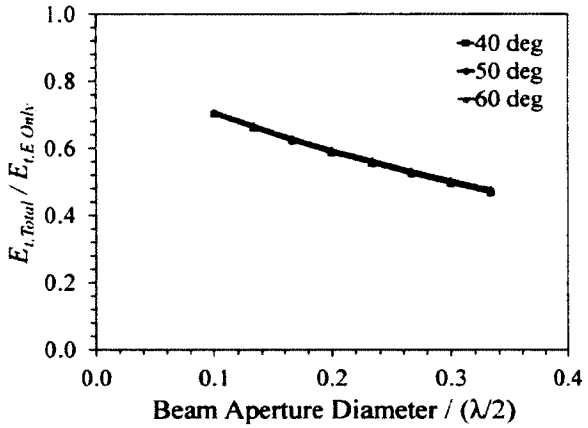

FIG. 88. Electric field and magnetic field contribution to the transverse deflection of the rf-dipole cavity designs with the varying beam aperture.

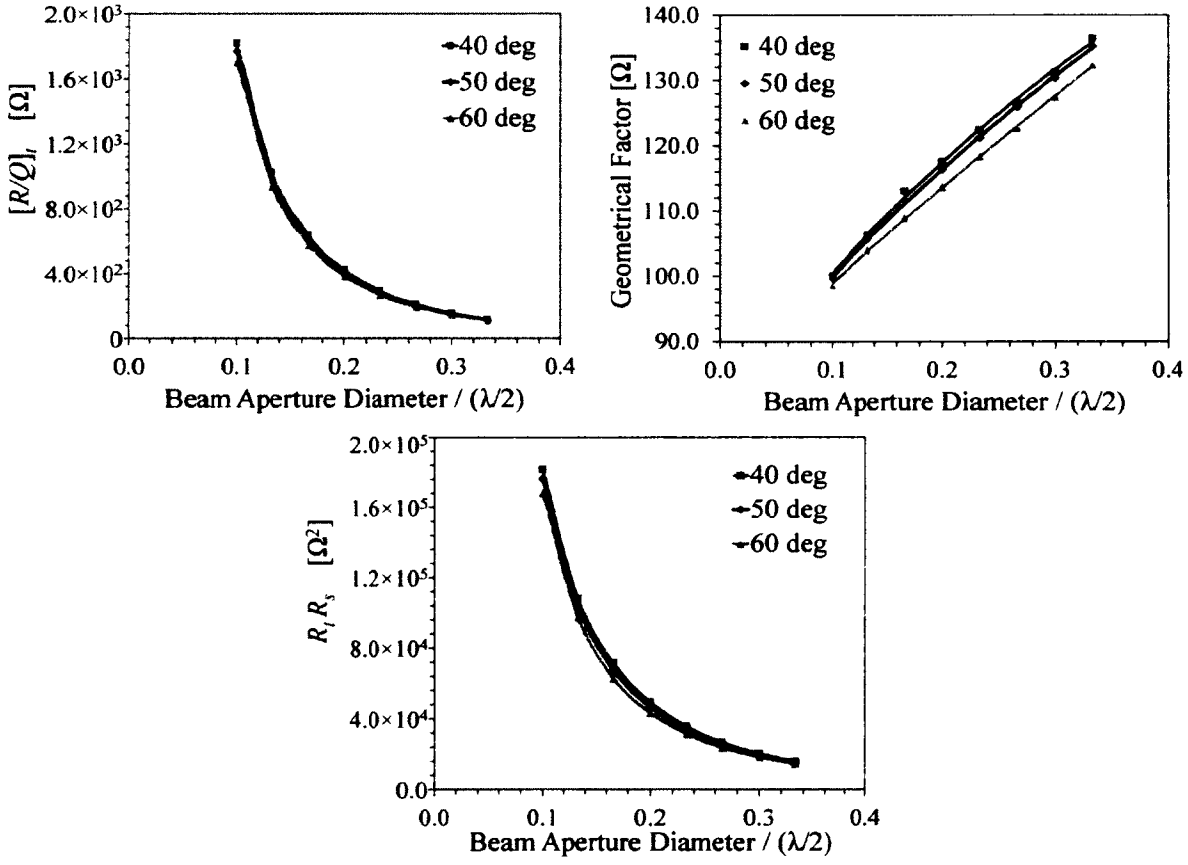

FIG. 89. R_t/Q, Geometrical Factor $G = QR_s$, and R_tR_s as function of the beam-line aperture for rf-dipole design with trapezoidal-shaped bars.

4.5 MULTI-CELL RF-DIPOLE CAVITIES

The rf-dipole geometry easily supports multi-cell cavity designs as shown in Fig. 90. where the electric and magnetic field profiles for the deflecting and crabbing mode are shown in Fig. 91 [88]. The rf properties of a 2 cell and 3 cell rf-dipole cavity are given in Table 12 at 400 MHz frequency with a constant beam aperture of 84 mm.

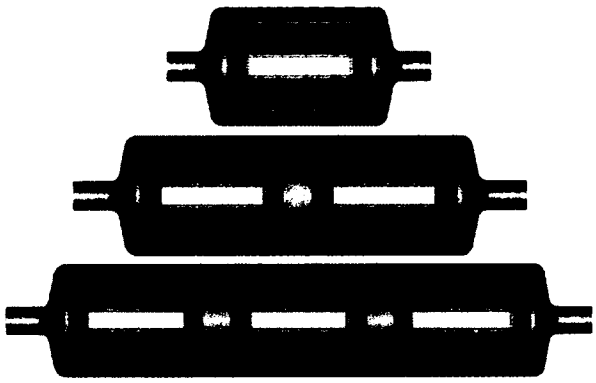

FIG. 90. Single cell, 2 cell and 3 cell rf-dipole cavities of 400 MHz with a beam aperture of 84 mm.

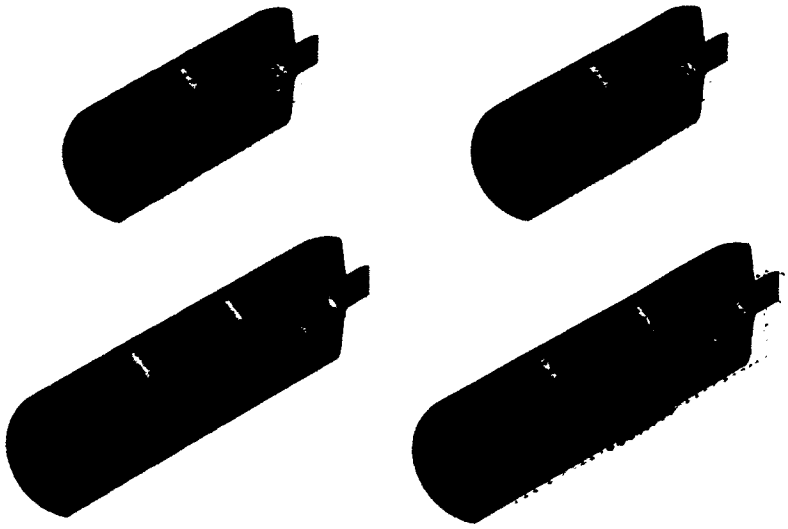

FIG. 91. Electric field (left) and magnetic field (right) of 2 cell (top) and 3 cell (bottom) rf-dipole cavities.

The main advantage of the multi-cell designs is the reduced total cavity and cryomodule length. However multi-cell designs have similar order modes (SOM) with

TABLE 12. Properties of the single cell, 2 cell and 3 cell 400 MHz rf-dipole geometries.

Parameter	Single cell	2 cell	3 cell	Units
Frequency of π mode	400.0	400.0	400.0	MHz
$\lambda/2$ of π mode	375.0	375.0	375.0	mm
Cavity Length	527.2	1047.0	1467.0	mm
Cavity Diameter	339.9	345.0	354.0	mm
Aperture Diameter	84.0	84.0	84.0	mm
Bar Length	350.0	345.0	345.0	mm
Bar Inner Height	80.0	85.0	85.0	mm
Angle	50.0	50.0	50.0	deg
Deflecting Voltage ($V_t{}^1$)	0.375	0.375	0.375	MV
Peak Electric Field ($E_p{}^1$)	3.90	4.26	4.75	MV/m
Peak Magnetic Field ($B_p{}^1$)	7.13	7.40	7.77	mT
B_p/E_p	1.76	1.74	1.64	mT/(MV/m)
Energy Content (U^1)	0.195	0.114	0.079	J
Geometrical Factor (G)	138.7	127.8	131.8	Ω
$[R/Q]_t$	287.2	488.4	708.1	Ω
$R_t R_s$	4.0×10^4	6.2×10^4	9.3×10^4	Ω^2

frequencies that are below the frequency of the fundamental deflecting and crabbing mode. The number of SOMs is directly related to the number of cells. For example, the 2 cell 400 MHz rf-dipole cavity has a SOM of 374.5 MHz and the 3 cell cavity has two SOMs with frequencies of 351.6 MHz and 376.8 MHz.

4.6 RF COUPLING

The rf power coupling in the rf-dipole cavity is achieved with coaxial type couplers. The coaxial type coupling allows more compact couplers with the additional possibility of using a variable coupler. A variable coupler is advantageous especially in processing multipacting conditions in the cavity [90]. The coaxial couplers are designed with known impedances of either 50 Ω or 75 Ω where the higher impedance is preferred in conditioning the multipacting levels. The characteristic impedance for a concentric cylindrical coupler is given by

$$Z = \frac{60}{\sqrt{\varepsilon_r}} \ln \frac{D}{d}, \tag{115}$$

where D and d are the outer and inner diameter of the two conductors. In vacuum, at an impedance of 50 Ω the ratio of the diameters (D/d) is equal to $\exp(5/6)$.

The rf-dipole geometry supports coupling through both electric and magnetic coupling. Magnetic coupling is achieved by a loop or hook connected to the end of the inner conductor where the electric coupling is simply achieved by the inner rod. The coupler position on the cavity is determined by field profile and maximum strength of coupling given by the external quality factor (Q_{ext}). Placed perpendicular to the magnetic field as shown in Fig. 92 the maximum coupling is achieved with the coupler placed at the center of the cavity, however which leads field enhancement at the coupler outer conductor increasing the power loss through the surface. The coupler is moved to the end of the cavity in order to reduce the field enhancement by a factor of 1.62 in the 499 MHz design and by 1.33 in the 400 MHz design, yet the strong magnetic field at the top provide adequate coupling. The coupling strength can be increased by inserting the inner conductor into the cavity, that will couple to the fields strongly.

The other option of coupling is the use of electric coupling to the on-axis transverse electric field. Coaxial type coupler with outer conductor diameter of 20 mm

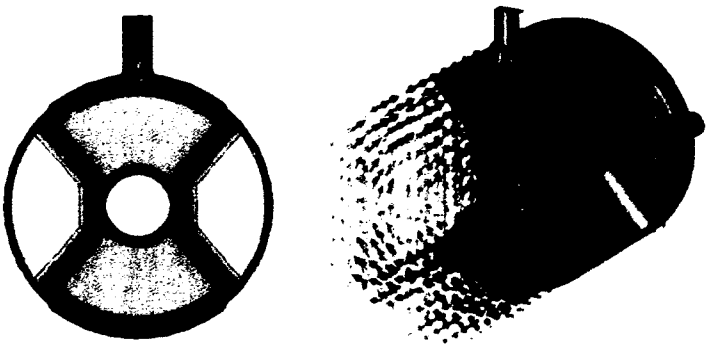

FIG. 92. Magnetic-type rf coupler.

was used in the 499 MHz rf-dipole cavity, which is same as the beam aperture diameter. In the 400 MHz rf-dipole cavity the outer conductor diameter is 36 mm. The coupler placed at the end plate provided sufficient coupling, where the dependence on Q_{ext} on the position are shown in Fig. 93 where Fig. 94 shows the position of the couplers with maximum coupling for the two rf-dipole cavities.

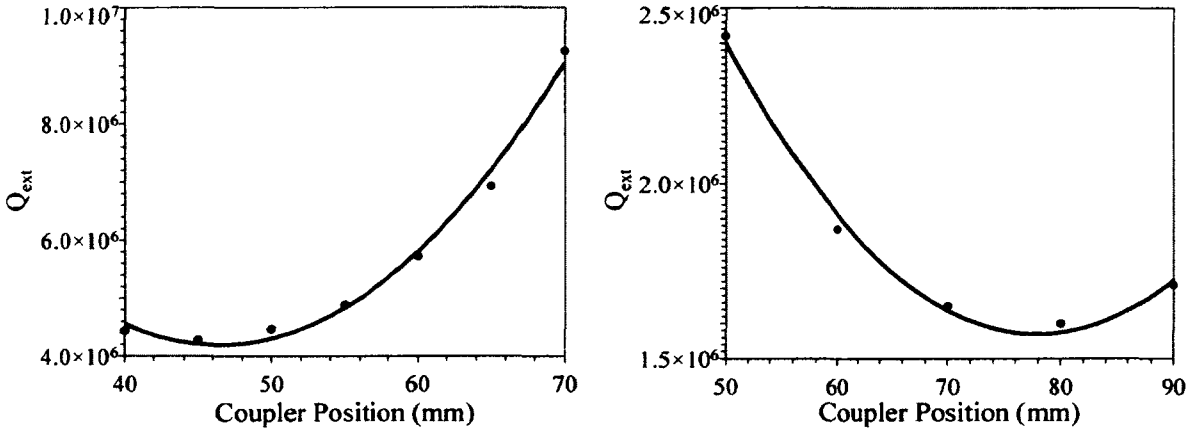

FIG. 93. Strength of rf coupling (Q_{ext}) as a function of the coupler position on the end plate for the 499 MHz (top) and 400 MHz (bottom) cavities.

The strongest coupling is achieved at 46 mm and 78 mm for the two rf-dipole cavities, however this places the ports closer to the edge of the cavity. Therefore a coupler position of 55 mm and 73 mm were selected for the two designs, considering the cavity fabrication with Q_{ext} closer to the optimum. Two coupler ports are required for input power pick up field probe, placed at each end plate of the rf-dipole

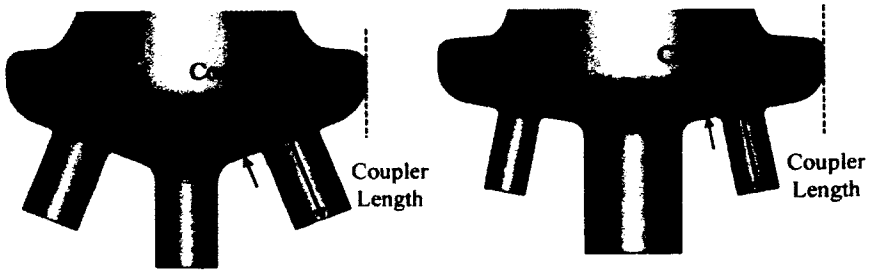

FIG. 94. Position of the coupler for the 499 MHz (left) and 400 MHz (right) cavities.

cavity. The asymmetry in the couplers introduce a small on-axis longitudinal electric field, therefore four coupling ports were used in the final cavity. Those would also simplify surface treatment of the cavities.

4.7 FINAL RF-DIPOLE DESIGNS

The final 499 MHz and 400 MHz rf-dipole cavities with coupling ports are shown in Fig. 95.

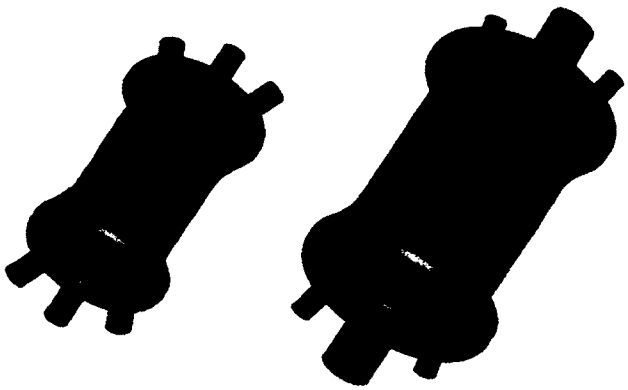

FIG. 95. Final rf-dipole cavity designs of 499 MHz (left) and 400 MHz (right).

The 499 MHz cavity is expected to deliver a transverse voltage of 3.3 MV and 3.4 MV for the 400 MHz cavity. Table 13 shows the rf properties of each design including the expected operational rf properties. The operational parameters are determined for several options of total number of cavities. The preferred options are to operate with one cavity achieving 3.3 MV by the 499 MHz cavity and to operate at 5.0 MV per cavity with two 400 MHz rf-dipole cavities to achieve the design requirement. A residual surface resistance (R_{res}) of 10 nΩ was assumed and the corresponding power

dissipation was calculated with Eq.22

$$P_{diss} = \frac{V_t^2}{G\left[\frac{R}{Q}\right]_t} R_s \tag{116}$$

for the relaxed operation conditions.

TABLE 13. Properties of the final 499 MHz and 400 MHz rf-dipole geometries.

Parameter			Units
Frequency of π mode	499.0	400.0	MHz
$\lambda/2$ of π mode	300.4	375.0	mm
Aperture Diameter	40.0	84.0	mm
Deflecting Voltage ($V_t{}^1$)	0.30	0.375	MV
Peak Electric Field ($E_p{}^1$)	2.86	4.02	MV/m
Peak Magnetic Field ($B_p{}^1$)	4.38	7.06	mT
Energy Content (U^1)	0.029	0.195	J
Geometrical Factor (G)	105.9	140.9	Ω
$[R/Q]_t$	982.5	287.0	Ω
$R_t R_s$	1.0×10^5	4.0×10^4	Ω^2
Total Transverse Voltage (V_t)	3.78	10.0	MV
No. of cavities	2/1	3/2	
Transverse Voltage Per Cavity	1.9/3.8	3.4/5.0	MV
Peak Electric Field (E_p)	19/37	37/54	MV/m
Peak Magnetic Field (B_p)	28/56	65/95	mT
Operational Temperature	2.0/4.2	2.0/4.2	K
R_{BCS}	2.0/110.0	1.3/70.0	nΩ
R_s	12.0/120.0	11.3/80.0	nΩ
P_{diss}	0.42/4.2	3.3/22.9	nΩ
Estimated Q_0	$8.8\times10^9/8.8\times10^8$	$1.3\times10^{10}/1.8\times10^9$	

The estimated Q_0 for the two rf-dipole cavities are on the order of $\sim 10^{10}$. This relates to a very low power dissipation per cavity during operation with relaxed transverse voltage specifications. The peak surface electric and magnetic fields are reasonably achievable at both V_t options of the 499 MHz cavity as well for the low V_t operation of the 400 MHz cavity. During rf tests the cavities were expected to be pushed to their limits of operation to determine the maximum operational field

levels. Achievable Q_0 would drop at higher R_{res} increasing the power dissipation through the cavity surfaces.

The rf properties related to superconducting rf-dipole deflecting and crabbing cavity were explained in this chapter. Higher order mode properties of the parallel-bar and rf-dipole geometries are discussed in the next chapter.

CHAPTER 5

HIGHER ORDER MODE PROPERTIES

The parasitic modes in any resonant rf structure are the modes that are present in the cavity in addition to the fundamental operating mode. As the beam passes through, these modes can get excited and may lead to energy losses in the beam. The beam-induced power depends on the intensity and the natural decay time of each mode when any other coupler is not present. The intensity of each mode is determined by the longitudinal and transverse $[R/Q]$ and the natural decay time given by $\tau_n = Q_{0,n}/\omega_n$ where ω_n is the frequency of each mode and $Q_{0,n}$ is its unloaded quality factor.

The modes excited by the charged particles may affect other particles in the same bunch or particles in bunches trailing behind, depending on the decay time of the wakefields. The shorter wakefields mostly act on the same bunch leading to single bunch effects, which depend more on the $[R/Q]$ as the decay times are relatively small. The multiple bunch effects have larger decay times and can act on trailing bunches as well. Furthermore, recirculating linacs or circular machines may generate more detrimental higher order mode (HOM) effects, compared to that from linacs with single pass beam. The multi pass beams may generate cumulative effects leading to multiple bunch instabilities due to larger decay times of those excited modes.

In an rf cavity the longitudinal and transverse impedance thresholds for given beam parameters define the acceptable levels of higher order mode excitation such that the instabilities can be avoided. The longitudinal effects lead to energy spread in the beam. In addition, a beam at an offset to the beam axis can generate transverse effects that can lead to emittance growth and instabilities due to transverse beam break up. Rigorous damping is required to extract the generated higher order mode power with sufficient coupling to those modes, in order to keep the mode excitation below the required impedance thresholds.

The high-current applications of superconducting rf cavities demand extremely low higher-order-mode-impedances during operation. On the contrary, the 499 MHz deflecting cavities for the Jefferson Lab 12 GeV upgrade operate with low beam

currents of 175 μA which, at a single pass, do not lead to heavy beam effects. However, the 400 MHz crabbing cavity for the LHC high luminosity upgrade have stringent impedance requirements. The parallel-bar and rf-dipole designs have attractive higher order mode properties that are favorable in achieving effective damping. In this chapter, higher order mode properties including HOM frequencies, $[R/Q]$ values of the parallel-bar and rf-dipole cavities are evaluated.

5.1 MODE SEPARATION

The parallel-bar design and rf-dipole designs do not have any lower order modes. The frequency separation between the fundamental operating mode and the next higher order mode increases as the design evolves from the parallel-bar geometry to the rf-dipole geometry. The frequency separation between the first two modes for the 499 MHz deflecting cavity design is shown in Table 14.

TABLE 14. Mode separation between fundamental mode and next higher order mode of 499 MHz designs shown in Fig. 38.

Design	Frequency Separation [MHz]
A	10.7
B	18.4
C	127.1
D	264.5
E	255.3
F	278.0

The parallel-bar designs with rectangular outer conductors have smaller mode separation between the fundamental mode and the next higher order mode. The straight parallel-bar geometries with cylindrical outer conductor drastically improve the mode separation by an order of magnitude compared to that of the designs with rectangular shaped outer conductor. In addition, the curved parallel bars further improves the mode separation as shown in Table 14.

The non-existence of lower order modes simplifies the design, implementation and operation of higher order mode dampers, which otherwise would require a notch-type filter to damp the lower order modes without coupling to the fundamental mode. The wider mode separation mentioned above also makes the design of higher order mode dampers less complicated, compared to that of rf designs with a narrow mode separation between the fundamental operating mode and HOM. Several HOM

damping techniques can be implemented to effectively damp the higher-order-mode impedance to acceptable levels given in the design specifications. Waveguide dampers or coaxial type high pass filters are two of those options that also provide compact designs of HOM couplers.

5.2 ANALYSIS OF HIGHER ORDER MODES

The higher-order modes in the parallel-bar and rf-dipole geometries can be categorized based on the field on axis and the direction in which the momentum is imparted on a particle passing through the axis. As shown in Table 15 the modes are categorized mainly as accelerating modes and deflecting modes in horizontal and vertical directions. The accelerating modes generate longitudinal wakefields, while the deflecting modes generate transverse wakefields in the cavity. The rf-dipole geometries do not have any hybrid modes.

TABLE 15. Mode categorization in parallel-bar and rf-dipole geometries.

Field component on axis	Type of mode	Effect on the beam
E_x and H_y	V_x	Deflection in horizontal direction
E_y and H_x	V_y	Deflection in vertical direction
E_z	V_z	Acceleration
H_z	...	Does not couple to the beam

5.3 HOM CALCULATION

The fundamental deflecting and crabbing modes and the other transverse modes in both horizontal and vertical directions in the parallel-bar and rf-dipole designs can impart a transverse momentum on a particle passing through the cavity given by

$$\vec{p}_t = \int_{-\infty}^{\infty} \vec{F}_t \, \mathrm{d}t = \frac{q}{v} \int_{-\infty}^{+\infty} \left[\vec{E}_t + (\vec{v} \times \vec{B}_t) \right] \mathrm{d}z, \tag{117}$$

where $\vec{F}_t$ is the transverse Lorentz Force, q is the charge of the particle, $\vec{v}$ is the velocity of the particle, and $\vec{E}_t$ and $\vec{B}_t$ are the corresponding transverse electric and magnetic field components. The transverse momentum can also be determined by

the Panofsky-Wenzel Theorem [15, 16] given by

$$\begin{aligned} \vec{p}_t &= -i\frac{q}{\omega}\int_{-\infty}^{+\infty}\vec{\nabla}_t E_z\,\mathrm{d}z\,. \\ &= -i\frac{q}{\omega}\lim_{r_0\to 0}\frac{1}{r_0}\int_{-\infty}^{+\infty}[E_z(r_0,z)-E_z(0,z)]\,\mathrm{d}z, \end{aligned} \tag{118}$$

where ω is the frequency of the deflecting mode, r_0 is the transverse offset in the direction of the deflection from the beam axis, and E_z is the longitudinal electric field component at the offset r_0.

The longitudinal momentum experienced by the accelerating modes in the parallel-bar and rf-dipole designs are given by

$$\vec{p}_t = \int_{-\infty}^{\infty}\vec{F}_z\,\mathrm{d}t = \frac{q}{v}\int_{-\infty}^{+\infty}\vec{E}_z\,\mathrm{d}z. \tag{119}$$

5.3.1 ON-AXIS FIELD COMPONENTS

The on-axis field components in all the modes can also be grouped based on the field orientation. The major on-axis field components of the modes 1, 2, 3, 4, 6, and 8 are shown in Fig. 96. The field components in mode 1 and 2 show the field orientations of a transverse mode in horizontal direction and mode 3 and 4 are the two field orientations of the accelerating modes. The mode 6 and 8 are the field orientations of the transverse mode in the vertical direction. The on-axis field components in any parallel-bar or rf-dipole geometries follow one of the field orientations shown in Fig. 96.

Based on the field components the longitudinal or transverse $[R/Q]$ for any mode in the parallel-bar or rf-dipole geometries can be determined as following [81].

Accelerating Modes:

$$\left[\frac{R}{Q}\right] = \frac{\left[\int_{-\infty}^{+\infty}E_z(z,x=0,y=0)e^{\frac{-j\omega z}{c}}\,\mathrm{d}z\right]^2}{\omega U}, \tag{120}$$

Deflecting Modes:

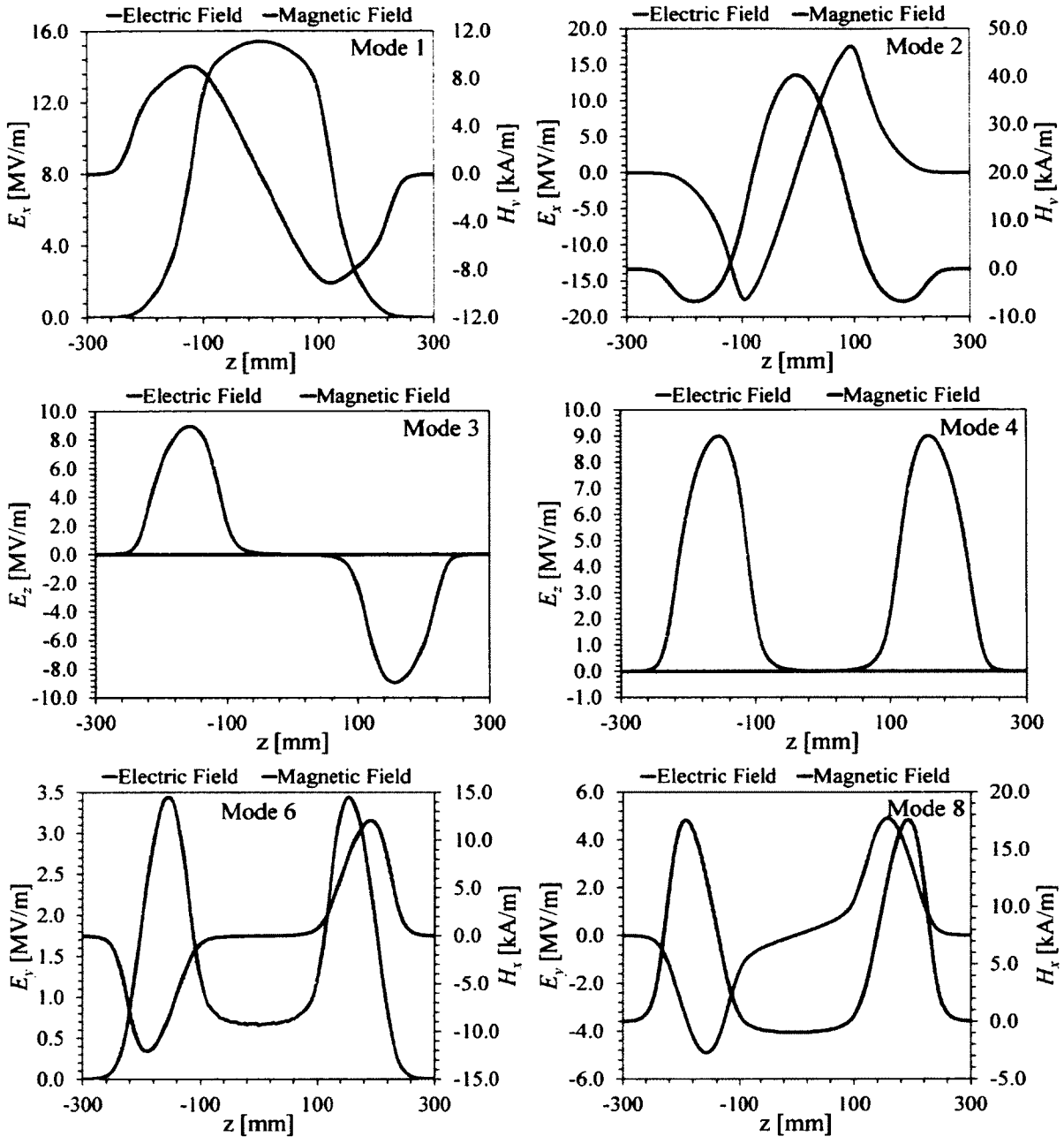

FIG. 96. On axis field components of the 499 MHz rf-dipole design shown in Fig. 38.

(a) In horizontal direction -

$$\left[\frac{R}{Q}\right] = \frac{\left[\int_{-\infty}^{+\infty} [E_x(z, x=0, y=0) + jcB_y(z, x=0, y=0]\, e^{\frac{-j\omega z}{c}}\, \mathrm{d}z\right]^2}{\omega U}. \quad (121)$$

(b) In vertical direction -

$$\left[\frac{R}{Q}\right] = \frac{\left[\int_{-\infty}^{+\infty} [E_y(z, x=0, y=0) - jcB_x(z, x=0, y=0]\, e^{\frac{-j\omega z}{c}}\, \mathrm{d}z\right]^2}{\omega U}. \quad (122)$$

where ω is the frequency of each mode, U is the stored energy in the cavity and $E_{x,y}$ and $B_{x,y}$ are the transverse electric and magnetic field components along the beam axis.

The R/Q for deflecting modes can also be determined by the Panofsky-Wenzel Theorem [15, 16] as

$$\left[\frac{R}{Q}\right] = \frac{\left[\int_{-\infty}^{+\infty} [E_z(z, x, y=r_0) e^{\frac{-j\omega z}{c}}\, \mathrm{d}z\right]^2}{(kr_0)^2\, \omega U}. \quad (123)$$

where $k = \frac{2\pi}{\lambda} = \frac{\omega}{c}$, r_0 is the offset from the beam axis in either horizontal or vertical direction and E_z is the longitudinal electric field component at an offset of r_0 to the beam axis.

5.4 HOM SPECTRUM

The longitudinal and transverse $[R/Q]$ listed below in Table 16 for the first few modes up to 1.5 GHz for the 499 MHz rf-dipole design shown in Fig. 38 are calculated following the Eqs. (120), (121), and (122) using CST Microwave Studio [13]. The $[R/Q]$ calculated for the deflecting modes by the direct integral method given by Eqs. (121) and (122) agrees with that calculated using the Panofsky-Wenzel Theorem given by the Eq. (123).

In a resonant cavity the higher-order modes with frequencies below the cutoff frequency of the beam aperture are considered to be the trapped modes, therefore are very critical in damping. The modes with frequencies above the cutoff frequency propagate through the beam aperture. The 499 MHz deflecting cavity for the Jefferson Lab 12 GeV upgrade has a beam aperture diameter of 40 mm while the 400

TABLE 16. Mode categorization in parallel-bar and rf-dipole geometries.

Frequency (MHz)	Field Orientation	$[R/Q]$ (Ω)
499.0	$E_x - Cos\ H_y - Sin$	982.5
777.1	$E_x - Sin\ H_y - Cos$	162.2
1036.1	$E_z - Sin$	31.5
1037.8	$E_z - Cos$	232.2
1175.7	$E_x - Cos\ H_y - Sin$	9.05
1330.6	$E_y - Cos\ H_x - Sin$	15.6
1372.2	$H_z - Cos$	0.0
1391.1	$E_y - Sin\ H_x - Cos$	0.16
1391.7	$E_z - Sin$	11.2
1491.5	$E_x - Sin\ H_y - Cos$	6.15

MHz crabbing cavity has a beam aperture diameter of 84 mm. When the aperture radius of the beam pipe is smaller than the length of the aperture the TE_{11} is the lowest cutoff mode. Otherwise the TM_{01} becomes the lowest cutoff mode. The cutoff frequency for the lowest mode in the beam aperture with a diameter less than the length of the beam pipe is given by

$$f_{cutoff} = \frac{cJ'_{11}}{2\pi R}, \tag{124}$$

where c is the speed of light, J'_{11} is the first zero of the Bessel function of $J'_n(x)$ of 1^{st} order and R is the radius of the beam aperture. The first zero of the Bessel Function J'_1 is 1.8412 and 2.4048 for the first zero of the Bessel Function J_0. For the two designs of 499 MHz and 400 MHz the cutoff frequencies for both TE_{11} and TM_{01} are shown in Table 17.

TABLE 17. Cutoff frequencies of 499 MHz and 400 MHz rf-dipole designs.

Design frequency (MHz)	Aperture radius (mm)	f_{cutoff} $[TE_{11}]$ (GHz)	$[TM_{01}]$ (GHz)
499	20.0	4.39	5.74
400	42.0	2.09	2.73

The $[R/Q]$ values are evaluated for all the 499 MHz cavity designs shown in Fig. 97. The fundamental deflecting crabbing mode is the lowest mode in each

design and has the highest $[R/Q]$. The higher-order mode spectra clearly show the improvement in the mode separation. With the increase in the mode frequency in the spectrum the $[R/Q]$ decreases, however the separation between the modes also decreases.

In the rf-dipole design with trapezoidal shaped loading elements (Design F) the modes are well separated compared to the spectrua in the previous design geometries. The wider separation in the spectrum makes the damping of the higher-order modes easier. Also separation between the fundamental deflecting and crabbing mode and the next neighbor mode in each design increases with the design evolution from Design A to Design F. In the final rf-dipole designs the frequency of the next neighbor mode is 1.5 times the frequency of the fundamental deflecting and crabbing mode. This higher mode separation and the non-existence of any lower-order mode in the rf-dipole geometry requires only a high pass coupling in damping the higher-order modes.

The higher-order mode spectrum for the 400 MHz rf-dipole design is shown in Fig. 98. The number of modes that requires damping in the 400 MHz rf-dipole design is lower due to the lower cutoff frequency with the large beam aperture compared to that of the 499 MHz rf-dipole design. This further reduces the amount of rf power that requires to be extracted through the higher order modes couplers for a given beam current. However the higher average beam current in the 400 MHz crabbing applications sets stringent impedance thresholds in damping the higher order modes.

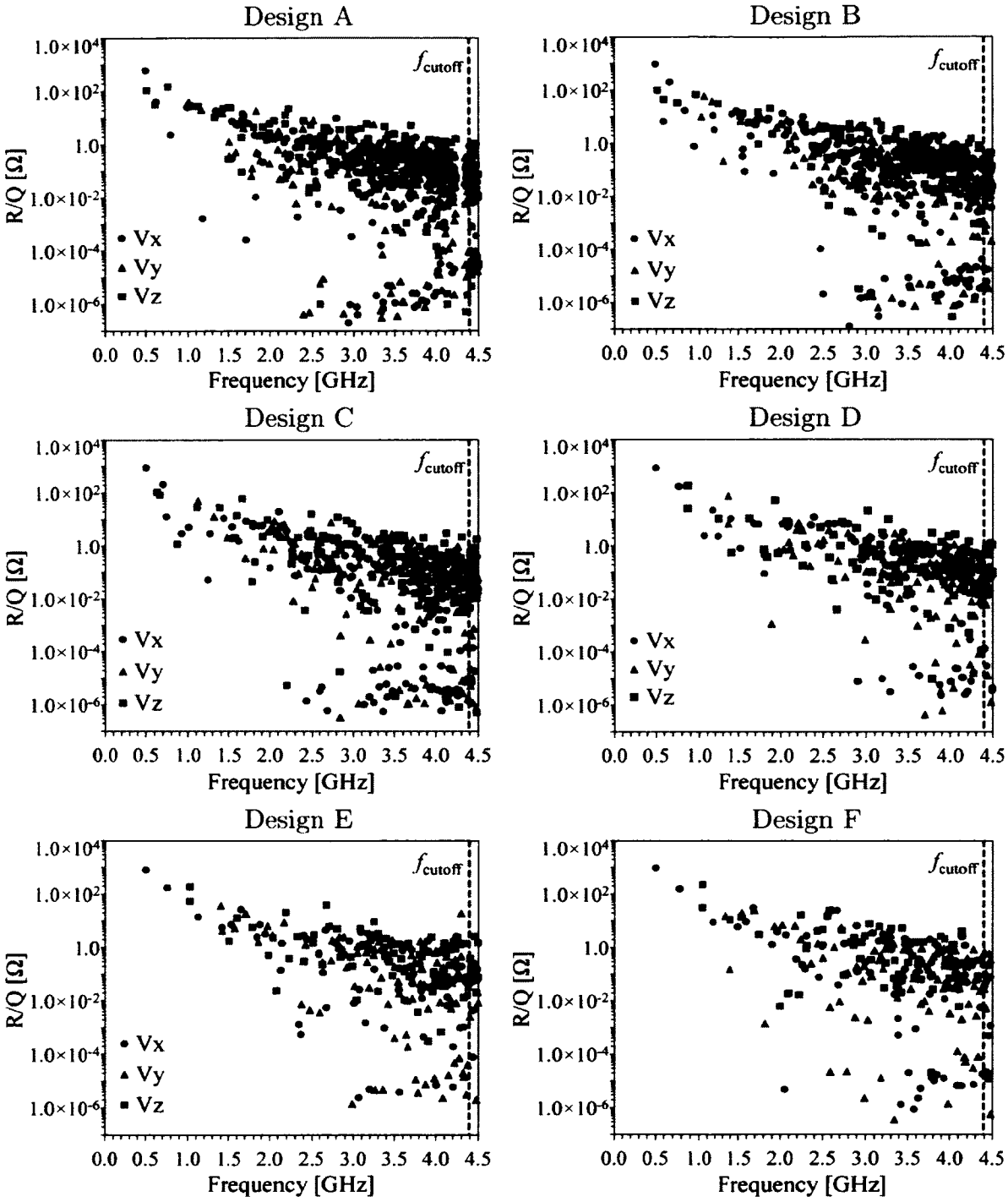

FIG. 97. Higher order mode spectrums of the 499 MHz designs shown in Fig. 38.

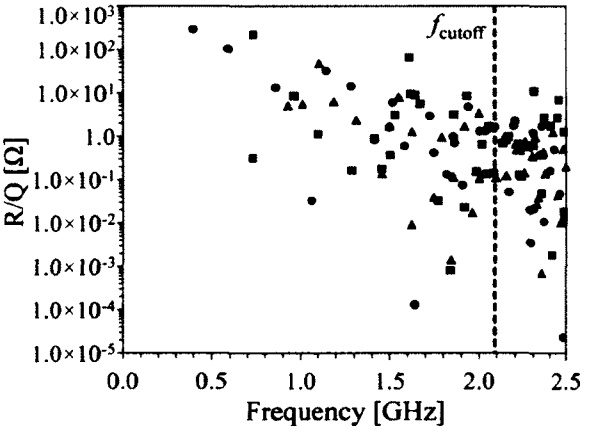

FIG. 98. Higher order mode spectrum of the 400 MHz design.

CHAPTER 6

MULTIPOLE ANALYSIS

The transverse voltage applied to particles in each bunch is required to be constant in order to deliver a uniform deflection of the beam. The complex rf cavity geometries with axial asymmetries may contribute to varying transverse voltage seen by the particles leading to beam dynamic perturbations that could limit the performance in the accelerator. Some of those transverse beam effects are linear beam-beam tune shift, chromaticity shift and amplitude detuning [22, 23]. Also, in deflecting and crabbing cavities, in order to minimize emittance growth, the transverse deflection should be identical for all particles irrespective of their transverse position. This chapter presents an approach that determines the effects due to field non-uniformity in rf cavities with time dependent electromagnetic fields, in relation to the beam effects. Furthermore, several methods are described where the field non-uniformity may be reduced effectively.

The motion of particles in an accelerator are characterized by a six dimensional vector (x, y, p_x, p_y, s, p_z) where s is the position along the machine, p_z is the momentum (or energy) of each particle, x and y are the horizontal and vertical positions, and p_x and p_y corresponds to momenta in horizontal and vertical directions. Unlike in magnets, rf cavities have a monopole component (b_0) where the integrated component corresponds to the accelerating voltage

$$\Delta p_z = \int b_0 \mathrm{d}s \,. \tag{125}$$

For deflecting and crabbing rf cavities the monopole component is zero, however it may exist in the presence of any deformation in the rf structure. The dipolar kick seen by the particles is given by the integrated dipole component (b_1)

$$\Delta p_x = \int b_1 \mathrm{d}s \,. \tag{126}$$

Higher order mode components above b_1 contribute to the transverse beam dynamics. Importantly, these transverse effects are harmful in circular particle accelerators.

The tune is the number of oscillations for a complete revolution where the corresponding tune shift (ΔQ) depends on the quadrupole mulipole component. The horizontal and vertical tune shift are given by

$$\Delta Q_{x,y} = \mp \frac{1}{4\pi} \frac{q}{p} b_2 \beta_{x,y} \tag{127}$$

where β is the beta function at the rf cavity. The variation of the tune with momentum defined as the chromaticity (ξ) is given by

$$\xi_{x,y} = \frac{\Delta Q_{x,y}}{\Delta p/p} = \mp \frac{1}{4\pi} \int b_2 \beta_{x,y}(s) \mathrm{d}s \tag{128}$$

The chromaticity shift depends on the sextupole component (b_3) and can be determined by

$$\Delta \xi_{x,y} = \pm \frac{1}{2\pi} \frac{q}{p} b_3 D \beta_{x,y} \tag{129}$$

where D is the dispersion. The amplitude detuning is the dependency of the tune on the amplitude of the oscillations which depends on the octupolar component (b_4) and is defined as

$$\Delta Q_{x,y} = \frac{3}{8\pi} \frac{q}{p} b_4 \beta_{x,y}^2 9 J_{x,y} \tag{130}$$

for a tune shift at 3σ where $J_{x,y}$ are the invariant of motion. The higher order multipole components until order $n = 4$ are of importance in studying the transverse beam dynamics effects. The numerical values obtained by rf cavities can be compared to that from magnets in the accelerator in understanding the severity of the effects and can be minimized by modifying the rf geometry.

6.1 FIELD NON-UNIFORMITY

The electromagnetic field non-uniformity determines the field quality that results in a non-uniform transverse voltage. In parallel-bar or rf-dipole rf geometries the orientation of the loading elements is the main contribution to the field non-uniformity. In the designs shown in Fig. 38, the field profile on axis varies with each bar geometry as shown in Fig. 99. The field varies across the beam aperture off the beam axis generating non-uniform transverse deflection.

The transverse fields in both horizontal and vertical directions across the beam aperture are analyzed for all the designs as shown in Fig. 38. All the designs have

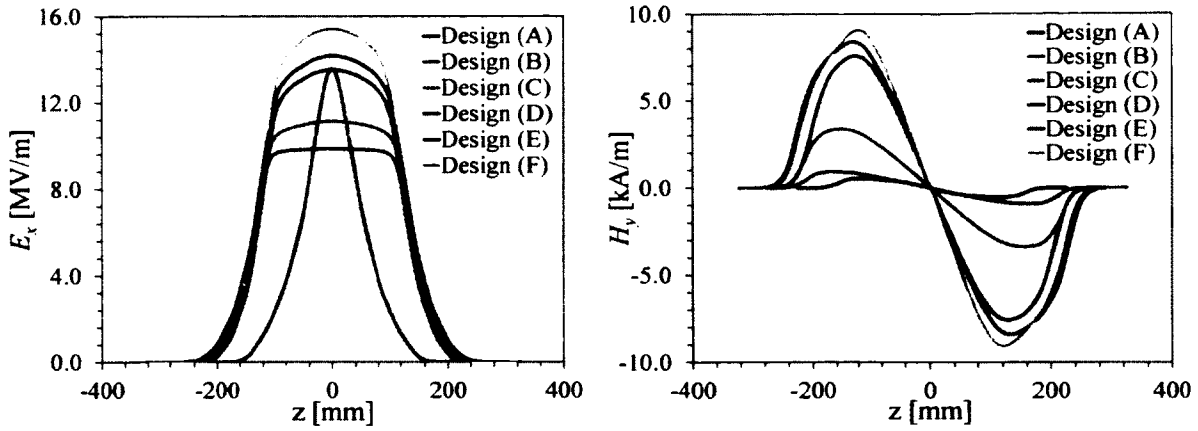

FIG. 99. On axis electric (left) and magnetic (right) field content of all parallel-bar designs shown in Fig. 38 normalized at a stored energy content of 1 J.

quadratic field variation across the beam aperture. The designs with straight cylindrical or race-track-shaped loading elements (Designs (A)-(C)) have more uniform field across the beam aperture with variations as low as ~0.5% at an offset of 10 mm as shown in Fig. 100. With more complicated loading elements (Designs (D)-(F))the non-uniformity increases as high as 3% for both transverse directions.

The normalized off-axis field variation within a radius of 10 mm are shown in Eqs. 131 - 136 for all the designs given in Fig. 38.

$$\text{Design (A):} \quad \frac{V_t(\Delta x, \Delta y)}{V_t(r=0)} = \begin{cases} 5.5 \times 10^{-5}\Delta x^2 \quad [\text{mm}], \\ -5.49 \times 10^{-5}\Delta y^2 \quad [\text{mm}], \end{cases} \tag{131}$$

$$\text{Design (B):} \quad \frac{V_t(\Delta x, \Delta y)}{V_t(r=0)} = \begin{cases} 5.12 \times 10^{-5}\Delta x^2, \\ -5.11 \times 10^{-5}\Delta y^2, \end{cases} \tag{132}$$

$$\text{Design (C):} \quad \frac{V_t(\Delta x, \Delta y)}{V_t(r=0)} = \begin{cases} 5.48 \times 10^{-5}\Delta x^2, \\ -5.47 \times 10^{-5}\Delta y^2, \end{cases} \tag{133}$$

$$\text{Design (D):} \quad \frac{V_t(\Delta x, \Delta y)}{V_t(r=0)} = \begin{cases} 1.8 \times 10^{-4}\Delta x^2, \\ -1.77 \times 10^{-4}\Delta y^2, \end{cases} \tag{134}$$

$$\text{Design (E):} \quad \frac{V_t(\Delta x, \Delta y)}{V_t(r=0)} = \begin{cases} 3.0 \times 10^{-4}\Delta x^2, \\ -2.88 \times 10^{-4}\Delta y^2, \end{cases} \tag{135}$$

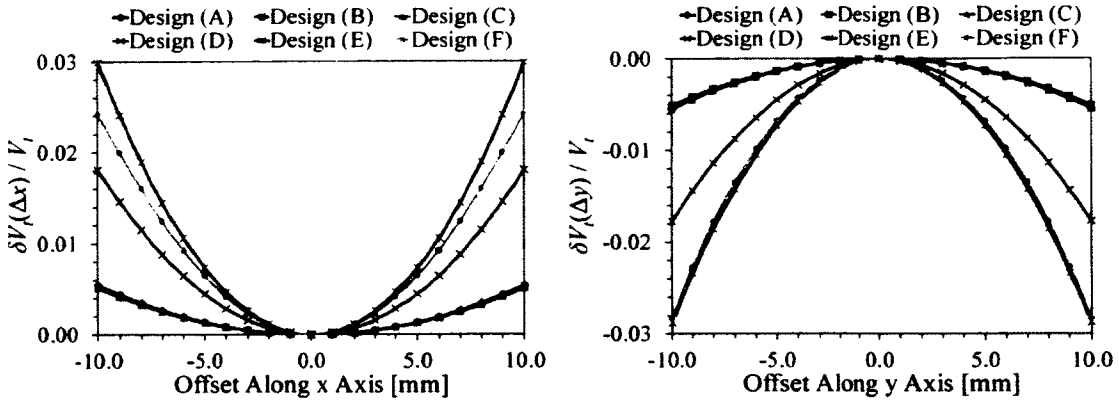

FIG. 100. Change in transverse deflecting voltage in horizontal (offset along x axis) and vertical (offset along y axis) directions normalized to the transverse voltage at on-axis for designs shown in Fig. 38 (The Designs (A) and (C) are identical).

$$\text{Design (F):} \qquad \frac{V_t(\Delta x, \Delta y)}{V_t(r=0)} = \begin{cases} 2.44 \times 10^{-4} \Delta x^2 \,, \\ -2.82 \times 10^{-4} \Delta y^2 \,, \end{cases} \tag{136}$$

In the rf-dipole design the height is reduced at the inner wall of the trapezoidal-shaped loading elements in order to reduce the peak electric field. However, this increases the non-uniformity across the beam aperture. Alternatively, the field non-uniformity can be reduced by curving the loading elements near the beam aperture region. The inward curving of the 499 MHz and 400 MHz rf-dipole cavities are shown in Fig. 101 where in both cases the inner bar surface moved inward around the beam aperture by a distance of 5 mm. The non-uniformity in the transverse field is almost completely canceled across the beam aperture within the transverse beam size of the designs. A field non-uniformity analysis was carried out for each design, evaluating the field across the beam aperture in horizontal (offset along x axis) and vertical (offset along y axis) as shown in Fig. 102 and Fig. 103 to determine the change in transverse voltage for both horizontal and vertical directions. The circular indentation with larger curvature is more effective in reducing non-uniformity evenly in both horizontal and vertical planes. Further optimization could lead to improved uniformity of the deflecting voltage off axis to the levels accepted beyond the transverse beam size.

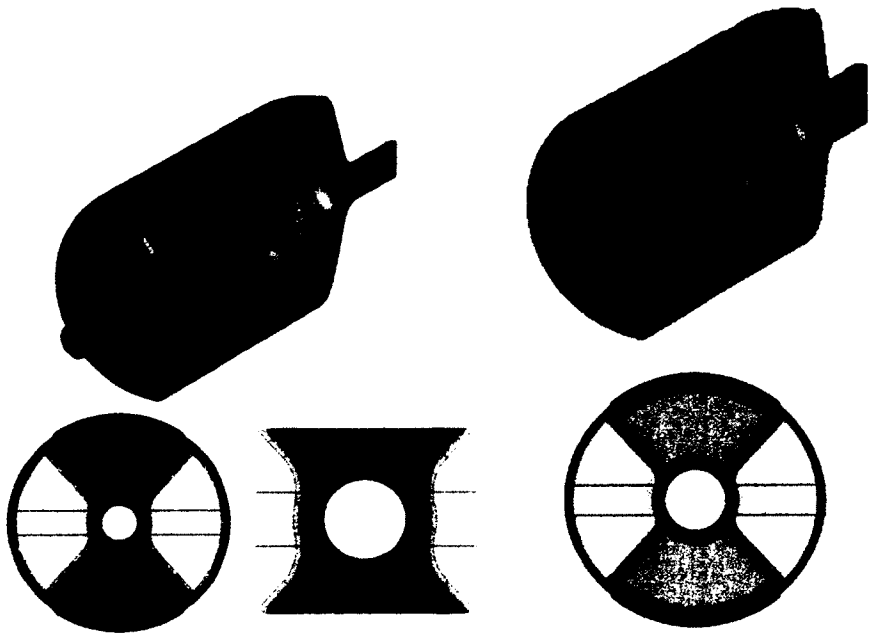

FIG. 101. Modified 499 MHz (left) and 400 MHz (right) rf-dipole designs with trapezoidal-shaped parallel bars indented in the beam-line area.

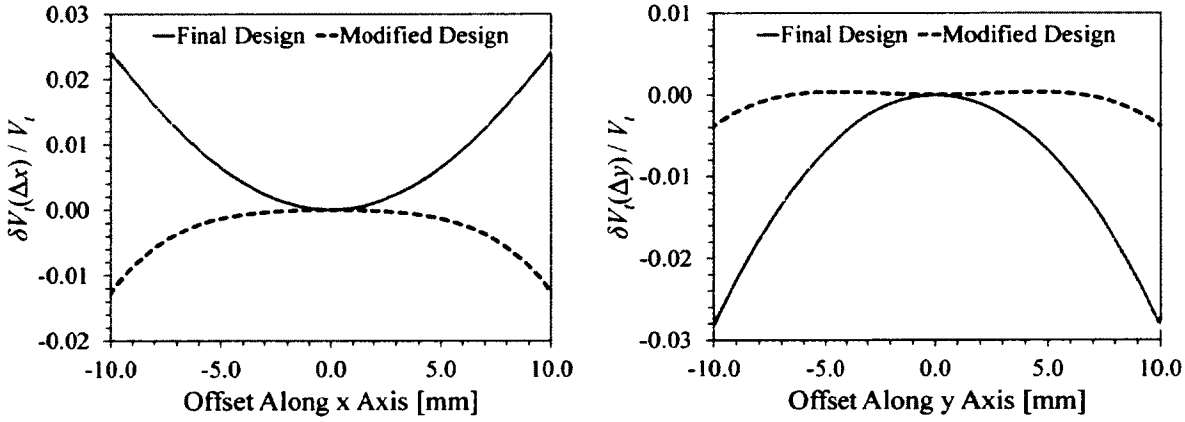

FIG. 102. Normalized transverse deflecting voltage in horizontal and vertical directions for design (F) shown in Fig. 38 and modified design shown in (Fig. 101) of the 499 MHz rf-dipole cavity.

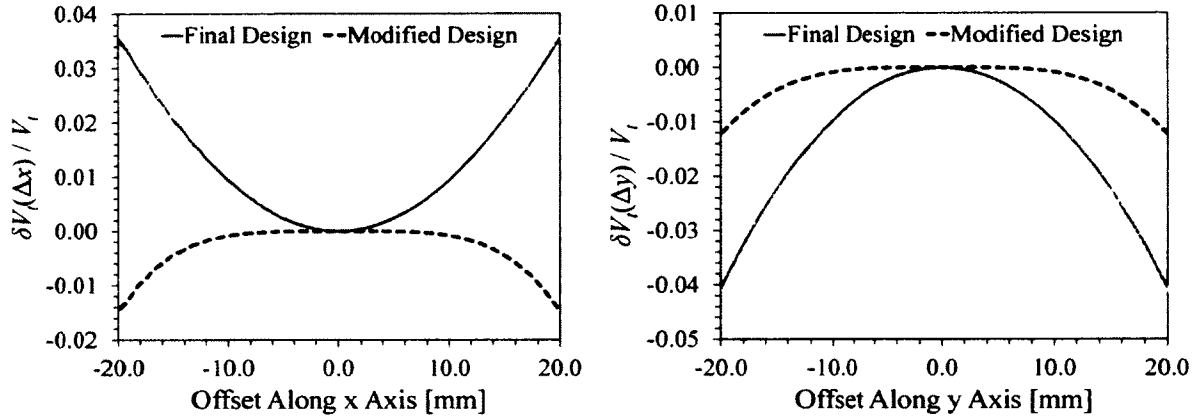

FIG. 103. Normalized transverse deflecting voltage in horizontal and vertical directions of the 400 MHz rf-dipole cavity with flat and curved loading elements shown in (Fig. 101).

6.2 MULTIPOLE COMPONENTS IN RF-DIPOLE CAVITY

The quality of transverse fields can be determined by the analysis of field non-uniformity across the beam aperture. In estimating the exact effects on the beam dynamics due to field non-uniformity, the method of calculating higher-order multipole components was adopted as described in Chapter 2. For simpler rf geometries such as the pill-box cavity, the multipole components can be determined analytically. The higher-order multipole components for rf-dipole cavities are determined numerically using both the methods proposed in Eqs. 45 and 46. The symmetry of the design in both horizontal and vertical planes, reduces the above expressions with normal multipole components where the skew components are zero. Therefore, Eq. 42 can be simplified as

$$E_z^{(n)}(z) = \frac{1}{r^n} \int_0^{2\pi} E_z(r, \phi, z) \cos(n\phi) \mathrm{d}\phi \,, \tag{137}$$

for the time independent rf-fields. The rf-dipole cavity has zero on-axis longitudinal electric field, where the transverse deflection is given by both transverse electric (E_x) and magnetic (H_y) fields.

The accurate extraction of electromagnetic fields are important in determining the higher order multipole component with precision. In reducing the errors introduced with field extrapolation, a finer tetrahedral mesh is used with multiple concentric cylinders within the beam aperture as shown in Fig. 104 with fixed number of points at each concentric cylinder. The 499 MHz deflecting is meshed with 60 points in each concentric cylinder and 64 points in each concentric cylinder of the 400 MHz crabbing cavity. The field data are obtained for two rf-dipole cavities with beam aperture radii of 20 mm and 42 mm; at three different radii of 5 mm, 10 mm, and 15 mm for the 499 MHz cavity and of 10 mm, 20 mm, and 30 mm for the 400 MHz cavity.

Following the definition of the multipole field components given in Eq. 39 the numerical data were obtained for $E_z(r, \phi, z)$ at different values of ϕ for several fixed radial distances of r_0. From the field data (E_m) acquired at each $r = r_0$ and ϕ_m of

$$\phi_m = 2\pi \frac{m}{M} \quad m = 0, 1, 2, .., M-1 \tag{138}$$

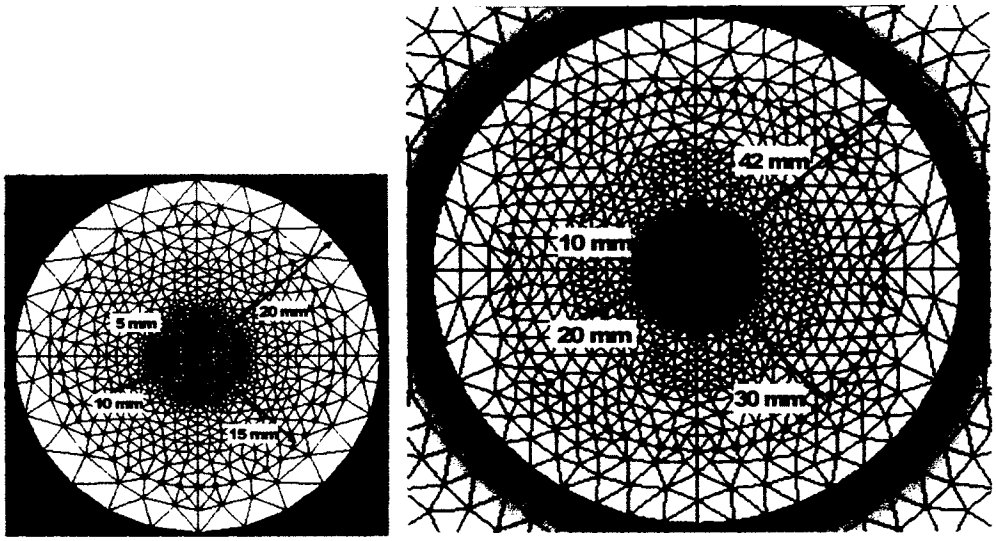

FIG. 104. Tetrahedral mesh used in concentric cylinders in extracting multipole field components of 499 MHz and 400 MHz rf-dipole cavities.

the multipole fields for an arbitrary n' can be constructed as

$$\sum_{m=0}^{M-1} E_m e^{-2\pi j n' \frac{m}{M}} = \sum_{m=0}^{M-1} \sum_{n=0}^{\infty} E_z^{(n)} r_0^n e^{2\pi j (n-n') \frac{m}{M}} , \tag{139}$$

where, for $n = n'$, it can be further simplified as

$$\sum_{m=0}^{M-1} E_m e^{-2\pi j n' \frac{m}{M}} = M E_z^{(n')} r_0^{n'} , \tag{140}$$

$$E_z^{(n)} = \frac{1}{M r_0^n} \sum_{m=0}^{M-1} E_m e^{-2\pi j n \frac{m}{M}} . \tag{141}$$

The accuracy of the multipole components determined using the polar basis is related to the dependence of the field on the radial distance and can be expressed as

$$\triangle E_z^{(n)} \approx \frac{\triangle E_m}{M r_0^n} , \tag{142}$$

where the accuracy of the multipole components are given by

$$\triangle B_n \approx \triangle E_z^{(n)} \frac{1}{M} \left(\frac{r}{r_0}\right)^n . \tag{143}$$

The dependence of the accuracy on radial distance (r_0) is dominant as clearly shown in Eq. 143, where the accuracy reduces drastically at higher orders of multipole components. Furthermore, the accuracy improves with the field data obtained at larger radii closer to the beam aperture radius and also using a higher number of data points (M) in obtaining the field data.

The Fourier-decomposed field components of $E_z^{(n)}(z)$ following Eq. 137 are calculated numerically using a MatLAB code [91] at each concentric cylinder normalized to a transverse voltage (V_t) of 1.0 MV . The field components as a function of z are shown in Fig. 105 and Fig. 106, for the two rf-dipole cavities up to order n=7.

The multipole components present in the rf-dipole geometry are of order $2n$ for $n = 1, 2, 3, ..$ with zero monopole, quadrupole, octupole components and non-zero dipole, sextupole and decapole components. The dipole component gives the net transverse voltage seen by the beam. The dipole and sextupole components can be calculated accurately at each radii. However, multipole components above $n = 5$ can be determined accurately only at larger radii. At radii closer to the beam axis the field data has high noise content. Also, as the order increases, the noise content increases and becomes dominant over the field content. At larger radii, the non-uniform field across the beam aperture has more linear variation hence the higher order field components can be extracted with improved accuracy. However, above n=7 the multipole field components are dominated by the noise content and cannot be determined accurately using numerical techniques.

The integrated monopole field component, gives the accelerating voltage for the rf cavity, and is zero for the rf-dipole cavity. The higher order multipole components determined by Eqs. 45 and 48 following the Panofsky-Wenzel Theorem can be expressed as

$$B_z^{(n)} = \frac{n}{\omega} E_z^{(n)}(z) \sin(\omega t) - j \frac{n}{\omega} E_z^{(n)}(z) \cos(\omega t) \quad \left[\mathrm{mT/m^{n-1}}\right] . \tag{144}$$

including both real and imaginary parts that corresponds to normal components. Skew components represented by A_z related to the $\sin(n\phi)$ form of $E_z^{(n)}(z)$ are zero in the rf-dipole geometry.

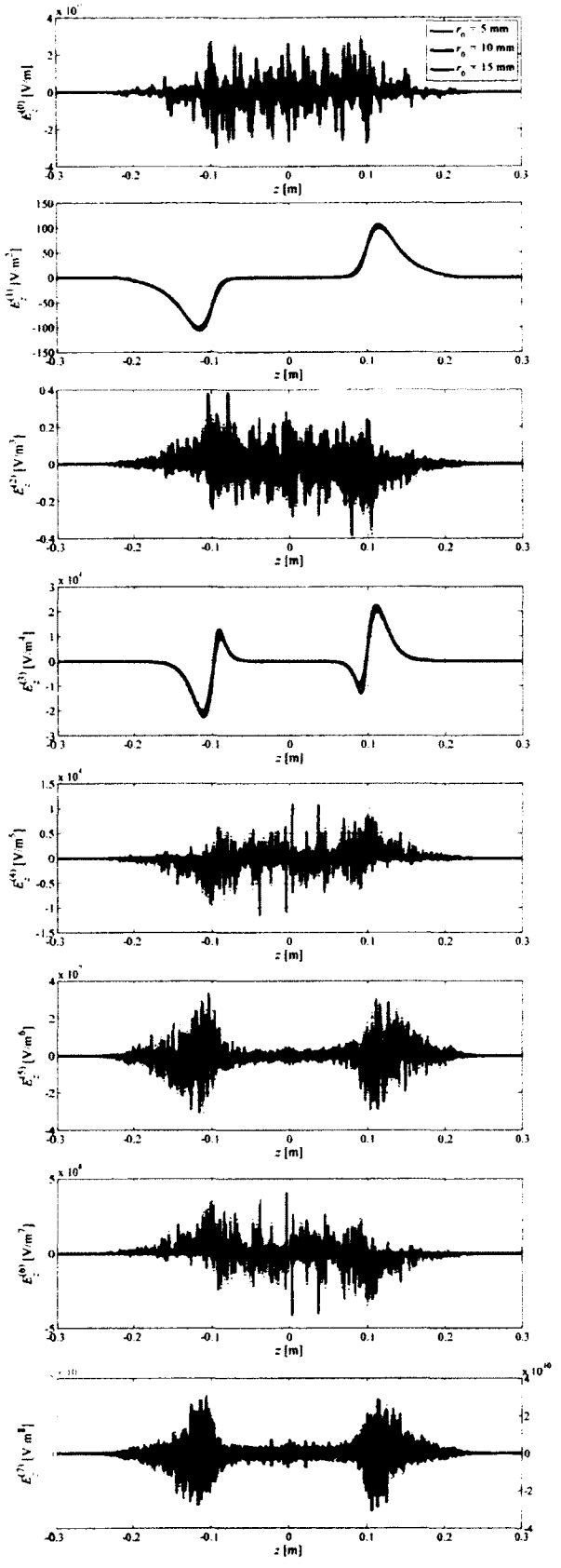

FIG. 105. Time independent multipole field components of $E_z^{(n)}(z)$ for the 499 MHz rf-dipole cavity at radii 5 mm, 10 mm, and 15 mm for orders $n = 0 - 7$.

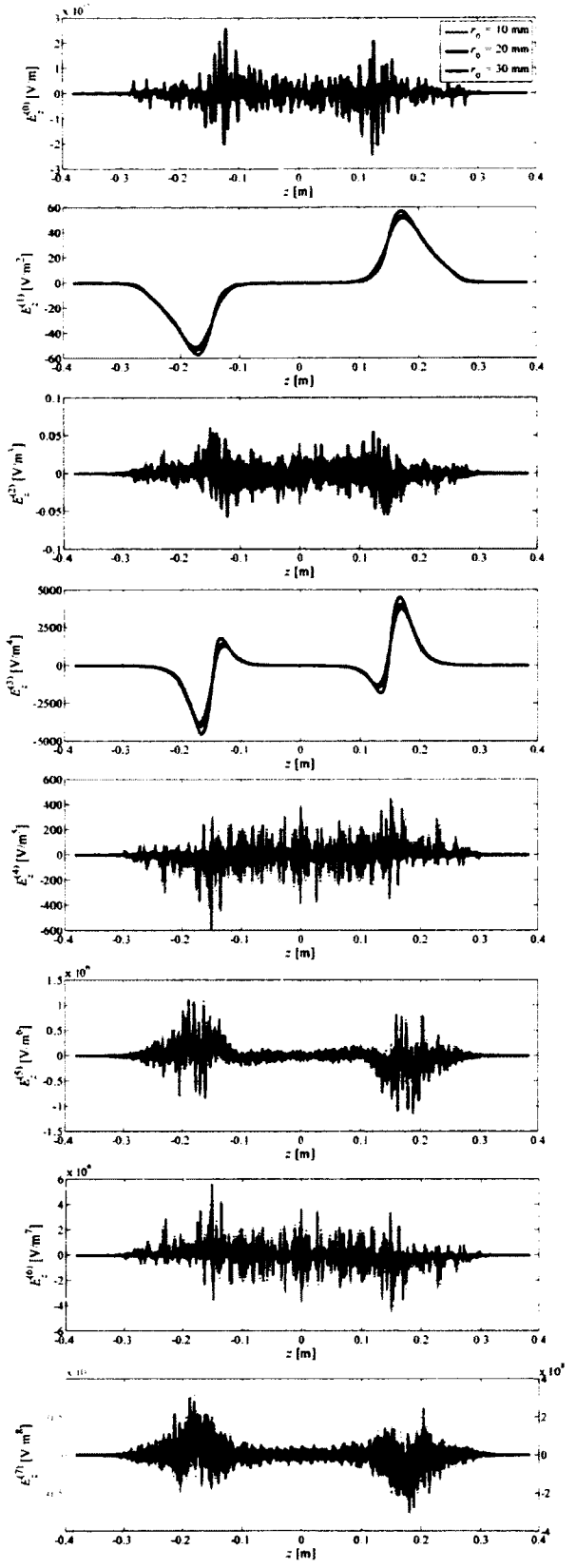

FIG. 106. Time independent multipole field components of $E_z^{(n)}(z)$ for the 400 MHz rf-dipole cavity at radii 10 mm, 20 mm, and 30 mm for orders $n = 0 - 7$.

The real part gives multipole components that are effective for a deflecting rf structure and the imaginary component for a crabbing rf structure. The numerical values are given in Table 18 and Table 19 for the 499 MHz deflecting cavity, and Table 20 and Table 21 for the 400 MHz crabbing cavity, normalized to a transverse voltage of 1.0 MV. At lower orders multipole components determined at each radius give accurate results, however at higher order the accuracy is achieved only at larger radii closer to the beam aperture radius. The rf-dipole cavity has zero accelerating voltage determined by b_0 compared to the transverse voltage of 1 MV determined by b_1.

TABLE 18. Real part of the normal multipole components of 499 MHz rf-dipole cavity at each r_0 of 5 mm, 10 mm and 15 mm.

Component	5 mm	10 mm	15 mm	Unit
V_z	0.034	0.1	0.094	V
V_t	0.997	0.998	0.998	MV
b_0	0.0	0.0	0.0	mT m
b_1	3.3	3.3	3.3	mT
b_2	-1.7×10^{-3}	-1.3×10^{-3}	-5.3×10^{-4}	mT/m
b_3	8.8×10^{2}	8.6×10^{2}	8.7×10^{2}	mT/m^2
b_4	1.3×10^{2}	24.6	4.5	mT/m^3
b_5	6.4×10^{5}	-7.1×10^{5}	-6.1×10^{5}	mT/m^4
b_6	-7.6×10^{6}	-3.5×10^{5}	-2.9×10^{4}	mT/m^5
b_7	7.5×10^{10}	-1.3×10^{9}	-7.1×10^{8}	mT/m^6

TABLE 19. Imaginary part of the normal multipole components of 499 MHz rf-dipole cavity at each r_0 of 5 mm, 10 mm and 15 mm.

Component	5 mm	10 mm	15 mm	Unit
b_0	$0.0j$	$0.0j$	$0.0j$	mT m
b_1	$-6.8\times10^{-10}j$	$-3.0\times10^{-10}j$	$-1.8\times10^{-9}j$	mT
b_2	$8.9\times10^{-9}j$	$8.8\times10^{-9}j$	$-1.2\times10^{-7}j$	mT/m
b_3	$4.1\times10^{-5}j$	$-3.5\times10^{-5}j$	$-7.6\times10^{-6}j$	mT/m^2
b_4	$4.7\times10^{-4}j$	$-1.7\times10^{-4}j$	$-1.0\times10^{-3}j$	mT/m^3
b_5	$1.0j$	$-0.1j$	$7.8\times10^{-3}j$	mT/m^4
b_6	$39.2j$	$2.4j$	$-6.3j$	mT/m^5
b_7	$3.5\times10^{5}j$	$-1.6\times10^{3}j$	$5.4\times10^{2}j$	mT/m^6

The effect of the imaginary parts of the multipole components b_n on the beam dynamics are negligible for the rf-dipole geometry whereas the actual effects are from

TABLE 20. Real part of the normal multipole components of 400 MHz rf-dipole cavity at each r_0 of 10 mm, 20 mm and 30 mm.

Component	10 mm	20 mm	30 mm	Unit
V_z	0.023	0.043	0.078	V
V_t	0.998	0.998	0.997	MV
b_0	0.0	0.0	0.0	mT m
b_1	3.3	3.3	3.3	mT
b_2	-3.7×10^{-4}	-1.7×10^{-4}	1.4×10^{-4}	mT/m
b_3	3.1×10^{2}	3.1×10^{2}	3.1×10^{2}	mT/m^2
b_4	7.2	0.8	-0.3	mT/m^3
b_5	-7.1×10^{4}	-5.2×10^{4}	-4.8×10^{4}	mT/m^4
b_6	-1.0×10^{5}	-2.9×10^{3}	4.7×10^{2}	mT/m^5
b_7	-3.5×10^{8}	-2.5×10^{7}	-1.0×10^{7}	mT/m^6

TABLE 21. Imaginary part of the normal multipole components of 400 MHz rf-dipole cavity at each r_0 of 10 mm, 20 mm and 30 mm.

Component	10 mm	20 mm	30 mm	Unit
b_0	$0.0j$	$0.0j$	$0.0j$	mT m
b_1	$-2.4\times10^{-10}j$	$-2.3\times10^{-9}j$	$-2.5\times10^{-9}j$	mT
b_2	$1.0\times10^{-7}j$	$-6.8\times10^{-8}j$	$-1.5\times10^{-8}j$	mT/m
b_3	$1.6\times10^{-5}j$	$-3.8\times10^{-6}j$	$-1.3\times10^{-6}j$	mT/m^2
b_4	$-2.0\times10^{-3}j$	$3.3\times10^{-4}j$	$3.4\times10^{-5}j$	mT/m^3
b_5	$-0.3j$	$3.6\times10^{-2}j$	$9.4\times10^{-3}j$	mT/m^4
b_6	$28.0j$	$-1.2j$	$-5.2\times10^{-2}j$	mT/m^5
b_7	$7.9\times10^{3}j$	$1.6\times10^{2}j$	$-31.0j$	mT/m^6

real parts of the multipole components. The corresponding components contributing from $E_z^{(n)}(z)\cos(\omega t)$ produces zero effect due to the sinusoidal off-axis longitudinal electric field in this particular geometry. The multipole components produced by any rf geometry need to be suppressed to minimize the effects on beam dynamics and are considered of no significance for the crabbing cavity for the LHC High Luminosity Upgrade within the following condition of

$$b_n R^{n-1} < 1.0 \text{ mT m} \tag{145}$$

where R is the beam aperture radius [92]. The calculated values of $b_n R^{n-1}$ for multipole components of the two rf-dipole cavities are well within the limit of 1.0 mT m. Multipole components exceeding the above criterion by a order or magnitude or higher needs to be carefully analyzed in determining the exact effects on the beam dynamics and modified further with changes on the rf geometry to reduce those components.

Similarly, higher order multipole components can be computed by the Lorentz force method using transverse electric and magnetic fields. Appendix B explains the approach of using the Lorentz force method.

6.2.1 MULTIPOLE COMPONENTS FOR RF-DIPOLE CAVITY WITH CURVED LOADING ELEMENTS

The multipole components were analyzed for the 400 MHz rf-dipole cavity with curved loading elements shown in Fig. 101. The multipole field data components ($E_z^{(n)}(z)$) are shown in Fig. 107 of the first 4 non-zero orders, normalized to a transverse voltage of 1.0 MV. The dipole component corresponding to the transverse voltage is equal for both designs with flat and curved loading elements with equal integrated area under the curves. This clearly shows that the curvature on loading elements does not affect the fundamental operating mode. The higher order component (b_3) shows the reduction in area under the curve, which relates to the suppressed multipole component. However, the curved bars increased multipole components for orders above $n = 3$. At higher orders of multipole components this increase is acceptable with the radial dependence of $1/r^n$, in order to reduce the lower order components. The curvature of the loading elements therefore allows to effectively suppress the higher order multipole components and maintain a uniform

beam across the beam aperture.

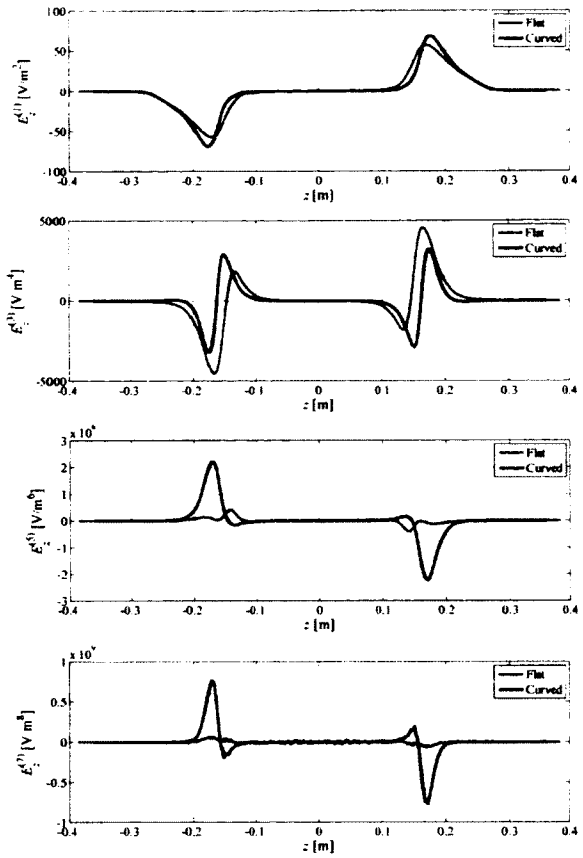

FIG. 107. Time independent multipole field components of $E_z^{(n)}(z)$ for the 400 MHz rf-dipole cavity with flat and curved elements for orders n=1, 3, 5, and 7.

The integrated normal multipole components (b_n) determined by the field extracted at r=30 mm are given in Table 22, normalized to a transverse voltage of 1.0 MV. The b_3 component is drastically reduced where b_5 increased slightly.

TABLE 22. Multipole components of 400 MHz rf-dipole cavity with flat and curved loading elements.

Component	Flat	Curved
b_1	3.3	3.3
b_2	-3.7×10^{-4}	-1.8×10^{-4}
b_3	3.1×10^{2}	2.4
b_4	7.2	-0.4
b_5	-7.1×10^{4}	-2.6×10^{5}
b_6	-1.0×10^{5}	6.2×10^{2}
b_7	-3.5×10^{8}	-7.4×10^{7}

CHAPTER 7

MULTIPACTING ANALYSIS

Multipacting is a complex phenomenon that limits the performance in any rf cavity, in which a large amount of secondary electrons are emitted from the cavity surface by the incident primary electrons. The primary electrons emitted by the cavity inner surface have kinetic energies and trajectories that depends on the electromagnetic fields in the rf cavity. The secondary electrons that are accelerated by the rf fields, may produce more electrons upon contact with the surface. This becomes a critical condition if the primary electrons have localized and sustainable resonant trajectories with the cavity rf fields and the impact energies corresponds to a secondary emission yield (SEY) greater than one, defined as

$$\text{SEY}(\delta) = \frac{\text{Number of secondary electrons}}{\text{Number of incident primary electrons}}. \tag{146}$$

The impact energies of the primary electrons that generate secondary electrons are non-relativistic and relativistic electrons have no effect on multipacting. A typical SEY curve has the following trend with varying impact energy shown in Fig. 108. The SEY curves show similar behavior and are generated by repeated measurements carried out on different materials [93, 94]. Materials used in rf applications, such as niobium, copper and aluminum with good conductivity have secondary emission coefficients greater than one. The critical range of impact energies varies for different material and also strongly depends on the condition of the surface. δ_{max} increases for wet surfaces and drops for surfaces after chemical etching and heat treatment. Microscopic models have been developed to determine the secondary electron emission including a set of parameters, which agrees with the measurements [95].

More than one secondary electron can be emitted from the surface at a SEY> 1. These electrons may further generate resonant electrons, building up a large amount of excess electrons near the surface. This continuous process can lead to an exponential increase in the electron current leading to a thermal breakdown of the rf cavity due to surface heating. The potential range of impact energies for Nb would

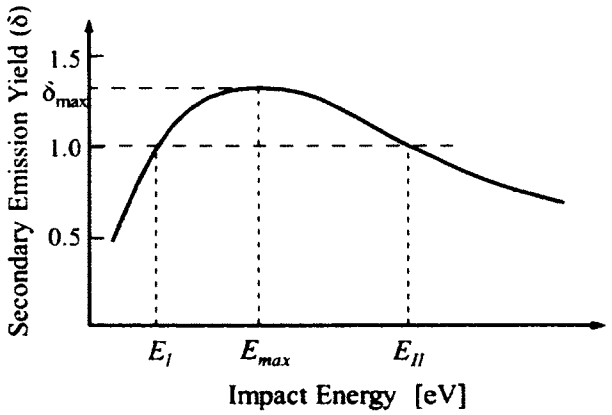

FIG. 108. Secondary emission yield with impact energy of the primary electrons.

be in the range of 20 eV to 2000 eV. The critical impact energy region where the SEY> 1 would be $E_I > 150$ eV and $E_{II} < 1050$ eV [45], with $E_{max} \simeq 350$ eV.

The secondary particles absorb the rf power supplied to the cavity limiting the achievable gradient in the cavity. Also electron resonances corresponds with rf field levels may cause a sharp reduction on the cavity performance, hence Q_0. The soft barriers on the gradient can be eliminated by cavity processing and cleaning. However hard barriers may not be eliminated by processing and requires reoptimizing the cavity geometry.

7.1 ORDER OF MULTIPACTING

The trajectory of resonant electrons and collisions on the cavity surface primarily depends on the rf field. The resonant electrons under electric field will have trajectories perpendicular to the surface where magnetic field results on trajectories parallel to the surface. The order of multipacting is defined as the number of rf periods between adjacent collisions. At lower orders of multipacting, electrons with sufficient impact energy may reach an electron avalanche faster that that from higher orders due to the frequency of collisions.

The energy of the secondary electrons traversing under the rf fields will result in one-point or two-point multipacting levels. In one-point multipacting the emitted secondary electrons travelling during a single rf period impact close to the location of emission. The order in which resonance occurs is related to integer multiples of rf periods. Two-point multipacting occurs when the collisions include two locations on

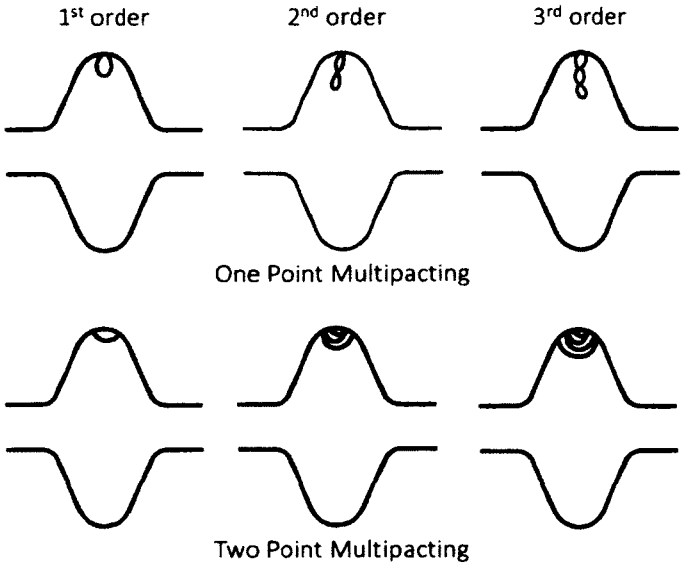

FIG. 109. Electron trajectories at different orders of multipacting for one-point and two-point multipacting levels.

the cavity surface, as in a parallel plate scenario. The order in two-point multipacting is given by the integer multiples of half rf periods, where electrons collide each surface in every half rf period.

The parallel-bar or rf-dipole geometries are susceptible to multipacting effects due to its geometry. The areas with parallel plate like geometry with the transverse electric field make the design more likely to have two-point multipacting present between the surfaces. For a parallel plate set-up with an alternating electric field, the resonant voltage and impact energy for two-point multipacting [96] are given by

$$V_n = \frac{m\omega^2 d^2}{(2n-1)\pi e}, \tag{147}$$

$$E_n = \frac{2m\omega^2 d^2}{(2n-1)^2\pi^2}, \tag{148}$$

where m is the mass of electron, ω is the rf frequency, d is the separation between the plates and n is the order of multipacting. Compared to the electric field, resonant electrons are not accelerated under the magnetic field, hence move in cyclotron orbits [45] and may lead to stable trajectories near the cavity surface, especially at high magnetic field regions. The magnetic field levels at which one-point multipacting can

possibly occur is given by

$$H_n \propto \frac{m\omega}{n\mu_0 e}. \tag{149}$$

and for two-point multipacting

$$H_n \propto \frac{2m\omega}{(2n-1)\mu_0 e}. \tag{150}$$

Exact relationship can be determined with numerical simulations for each given cavity geometry. For higher orders of resonances the impact energy decreases resulting in a probable multipacting condition at lower field levels. However this analytical method cannot be applied to the complete cavity design due to its complexity in the geometry and rf fields. Therefore an advanced numerical code is used to identify probable multipacting conditions in the parallel-bar and rf-dipole cavities.

7.2 MULTIPACTING IN PARALLEL-BAR AND RF-DIPOLE GEOMETRIES

Numerical tools important in evaluating multipacting levels in complex rf structures. Several 2-dimensional and 3-dimensional tools have been developed over the years that analyzes the multipacting levels [97]. Multipacting levels were analyzed for the parallel-bar and rf-dipole geometries shown in Fig. 38 using the 3D parallel tracking code Track3P from the ACE3P code suite developed by SLAC [98, 99]. The code has been successfully used to determine multipacting conditions present in many complex cavity designs and components, and has been extensively benchmarked over measured data [98, 99]. Considering the symmetry of the geometries, multipacting levels were studied with primary electrons generated in a volume of $^1/_8$ and colliding on any surface in entire volume.

The electromagnetic fields required for Track3P were obtained from Omega3P, the eigenmode solver in the ACE3P code suite. The primary electrons for the simulations are emitted from the surface in the first full rf period where they follow the electromagnetic fields and may collide with the cavity surface generating secondary electrons based on the impact energy of the incident primary electron. Then, the emitted secondary electrons are traced for a longer time (50 rf periods) to identify the resonant particles. The data from Track3P is used to determine the order and type of multipacting and the corresponding trajectories of resonant particles.

The resonant conditions were scanned for the fundamental deflecting mode up

to a transverse voltage (V_t) level of 3.0 MV per cavity. This is equivalent to a field gradient of

$$E_z\left(x_0 = 5mm\right) = x_0 \frac{\omega}{c} \frac{V_t}{\lambda/2}. \tag{151}$$

along the beam line at an offset (x_0) of 5 mm and $\lambda/2$ is the half wave length.

Figure 110 shows impact energies and multipacting order of the resonant particles on parallel-bar and rf-dipole geometries. Considering ⅛ of the volume in rectangular-shaped parallel-bar cavities most of the resonant trajectories lie on the top surface of the cavity which is also the high magnetic field region. With the existence of fewer resonant particles the corresponding orders of multipacting vary from 1-6. The data from the Track3P code show that the impact energies of resonant particles of the rectangular-shaped designs are below 400 eV.

As the geometry changes to cylindrical-shaped cavities the number of resonant particles increases where the majority of the particles exist in the magnetic field region, at multipacting order of one. The end plate slope also introduces resonant trajectories with low multipacting orders. The impact energy range expands into a wider range and falls within the critical impact energy range for niobium.

The resonant particles in the magnetic field region generate 2-point multipacting levels near edges of the parallel-bar loading elements. Any parallel-bar geometry does not indicate any resonant conditions in the electric field region. The rf-dipole geometry (Design (E)) shifts the resonant levels into the high magnetic field region at the center of the cavity.

7.3 MULTIPACTING IN 499 MHZ DEFLECTING CAVITY

The multipacting levels were analyzed in the 499 MHz rf-dipole cavity using the Track3P code [98. 99]. The impact energy obtained for multiple orders of resonant particles shown in Fig. 111 indicate two distinct multipacting barriers at low transverse voltage. The first barrier exist around 1.0 MV and the second barrier at a range of 2.0 - 3.0 MV. The first barrier has a wider impact energy range that agrees with the critical impact energy range for niobium, while the impact energies of the resonant particles in the second barrier are low, still in a range that can generate secondary electrons. The majority of the resonant particles are first and second order and lies on the top of the cavity where the high magnetic field region exist and on the end plates of the cavity, and exist at very low transverse voltage as shown in

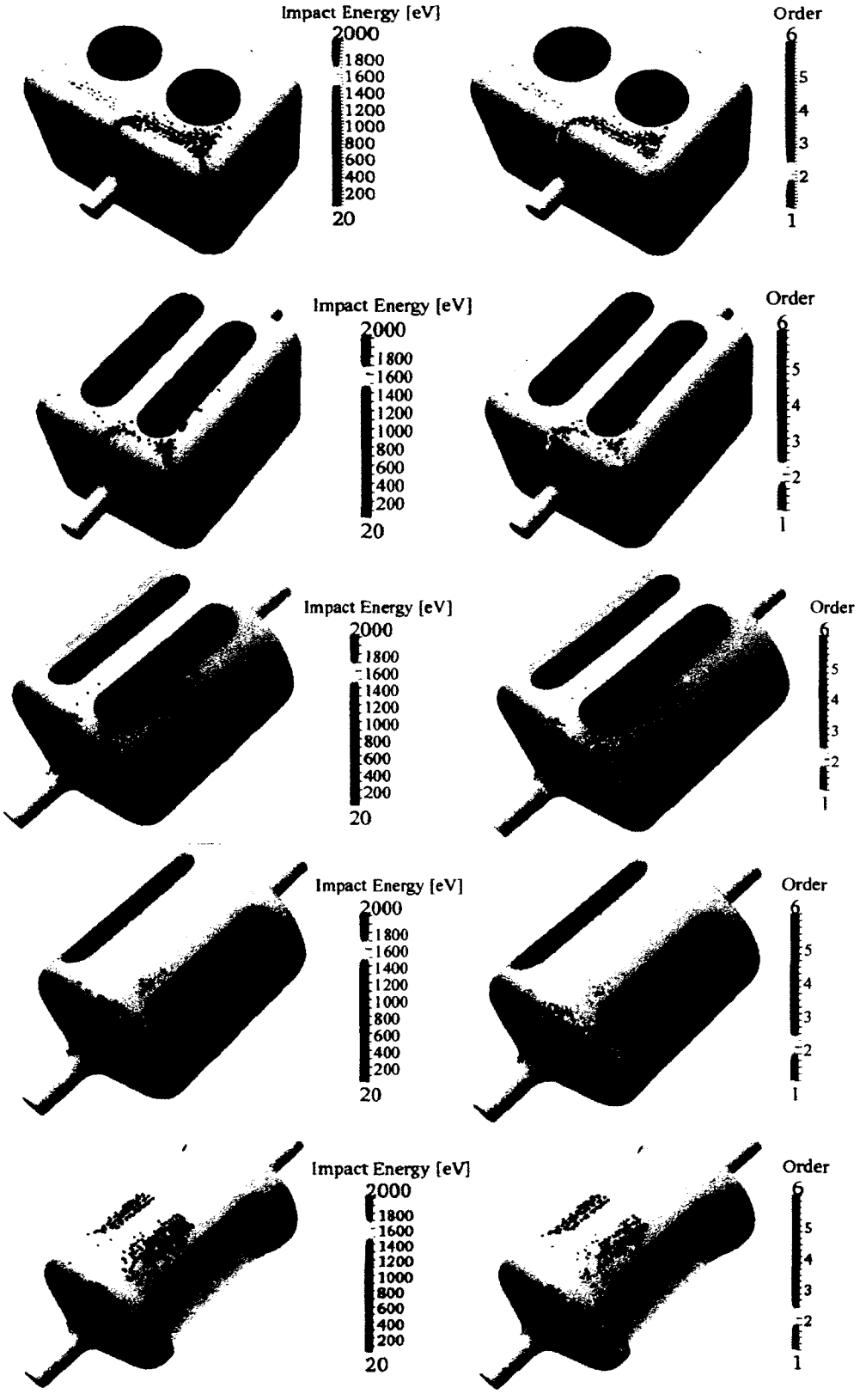

FIG. 110. Position of the resonant particles with corresponding impact energy (left) and multipacting order (right) for Designs (A), (B), (C), (D) and (E).

Fig. 111. The few resonant particles at very high transverse voltages exist at the cavity edges with very low impact energies that are not adequate to generate any secondary electrons. Therefore, no significant multipacting levels exist in the cavity at high transverse voltages. Following the data obtained through simulation, it can be seen that the 499 MHz cavity can be operated multipacting free at the design requirement of 3.78 MV. The multipacting barriers observed at low energies will need to be processed and the cavity conditioned to eliminate any multipacting levels.

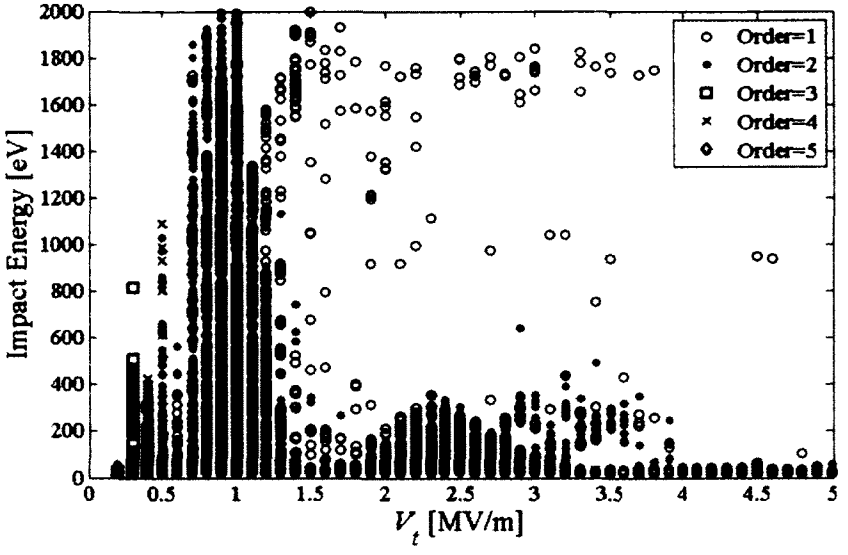

FIG. 111. Electron impact energy in the 499 MHz rf-dipole cavity with varying transverse voltage.

The impact energies of the resonant particles in the high magnetic field region are below 200 eV as shown in Fig. 113, where at the end plates the resonant particle impact energies rise as higher as 1500 eV. The resonant particles with the maximum impact energy exist the input power coupler port. Except in few resonant particles most of the resonant particles are of order one or two.

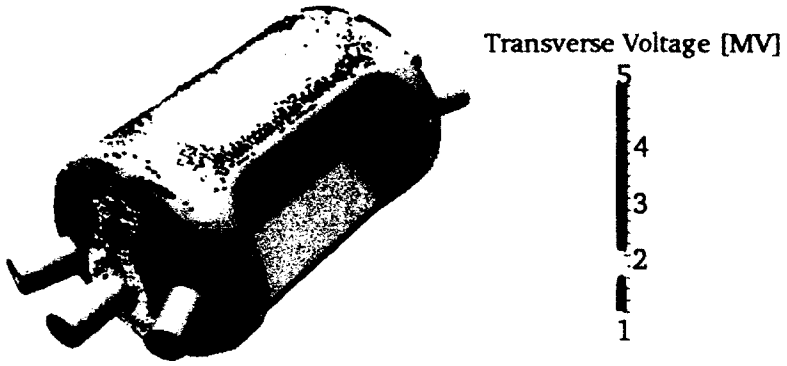

FIG. 112. Position of the resonant particles in the 499 MHz rf-dipole cavity with varying transverse voltage.

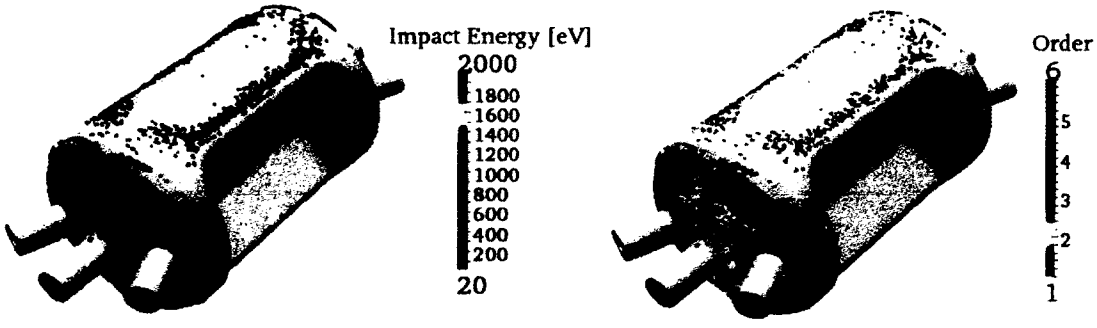

FIG. 113. Position of the resonant particles on the rf-dipole cavity with corresponding impact energy (left) and multipacting order (right).

7.4 MULTIPACTING IN 400 MHZ DEFLECTING CAVITY

Similar analysis was performed to determine the multipacting levels of the 400 MHz crabbing cavity. Figure 114 shows two multipacting barriers below 2.5 MV. Most of the order 1 multipacting levels at higher transverse voltages disappear at operation with higher rf-cycles. Resonant particles above 2.5 MV exist at the input coupler. As shown in Fig. 116 the resonant particles with the critical impact energies lie primarily on the end plates of the rf-dipole cavity where the multipacting is of order 1 [100].

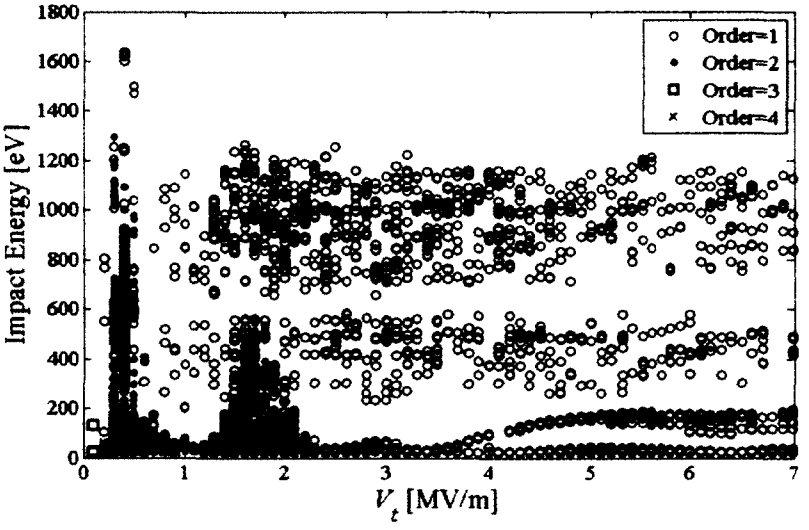

FIG. 114. Electron impact energy in the 400 MHz rf-dipole cavity with varying transverse voltage.

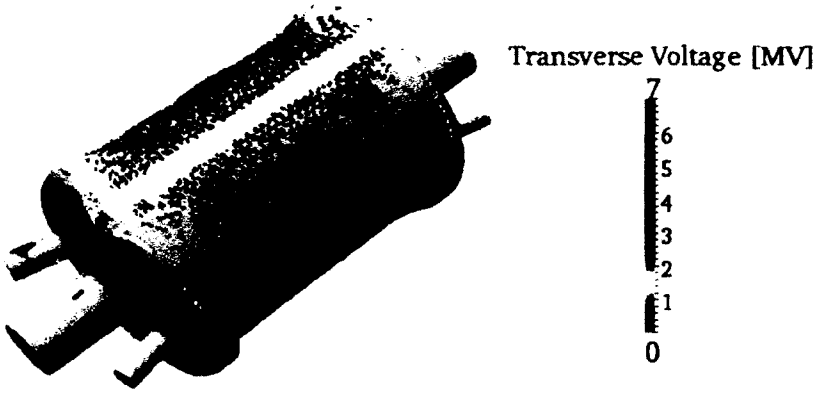

FIG. 115. Position of the resonant particles in the 400 MHz rf-dipole cavity with varying transverse voltage.

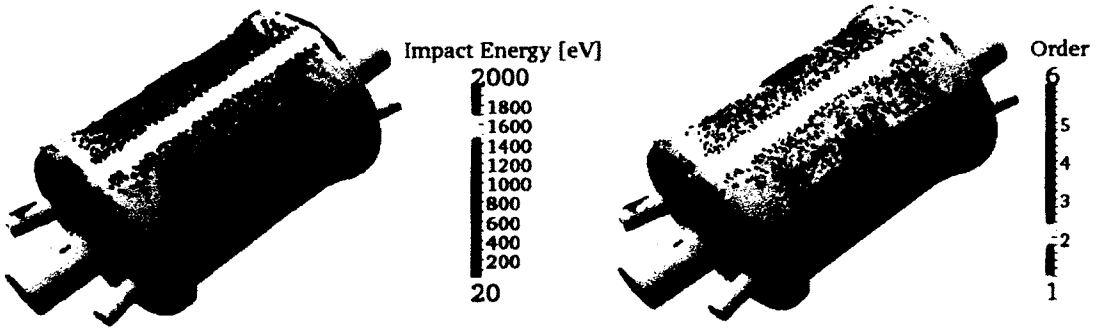

FIG. 116. Position of the resonant particles on the rf-dipole cavity with corresponding impact energy (left) and multipacting order (right).

CHAPTER 8

FABRICATION

A variety of manufacturing methods such as machining, deep-drawing, hydroforming have been used in fabricating superconducting rf cavities [101]. Niobium is the chosen material due to the high critical temperature. It also has good metallurgical properties that allow the use of standard fabrication methods. The rf-dipole designs of operating frequencies 499 MHz and 400 MHz were fabricated with niobium sheets and ingots using machining. The 499 MHz deflecting cavity was fabricated at the Jefferson Lab [102] and the 400 MHz rf-dipole cavity was manufactured by and as part of a collaboration with Niowave Inc. [103]. The two cavities were fabricated using high purity niobium sheets with high RRR [104]. The detailed procedure followed in fabrication of the two cavities are described here.

8.1 ROOM TEMPERATURE DESIGN

A superconducting rf cavity experiences several alterations in the cavity geometry during the transition from room temperature cavity to the cavity operating operating at cryogenic temperatures. These transitions change the operating frequency in which it is designed to be operated at, and therefore need to be taken into account at the point of cavity fabrication. The alterations occur during cavity processing where material is removed from the cavity inner wall leading to an increase in the cavity volume. An average a layer of 150 μm is removed from the cavity inner wall in order to remove the damaged layer.

Another key effect is the thermal shrinkage experienced by the cavity when cooled down to cryogenic temperatures. The design frequency of the room temperature cavity is determined considering all these effects. The thermal shrinkage of niobium has a linear dependence at higher temperatures and constant below $\sim$ 10 K [105]. The linear thermal expansion coefficient ($\alpha_L = \frac{1}{L}\frac{dL}{dT}$) of niobium at room temperature is 0.7×10^{-5} per K and zero at cryogenic temperatures, which relates to the change in length from cryogenic temperature (CT) to room temperature (RT) as following

$$\frac{L_{RT} - L_{CT}}{L_{RT}} = 143 \times 10^{-5}\,. \tag{152}$$

The inverse proportionality of length to cavity frequency gives the simplified relation for change in frequency of

$$f_{CT} = \frac{1}{1 - 143 \times 10^{-5}} f_{RT} \,. \tag{153}$$

that reduces the size of the cavity and increases the frequency when cooled down.

The estimated room temperature frequency was determined for the two rf-dipole cavities as shown in Table 23 considering the above mentioned affects and further taking into account the fact the measurements are taken in air. The measurements taken in air as opposed to vacuum shows a frequency shift corresponding to the dielectric constant of air 1.00059 that gives a lower frequency compared to that measured in vacuum.

TABLE 23. Frequency adjustment of the room temperature rf-dipole cavities.

	499 MHz Cavity		400 MHz Cavity	
	Δf [kHz]	f [kHz]	Δf [kHz]	f [kHz]
Operating cavity at cryo temperature		499000.0000		400000.0000
Cavity at room temperature in vacuum and after surface treatment	-713.546	498286.4538	-571.981	399428.0191
Cavity at room temperature in air after surface treatment	-146.929	498139.5243	-117.779	399310.2399
Welded cavity in air	288.087	498427.6113	64.175	399374.4148

The target room temperature frequency is lower than the operating frequency. The cool down process of the cavities increases the frequency by a factor 1.001432 and evacuating cavity into vacuum also increases the frequency by a factor of 1.000295. The effect of surface treatment on the cavities shows a wide variation between the two rf-dipole cavities. The distinction can be accounted for removal of material from the magnetic field region to that in the electric field region. The material removed in magnetic field region reduces the frequency where the latter increases the frequency. The frequency deviation produced by the material removed at the larger electric field region in the 400 MHz cavity almost cancels the deviation due to the material removed in the magnetic field region. The frequency shift due to material

removed in the magnetic field region results with a higher deviation that reduces the cavity frequency after surface treatment. In the 499 MHz cavity the smaller electric field region produces a higher frequency deviation contributed by the magnetic field region, hence the 288 kHz frequency drop.

8.2 FABRICATION OF 499 MHZ DEFLECTING CAVITY

The 499 MHz cavity was fabricated with the combined process of stamped parts using niobium sheets with RRR > 300 and machined parts using ingot with RRR > 250 [106]. Figure 117 shows the assembly of the parts where the center shell and end plates that were formed by stamping. The shoulder blocks were machined using niobium ingots to incorporate larger thickness to reduce the stresses and also due to complexity of the geometry [107]. The fabrication process of the 499 MHz cavity is shown in Fig. 118.

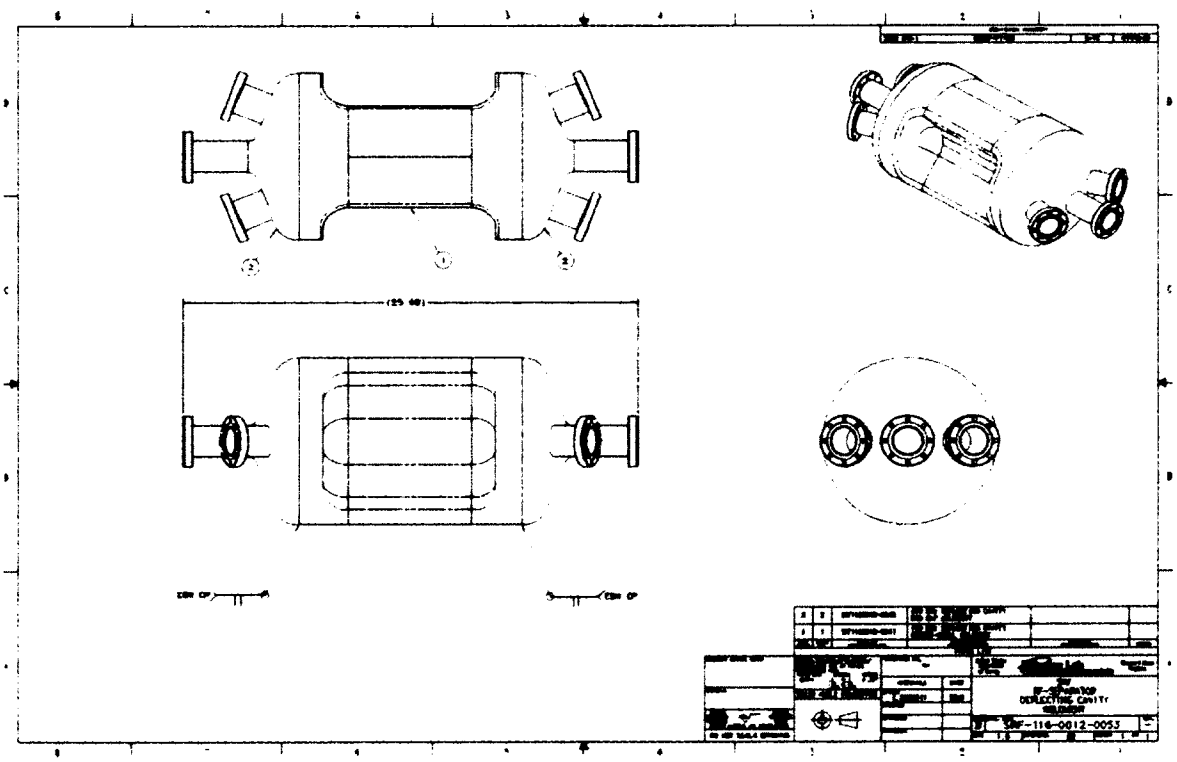

FIG. 117. Fabrication drawing of the 499 MHz rf-dipole cavity.

The beam ports and coupler ports of 40 mm diameter were brazed with NbTi flanges, that use Al-Mg diamond shaped gaskets to achieve vacuum. The end plates

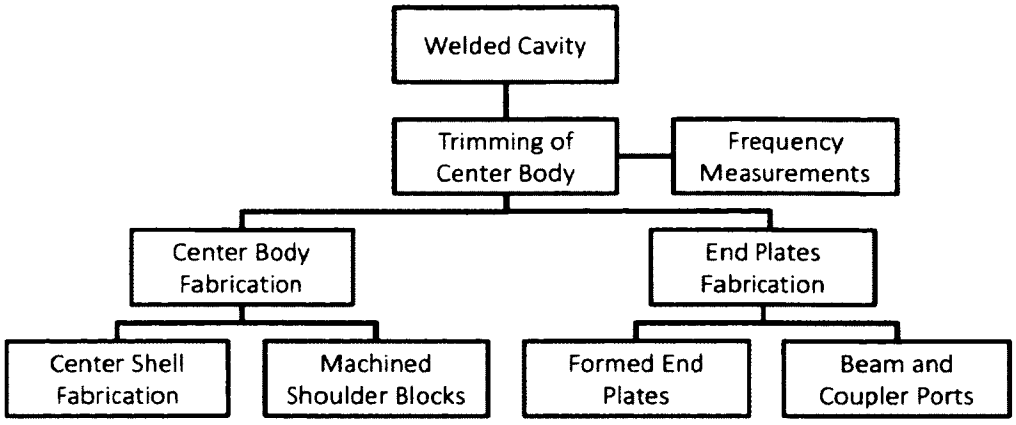

FIG. 118. Fabrication sequence of the 499 MHz rf-dipole cavity.

were stamped with niobium sheets of 3 mm thickness, with a set of forming dies, then another set of machining dies were used to trim the end caps to the required dimensions (Fig. 119). Figure 120 show the stamping of the end plates by pressing them in 150 ton press. The coupler ports opening were cut on the end plates and the beam and coupler ports were welded first inside and then outside with an electron beam welding machine [108].

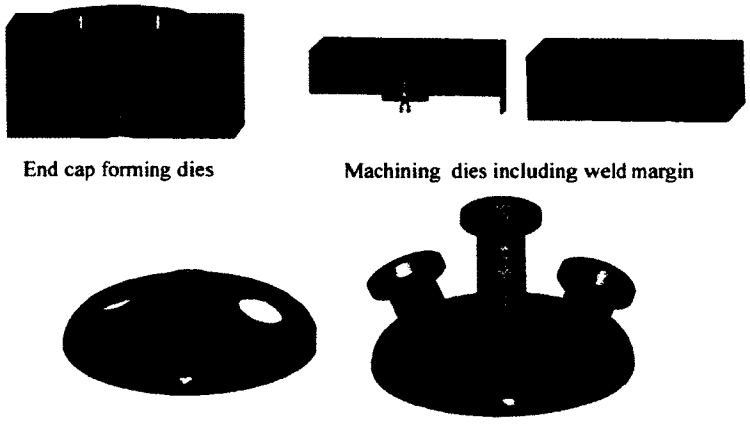

FIG. 119. Set of dies used in fabricating end plates of the 499 MHz cavity.

The center shell was formed following a similar procedure in two parts using a set of forming dies as shown in Fig. 121. The formed parts were trimmed in a computer numerical control (CNC) machine including the welding seams and additional length for frequency adjustment. A set of copper parts were made initially to verify the

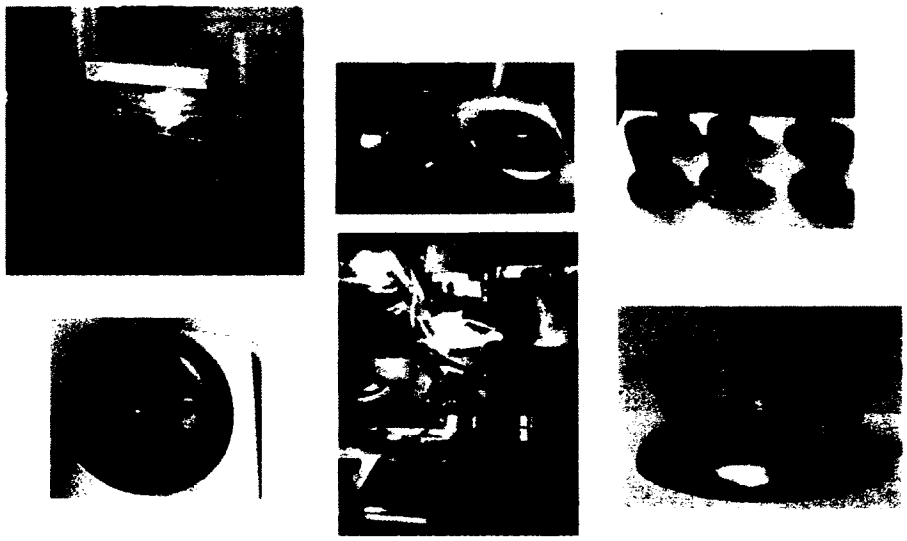

FIG. 120. Formed and welded end plates of the 499 MHz cavity.

stamping dies and the CNC machine cutting profile accuracy.

The room temperature cavity frequency was correctly achieved by measuring the frequency before the final weld of the parts cavity frequency with parts pressed together. In the rf-dipole cavity the frequency is adjusted by trimming the center shell. The estimated sensitivity of frequency to the center shell length is $\mathrm{d}f/\mathrm{d}z = -248$ kHz/mm, where trimming the center shell increases the cavity frequency.

The shoulder blocks shown in Fig. 122 were the transition part connecting the center shell and end plates. The parts were machined in a CNC machine with the 3-D model directly fed to the machine. The machining process supports the capability of part machined with varying thickness as opposed to stamping.

Figure 123 shows the parts pressed together before electron beam welding of the cavity. Several iterations of frequency measurements and center shell trimming were performed to achieve the target design frequency at room temperature.

The center shell exhibited spring back after the welding of the two halves as shown in top left image in Fig. 124, which did not form a smooth transition between the surfaces when placed with the shoulder blocks. This complicated the welding process where it is essential to have parts matched with precision to avoid any sharp steps after the welding. A set of collapsible fixtures was manufactured as shown in Fig. 124 that constraints the center shell to its original shape and an additional

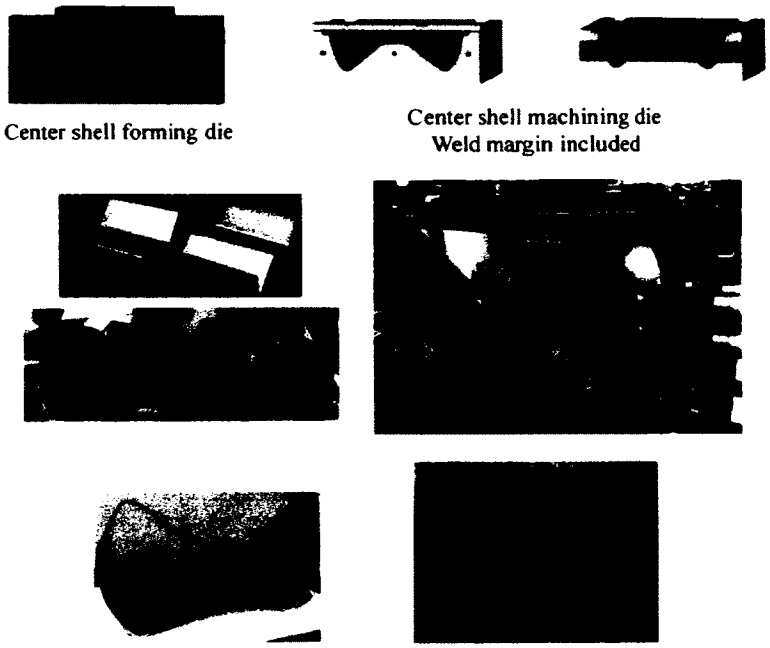

FIG. 121. Formed and welded center shell of the 499 MHz cavity.

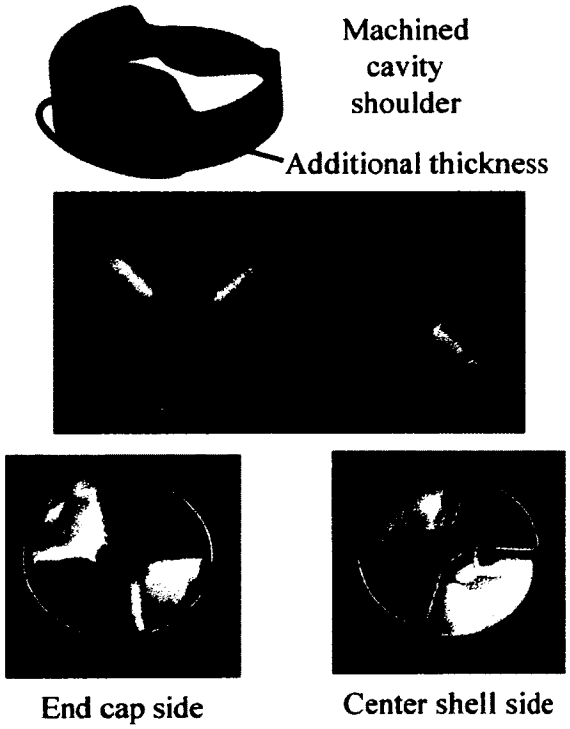

FIG. 122. Machined shoulder block of the 499 MHz cavity.

FIG. 123. Parts assembly of the 499 MHz cavity.

support to hold the center shell to the shoulder block [102]. The clamped parts were tack-welded initially and the fixtures were removed before the final welding where it is first welded from inside and with another weld from outside at the electron beam welding machine.

The welded parts experienced a slight dislocation during the weld assembly on one side of the center body and introduced a small step that was visible during the examination after welding. The inner surface was ground using a tool with abrasive material in order to smoothen the surface. All the parts were aligned with all the ports in the horizontal plane in the final assembly as shown in Fig. 125. The parts were welded together from outside with full penetration by leveling all the ports in the horizontal plane [102].

8.3 FABRICATION OF 400 MHZ CRABBING CAVITY

The 400 MHz rf-dipole cavity was designed and fabricated with four identical side ports, as shown in Fig. 95. The cavity was fabricated in four parts including the two end plates and the two halves of the center shell, using 3 mm thick Nb sheets with a residual resistivity ratio (RRR) of 355-405. The diameter of the beam ports of the cavity was 84 mm, which is an LHC requirement [69], and the diameter of the four side ports was selected to be 36 mm.

The end plates were deep drawn using a set of dies and niobium sheets and welded with the beam ports as shown in Fig. 127. The beam ports and side ports were formed by rolling niobium sheets and brazed with stainless steel conflat flanges. The beam port flanges were 6″ in diameter and the coupler port flanges were of $2^3/_4$″. The center shell was formed with two pairs as shown in Fig. 128 with a single sheet

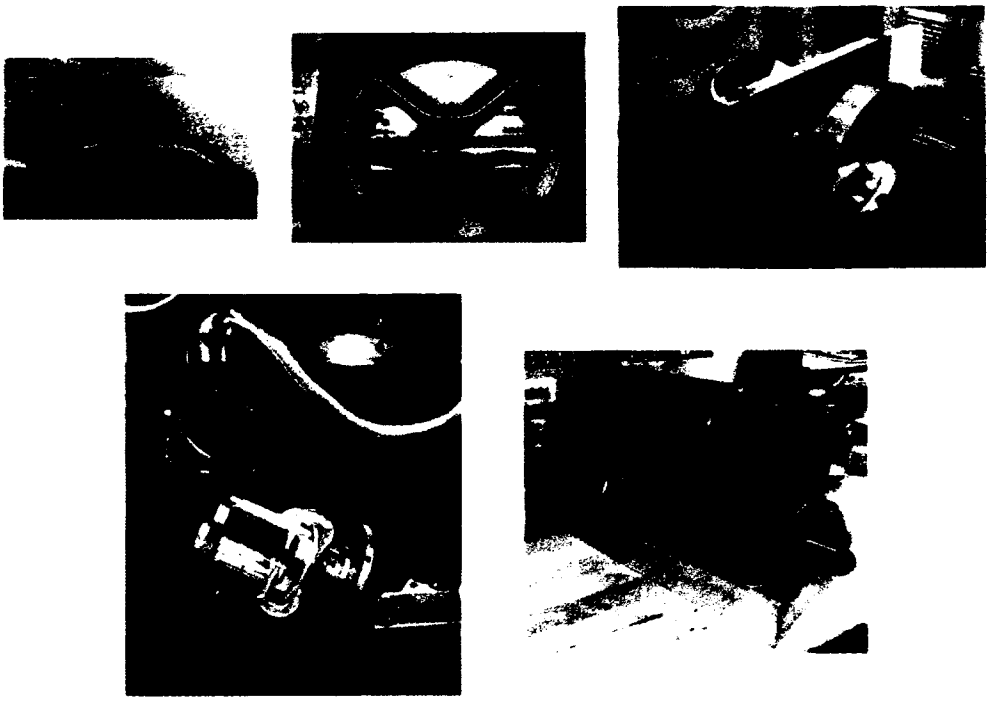

FIG. 124. Welding process of the center shell and shoulder blocks of the 499 MHz cavity.

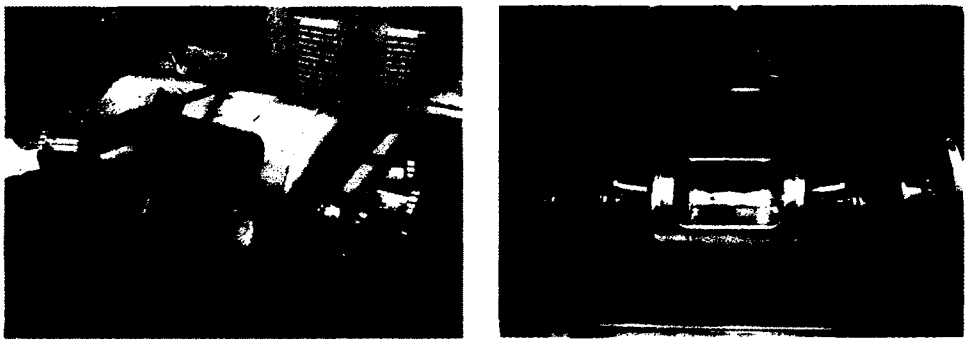

FIG. 125. Final assembly of parts of the 499 MHz cavity.

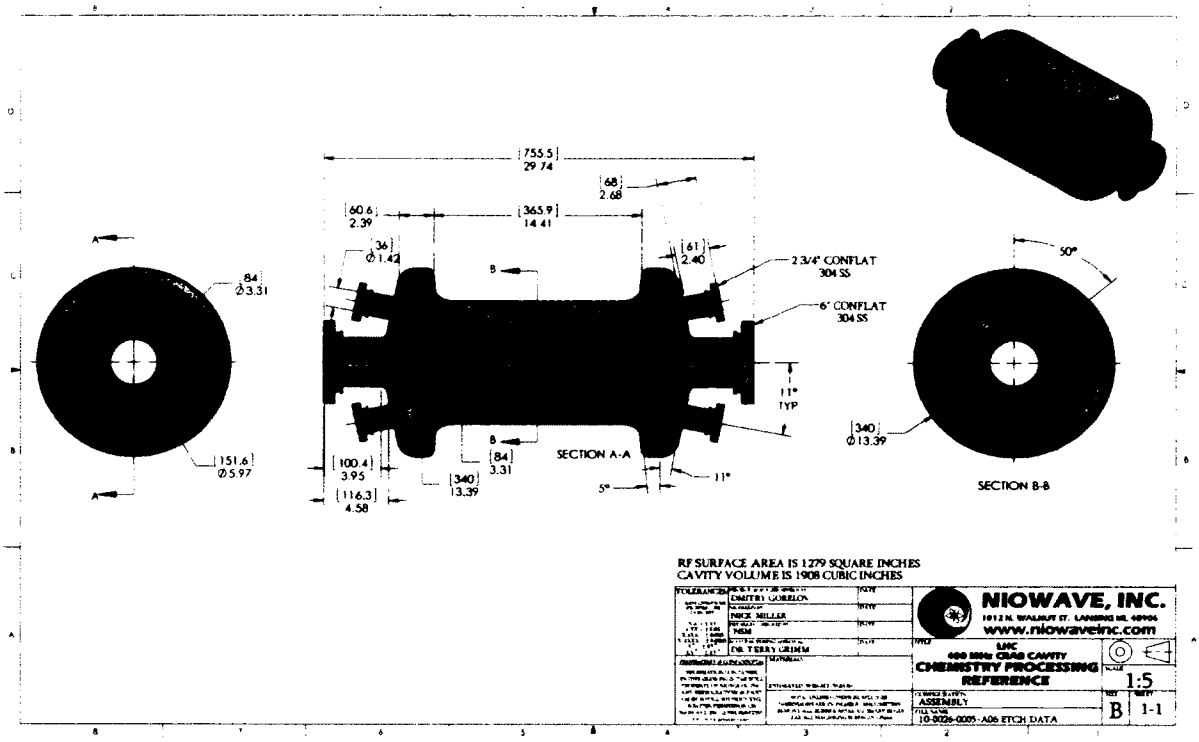

FIG. 126. Fabrication drawing of the 400 MHz rf-dipole cavity.

of niobium and electron beam welded [103]. The center shell was trimmed to obtain the design frequency at room temperature and then electron beam welded with the end plates.

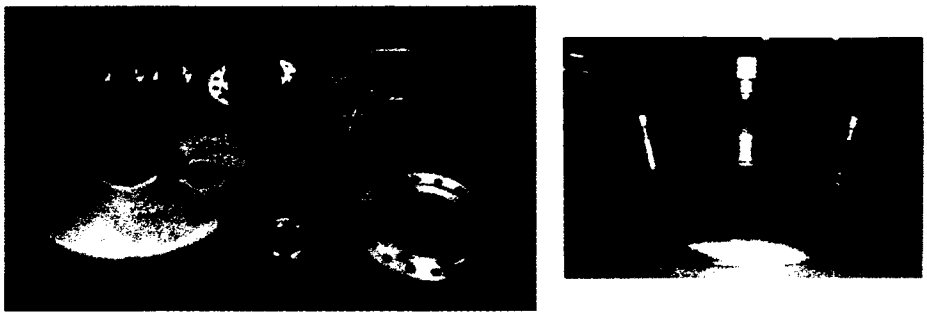

FIG. 127. Fabrication of end plates of the 400 MHz rf-dipole cavity.

FIG. 128. Fabrication of center shell of the 400 MHz rf-dipole cavity.

8.4 SURFACE INSPECTION

Following the final welding the cavities were evacuated and tested for any possible leaks. The final welded cavities are shown in Fig. 129.

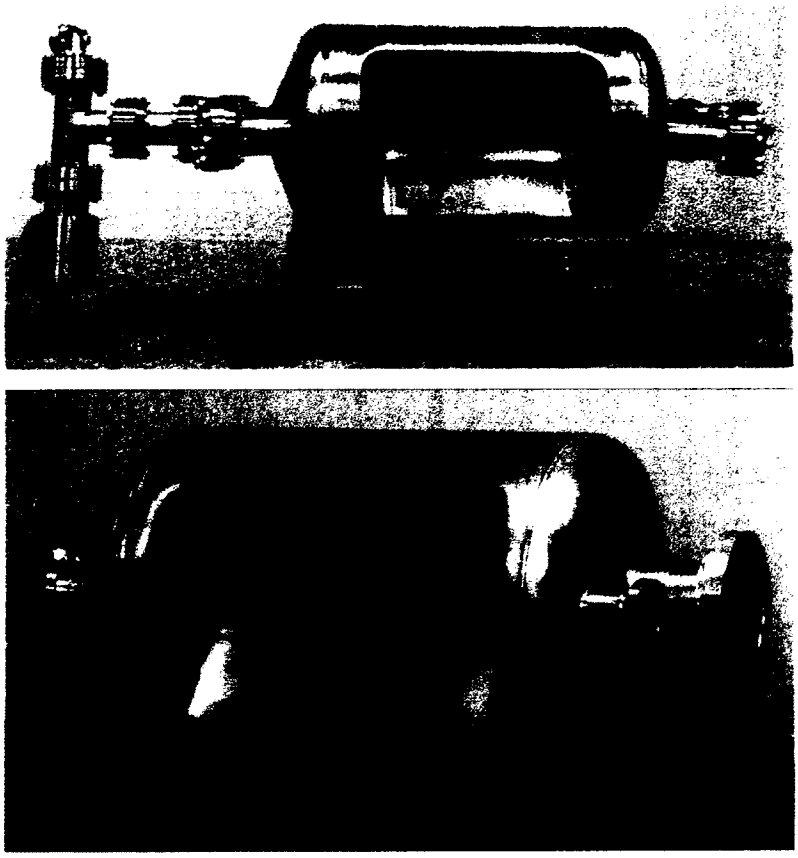

FIG. 129. Fabricated 499 MHz (top) and 400 MHz (bottom) rf-dipole cavities.

In the 499 MHz cavity the welding seams were scanned using a borescope. All the welding seams in the 400 MHz cavity were also scanned using the optical inspection system at Jefferson Lab [109]. No defects or irregularities were found in all the welding seams except on the welding seams at two beam pipes as shown in Fig. 130. The welding seams were smoothened by griding the uneven seams.

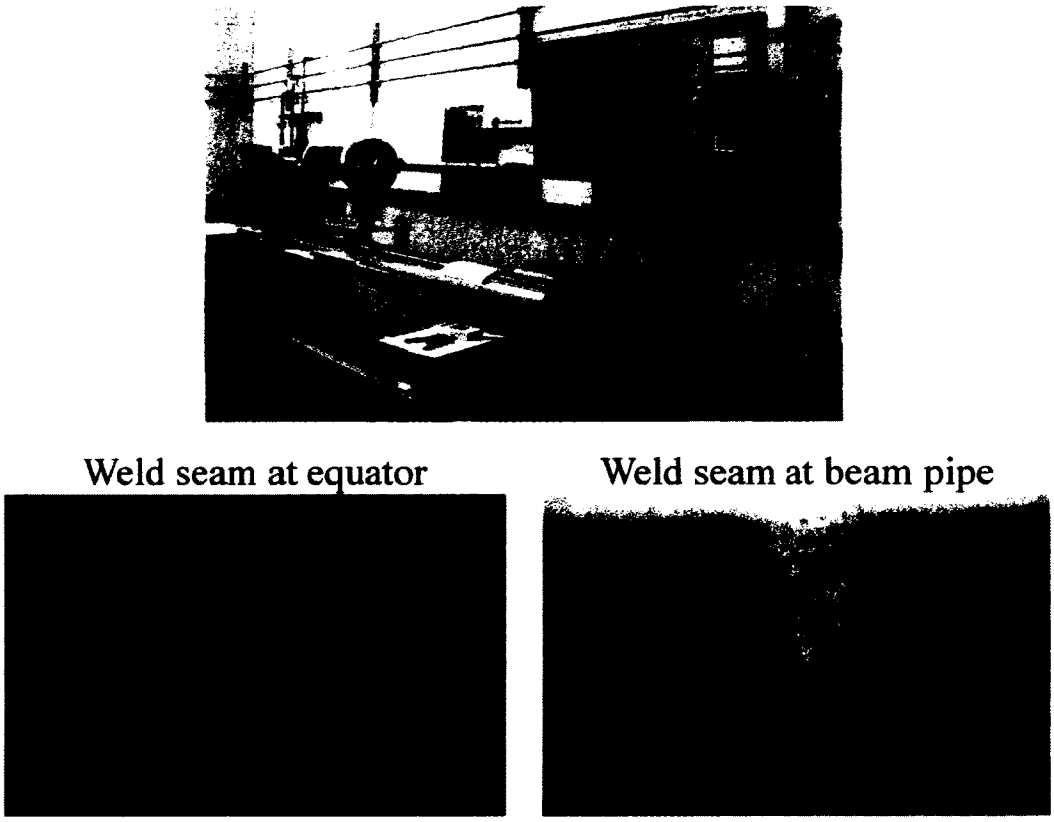

FIG. 130. Optical inspection system (top) and one of the welding seam at equator and beam pipe of the 400 MHz cavity.

8.5 BEAD PULL MEASUREMENTS

The rf-dipole fundamental mode includes both on-axis transverse electric and magnetic fields. A bead-pull method [110] was used to measure and evaluate the on-axis field components. The shift in resonant frequency due to field perturbation was measured using a teflon spherical bead (dielectric bead) with a relative dielectric constant (ε_r) of 2.05 and an aluminum spherical bead (metallic bead). The dielectric bead measures only the on-axis electric field. Since the transverse electric field component (E_x) is the only on-axis electric field component this method measures the transverse electric field contribution to the net deflection. The metallic bead measures both on-axis electric and magnetic field components; in the case of the rf-dipole cavity E_x and H_y components. The perturbed fields for the dielectric and metallic beads were determined by

$$\frac{\Delta f}{f} = -\frac{\pi r^3}{U}\left[\varepsilon_0 \frac{\varepsilon_r - 1}{\varepsilon_r + 2} E_0^2\right], \tag{154}$$

$$\frac{\Delta f}{f} = -\frac{\pi r^3}{U}\left[\varepsilon_0 E_0^2 - \frac{1}{2}\mu_0 H_0^2\right]. \tag{155}$$

The field perturbation measurements in the 499 MHz cavity were obtained from the dielectric and metallic beads of diameters of 7.94 mm. The measurements were compared with the simulations from CST Microwave Studio are shown in Fig. 131. The contribution to the deflecting voltage from the on-axis magnetic field (H_y) is very small compared to that from the electric field (E_x). The contribution from the on-axis magnetic field is the small perturbation at the entrance and exit of the cavity as seen in the measurements from the metallic bead shown in Fig. 132.

The measurements show a slight deviation from the field data obtained from simulation on one side of the cavity, which could be due to the step observed during the fabrication. The change in field profile drops the transverse voltage by 2% determined considering the transverse electric field since the transverse effect due to magnetic field is very small.

The measurements of the 400 MHz cavity are in complete agreement with the simulation data as shown in Fig. 132. obtained with dielectric and metallic beads of diameters of 6.34 mm and 7.12 mm respectively. Similarly the contribution from the on-axis magnetic field is very small compared to that from the on-axis electric field.

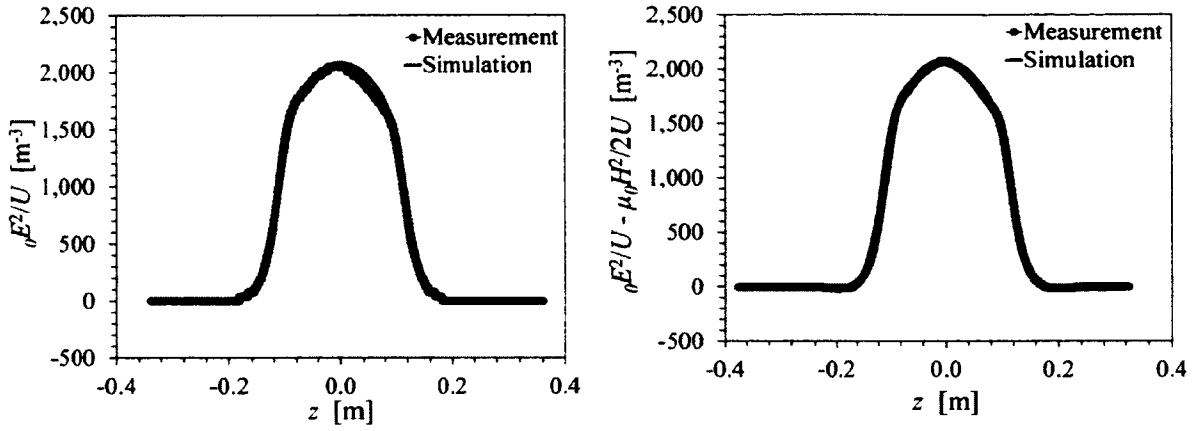

FIG. 131. Bead pull measurements of the 499 MHz rf-dipole cavity from the dielectric (left) and metallic (right) spherical beads.

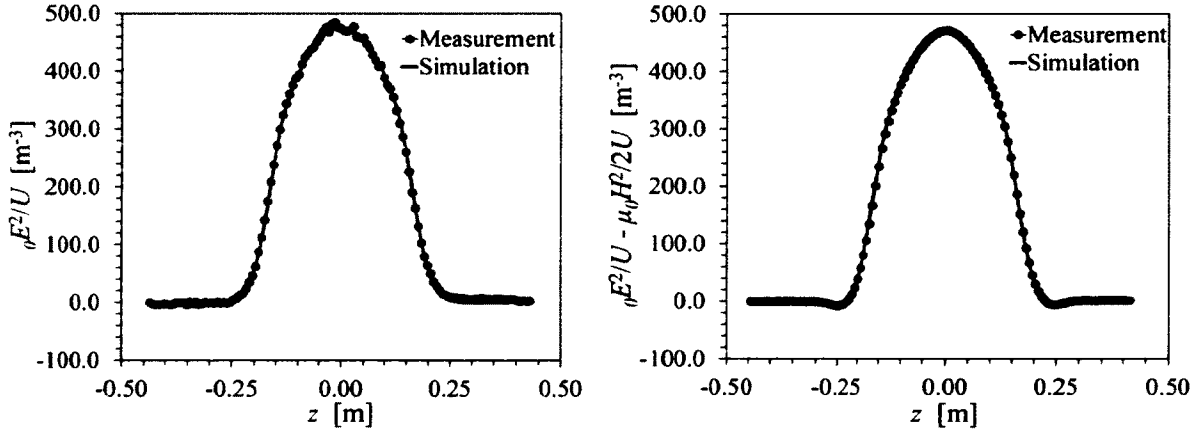

FIG. 132. Bead pull measurements of the 400 MHz rf-dipole cavity from the dielectric (left) and metallic (right) spherical beads.

CHAPTER 9

CAVITY PROCESSING AND ASSEMBLY

The performance a superconducting rf cavity is directly related to the condition of the cavity surface. It is essential that the inner surface be residue-free and smooth. The key idea of surface processing is to obtain as close to an ideal niobium surface as possible, where the surface resistance is at its minimum, reducing the power dissipation that would give a higher unloaded quality factor (Q_0). Also a smooth inner surface without any pits of protrusions is necessary to avoid any occurrence of field emission or thermal breakdown in order to obtain high gradients.

Extensive research has been carried over the years in achieving a smooth and clean inner surfaces, especially applicable to superconducting cavities. Various advanced techniques have been proven effective in cavity processing including diagnostic methods to improve the quality of the surface of superconducting cavities. The key processing steps of the procedures primarily focus on chemical processing, heat treatment, and high pressure rinsing. Furthermore, processing techniques such as He processing, low temperature baking improve or overcome limitations in achieving high performance.

9.1 CHEMICAL PROCESSING TECHNIQUES

The best performance of superconducting cavities requires the cavity inner surface to be close to an ideal Nb surface, with no imperfections, most importantly in the thin layer of penetration depth (for Nb <100 nm) of the rf fields. The cavity surface may consist of impurities introduced during the process of Nb sheet production and oxidation or residual deposits. The process of handling due to forming and fabrication may also introduces damage to the cavity leading to non-uniform inner surface, with pits and protrusions. The chemical processing method etches the damaged layer from the cavity surface through a series of chemical reactions. Two techniques that are primarily used are the buffered chemical polishing (BCP) and electro polishing (EP). In addition a new technique named centrifugal barrel polishing uses the tumbling process in etching the cavity surface, and is capable of achieving a mirror-like finish.

9.1.1 BUFFERED CHEMICAL POLISHING (BCP)

Buffered chemical polishing is the most commonly used process for surface treatment.

$$6Nb + 10HNO_3 \rightarrow 3Nb_2O_5 + 10NO + 5H_2O \quad (156)$$

$$Nb_2O_5 + 10HF \rightarrow 2NbF_5 + 5H_2O \quad (157)$$

The hydrofluoric acid is the key component that removes the Nb in the form of niobium pentoxide (Nb_2O_5), formed during the oxidation process with the reaction of nitric acid and the Nb material. The above process is highly exothermic; therefore phosphoric acid is added to the solution in order to reduce the interaction rate. For rf cavities, the typical etching rate is 1-2 μm/min with an acid mixture of HF:HNO_3:H_3PO_4 at a ratio of 1:1:2 and for components that requires a faster etching rate follows a ratio of 1:1:1 at an etching rate of 5-7 μm/min.

In the BCP process the heat generated increases the etching rate. In heavy bulk BCP polishing the process is done in an enclosed cabinet where the acid mixture is cooled externally and circulated through the cavity. The temperature of the acid mixture in the sump is controlled and maintained around 8 °C. The etching rate drops as Nb gets dissolved in the acid mixture and is replaced with a new acid mixture. During the table-top polishing the process is carried out in a fume hood, with the cavity submerged on a water bath and the acid mixture is stirred manually. In this the method the typical etching rate is about 1-2 μm/min at an temperature of 20 °C. With the completion of etching it is essential to thoroughly rinse the cavity to remove the acid film remaining on the surface due to the high viscosity of the mixture that prevents the hydrogen absorption in the niobium.

9.1.2 ELECTRO POLISHING (EP)

The process of electropolishing also uses an acid mixture consisting of sulfuric acid (H_2SO_4) and hydrofluoric acid (HF) with 95% and 48% concentrations, mixed 9:1 ratio. In addition the process is enhanced by applying a constant positive potential to the cavity surface. The cavity surface is the anode and an aluminum rod is inserted which is the cathode. The cavity assembled in a horizontal set up is half-filled with the cavity mixture and rotated at about 1 rpm, during the etching process. The

chemical reaction is following:

$$2Nb + 5SO_4^{--} + 5H_2O \rightarrow Nb_2O_5 + 10H^+10e^- \quad (158)$$

$$Nb_2O_5 + 10HF \rightarrow 2NbF_5 + 5H_2O \quad (159)$$

The surfaces closer to the cathode are etched more than the surfaces that are further from the cathode. Electropolishing delivers smother surface finish compared to that from BCP processing. The typical etching rate of electro polishing is 0.1-0.2 μm/min, at current densities of 15-20 mA/cm^2. The circulated acid mixture is kept at temperature of 20 ^{o}C.

9.2 BULK CHEMICAL ETCHING

The rf-dipole cavities were processed at Jefferson Lab in preparation for the rf testing following the standard cavity processing procedure [111]. The cavities were chemically etched using the bulk BCP process in order to remove the typical damaged layer of 120-150 μm, in a closed cabinet as shown in Fig. 133. The acid mixture was inserted from the bottom three ports and removed from the top three ports of the cavity, mounted vertically, using a manifold and circulated through the cavity in one direction.

The 499 MHz deflecting cavity was processed for the first time at an etching rate of 2.06 μm/min, with the BCP acid mixture at an controlled temperature of 8 ^{o}C, circulated at a rate of 4 gpm. The cavity was polished in intervals of 15 minutes and repeated 8 times where the cavity was overturned each interval to obtain a uniform removal, finally followed by a rinse for 5 minutes using DI water. The geometry of the rf-dipole cavity does not allow a uniform acid flow in the cavity, therefore leads to a non-uniform removal on the inner surface. The average removal during the first BCP process is shown in Fig. 134, measured with an ultrasonic probe at different locations on the cavity. The measurements were obtained from the Panametrics 25DL-Plus ultrasonic precision thickness gauge with a resolution of 1 μm [112]. From repeated measurements it is estimated that the amounts removed are accurate to ± 10 μm. Due to the cavity geometry, the acid has a slower flow rate at top and bottom cylindrical parts where the average removal is higher compared to that at the center of the cavity. The average removal of the 499 MHz cavity is 108 μm.

The BCP process was repeated after the first rf measurements due to hard quench

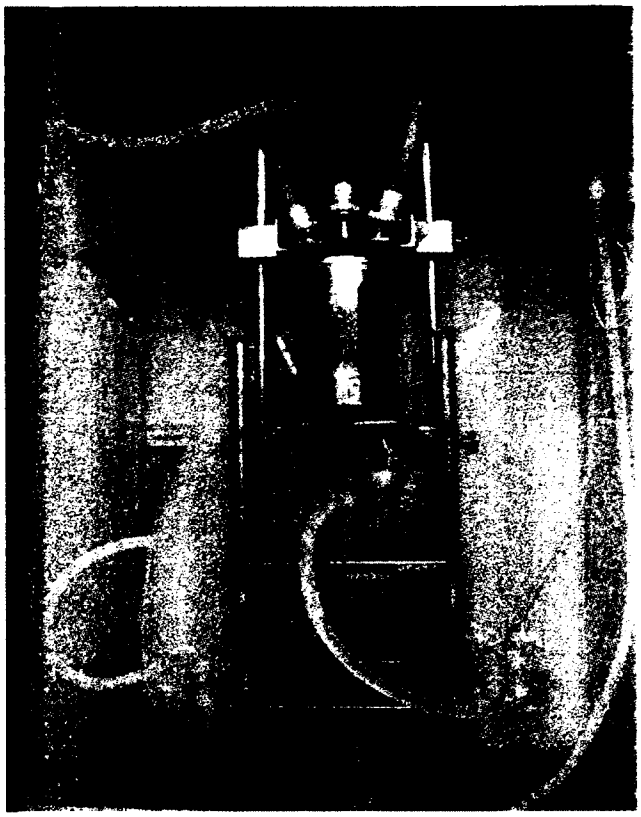

FIG. 133. 499 MHz cavity mounted in a closed cabinet for BCP process.

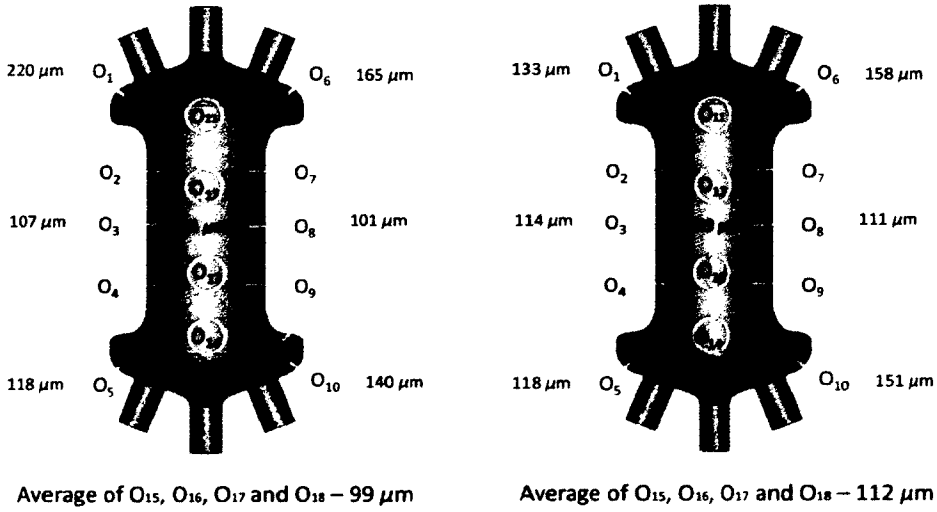

FIG. 134. Average surface removal measured with an ultrasonic probe from bulk BCP process.

observed at lower operating fields than expected. The second polishing time was increased to 70 minute intervals and processed twice with cavity overturned in between, with similar operating conditions as previous. The measured removal rate increased as shown in Figure 134 with an average removal of 198 μm.

The 400 MHz crabbing cavity was processed at a low etching rate of 1.8 μm/min due to a contamination in the acid mixture by glycol. The cavity was processed by a temperature-controlled acid mixture at 8 °C in order to minimize the absorption of hydrogen into the surface in a closed vertical cabinet for 17 minutes for a nominal removal of 30 μm. For each iteration of 30 μm removal, the cavity was overturned to obtain a uniform removal and the process was repeated four times aiming a total nominal removal of 120 μm. Figure 135 shows the average removal measured using the Panametrics 25DL-Plus ultrasonic precision thickness gage. The average removal was 81 μm; however at the center of the cavity the removal was an average of 67 μm while at the top and bottom of the cavity the average removal was 95 μm.

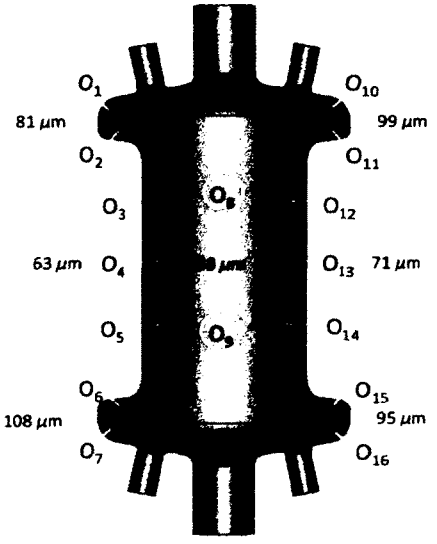

FIG. 135. Average surface removal measured with an ultrasonic probe from bulk BCP process.

9.3 ULTRASONIC RINSING

The ultrasonic rinsing process is an important step through out the cavity treatment procedure. This rinsing degreases the cavity by immersing the cavity completely

in a solution consisting of ultra-pure water and soap detergent, and ultrasonically agitated during the process for about 30 minutes. The soap detergent named Micro90 is a concentrated cleaning solution that can remove soils including oil, grease, wax, tar, flux, particulates, hard water stains, and biological debris. The cavity is ultrasonically rinsed after every chemical etching process and specifically before the heat treatment process to prevent any contaminants getting absorbed into the cavity material at high temperatures in a solution of ultra-pure water and soapy detergent for about 30 min. After this process the cavity is rinsed thoroughly with ultra-pure water. This treatment is applied also to all the ancillary components and hardware that are assembled on the cavity, such as flanges, antennas, nuts, bolts and washers as shown in Fig. 136.

FIG. 136. Ancillary components required in cavity assembly.

9.4 HEAT TREATMENT

The cavities were heat-treated in a high-vacuum furnace as shown in Fig. 137, following the bulk chemistry at 600 °C for a duration of 10 hours for degassing of the hydrogen that was absorbed into the surface during the bulk BCP process [113]. Figures 138 and 139 show the decrease of partial pressure of hydrogen and other elements during the heat treatment, measured using a residual gas analyzer (RGA). The heating process was initiated after the furnace reached a pressure of 10^{-6} torr. From experience a good level of degassing is achieved with a hydrogen partial pressure below 10^{-6} torr at the end of the process [114]. The levels of hydrogen removed during the second heat treatment is low compared to that removed during the first heat treatment.

FIG. 137. 499 MHz cavity in the high-vacuum furnace.

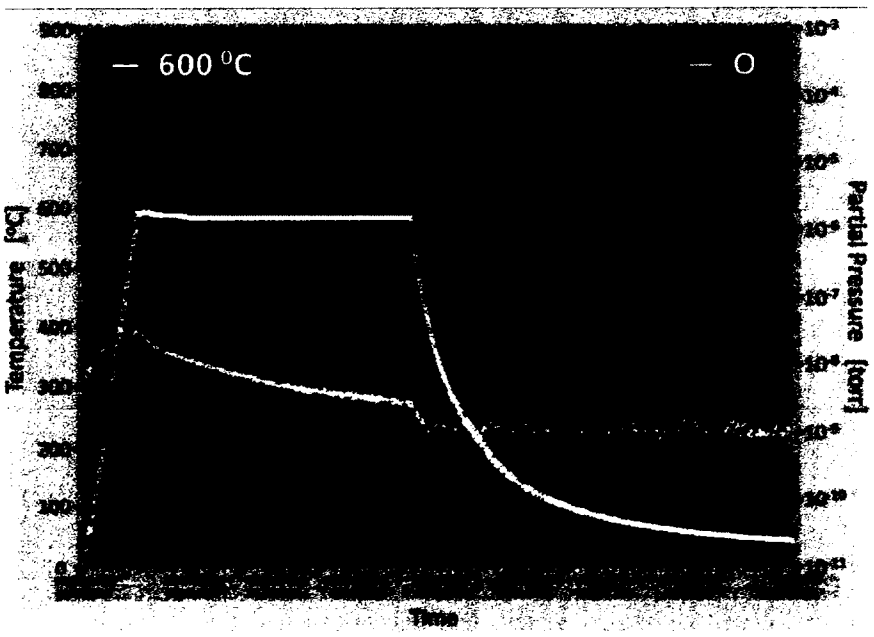

FIG. 138. Furnace temperature and hydrogen partial pressure level during high-vacuum heat treatment of the 499 MHz cavity .

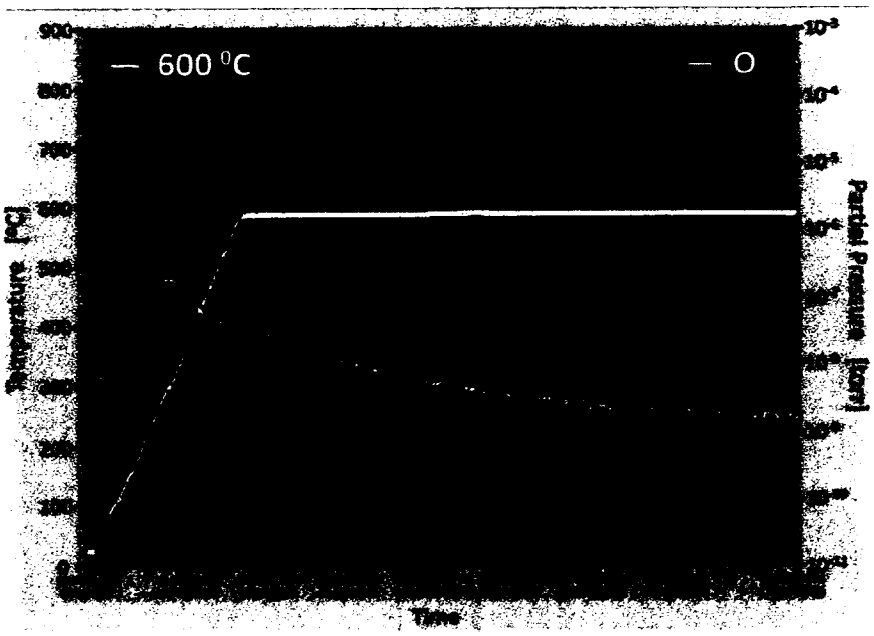

FIG. 139. Furnace temperature and hydrogen partial pressure level during high-vacuum heat treatment of the 400 MHz cavity.

9.5 LIGHT CHEMICAL ETCHING

The heat treatment may result with a cavity contaminated by the various elements that exist in the high-vacuum furnace and get deposited on the surface at high temperature. Therefore it is essential to clean the surfaces with a light chemical etching. The cavities were etched in a light BCP process to remove 10-20 μm to eliminate the contamination due to the high-temperature heat treatment. The 499 MHz was initially lightly etched with the measured average removal of 10 μm and 20 μm during the second etching.

The 400 MHz cavity was processed with an average removal of 10 μm. A second light chemical etching was carried out after the first rf measurements, in preparation for a second rf test in order to identify the cause of low Q described in Chapter 10. An average layer of 15 μm was removed during the second light BCP processing.

9.6 HIGH PRESSURE RINSING

After the light chemical etching prior to the cavity assembly, the interior of the cavity was thoroughly cleaned by a jet of ultra-pure water pressurized at 1250 psi. High pressure rinsing is used to remove any contaminants or particles on the cavity

surface, that would cause field emission limiting the cavity performance. This process is very important and therefore carried out in a clean room environment where the cavity remains until fully assembled.

The cavity was assembled vertically and water was sprayed using a nozzle attached at the top of a wand that moves up and down inside the cavity. The cavity was mounted on a leveled table and rotates in order to cleans all the surfaces. Therefore, the cavity needs to be perfectly aligned vertically in order to prevent scratching of the surface by the wand. The rinsing was done at a cavity rotation of 1 rpm with typical wand speed of 0.5 cm/min and flow rate of 15 l/min. The 499 MHz cavity was rinsed with a smaller nozzle due to the small beam aperture in iteration of 2 passes of 60 minutes each. The 400 MHz cavity was high-pressure rinsed in 3 passes of 75 minutes each with ultra pure water.

9.7 CAVITY ASSEMBLY

The cavity assembly is a vital process performed methodically in order to minimize particulates trapping inside the enclosed cavity. Hence it is carried out in class 10 clean room. The cavities were assembled with fixed input coupler at the bottom and pick-up probe at the top of the cavity as shown in Fig. 140, and mounted into a test stand for vertical testing. In sealing the ports, diamond shaped Al gaskets were used in the 499 MHz cavity, while Cu gaskets were used in the 400 MHz cavity, which had standard conflat flanges. The additional ports were blanked with stainless steel flanges. Both cavities were connected to the vacuum for evacuation through the bottom beam port connected through a vacuum valve and relief valves.

The assembled cavities were evacuated and the pressure was monitored with an residual gas analyzer (RGA). The level of water, helium, oxygen and other residual gasses were monitored during the evacuation process when the pressure level is below 3×10^{-6} mbar. All the port connections were scanned by spraying helium gas. The cavities were kept under vacuum constantly evacuating for duration of about three hours and considered leak-tight at a pressure level below 10^{-8} torr. The test stand with the leak-tight cavity was then attached onto a test stand as shown in Fig. 141.

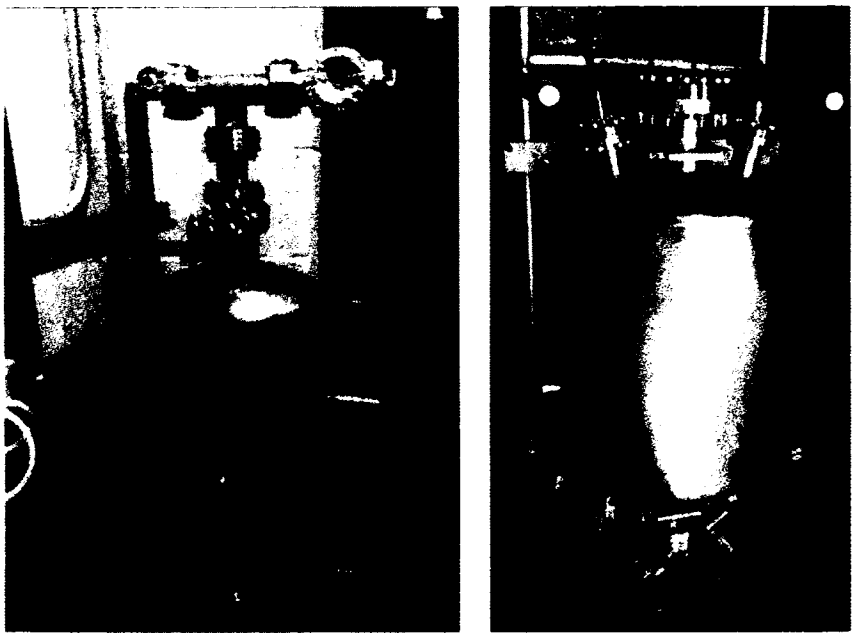

FIG. 140. 499 MHz (left) and 400 MHz (right) cavities assembled on the test stands.

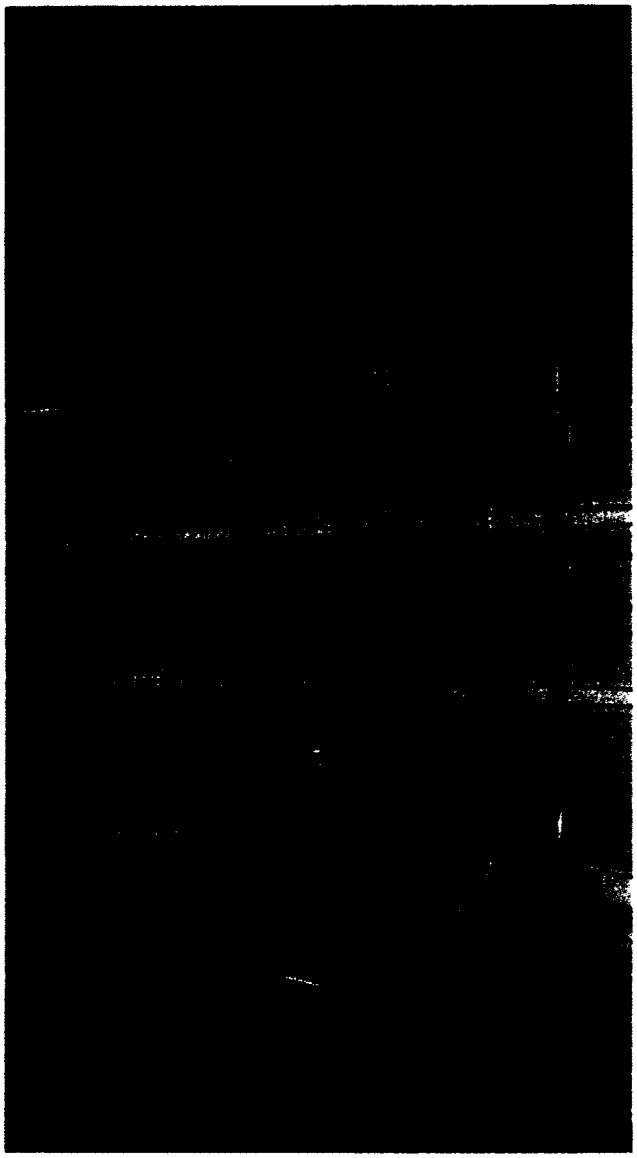

FIG. 141. Fully assembled 499 MHz cavity ready to be loaded in to the cryostat.

9.8 LOW TEMPERATURE BAKING

Low temperature baking also known as in-situ baking is used to improve the intrinsic quality factor [115]. The exact phenomenon of in-situ baking is not well understood; however it is shown to improve the Q-slope. The baking is done in a range of 100-140 °C as a final treatment of bulk niobium cavities. Several procedures exist in conducting in-situ baking, where the cavities are heated in the dewar by heating the helium gas. Another procedure is to perform the baking in a bake-box and baked by heated nitrogen gas.

The 400 MHz cavity was baked at low temperature of 120 °C for a period of 24 hours in order to remove water inside the cavity. At the end of mild baking the water vapor partial pressure measured through the RGA was below 7×10^{-7} mbar.

9.9 HE PROCESSING

He processing of superconducting cavities is performed at cryogenic temperature in order to eliminate any field emission conditions present during cavity operation [116]. Generally, the field emitters are processed by the rf fields. However for field emission with higher intensity the processing can be done introducing a small amount of helium into the cavity at low pressure ($\sim 10^{-5}$ torr). The rf power is increased then to a higher level where the field emitters are removed by the bombardment of helium ions. The rf-dipole cavities were not processed by helium.

CHAPTER 10

RF TESTS AND MEASUREMENTS

The performance of any rf cavity is measured by the intrinsic quality factor (Q_0) and the maximum gradient achieved. The goal is to achieve a high and constant Q_0 while pushing the gradient and corresponding peak fields close to the theoretical limits. This chapter will describe the rf measurements of the quality factor as a function of the transverse gradient, transverse voltage, and peak electric and magnetic fields for the 499 MHz deflecting cavity and the 400 MHz crabbing cavity, including the measured surface impedance as a function of temperature, pressure sensitivity as a function of frequency, and frequency change due to Lorentz force detuning as a function of transverse gradient.

10.1 VERTICAL TEST CRYOSTAT ASSEMBLY

The rf measurements were performed at the vertical test facility at Jefferson Lab [117]. As shown in Fig. 142, the rf cavity was loaded in the vertical test cryostat inserted in a radiation shielded pit [118]. Each test cryostat is equipped with pressure sensors, temperature sensors, liquid helium level sensors, cold and warm helium supply lines, and other ancillaries with isolation and control valves. The evacuated cavity attached to the test stand was connected to a vacuum pump that constantly evacuated through out the rf measurements. However, during the 400 MHz cavity rf tests the cavity was sealed with the vacuum valve with no constant evacuation, due to the unavailability of the facilities. Therefore, the cavity was provided with additional relief valves for safety, and during assembly the cavity was evacuated to a very low pressure level.

The cavities were gradually cooled down using liquid He below critical temperature (T_c) of 9.25 K to reach the superconducting state and rf measurements are taken at cryogenic temperatures of 4.2 K and 2.0 K. The cavities were tested in cw operation using a 500 W rf amplifier at both low power and high power [119]. The cavities were connected to the external power source using high power rf cables and a set of power meters were attached to the system to measure the incident power,

reflected power and transmitted power as shown in Fig. 142. Each test cryostat was equipped with an automated rf control and data acquisition system [120].

10.2 CIRCUIT MODEL OF A RESONANT CAVITY

The standard method for estimating the performance of a superconducting rf cavity is with a series of rf measurements carried out at low power and high power without beam loading. The measurements are obtained in continuous wave (cw) operation. A 1-port cavity system with a single rf power source including couplers can be represented by an parallel RLC equivalent circuit. The complete equivalent circuit of the rf cavity with the power source is shown in Fig. 143.

The cavity rf properties can be determined by simplifying the parallel circuit model for the fundamental electromagnetic mode of operation with resonant frequency ω_0. The corresponding rf properties can be defined as follows,

Dissipated Power:

$$P_{diss} = \frac{1}{2}\frac{V_c^2}{R}, \tag{160}$$

Shunt Impedance:

$$R_{sh} = 2R, \tag{161}$$

Intrinsic Quality Factor:

$$Q_0 = \omega_0 CR = \frac{1}{\omega_0}\frac{R}{L} = R\sqrt{\frac{C}{L}}. \tag{162}$$

Total Impedance:

$$Z = n_1^2 R_G + \frac{R}{1 + 2j\frac{Q_0}{\omega_0}\triangle\omega}, \tag{163}$$

Stored Energy:

$$U = \frac{1}{2}CV_c^2 = \frac{1}{2}\frac{Q_0}{\omega_0 R}V_c^2, \tag{164}$$

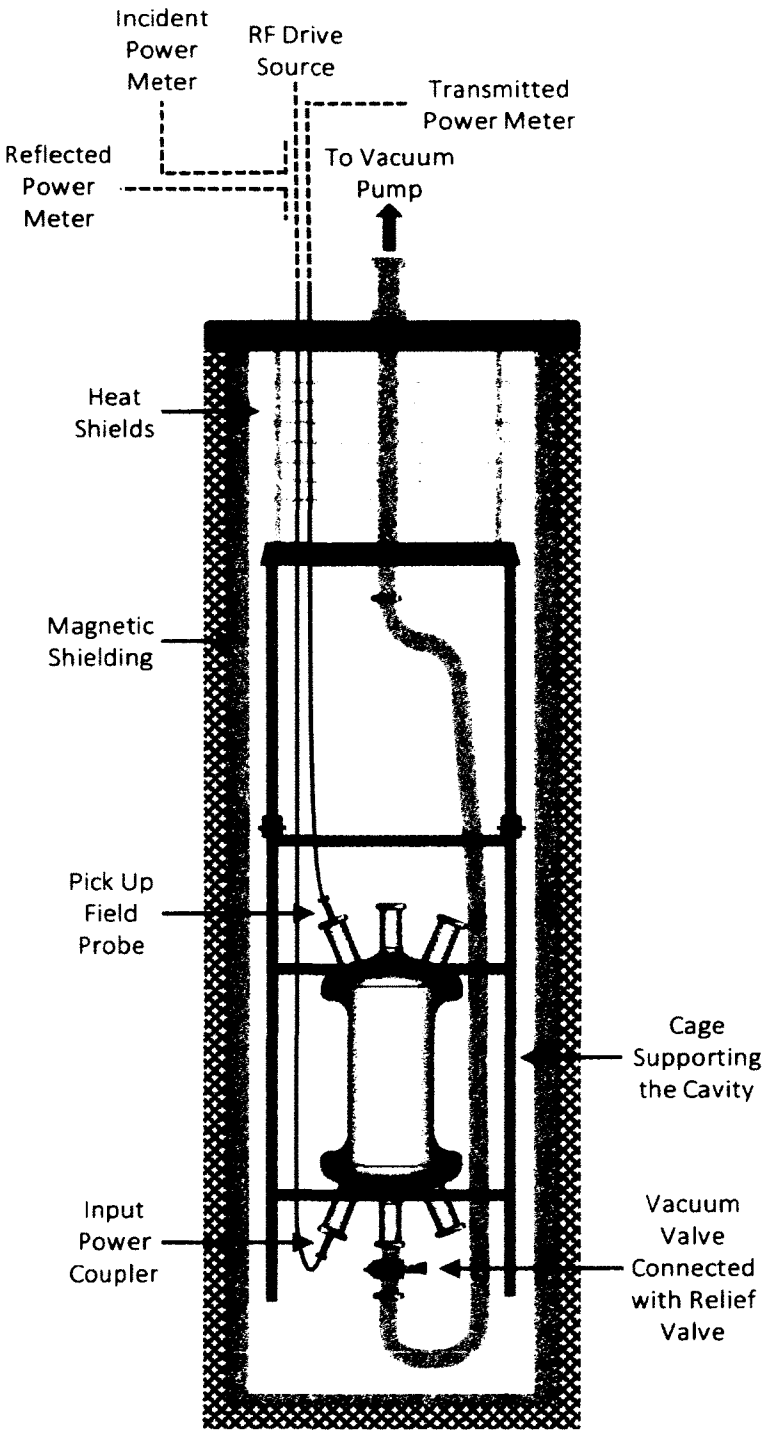

FIG. 142. Schematic of vertical test cryostat with the rf cavity.

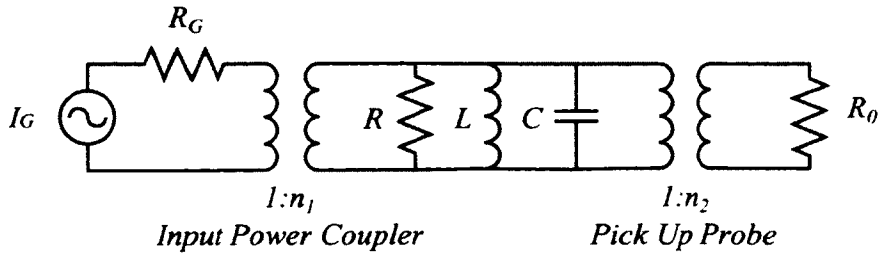

FIG. 143. Equivalent circuit of the rf cavity with input power coupler and pick up field probe.

Coupling Coefficient:

$$\beta = \frac{R}{n_1^2 R_G}. \tag{165}$$

Loaded Quality Factor:

$$\frac{1}{Q_L} = \frac{P_{diss}}{\omega_0 U} = \frac{1}{Q_0} + \frac{1}{Q_{ext1}} + \frac{1}{Q_{ext2}}, \tag{166}$$

where V_c is the cavity voltage and Q_{ext1} and Q_{ext2} are the coupling strengths of input and pick up couplers.

10.3 CALIBRATION OF INPUT POWER AND PICK UP PROBES

The resonant mode, which is the deflecting or crabbing mode in the rf-dipole cavity, is excited by the incident rf power at the input power coupler, supplied by the rf amplifier, and the pick up field probe measures the transmitted power. Fixed rf coupling is used in both input power coupler and pick-up field probe. The input power coupler and pick-up field probes are calibrated to achieve coupling strengths, Q_{ext1} and Q_{ext2}, that would correspond to coupling coefficients of $\beta_1 \approx 1$ and $\beta_2 \ll 1$. Therefore, coupling is set to deliver $Q_{ext1} \approx Q_0$ and $Q_{ext2} \gg Q_0$. The coupling strength (Q_{ext1}) for the input coupler is selected to be closer to Q_0 at 2.0 K and one-to-two orders of magnitude higher for the pick up probe, for the two rf-dipole cavities.

The coupling was calibrated using an auxiliary antenna at one of ports opposite the port of calibration and exciting the fundamental operating mode through antenna probe. The transmitted signal is measured using a network analyzer through the

probe of the port of calibration, either being the input coupler or the pick up coupler. The length of antenna is set such away that there is just enough coupling to produce the fields without generating any perturbations in the field profile. The loaded quality factor is measured (Q_L) with the s-parameter of S_{21} and coupling factor (β) of the antenna determined by the detuned and resonant amplitudes of S_{11}, which are used to determine the Q_{ext} as following

$$Q_{ext} = \frac{4\beta Q_L}{(1+\beta)} 10^{|S_{21}\,[dB]|/10}. \tag{167}$$

The coupling rods are trimmed to achieve the required Q_{ext} as presented in Table 24.

TABLE 24. Expected, calibrated and measured coupling strengths of input coupler (Q_{ext1}) and pick up coupler (Q_{ext2}).

	499 MHz Cavity		400 MHz Cavity	
	Q_{ext1}	Q_{ext2}	Q_{ext1}	Q_{ext2}
Expected	8.8×10^{9}	8.8×10^{10}	1.3×10^{10}	2.0×10^{10}
Calibrated	7.0×10^{9}	8.0×10^{10}	2.8×10^{9}	8.6×10^{10}
Measured	5.6×10^{9}	8.7×10^{10}	3.0×10^{9}	9.7×10^{10}

The incident, transmitted and reflected power levels to and from the cavity are measured by the power meters (Fig. 142). The Q_{ext1} and Q_{ext2} are determined by pulsing the incident power and measuring the reflected and transmitted power pulses. Figure 144 shows the reflected power pulses corresponding with the pulsed incident power. Critical coupling produces a stream of pulses of equal amplitude and with reduced amplitude when $\beta < 1$. The input coupling was fixed at a $Q_{ext1} = 5.6 \times 10^9$ and 3.0×10^9 that will result a slightly over coupled β in the 499 MHz design and under coupled in the 400 MHz cavity at 2.0 K.

10.4 EXPERIMENTAL SET UP FOR RF MEASUREMENTS

The schematic of the rf system used for measurements, shown in Fig. 145, uses the phase locked loop (PLL) circuit in driving the cavity with the low level rf system (LLRF) [121]. In general, the cavity resonant frequency (ω_0) shifts during operation due to pressure fluctuations, Lorentz force effects, and microphonics. In this method the LLRF system tracks the cavity resonant frequency.

The low noise amplifier (LNA) with the variable attenuators ensures that the rf

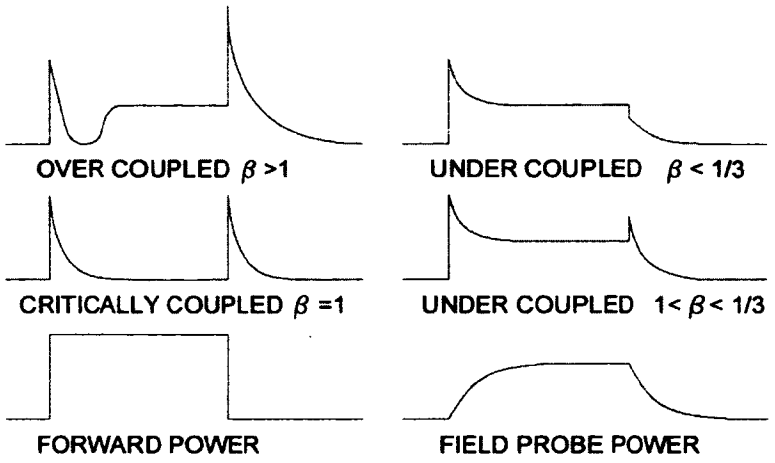

FIG. 144. Wave forms of incident and reflected power.

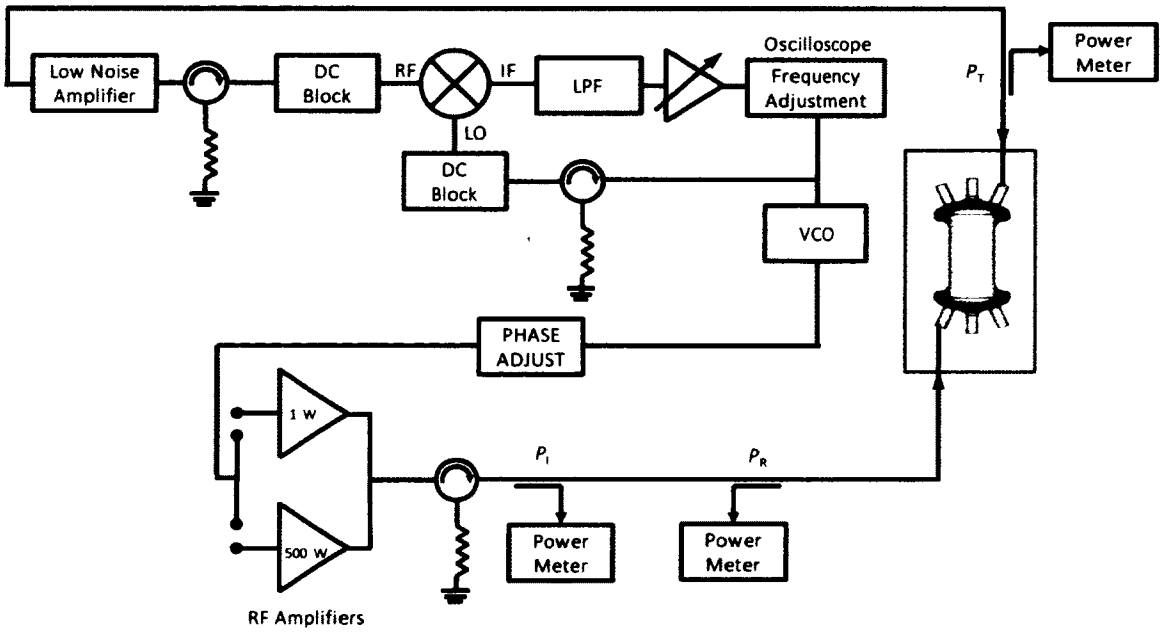

FIG. 145. Schematic of the rf system used for the Q_0 vs. field measurements.

signal to the mixer is not over driven or under driven, and is also used to adjust any oscillations in the loop gain. The loop gain is proportional to cavity gradient, therefore it is constantly adjusted at each power level, increasing at higher gradients, to maintain a stable system of operation. A trombone type phase shifter is used defore LNA to adjust the phase manually to minimize the reflected power and maximize the transmitted power.

The feedback signal is provided by the transmitted power from the cavity which is also the RF signal into the mixer, and fraction of the signal sent to the rf amplifier, is fed as local oscillator (LO) input. The output from the mixer intermediate frequency (IF) signal passes through a low pass filter (LPF) that removes the frequency content and generates a signal proportional to the phase difference between the two RF and LO signals. The LPF also reduces the noise content by limiting the loop bandwidth without compromising the cavity locking time. The variable loop amplifier provides the feasibility of adjusting loop gain without changing the phase unlike in LNA. The variable controlled oscillator (VCO) corrects the signal to follow the resonant frequency of the cavity and is also displayed on a frequency counter. A directional coupler with phase and amplitude controls sends the signal to the rf power amplifier. The measurement system is also incorporated with set of interlocks to prevent excessive levels of power being supplied to the cavity.

10.5 FUNDAMENTAL EQUATIONS OF RF MEASUREMENTS

The rf measurements obtained in terms of power are then used to determine the intrinsic quality factor, gradient, voltage. The cavity equations related to low and high power measurements are derived for both cw and pulsed mode operation.

10.5.1 DECAY MEASUREMENTS

Decay measurements are obtained during pulsed operation. The reflected power signals are analyzed initially to determine whether the cavity is operating in over coupled or under coupled state. The decay time (τ) measurements are obtained from the transmitted signal by turning off the rf drive signal, through the crystal detector in the rf control system (Fig. 145). The loaded quality factor is determined by decay time while power measurements determine the Q_0. The coupling strength (Q_{ext2}) is determined by,

$$Q_{ext} = P_{diss} P_t Q_0 \tag{168}$$

where P_t is the transmitted power.

10.5.2 CW MEASUREMENTS

The Q_{ext2} determined through decay measurements is further used to calculate the cavity properties in cw operation. The cavity gradient is found by

$$E = \sqrt{P_t Q_{ext2} \left[\frac{R}{Q}\right]}, \tag{169}$$

and the intrinsic quality factor is given by

$$Q_0 = \frac{E^2 P_{diss}}{\left[\frac{R}{Q}\right]}. \tag{170}$$

10.6 Q_0 VS. FIELD MEASUREMENTS

The performance of the rf-dipole cavity was obtained by measuring the unloaded quality factor (Q_0) as a function of the transverse voltage. Figures 146, 147, and 149 show the measured unloaded quality factor as functions of the transverse electric field (E_t), transverse voltage (V_t), peak surface electric field (E_p), and peak surface magnetic field (B_p) of the 499 MHz and 400 MHz rf-dipole cavity.

10.6.1 499 MHZ DEFLECTING CAVITY

The 499 MHz deflecting cavity underwent two sets of rf tests following two iterations of cavity processing as described in Chapter 10. The measured intrinsic quality factor (Q_0) of the first rf test (Fig. 146) shows fairly uniform Q_0 of 1.6×10^{10} at 2.0 K and a small drop in Q_0 at 4.0 K. At both cryogenic temperatures of 2.0 K and 4.2 K the cavity experienced a hard quench at relatively low gradient around 10 MV/m. The cavity achieved a deflecting voltage of 2.9 MV at 4.2 K with a peak electric field of 28 MV/m and a peak magnetic field of 42 mT. During the 2.0 K rf test the cavity achieved a slightly higher transverse voltage of 3.15 MV with peak electric and magnetic fields of 30 MV/m and 46 mT. At both cryogenic temperatures the 499 MHz cavity achieved similar peak fields with a sudden drop in Q_0 resulting a hard quench. The observed hard quench at low fields could possibly be due to a defect on the surface. The cavity could not deliver the expected target transverse

voltage of 3.3 MV, therefore the cavity was reprocessed and the rf measurements were repeated.

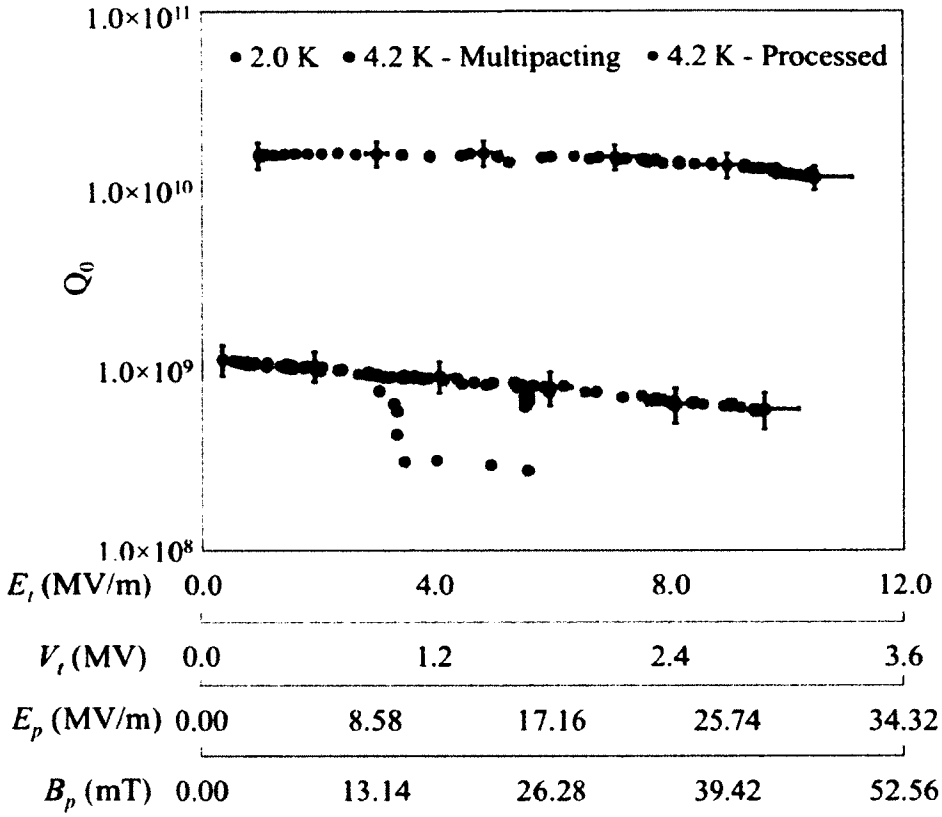

FIG. 146. Quality factor at 4.2 K and 2.0 K of the first rf tests of 499 MHz cavity.

The 499 MHz cavity was reprocessed, repeating the bulk BCP and removing a layer of ~ 200 μm, in order to remove the defects on the cavity surface. The rf tests performed on the reprocessed cavity shows a considerable improvement on Q_0 due to the processed defect. However, the cavity experienced a hard quench at both 4.2 K and 2.0 K, although at a higher field level thna during the previous test, and it could possibly be that the defect was not completely processed. As described in Chapter 9, the cavity showed a slight edge at the center body at one of the welding seam of the center shell with the shoulder block. The second bulk BCP may have processed the step as shown by the improved results, however it may not have completely removed it.

The 499 MHz rf-dipole cavity achieved a gradient of 14 MV/m at 2.0 K and 13.0 MV/m at 4.2 K. The transverse gradient corresponds to a transverse voltage of 4.2

MV at 2.0 K and 3.9 MV at 4.2 K. The second rf tests delivered the performance expected by the 499 MHz deflecting cavity and surpassed the required transverse voltage of 3.3 MV at both cryogenic temperatures of 4.2 K and 2.0 K. The measured Q_0 dropped to about 8.5×10^{10} at 2.0 K with a fairly uniform variation until 12.0 MV/m then showed a gradual drop in Q_0 which was followed by a hard quench. The rf measurements were repeated by gradually decreasing the rf power, and Q_0 shows a drop as shown in Fig. 147. The rf measurements were continued at very low gradient over a large period of time and Q_0 recovered to its initial value after about 6 hours of operation. This was possibly due to a localized heating occurred at high rf fields, that resulted in degrading the measured Q_0 and eventually shifting the cavity to a normal conducting state. The rf test at 2.0 K was repeated 3 times at 2.0 K and similar behavior in Q_0 was observed, and during all the tests the cavity was maintained with a liquid helium level above the cavity. The measured Q_0 at 4.2 K is identical to that achieved in the first rf test with a higher transverse gradient.

The cavity achieved peak surface electric fields of 37 MV/m and 40 MV/m, and peak magnetic fields of 57 mT and 61 mT at 4.2 K and 2.0 K respectively. This shows that the rf-dipole cavity is capable of achieving reasonably high peak surface fields. The maximum dissipated power did not exceed 5.0 W at 2.0 K and less than 40 W at 4.2 K. The maximum rf input power required at 2.0 K was 5.2 W with the cavity operating closed to critically coupled state, where the reflected power is very small. At 4.2 K the cavity was driven at a maximum rf input power of 82 W at the highest gradient point. The 499 MHz deflecting cavity demonstrates that the cavity can achieve the design requirement of the transverse voltage by one cavity.

Figure 148 shows the field emission levels observed during rf tests at cryogenic temperatures of 2.0 K and 4.2 K. The radiation levels observed are fairly negligible in the 499 MHz cavity, given that the cavity did not reach higher peak fields to generate higher levels of radiation.

10.6.2 400 MHZ CRABBING CAVITY

The Q-curve at 4.2 K shows a distinctive slope compared to that observed in 499 MHz cavity, while it is relatively flat at 2.0 K as shown in Fig. 149. This is a fairly common feature that has been often observed in low-frequency superconducting cavities [11, 122]. Its origin is still poorly understood but possibly related to the heat transfer between niobium and liquid He.

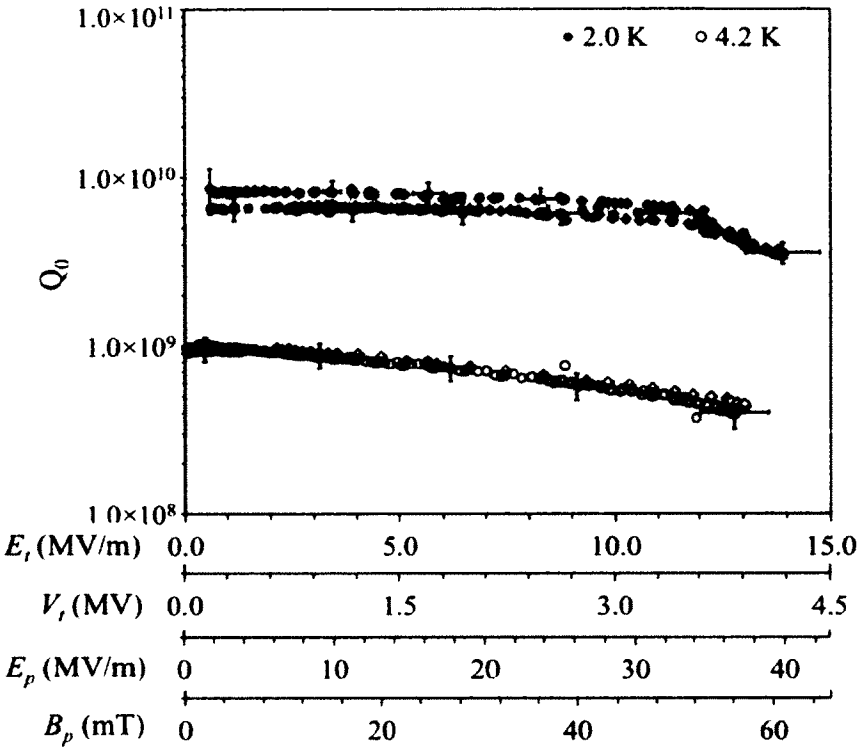

FIG. 147. Quality factor at 4.2 K and 2.0 K of the second rf tests of 499 MHz cavity.

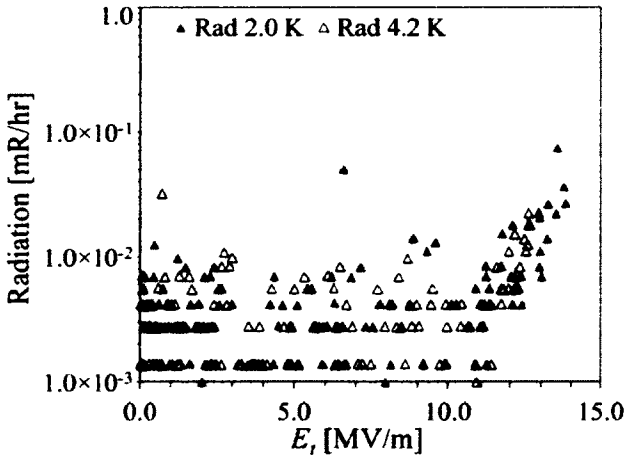

FIG. 148. Field emission at 4.2 K and 2.0 K rf tests.

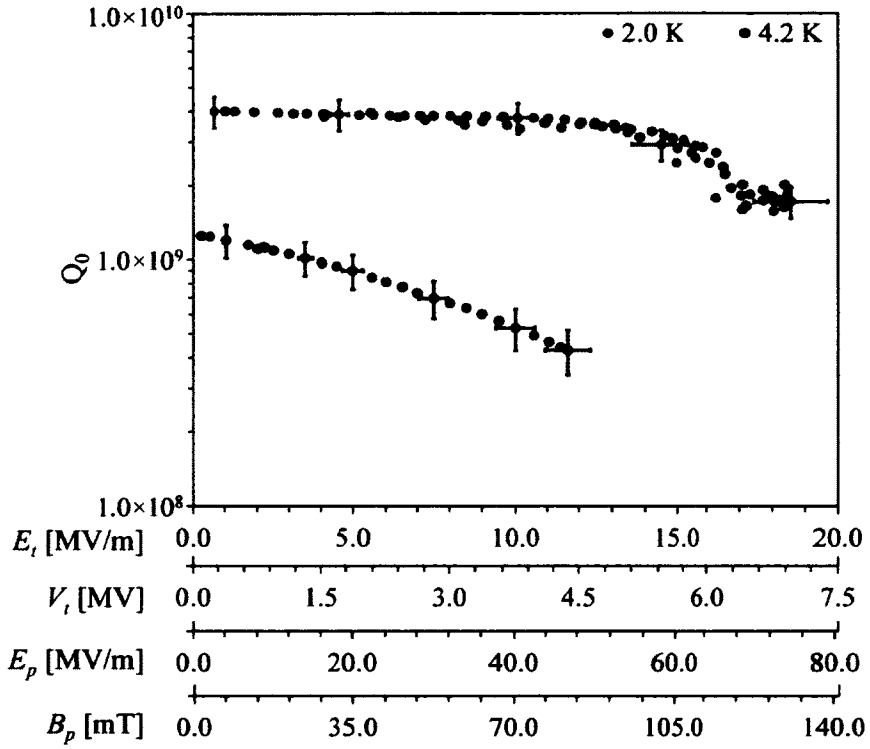

FIG. 149. Quality factor at 4.2 K and 2.0 K of the first rf tests of the 400 MHz cavity.

During the 4.2 K tests, the cavity achieved a transverse voltage of 4.35 MV that corresponds to a transverse deflecting field of 11.6 MV/m and was limited by the rf power available. The cavity was dissipating over 150 W at 11.6 MV/m. At 2.0 K the Q-curve was flat with increasing gradient. The cavity achieved a transverse voltage of 7.0 MV where a quench was observed. The Q-curve was flat until 5.0 MV and dropped possibly due to field emission. Figure 150 shows the radiation produced by field emission during the 4.2 K and 2.0 K high power rf tests and measured at the top of the dewar. Since the cavity was sealed and not actively pumped there was no opportunity to do He processing [41]. During the 2.0 K test the cavity reached cw peak surface fields of 75 MV/m and 131 mT. The achieved cw voltage of 7.0 MV is twice the design voltage of 3.4 MV for the crabbing cavities for the proposed LHC High Luminosity upgrade [69].

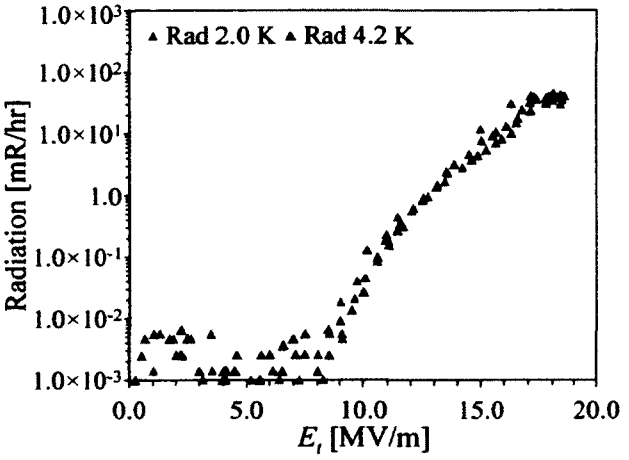

FIG. 150. Field emission at 4.2 K and 2.0 K rf tests.

The source of the low Q performance obtained during the rf measurements for the 400 MHz cavity was directly related to the losses contributing from the stainless blank flanges at beam ports where the details are explained in Section 10.8. The stainless steel (SS) flanges were then replaced with two SS blank flanges coated with a thin film of niobium provided by CERN. Figure. 151 shows the improved performance of the 400 MHz cavity where Q_0 increased at both 4.2 K and 2.0 K. Similar to the first test the maximum gradient achievable was limited by the input power. During the rf measurements at both cryogenic temperatures of 4.2 K and 2.0 K the 400 MHz cavity successfully reached the gradients achieved by the previous rf tests. At 2.0

K the intrinsic quality factor increased by a factor above three at low fields and the subsequent Q_0 drop is due to the field emission levels present in the cavity.

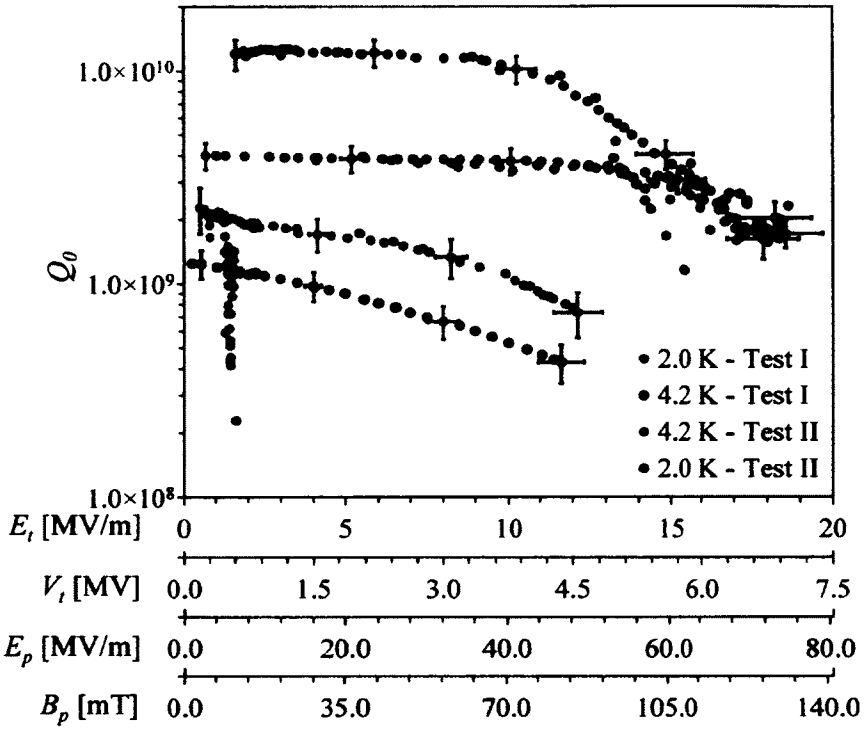

FIG. 151. Quality factor at 4.2 K and 2.0 K of the second rf tests of the 400 MHz cavity.

10.7 MULTIPACTING LEVELS

Multipacting levels were clearly observed in the 499 MHz cavity as shown in Fig. 152, during the very first rf test at 4.2 K. The resonant conditions were observed for a transverse voltage range of $0.8 - 1.8$ MV which was also seen in the Fig. 113 obtained by the numerical simulations done using Track3P code in the SLAC ACE3P suite. As the input power was increased the multipacting levels were processed and did not reoccur in the following rf test at 2.0 K. The 499 MHz cavity was reprocessed and retested at both 2.0 K and 4.2 K. No multipacting levels were observed in the reprocessed cavity.

The 400 MHz cavity was initially tested at 2.0 K followed by a test at 4.2 K and another test at 2.0 K. In the first 2.0 K high power rf test a multipacting barrier was observed at very low fields. After a few minutes the input power was increased, the

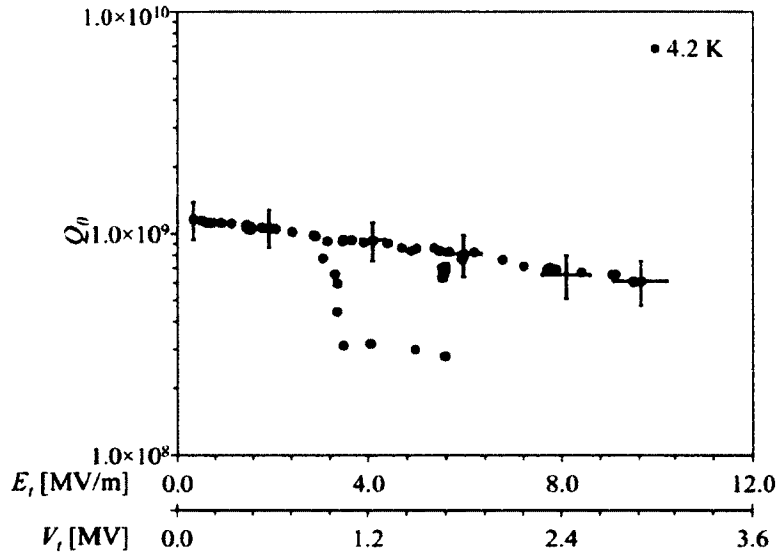

FIG. 152. Multipacting levels observed in 499 MHz cavity during 4.2 K rf test.

multipacting level disappeared, and the transverse voltage jumped to about 2.5 MV. As shown in Figure 114, both the barriers were easily processed with increasing input power, and were shown to be soft multipacting barriers. The input power was then decreased down to 1 MV in small steps and no multipacting levels were observed. Further multipacting levels were not observed during the remainder of the 2.0 K test or on the following 4.2 K and 2.0 K tests. This observation is consistent with what was expected from the simulations.

10.8 SURFACE RESISTANCE MEASUREMENTS AND POWER DISSIPATION

The effective surface resistance (R_s) was calculated by $R_s = G/Q_0$ using the unloaded quality factor measured during the cavity cooling down process from 4.2 K to 2.0 K for the 499 MHz and 400 MHz cavities where the geometrical factors (G) are given in Table 13. The rf measurements were performed at very low gradient.

Figures 153 and 154 show the surface resistance curves of the 499 MHz cavity measured after each surface treatment. In the first set of measurements the cavity was operated at a field range of 1.6 - 1.75 MV/m that corresponds to a transverse voltage range of 0.48 - 0.53 MV. The second set of measurements were obtained at a slightly higher field range of 1.0 - 3.5 MV/m.

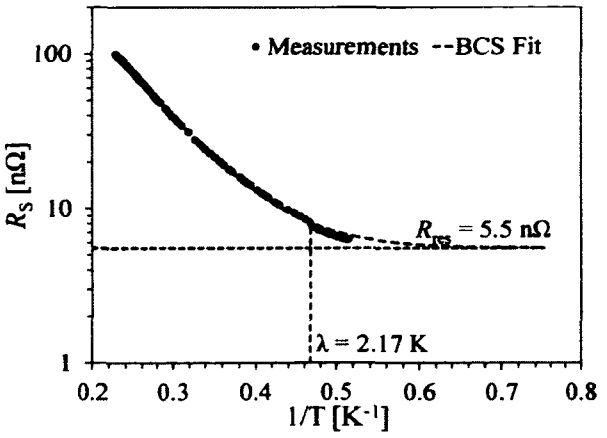

FIG. 153. Effective surface resistance during the cavity cool down from 4.2 K to 2.0 K of the first rf test of 499 MHz cavity.

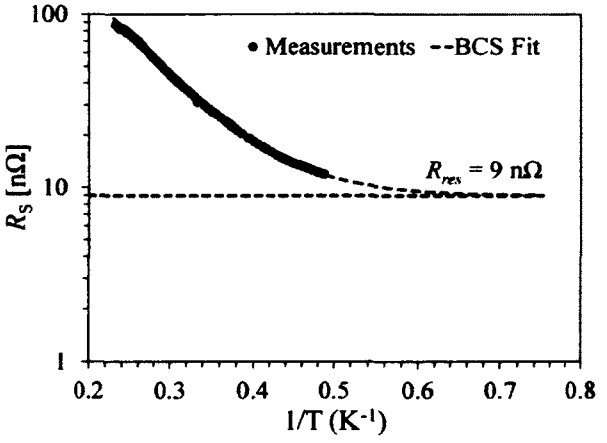

FIG. 154. Effective surface resistance during the cavity cool down from 4.2 K to 2.0 K of the second rf test of 499 MHz cavity.

The surface resistance data are fitted following the BCS theory given by Eq. 105 [123]. The residual resistances were 5.53 nΩ and 8.97 nΩ of the two rf tests. The increase in the residual surface resistance was possibly due to the increased amount of hydrogen absorbed during the second surface treatment where the cavity was processed for a longer duration in order to remove an average layer of 200 μm. The increase in the residual resistance was below the expected 10 nΩ.

$$R_s\,[n\Omega] = \frac{2.6 \times 10^4}{T\,[\mathrm{K}]} \exp\left[-\frac{18.67}{T\,[\mathrm{K}]}\right] + 5.53 \tag{171}$$

$$R_s\,[n\Omega] = \frac{1.5 \times 10^4}{T\,[\mathrm{K}]} \exp\left[-\frac{16.1}{T\,[\mathrm{K}]}\right] + 8.97 \tag{172}$$

The surface resistance measurements of the 400 MHz cavity were taken at a field range of 0.5 - 0.65 MV/m that corresponds to 0.2 - 0.25 MV. The estimated residual surface resistance of 34 nΩ, shown in Fig. 155, was determined by fitting the measured data with the BCS theory [123]. The best fit to our data was

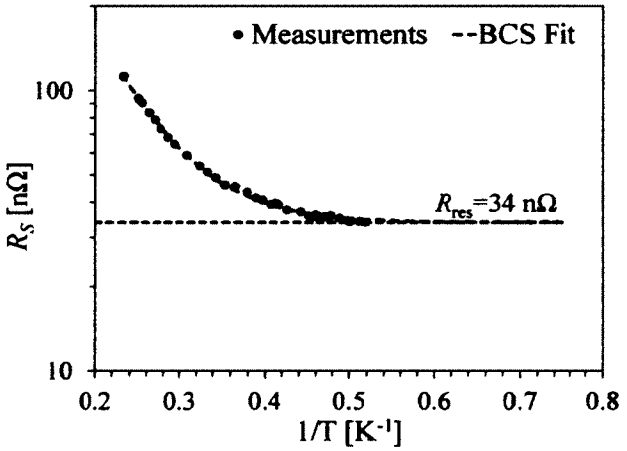

FIG. 155. Effective surface resistance during the cavity cool down from 4.2 K to 2.0 K of the first rf test of 400 MHz cavity.

$$R_s\,[n\Omega] = \frac{2.6 \times 10^4}{T\,[\mathrm{K}]} \exp\left[-\frac{18.1}{T\,[\mathrm{K}]}\right] + 33.9\,. \tag{173}$$

The measured losses in the 400 MHz cavity were higher and Q_0 was lower than

expected due to the high residual surface resistance. Therefore careful analysis was done to identify the surface losses. It was found that surface losses at the beam port stainless flanges were significant. The surface magnetic field on the beam port and coupler ports at a stored energy content of 1 J is shown in Fig. 156. During the tests the beam ports were blanked with stainless steel flanges and these were found to give rise to non-negligible losses as shown in Table 25. Losses at the blanked side ports were insignificant. Losses calculated at the beam ports give an unloaded quality factor (Q_0) of 3.8×10^9 which agrees with the measured Q_0 of 4.0×10^9 at 2.0 K. The expected BCS resistance for Nb at 400 MHz is $R_{BCS} = 1.3$ nΩ at 2.0 K and $R_{BCS} = 70.0$ nΩ at 4.2 K [123]. Therefore the losses at the beam ports are dominant at 2.0 K; however at 4.2 K the BCS losses are higher and do not dominate the losses at the beam ports.

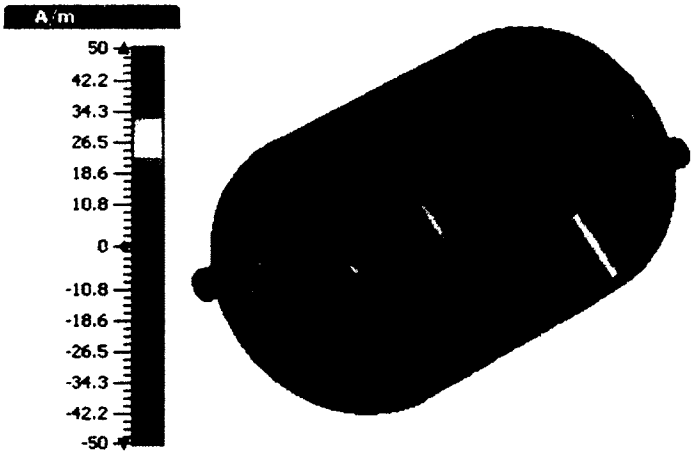

FIG. 156. Surface magnetic field on beam and coupler ports at a energy content of 1 J.

The surface resistance measurements of the 400 MHz cavity was taken at a field range of 1.1 - 1.25 MV/m during the second rf test. The corresponding residual resistance was estimated with a BCS fit. The surface resistance measurements obtained during the second rf measurements shows the improvement in the unloaded quality factor, which clearly indicate that the contribution to the high residual resistance of 34 nΩ was not due to the cavity inner surface. The estimated residual resistance dropped to 10 nΩ as shown in Fig. 157 with the niobium coated blank flanges at the beam ports.

TABLE 25. Port losses at beam and coupler ports

Parameter	Value	Units
Surface resistance of stainless steel	0.033	Ω
Beam Ports		
Power loss at beam ports[2]	0.69	W
Q_0 due to the power loss at beam ports	3.8×10^9	
Side Ports		
Power loss at side ports[2]	0.0076	W
Q_0 due to the power loss at side ports	3.3×10^{11}	

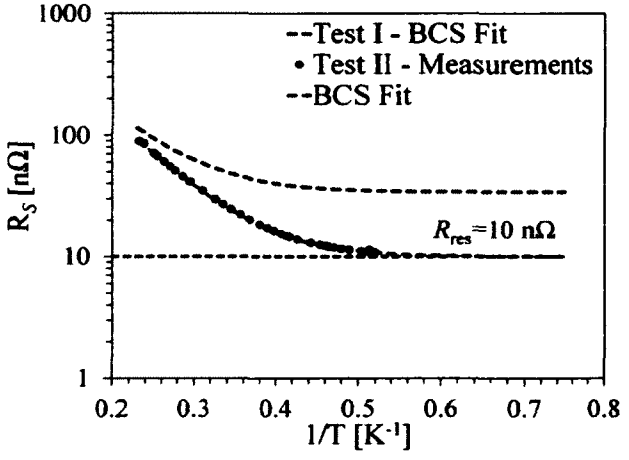

FIG. 157. Effective surface resistance during the cavity cool down from 4.2 K to 2.0 K of the second rf test for 400 MHz cavity.

$$R_s\ [n\Omega] = \frac{2.6 \times 10^4}{T\ [\mathrm{K}]} \exp\left[-\frac{18.67}{T\ [\mathrm{K}]}\right] + 10.0\,. \tag{174}$$

10.9 MEASUREMENTS OF MECHANICAL PROPERTIES

10.9.1 PRESSURE SENSITIVITY

The rf-dipole cavity sensitivity to the pressure was measured in a low power rf test in cw operation during the cool down of the cavity from 4.2 K to 2.0 K. The cavity showed a pressure sensitivity of 380 Hz/torr in the 499 MHz cavity and 483 Hz/torr in the 400 MHz cavity as shown in Fig. 158 and Fig. 159. The larger surface area in the 400 MHz cavity results with a higher sensitivity compared to that in the 499 MHz cavity. This can be substantially reduced by including stiffeners at appropriate locations.

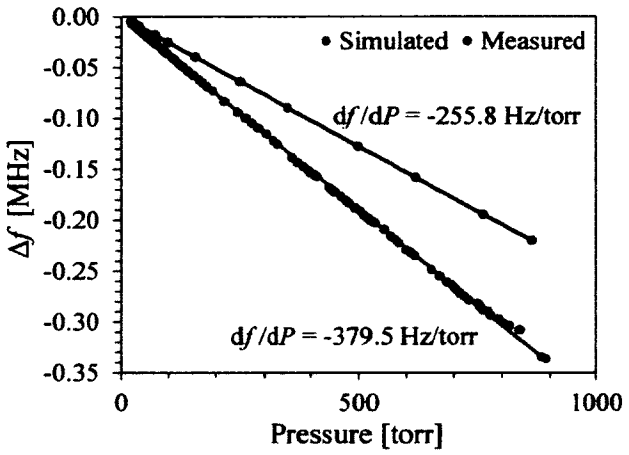

FIG. 158. Pressure sensitivity of the 499 MHz rf-dipole cavity.

10.9.2 LORENTZ FORCE DETUNING

The Lorentz force detuning is an effect where the cavity is deformed by the radiation pressure [124] given by

$$P = \frac{1}{4}\left[\mu_0 H^2 - \epsilon_0 E^2\right]\,. \tag{175}$$

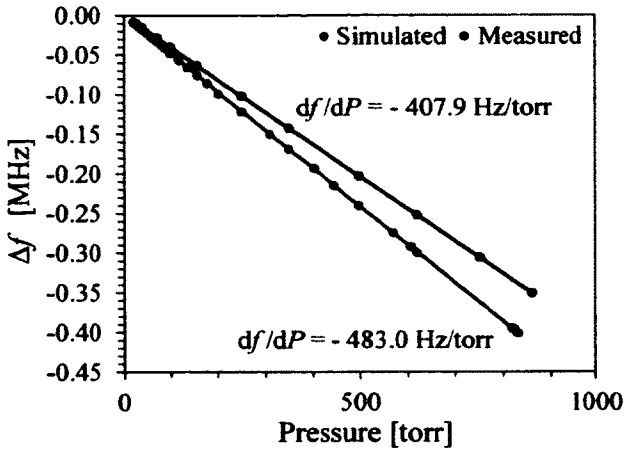

FIG. 159. Pressure sensitivity of the 400 MHz rf-dipole cavity.

The magnetic field applies pressure and deforms the surface outward, while deformation due to electric field is inward. The change in cavity resonant frequency due to Lorentz force detuning is related to the cavity gradient (E_t) given by

$$\triangle f = k_L E_t^2 \tag{176}$$

where $k_L < 0$ is the Lorentz coefficient.

The Lorentz force detuning was measured for the two rf-dipole cavities as shown in Fig. 160 and Fig. 161. At both 4.2 K and 2.0 K the Lorentz coefficients were calculated to be $k_L = -56$ Hz/(MV/m)^2 and $k_L = -122$ Hz/(MV/m)^2. The measured coefficient is relatively high in the 400 MHz cavity due to large flat surfaces in the rf-dipole cavity, and can be reduced by adding stiffeners at appropriate locations.

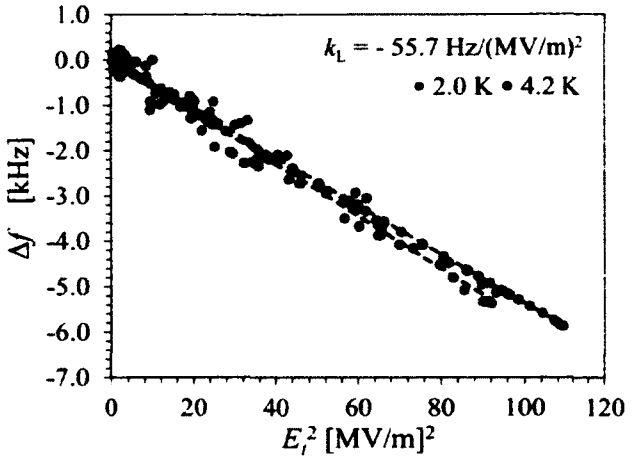

FIG. 160. Lorentz force detuning of the 499 MHz cavity at 4.2 K and 2.0 K rf tests.

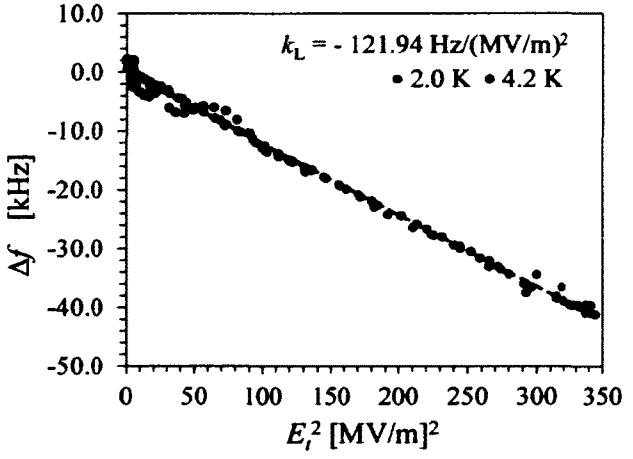

FIG. 161. Lorentz force detuning of the 400 MHz cavity at 4.2 K and 2.0 K rf tests.

CHAPTER 11

SUMMARY AND CONCLUSIONS

The thesis presents the detailed optimization and demonstration of the rf-dipole cavity and its evolution from the parallel-bar cavity as a novel design for deflecting and crabbing cavities to be used in particle accelerators. The rf-dipole design possesses excellent rf properties, is capable of operating at high gradients, achieve high peak surface fields and high shunt impedance. The novel rf-dipole cavity is a very attractive design for deflecting and crabbing applications with low operating frequencies, that require compact rf structures. Furthermore, the rf-dipole geometry supports a wide higher-order mode separation with no lower order modes.

The design optimization identifies the important parameters in optimizing the rf-dipole design in order to achieve low peak surface field ratios and high shunt impedance. The optimized balanced peak field ratio of $\sim$ 1.7 mT/(MV/m) have clearly demonstrated reaching high electric and magnetic surface fields.

Two rf-dipole cavities with operating frequencies of 499 MHz and 400 MHz have been designed and fabricated as proof-of-principle cavities. The 499 MHz cavity was developed as an option for the separator for the Jefferson Lab 12 GeV upgrade, and the 400 MHz is under consideration for the crabbing system for the High Luminosity Upgrade of the CERN Large Hadron Collider.

RF test have been performed successfully at cryogenic temperatures of 4.2 K and 2.0 K. The 499 MHz cavity achieved transverse voltages of 3.9 MV at 4.2 K and 4.2 MV at 2.0 K that exceed the design requirement of 3.3 MV. The 400 MHz cavity achieved a transverse voltage of 4.35 MV at 4.2K –limited by available rf power– and 7.0 MV at 2.0 K, more than twice the design requirement of 3.4 MV.

The 400 MHz cavity demonstrated maximum peak surface electric and magnetic fields of 75 MV/m and 131 mT, close to the theoretical limits. This shows that the rf-dipole cavity is capable of achieving high gradients with high peak surface fields. Peak surface electric and magnetic fields achieved by the 499 MHz cavity are 40 MV/m and 61 mT respectively which was followed by a hard quench. The lower surface fields achieved by the 499 MHz are possibly due to a weld defect at the center body of the cavity. The 400 MHz cavity initially achieved a lower intrinsic quality factor than

expected; however the measured losses were consistent with those associated with the beam pipe stainless steel flanges. The Q_0 was significantly improved by reducing the surface losses at the blank flanges by coating them with niobium. Both the 499 MHz and 400 MHz cavities have shown that low residual losses can be achieved.

Two different procedures were followed in fabricating the two rf-dipole cavities. Most of the parts of were stamped and certain parts of the 499 MHz cavity were machined with niobium ingots. The complexity of the process followed in the 499 MHz cavity required several sets of fixtures in support of accurate welding of the parts. On the other hand all the parts of 400 MHz cavity parts were stamped and welded in an electron beam welding machine. Therefore the fabrication method followed by the 400 MHz cavity would be the efficient way of fabricating the rf-dipole cavities.

The standard cavity surface treatment methods were carried out in processing the rf-dipole cavities. The buffered chemical processing (BCP) was used to remove the damaged layer from the cavity inner surface. The cavities were heat-treated to remove the hydrogen absorbed during the chemical treatment and were high-pressure rinsed with high-purity water to reduce field emission from surface contaminants.

Multipacting is always a concern in novel geometries of superconducting cavities. Simulations carried out for both the rf-dipole cavities showed several multipacting barriers existing at low operating gradients. The rf measurements also showed similar multipacting barriers in agreement to the simulations. The multipacting levels were easily processed and did not reoccur in any of the rf test following the initial test. The 499 MHz cavity also demonstrated that the multipacting levels do not exist in the reprocessed cavities.

The proof-of-principle cavities have demonstrated that high performance can be achieved by the rf-dipole cavity. The rf-dipole geometry can be modified into a square-shaped geometry to obtain a more compact deflecting and crabbing cavity design. The next generation prototype rf-dipole design has been further optimized to meet all the design requirements of the LHC High Luminosity Upgrade [89]. The prototype cavity has also been optimized to further reduce the higher order multipole components and reduce any beam dynamics effects. The new design also includes higher order mode couplers to damp the HOM impedances below the longitudinal and transverse thresholds.

BIBLIOGRAPHY

[1] S. Belomestnykh and V. Shemelin, in *Proceedings of the 2005 International Workshop on RF Superconductvity, Ithaca, New York* (LEPP, Cornell University, 2005) p. 2.

[2] J. R. Delayen, in *Proceedings of the 2001 Workshop on RF Superconductivity, Tsukuba, Japan* (FNAL, 2001) p. 152.

[3] J. R. Delayen, in *Proceedings of the 2003 Workshop on RF Superconductivity, Lbeck/Travemnder, Germany* (DESY, 2003) p. 486.

[4] J. R. Delayen, in *Proceedings of the 2012 Linear Accelerator Conference, Tel-Aviv, Israel* (JACoW, 2012) p. 758.

[5] A. Facco, in *Proceedings of the 2005 Workshop on RF Superconductivity, Ithaca, New York* (Cornell University, 2005) p. 21.

[6] J. P. Turneaure and N. T. Viet, Appl. Phys. Lett. **16**, 333 (1970).

[7] C. Lyneis, in *Proceedings of the 1980 Workshop on RF Superconductivity, Karlsruhe, Germany* (1980) p. 119.

[8] J. K. Sekutowicz, *Superconducting elliptical cavities*, Tech. Rep. CERN-2011-007 (CERN, 2012) cAS - CERN Accelerator School: Specialised Course on RF for Accelerators.

[9] P. Kneisel, R. Vincon, and J. Halbritter, Nucl. Instrum. Methods Phys. Res., Sect. A **188**, 669670 (1981).

[10] J. R. Delayen and H. Wang, Phys. Rev. ST Accel. Beams **12**, 062002 (2009).

[11] J. R. Delayen, in *Proceedings of the 2010 Linear Accelerator Conference, Tsukuba, Japan* (LINAC10 OC, 2010) p. 377.

[12] K. Halbach and R. F. Holsinger, Particle Accelerators **7**, 213 (1976).

[13] "Microwave Studio, CST GmbH, Darmstadt, Germany," (2012), `http://www.cst.com`.

[14] "Ansys academic research, release 13.0, structural mechanics analysis, ansys, inc." (2010), `http://www.ansys.com`.

[15] W. K. H. Panofsky and W. A. Wenzel, Rev. Sci. Instrum. **27**, 967 (1956).

[16] M. J. Browman, in *Proceedings of the 1993 Particle Accelerator Conference, Washington, D.C.* (IEEE Catalog No 93CH3279-7, 1993) p. 800.

[17] S. U. De Silva and J. R. Delayen, Phys. Rev. ST Accel. Beams **16**, 012004 (2013).

[18] I. R. Campisi, in *Proceedings of the 2001 Conference on RF Superconductivity, Tsukuba, Japan* (FNAL, 2001) p. 132.

[19] S. Belomestnykh, in *Proceedings of the 2007 International Workshop on RF Superconductvity, Beijing, China* (Peking University, 2007) p. 419.

[20] S. U. De Silva and J. R. Delayen, in *Proceedings of the 2012 Linear Accelerator Conference, Tel-Aviv, Israel* (JACoW, 2012) p. 981.

[21] A. Wolski, *Maxwell's Equations for Magnets*, Tech. Rep. CERN-2010-004 (CERN, 2011) cERN Accelerator School CAS 2009: Specialised Course on Magnets.

[22] D. T. Abell, Phys. Rev. ST Accel. Beams **9**, 052001 (2006).

[23] J. B. García, R. Calaga, R. D. Maria, M. Giovannozzi, A. Grudiev, and R. Tomás, in *Proceedings of the 2012 International Particle Accelerator Conference, New Orleans, USA* (IPAC'12 OC / IEEE, 2012) p. 1873.

[24] H. K. Onnes, Electrician **67**, 657 (1911).

[25] W. Meissner and R. Ochsenfeld, Naturwissenschaften **21**, 787 (1933).

[26] C. J. Gorter and H. B. G. Casimir, Physica **1**, 306 (1934).

[27] F. London and H. London, Proc. R. Soc. Lond. A **149**, 71 (1935).

[28] A. B. Pippard, Proc. R. Soc. Lond. A **216**, 547 (1953).

[29] V. L. Ginzburg and L. D. Landau, Zh. ksp. Teor. Fiz. **20**, 1064 (1950), english Translation: L. D. Landau, Collected Papers, Pergamon Press, Oxford, p. 546, 1965.

[30] J. Bardeen, L. N. Cooper, and J. R. Schrieffer, Phys. Rev. **106**, 162 (1957).

[31] J. Bardeen, L. N. Cooper, and J. R. Schrieffer, Phys. Rev. **108**, 1175 (1957).

[32] L. N. Cooper, Phys. Rev. **104**, 1189 (1956).

[33] D. C. Mattis and J. Bardeen, Phys. Rev. **111**, 412 (1958).

[34] R. G. Chambers, Proc. R. Soc. of Lon., Ser. A **215**, 481 (1952).

[35] M. Tinkham, *Introduction to Superconductivity* (Dover, United States, 1996).

[36] J. Halbritter, Zeitschrift für Physik **238**, 466 (1970).

[37] J. Halbritter, in *Proceedings of the 1984 Conference on RF Superconductivity, Geneva, Switzerland* (1984) p. 427.

[38] J. Halbritter, J. Phys. Colloques **45**, 315 (1984).

[39] B. Bonin and R. W. Röth, in *Proceedings of the 1991 Workshop on RF Superconductivity, Hamburg, Germany* (DESY, 1991) p. 210.

[40] J. Halbritter, P. Kneisel, and K. Saito, in *Proceedings of the 1993 Workshop on RF Superconductivity, Newport News, Virginia, USA* (1993) p. 617.

[41] H. A. Schwettman, J. P. Turneaure, and R. F. Waites, J. Appl. Phys. **45**, 914 (1974).

[42] J. Knobloch, IEEE Transactions on Applied Superconductivity **9**, 1016 (1999).

[43] B. Bonin, *Field emission in RF cavities*, Tech. Rep. CERN-96-03 (CERN, 1996) cAS - CERN Accelerator School : Superconductivity in Particle Accelerators.

[44] R. H. Fowler and L. Nordheim, Proc. Roy. Soc. London A **119**, 173 (1928).

[45] H. Padamsee, J. Knobloch, and T. Hays, *RF Superconductivity for Accelerators* (Wiley-VCH, Germany, 2008).

[46] P. Emma, J. Frisch, and P. Krejcik, *A Transverse RF Deflecting Structure for Bunch Length and Phase Space Diagnostics*, Tech. Rep. LCLS-TN-00-12 (SLAC, 2000).

[47] A. Zholents, P. Heimann, M. Zolotorev, and J. Byrd, Nucl. Instrum. Methods Phys. Res., A **425**, 385389 (1999).

[48] M. Cornacchia and P. Emma, Phys. Rev. ST Accel. Beams **5**, 084001 (2002).

[49] P. R. Phillips, Rev. Sci. Instrum. **32**, 13 (1961).

[50] R. B. Palmer, *Energy scaling, crab crossing and the pair problem*, Tech. Rep. SLAC-PUB-4707 (SLAC, 1988).

[51] K. Oide and K. Yokoya, Phys. Rev. A, Gen. Phys. **40**, 315 (1989).

[52] W. Herr and B. Muratori, *Concept of luminosity*, Tech. Rep. CERN-2006-002 (CERN, 2006) cAS - CERN Accelerator School: Intermediate Course on Accelerator Physics.

[53] M. Bell, P. Bramham, and B. W. Montague, Nature **198**, 277 (1963).

[54] O. H. Altenmueller, R. R. Larsen, and G. A. Loew, Rev. Sci. Instrum. **35**, 438 (1964).

[55] H. Hahn and H. J. Halama, Rev. Sci. Instrum. **36**, 1788 (1965).

[56] H. Hahn, Rev. Sci. Instrum. **34**, 1094 (1963).

[57] A. Citron, G. Dammertz, M. Grundner, L. Husson, R. Lehm, H. Lengeler, D. E. Plane, and G. Winkler, Nucl. Instrum. Methods **155**, 93 (1978).

[58] K. Hosoyama, K. Hara, A. Kabe, Y. Kojima, Y. Morita, H. Nakai, L. S. Peng, K. Ohkubo, H. Hatori, and M. Inoue, in *Proceedings of the 1998 Asian Particle Accelerator Conference, Tsukuba, Japan* (KEK Proceedings 98-10, 1998) p. 828.

[59] C. W. Leemann, D. R. Douglas, and G. A. Krafft, Annual Review of Nuclear and Particle Science **51**, 413 (2001).

[60] J. F. Benesch *et al.*, in *Proceedings of the 2005 Particle Accelerator Conference, Knoxville, Tennessee* (IEEE Catalog No 05CH37623C, 2005) p. 1482.

[61] L. S. Cardman and L. Harwood, in *Proceedings of the 2007 Particle Accelerator Conference, Albuquerque, New Mexico* (IEEE Catalog Number: 07CH37866, 2007) p. 58.

[62] C. W. Leemann and C. G. Yao, in *Proceedings of the 1990 Linear Accelerator Conference, Albuquerque, New Mexico* (Los Alamos Report LA-12004-C, 1991) p. 232.

[63] C. Hovater, G. Arnold, J. Fugitt, L. Harwood, R. Kazimi, G. Lahti, J. Mammosser, R. Nelson, C. Piler, and L. Turlington, in *Proceedings of the 1996 Linear Accelerator Conference, Geneva, Switzeland* (CERN 96-07, 1996) p. 77.

[64] M. Spata, *11 GeV Separator Requirements*, Tech. Rep. JLAB-TN-13-043 (JLab, 2013).

[65] L. Evans and P. Bryant, Journal of Instrumentation **3** (2008).

[66] T. S. Pettersson and P. Lefèvre, *The Large Hadron Collider: Conceptual Design*, Tech. Rep. CERN-AC-95-05 LHC (CERN, Geneva, 1995).

[67] G. Aad and et. al., Physics Letters B **716**, 1 (2012).

[68] S. Chatrchyan and et. al., Physics Letters B **716**, 30 (2012).

[69] P. Baudrenghien, *Functional Specifications of the LHC Prototype Crab Cavity System*, Tech. Rep. CERN-ACC-NOTE-2013-003 (CERN, 2013).

[70] R. Calaga, in *Proceedings of the Chamonix 2012Workshop on LHC Performance, Chamonix, Switzerland* (2012) p. 363.

[71] O. Brüning and F. Zimmermann, in *Proceedings of the 2012 International Particle Accelerator Conference, New Orleans, USA* (2012) p. 127.

[72] R. Calaga, in *Proceedings of the 2011 Conference on RF Superconductivity, Chicago, Illinois* (2011) p. 988.

[73] W. Herr, *Features and implications of different LHC crossing schemes*, Tech. Rep. LHC Project Report 628 (CERN, 2003).

[74] Y.-P. Sun, R. Assmann, J. Barranco, R. Tomás, T. Weiler, F. Zimmermann, R. Calaga, and A. Morita, Phys. Rev. ST Accel. Beams **12**, 101002 (2009).

[75] H. Padamsee, *RF Superconductivity* (Wiley-VCH, Germany, 2009).

[76] P. N. Ostroumov, B. Mustapha, Z. A. Conway, R. L. Fischer, S. Gerbick, M. Kedzie, M. P. Kelly, I. V. Gonin, and S. Nagaitsev, in *Proceedings of the 2012 International Particle Accelerator Conference, New Orleans, Louisiana, USA* (IPAC'12 OC/IEEE, 2012) p. 2295.

[77] T. Weiland, Electronics and Communications (AEÜ) **31**, 116 (1977).

[78] T. Weiland, Particle Accelerators **17**, 227 (1985).

[79] J. R. Delayen and S. U. De Silva, in *Proceedings of the 2011 Particle Accelerator Conference, New York, New York* (PAC'11 OC/IEEE, 2011) p. 1021.

[80] J. R. Delayen and S. U. De Silva, in *Proceedings of the 2011 Conference on RF Superconductivity, Chicago, Illinois* (2011) p. 219.

[81] S. U. De Silva and J. R. Delayen, in *Proceedings of the 2010 International Particle Accelerator Conference, Kyoto, Japan* (IPAC'10/ACFA, 2010) p. 3075.

[82] S. U. De Silva and J. R. Delayen, in *Proceedings of the 2011 Conference on RF Superconductivity, Chicago, Illinois* (2011) p. 135.

[83] S. U. De Silva and J. R. Delayen, in *Proceedings of the 2009 Conference on RF Superconductivity, Berlin, Germany* (ISSN 1868–5781 / Reports of the Helmholtz Centre Berlin (HZB-Berichte), 2009) p. 589.

[84] S. U. De Silva and J. R. Delayen, in *Proceedings of the 2010 Linear Accelerator Conference, Tsukuba, Japan* (LINAC10 OC, 2010) p. 812.

[85] S. U. De Silva and J. R. Delayen, in *Proceedings of the 2011 Particle Accelerator Conference, New York, New York* (PAC'11 OC/IEEE, 2011) p. 1018.

[86] S. U. De Silva and J. R. Delayen, in *Proceedings of the 2011 Particle Accelerator Conference, New York, New York* (PAC'11 OC/IEEE, 2011) p. 1015.

[87] S. U. De Silva and J. R. Delayen, in *Proceedings of the 2012 International Particle Accelerator Conference, New Orleans, USA* (IPAC'12 OC / IEEE, 2012) p. 2411.

[88] S. U. De Silva and J. R. Delayen, in *Proceedings of the 2013 International Conference on RF Superconductivity, Paris, France* (JACoW, 2013) p. 1176.

[89] S. U. De Silva, H. Park, J. R. Delayen, and Z. Li, in *Proceedings of the 2013 Particle Accelerator Conference, Pasadena, California* (JACoW, 2013) p. 862.

[90] E. Somersalo, P. Ylä-Oijala, and D. Proch, in *Proceedings of the 1995 Particle Accelerator Conference, Dallas, Texas, USA* (IEEE, 1995) p. 1500.

[91] MATLAB, *Version 7.12.0.635 (R2011a)* (The MathWorks Inc., Natick, Massachusetts, 2011).

[92] S. Fartoukh, "Private communication," .

[93] H. Padamsee and A. Joshi, Journal of Applied Physics **50**, 1112 (1979).

[94] R. Calder, G. Dominichini, and N. Hilleret, Nucl. Instrum. Methods **13**, 631 (1986).

[95] M. A. Furman and M. T. F. Pivi, Phys. Rev. ST Accel. Beams **5**, 124404 (2002).

[96] A. Hatch, Nucl. Instrum. Methods **41**, 261 (1966).

[97] F. L. Krawczyk, "emph "bibinfo title STATUS OF MULTIPACTING SIMULATION CAPABILITIES FOR SCRF APPLICATIONS, Tech. Rep. LA-UR-01-6447 (Los Alamos National Laboratory, 2001).

[98] K. Ko, A. Candel, L. Ge, A. Kabel, R. Lee, Z. Li, C. Ng, V. Rawat, G. Schussman, and L. Xiao, in *Proceedings of the 2010 Linear Accelerator Conference, Tsukuba, Japan* (LINAC10 OC, 2010) p. 1028.

[99] K. Ko, N. Folwell, L. Ge, A. Guetz, L. Lee, Z. Li, C. Ng, E. Prudencio, G. Schussman, R. Uplenchwar, and L. Xiao, Physica C: Superconductivity **441**, 258 (2006).

[100] S. U. De Silva, A. Castilla, and J. R. Delayen, in *Proceedings of the 2013 International Particle Accelerator Conference, Shanghai, China* (JACOW, 2013) p. 2483.

[101] J. L. Kirchgessner, in *Proceedings of the 1987 Workshop on RF Superconductivity, Illinois, USA* (Argonne National Laboratory, 1987) p. 533.

[102] H. Park, S. U. DeSilva, and J. R. Delayen, in *Proceedings of the 2013 Particle Accelerator Conference, Pasadena, California, USA* (JACOW, 2013) p. 865.

[103] D. Gorelov, T. Grimm, S. U. De Silva, and J. R. Delayen, in *Proceedings of the 2012 International Particle Accelerator Conference, New Orleans, USA* (IPAC'12 OC / IEEE, 2012) p. 2411.

[104] H. R. S. Moura and L. de Moura, AIP Conf. Proc. **927**, 165 (2007).

[105] J. E. Jensen, W. A. Tuttle, R. B. Stewart, H. Brechna, and A. G. Prodell, *Brookhaven National Laboratory Selected Cryogenic Data Notebook, Volume 2* (Brookhaven National Laboratory, Associated Universities, Inc., USA, 1980).

[106] H. Park, S. U. DeSilva, and J. R. Delayen, in *Proceedings of the 2012 International Particle Accelerator Conference, New Orleans, Louisiana, USA* (JACOW, 2012) p. 2450.

[107] H. Park, S. U. DeSilva, and J. R. Delayen, in *Proceedings of the 2011 Conference on RF Superconductivity, Chicago, Illinois, USA* (JACOW, 2011) p. 188.

[108] J. Brawley, J. Mammosser, and L. Phillips, in *Proceedings of the 1997 Workshop on RF Superconductivity, Abano Terme (Padova), Italy* (INFN - Legnaro National Laboratory, 1997) p. 518.

[109] R. L. Geng, in *Proceedings of the 2011 Conference on RF Superconductivity, Chicago, Illinois* (ANL, Chicago, Illinois, 2011) p. 798.

[110] L. C. Maier and J. C. Slater, Journal of Applied Physics **23**, 68 (1951).

[111] P. Kneisel, Nucl. Instrum. Methods Phys. Res., Sect. A **557**, 250 (2006).

[112] "Panametrics 25DL-Plus Ultrasonic Precision Thickness Gage," `http://www.olympus-ims.com/en/25dl-plus`.

[113] B. Bonin and R. Röth, Particle Accelerators **40**, 59 (1992).

[114] G. Ciovati, G. Myneni, F. Stevie, P. Maheshwari, and D. Griffis, Phys. Rev. ST Accel. Beams **13**, 022002 (2010).

[115] P. Kneisel, in *Proceedings of the 1999 Workshop on RF Superconductivity, Santa Fe, New Mexico, USA* (LANL, 1999) p. 328.

[116] J. Kirchgessner, J. Graber, W. Hartung, J. Lawton, D. Moffat, H. Padamsee, D. Rubin, J. Sears, and Q. S. Shu, in *Proceedings of the 1989 Particle Accelerator Conference, Chicago, Illinois, USA* (IEEE, 1989) p. 482.

[117] C. Reece, P. Denny, and A. Reilly, in *Proceedings of the 2013 International Conference on RF Superconductivity, Paris, France* (JACOW, 2013) p. 213.

[118] C. Reece, B. Almeida, T. Powers, and J. Susta, in *Proceedings of the 1991 Particle Accelerator Conference, San Francisco, California, USA* (IEEE, 1991) p. 2325.

[119] "TOMCO RF Amplifier," `http://www.tomcorf.com/productlist.html`.

[120] C. Reece, P. Kushnick, and T. Powers, in *Proceedings of the 1991 Particle Accelerator Conference, San Francisco, California, USA* (IEEE, 1991) p. 1508.

[121] T. Powers, in *Proceedings of the 2005 Workshop on RF Superconductivity, Ithaca, New York, USA* (Cornell University, 2005) p. 40.

[122] M. Kelly, in *Proceedings of the 2007 Conference on RF Superconductivity, Beijing, China* (Peking University, Beijing, China, 2007) p. 44.

[123] J. Halbritter, Zeitschrift für Physik **266**, 209 (1974).

[124] J. C. Slater, Rev. Mod. Phys. **18**, 441 (1946).

APPENDIX A

800 MHZ PARALLEL-BAR CAVITY PROTOTYPE

A half scaled cavity with exact half dimensions of a 400 MHz elliptical cavity was fabricated by Niowave Inc [86]. The 800 MHz model was carved using an Al block with separate end plates clamped together as shown in Fig. 162. The HOM spectrum of the elliptical cavity is shown in Fig. 163.

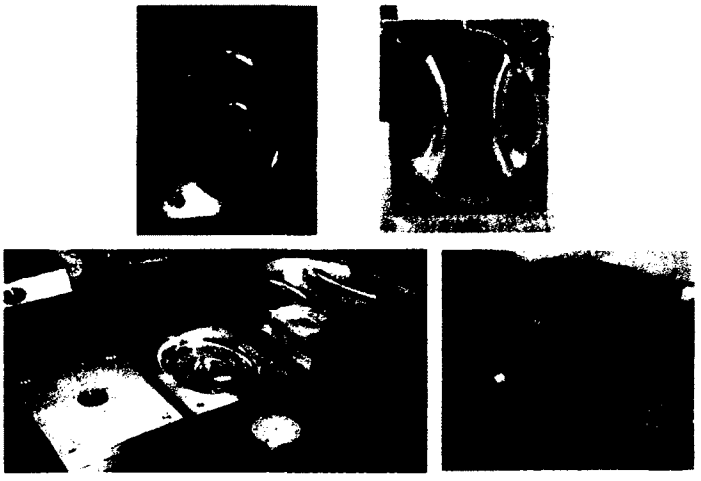

FIG. 162. 800 MHz elliptical cavity.

All the modes measured up to 4.0 GHz using a network analyzer were compared with the simulation results obtained from CST Microwave Studio [13]. The modes were measured and identified using different coax type and loop type probe combinations. All the modes that were generated by the CST Microwave Studio were identified on the measured data and were in good agreement. The electric and magnetic field profiles of the first ten modes are listed in Table. 26.

TABLE 26. Field profile of the first 10 modes of the 800 MHz elliptical cavity.

Mode	Frequency (MHz)	E Field		H Field	
		yz plane	xz plane	yz plane	xz plane
1	800.46	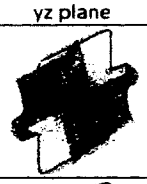		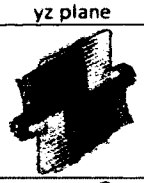	
2	1219.55				
3	1354.89				
4	1356.75				
5	1609.49				
6	1702.66				
7	1898.14				
8	1969.25				
9	2053.16				
10	2054.27				

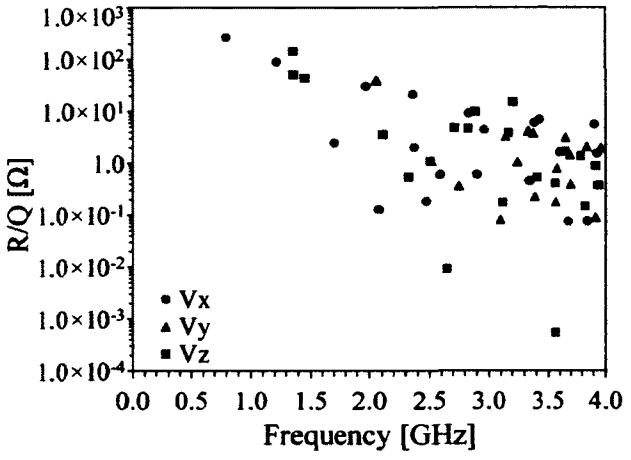

FIG. 163. Higher order mode spectrum of the 800 MHz elliptical cavity.

APPENDIX B

HIGHER ORDER MULTIPOLE COMPONENTS

The multipole components can also be determined using the Lorentz force method given by the Eq. 46, with transverse electric and magnetic field components.

$$\Delta p_t^{(n)}(z) = \frac{q}{c} r^{n-1} \int_{-\infty}^{+\infty} \left[E_x^{(n)}(z) \cos(j\omega t) + jcB_y^{(n)} \sin(j\omega t) \right] \mathrm{d}z \,. \qquad (177)$$

The real and imaginary parts of the normal multipole components can be expressed by expanding Eq. 49 as,

$$B_z^{(n)} = \frac{1}{c} \left[E_t^{(n)}(z) \cos(\omega t) - cB_t^{(n)}(z) \sin(\omega t) \right] + j \frac{1}{c} \left[E_t^{(n)}(z) \sin(\omega t) - cB_t^{(n)}(z) \cos(\omega t) \right] \qquad (178)$$

The similar extraction of the horizontal electric field and vertical magnetic field components ($E_x^{(n)}(z)$ and $H_y^{(n)}(z)$) are shown in Figs. 164 and 165 for the fields extracted at a radius of 15 mm for the 499 MHz. Figures 166 and 167 show the $E_x^{(n)}(z)$ and $H_y^{(n)}(z)$ for the 400 MHz cavity where the fields were extracted at a radius of 30 mm.

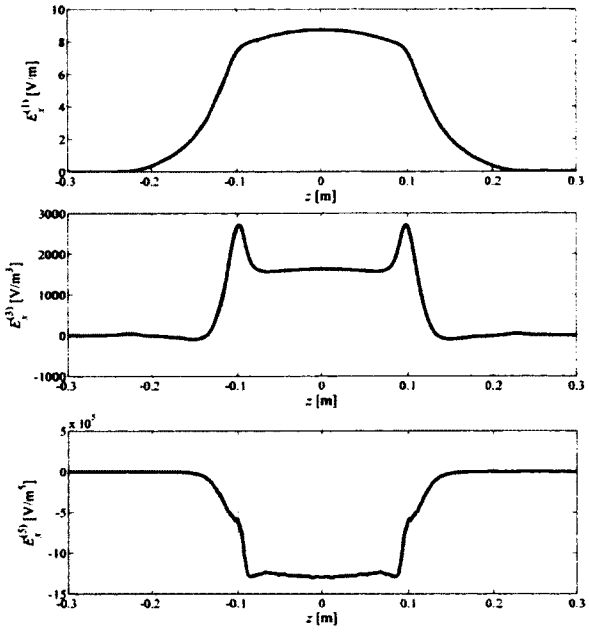

FIG. 164. Time independent multipole field components of $E_x^{(n)}(z)$ for the 499 MHz rf-dipole cavity for orders n=1, 3, and 5.

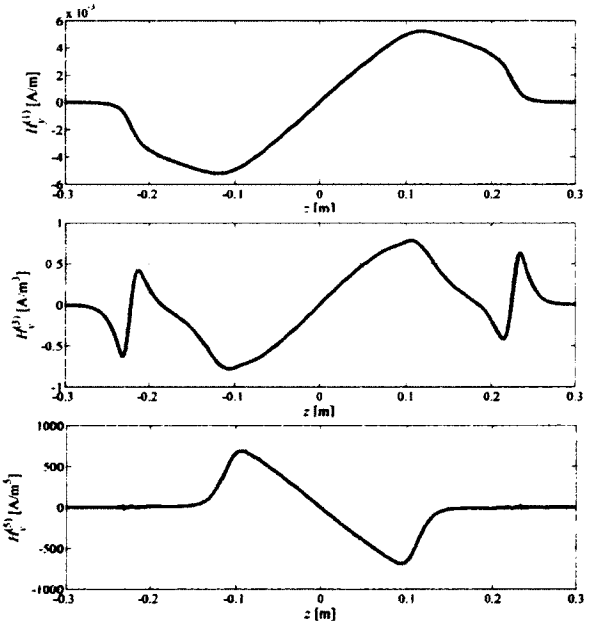

FIG. 165. Time independent multipole field components of $H_y^{(n)}(z)$ for the 499 MHz rf-dipole cavity for orders n=1, 3, and 5.

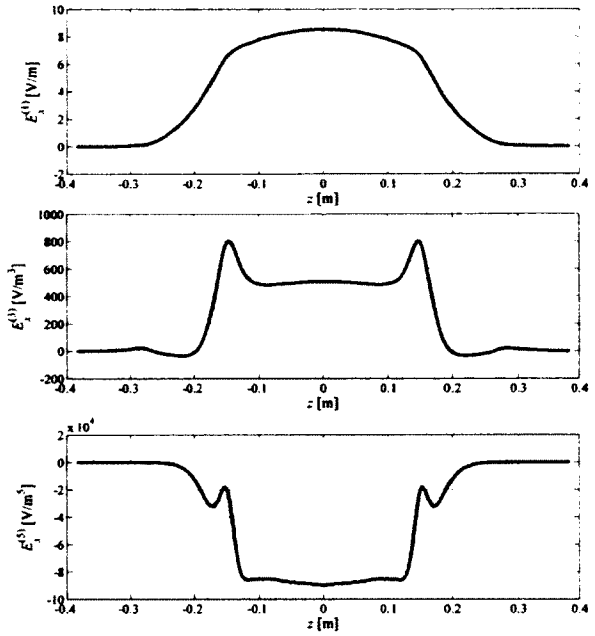

FIG. 166. Time independent multipole field components of $E_x^{(n)}(z)$ for the 400 MHz rf-dipole cavity for orders n=1, 3, and 5.

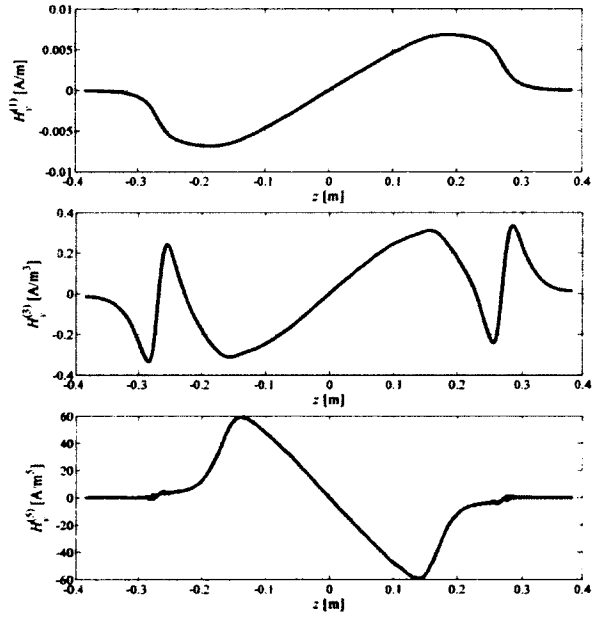

FIG. 167. Time independent multipole field components of $H_y^{(n)}(z)$ for the 400 MHz rf-dipole cavity for orders n=1, 3, and 5.

VITA

Subashini Uddika De Silva
Department of Physics
Old Dominion University
Norfolk, VA 23529

Subashini De Silva was born on March 28, 1981 in Colombo, Sri Lanka. She obtained Bachelor degree in Physics from University of Colombo, Sri Lanka in 2004. At the same time she completed her second Bachelor degree in Information Technology, as an external student from the same university.
Subashini joined the Department of Physics at Old Dominion University Norfolk, VA, USA as a graduate student in 2006, and completed her Masters degree in Physics in 2008.

Typeset using LaTeX.